



The
University
Of
Sheffield.

**Formation and Three-dimensional Microstructure of
Porous Ceria-Related Nanomaterials**

By:

Carlos Mauricio Brambila Renteria

A thesis submitted in partial fulfilment of the requirements for the degree of
Doctor of Philosophy

The University of Sheffield

Faculty of Engineering

Department of Materials Science and Engineering

November 2019

Abstract

Notwithstanding the promising catalytic properties of novel porous ceria nanomaterials, their nanostructure has remained incompletely explored. Ceria and its related materials have remained at the centre of extensive catalytic applications. More recently, the capabilities of these materials have been combined with novel porous morphologies to overcome new challenges in environmental and industrial catalysis. This study aims to determine the nanoscale mechanisms that drive the formation of porous ceria nanomaterials. Such an understanding is instrumental in advancing the design and applications of these novel materials. By implementing different techniques across electron microscopy, this work complements the findings of catalysis groups who have evidenced the higher catalytic performance of porous vs non-porous ceria nanomaterials.

Based on a review of the literature, two fabrication methods of porous ceria were selected. In one case, pores were induced by annealing ceria nanomaterials at 800 and 950 °C. In the other, porous ceria was synthesised from a precursor via a nanocasting method. The intermediate and final products of these two approaches were characterised in detail using electron microscopy for imaging, analysis and tomographic reconstructions. For pre-synthesised nanoparticles, the studies here were able to resolve, for the first time, the full 3D shape and location of the pores, as well as their crystallographic alignment. Furthermore, the present work has shown transformations at previously unpublished near-sintering temperatures. This experiment rendered the first reported occurrence of porous defects in annealed nanocubes. The present work shows a novel image-processing algorithm, which expands the capabilities of reduced-information tomography techniques to reconstruct porous materials. Further research could use this new method to reconstruct currently unresolved porous and multi-phase structures. As for nanocasting products, the advanced characterisations determined the correlation between characteristics of the template and the product. To establish this relation here is reported the first infiltration of MSU-F to form a silica/ceria composite.

Acknowledgements

This work was supported by Federal Trust number 2137, CONACYT-Ministry of Energy-Hydrocarbons, under the declaration HYDROCARBONS–HUMAN RESOURCES 2013-01. This declaration is a collaborative project between the Ministry of Energy, SENER, and the National Council of Science and Technology, CONACYT (Mexico), which seeks to train human resources specialised in the petrol industry. Its main objective is to complement the assimilation, innovation and technological development in subjects related with exploration, exploitation and refining of hydrocarbons; the production of basic petrochemicals and the prevention of pollution, as well as for bioremediation associated with activities of the petrol industry.

The present doctoral research was carried out under the supervision of Dr Günter Möbus, who provided regular progress monitoring and oversaw the thesis production. Pastoral support was provided by the postgraduate research tutor, Dr Tom Hayward. Electron microscopy training and experimental work were performed at the Sorby Centre, within the Department of Materials Science and Engineering. The hydrothermally treated ceria raw materials have been gratefully received from Prof S. Seal, University of Central Florida. TEM support in the Sorby Centre was thankfully received from Dr J. Nutter and Dr I. M. Ross.

I, the author, confirm that the Thesis is my own work. I am aware of the University's Guidance on the Use of Unfair Means (www.sheffield.ac.uk/ssid/unfair-means). This work has not previously been presented for an award at this, or any other, university.

Contents

1	Introduction	1
2	Literature Review	5
2.1	The role of materials science in catalysis	5
2.1.1	The state-of-the-art in catalytic materials	6
2.1.1.1	Nanostructuring of metal oxides for catalysis.....	7
2.1.1.2	Economic and environmental importance of metal oxide catalysts	9
2.1.1.3	Metal oxide nanostructures in catalysis	10
2.1.2	Catalytical activity in porous oxides and other materials	11
2.1.2.1	The influence of porosity on the catalytic behaviour of oxides	13
2.1.3	Mesoporous materials for catalysis	14
2.1.3.1	Outstanding challenges in MPS technologies	18
2.1.4	Synthesis and characterisation methods of porous catalytic materials.....	18
2.1.4.1	Nanocasting.....	19
2.1.4.2	Characterisation of nanoporous materials.....	20
2.2	Catalytic potentials of porous ceria nanomaterials	21
2.2.1	The significance of CeO ₂ for industrial catalysis.....	22
2.2.1.1	The use of ceria in CO oxidation.....	23
2.2.1.2	The role of ceria in CO ₂ conversion	24
2.2.1.3	Applications of ceria in organic catalysis and biomedical research.....	25
2.2.2	The effects of nanoscale morphology on the activity of nanoceria	28
2.2.3	Selective preparation methods of ceria nanomaterials	29
2.2.3.1	Crystal-growth directed methods	31
2.2.3.2	Surfactant-assisted methods.....	32
2.2.3.3	Template-assisted methods	33
2.2.3.4	Alternative preparation methods	34
2.2.4	Crystalline defects, vacancies and cavities in ceria nanomaterials	34
2.3	The capabilities of advanced TEM for the study of porous nanocatalysts	38
2.3.1	The role of TEM in nanomaterials research	38
2.3.2	Advanced TEM techniques and their use in heterogeneous catalysis.....	41
2.3.2.1	High-resolution transmission electron microscopy (HRTEM).....	41
2.3.2.2	High-angle annular dark-field scanning TEM (HAADF-STEM).....	42
2.3.2.3	Energy-dispersive X-ray spectroscopy (EDS)	43

2.3.2.4	Electron-energy-loss spectroscopy (EELS) and energy-filtered TEM (EFTEM).....	44
2.3.3	Electron Tomography (ET).....	46
2.3.4	The capabilities of TEM in studying nanoporous materials	48
3	<i>Experimental Methods</i>	51
3.1	Electron microscopy instrumentation	51
3.1.1	JEOL JEM-2010F	52
3.1.2	JEOL JEM-3010.....	53
3.1.3	Electron tomography instrumentation	53
3.1.4	Philips EM-420	54
3.1.5	JEOL JEM-F200	55
3.1.6	Scanning Electron Microscopes Inspect F/F50.....	55
3.2	Digital image analysis and processing	56
3.2.1	ImageJ.....	56
3.2.2	TomoJ.....	57
3.2.3	Chimera.....	57
3.2.4	Adobe Creative Cloud	58
3.3	Further experimental methods	58
4	<i>Ageing of Metastable Ceria Nanomaterials</i>	59
4.1	Effect of room-temperature storage	60
4.1.1	Sample preparation of air-stored nanocubes and nanorods	61
4.1.2	TEM of air-stored ceria nanorods	61
4.1.3	TEM imaging of aged ceria nanocubes	67
4.2	Near-sintering heat-treatment ageing	71
4.2.1	Heat-treatment procedure	72
4.2.2	TEM imaging of ceria nanorods after heat treatment at 800°C	73
4.2.2.1	Integrity of the terminal morphology of nanorods after annealing at 800° C.....	77
4.2.2.2	Discovery of negative-rod defects.....	78
4.2.3	TEM of ceria nanorods annealed in powder form at 950 °C.....	79
4.2.4	TEM of ceria nanorods annealed in a heat-resistant sample at 950 °C.....	87
4.2.5	HRTEM of ceria nanocubes annealed in powder form at 950 °C.....	92
4.2.5.1	Discovery of porosity defects in annealed nanocubes	96
5	<i>Electron Tomography of Mesoporous CeO₂ Nanorods</i>	98
5.1	Tomography of porous rods	100
5.1.1	Image acquisition	100

5.1.1.1	Tilt-series acquisition	103
5.1.2	Image alignment and pre-processing	106
5.1.2.1	Image alignment	106
5.1.2.2	Image pre-processing	111
5.1.3	Image processing	116
5.1.4	3D visualisation	118
5.2	Supplementary tomographic studies	124
5.2.1	Theoretical missing-wedge reconstructions	125
5.2.2	Tomography of a non-porous rod	126
5.2.3	Further modifications of geometric tomography from one-dimensional information	130
5.2.3.1	Application of GT for cross-sectional reconstructions	132
5.2.3.2	Shape-from-contour cross-sectional reconstructions	134
6	<i>Formation of Functional Composites and Porous Materials via Nanocasting</i>	<i>137</i>
6.1	Study of opals and inverse-opal formation	138
6.1.1	Self-assembly of colloidal crystals from PS beads	139
6.1.1.1	Colloidal Vertical Deposition	139
6.1.1.2	Centrifugation	139
6.1.1.3	Sedimentation	140
6.1.2	Characterisation of polystyrene opals	140
6.1.2.1	Visible-light microscopy (VLM)	141
6.1.2.2	Scanning electron microscopy	144
6.1.2.3	Transmission electron microscopy	147
6.1.3	Self-assembly of colloidal crystals from green-synthesised SiO ₂ beads	148
6.1.4	Infiltration of polystyrene opals with ceria precursor	152
6.1.5	Calcination of PS-opal/ Ce(NO ₃) ₃ ·6H ₂ O composite	155
6.2	Study of mesoporous silica and MPS-based catalytic composites	159
6.2.1	TEM study of MSU-F mesoporous silica and MSU-F/CeO ₂ composite	160
6.2.1.1	Three-dimensional TEM of MSU-F	161
6.2.1.2	Preparation and characterisation of MSU-F/CeO ₂ composite	162
6.2.1.3	Chemical etching of MSU-F/CeO ₂ composite	169
6.2.2	Study of SBA-15 and SBA-15-based composites	172
6.2.2.1	Preparation and characterisation of SBA-15/CeO ₂ composite	173
6.2.2.2	Preparation and characterisation of SBA-15/CuO composite	175
7	<i>Discussion</i>	<i>189</i>
7.1	Main findings	189

7.1.1	The effect of heat treatment on ceria nanomaterials	189
7.1.2	Formation mechanism of heat-induced defects in CeO ₂ nanomaterials.....	190
7.1.3	Microstructure of casted porous nanomaterials and composites	191
7.1.4	Formation mechanisms of nanocasting products	192
7.1.5	The capabilities of electron microscopy in the study of porous nanomaterials	194
7.1.6	The adoption of geometric tomography to the study of porous nanomaterials	194
7.1.7	The impacts of findings in catalysis applications and the science of porous materials	196
7.2	Consensus of findings across experimental areas.....	197
	<i>Conclusions</i>	200
	<i>Publications</i>.....	203
	<i>References</i>	204

Chapter One

Introduction

The advancement in the design and application of nanomaterials requires characterisation techniques that keep up with their ever-decreasing size and increasing complexity. In particular, catalytic applications rely on the finest morphological and chemical features of functional materials. Given the redox capabilities of CeO_2 and the importance of porous nanostructures for heterogeneous catalysis, there has been a prevalent interest in the development of porous ceria nanomaterials. However, despite the abundant research publications on their catalytic properties, the nanostructure and growth-history of these materials have remained largely unexplored. The present work seeks to further the understanding of a selection of relevant porous ceria nanomaterials by using a diversity of imaging and microanalysis techniques across electron microscopy. By characterising intermediate, as well as final, synthesis products, this research provides valuable insight into the formation mechanism of pores and other defects inside ceria nanostructures.

The materials selected for this project belong to three major groups: opals, mesoporous silicas, and nanoshapes of ceria containing pores as by-products. As well as being selected for their relevant applications, this catalogue of materials serves the present study as it systematically covers a wide range of properties. Considering their variety of properties, the characterisation work presented here is not only relevant for the preparation and uses of the materials being investigated but contributes to the understanding of nanoscale porous materials in general. This variety of materials showcases the capabilities of electron microscopy characterisation techniques by covering a wide range of pore sizes; 100-200 nm for opals, 8-20 nm for mesoporous silica (MPS) and 2-5 nm for ceria nanoparticles. Amongst ceria nanoshapes, nanorods are of particular interest, as they present higher catalytic performance than other ceria nanostructures of the similar surface area [1]. This is attributed to the presence of exposed planes and to the prevalence of $\{100\}$ and $\{110\}$ surfaces. More recently, there have been reports of heat-induced defects in ceria nanorods, which seem to enhance their catalytic performance [2], [3]. The detailed morphology of the rod has been well established in the literature [4]. Nevertheless, the three-dimensional shape and distribution of these heat-induced defects have remained a matter of debate.

Opals are colloidal crystals consisting of self-assembled nanospheres, which present close-packed ordering in the long-range. Opal materials can be found widely across the literature as templates for the fabrication of porous materials. Briefly, colloidal crystals are deposited from a suspension of nanospheres. After their assembly, opals are infiltrated with a ceria precursor, which converts into CeO_2 upon calcination. Then, the opal template is removed to produce an inverse opal structure, which presents a highly accessible porous structure with long-range periodicity. Notwithstanding the prevalence of this preparation method, the intermediate products leading to the inverse opal structure have remained unexplored. The present work characterised the several phases formed during the fabrication of inverse opals, thus improving the understanding of their formation mechanism.

Mesoporous silicates (MPS) are a large family of materials that consist mostly of ordered arrays of pores separated by thin walls of silica, which may contain small amounts of aluminium, magnesium and other elements. For this work, two varieties of MPS have been selected. First, one of the most popular materials of this type, SBA-15, which consists of highly ordered pores of constant size. Secondly, MSU-F silica, which is an exceptional MPS structure in that its pores lack periodical ordering, and have a narrow pore-size distribution around 20 nm, making it one of the widest pore sizes across MPS materials [5]. Due to its wide pores, the processing presented here provides valuable insight into its mechanical stability. Despite the widespread use of MPS materials as templates for the fabrication of porous materials, a formal study of the nanostructure of the casted products has not been found.

As mentioned above, the literature abounds with catalytic studies of the selected materials, which have established their relevance for multiple applications. Nonetheless, there is a significant imbalance between the catalytic characterisations of these materials and the studies of their nanostructure, as identified by several authors [6]–[8]. By incorporating comprehensive electron microscopy studies, this work aims to contribute to the understanding of nanostructured porous materials. Often, novel porous nanomaterials are characterised using traditional porosity techniques, such as mercury-intrusion porosimetry or hydrogen adsorption. These techniques are not a substitute for electron microscopy, as they fail to provide the accurate shapes and sizes of individual pores and other nanoscale properties. These fine features directly influence the defect chemistry and performance of catalytic materials.

The incorporation of advanced electron microscopy to the study of nanoporous materials presents numerous challenges, which will be addressed throughout the present work. Foremost, the three-dimensional distribution of pores limits the capabilities of conventional two-dimensional imaging techniques. To overcome this challenge, the present work presents a novel algorithm of electron tomography, which benefits from the method of geometric tomography [9] and expands its capabilities to reconstruct porous materials for the first time. Moreover, the present work uses advanced TEM techniques for the exploration of heat-treated ceria nanorods

and cubes. These studies investigate the defect-behaviour of these materials at temperatures higher than those previously reported by the available literature.

A third related area of the study reported here consists of a comprehensive exploration into the formation mechanisms of materials made from the aforementioned templates, MPS and opal materials. This study provides valuable insight into the effects of the template properties and preparation conditions. Mainly, the study contributes to the understanding of the nanoscale mechanisms involved in template-infiltration, which have remained a matter of debate [10]. Moreover, by studying template materials with a diversity of structural properties, the present work provides insight into the properties of the templates that dictate the structural continuity and quality of nanocasted products.

The design and preparation of nanoporous materials benefit from the understanding of the nanoscale phenomena explored in this work, such as the crystallographic effects of heat treatment and the nanoparticulate aggregation inside porous templates. The common belief in the catalysis community is that heat treatment of active materials is always detrimental to their performance [11]. This view has been contrasted by the recent investigations into the heat-induced defects in ceria nanomaterials [2], [3], [12], [13]. The present work reports the transformations of ceria nanomaterials under different heating conditions and uses a variety of TEM characterisations to identify the nanoscale properties that give rise to the improved catalytic performance established in the literature [2], [14].

The advances in the characterisation methodologies proposed throughout these experiments provide significant benefits beyond the understanding of the materials of interest. Frequently, the Bragg-enhanced-contrast artefacts present during conventional TEM impede the acquisition of suitable tilt series. Therefore, researchers often combine electron tomography with advanced TEM techniques that can suppress those artefacts, such as EFTEM or HAADF-STEM [15], [16]. Another viable alternative can be found in [17], where geometric tomography has been shown to reconstruct reliable three-dimensional objects by suppressing imaging artefacts with image processing. Therefore, the development of a modified form of the geometric tomography algorithm, as presented in this report, allows porous materials to be characterised in three-dimensions without the need for sophisticated advanced TEM instrumentation.

The present dissertation introduces the relevance and background of the experimental work by covering an extensive range of related literature. Then, the major experimental work is presented. Chapter 3 outlines the main experimental methodologies applied during this project. Chapter 4 explores the morphological and structural effects of ageing on metastable ceria nanomaterials. In Chapter 5, those heat-induced defects are characterised in three-dimensions using novel methods within electron tomography. Chapter 6 presents a comprehensive study of the formation of porous materials via nanocasting. Lastly, a discussion is presented covering the main findings across the experimental areas, and the contributions of this work.

The following list summarises the overall aim and objectives met in each experimental section of this work:

- This study aims to determine the nanoscale mechanisms that drive the formation of porous ceria nanomaterials by implementing different techniques across electron microscopy.
- In order to understand the formation and growth mechanisms of porous defects in ceria nanorods, the present work introduces a methodology of heat treatment followed by transmission electron microscopy characterisations. These results are summarised in Chapter 4.
- Particular emphasis is placed on the three-dimensional structure of pores in different nanomaterials, which have been established as relevant to the catalysis community by the cited literature. Chapter 5 of the present work reports the use of electron tomography to achieve this objective.
- Chapter 6 reports the experimental study of infiltration mechanisms driving the fabrication of template-replication products. In order to explore these effects at various magnifications, this work incorporates characterisation methodologies using scanning electron microscopy, visible light microscopy, as well as transmission and scanning-transmission electron microscopy.

Chapter Two

Literature Review

This chapter presents the most relevant publications which surround and precede the present research. This review is not meant as an exhaustive list of the literature on the subject, nor as a chronological account of the texts regarding the topic. The aim herein is only to place the present work in the wider context of the scientific conversation. To this end, the sampled literature covers the major aspects of this work: the field of application, the material of interest and choice of methodology. Respectively, heterogeneous catalysis, porous nanocerium and advanced transmission electron microscopy.

The first section explores the literature on heterogeneous catalysis to convey the main developments and outstanding challenges. Emphasis is placed on the most important applications, and discuss the expanding role of porous nanomaterials in catalytic technologies. The following subchapter outlines the current importance of ceria-based materials for industrial catalysis. This section briefly introduces the major properties of CeO₂ at the nanoscale, which substantiate the research uncovering its new potentials. The review finishes with an exploration into the main contributions of advanced transmission electron microscopy to the field of nanocatalysts, with an emphasis on the study of three-dimensional porosity.

2.1 The role of materials science in catalysis

A solid-state catalyst is a functional material, which is used to alter the rate of chemical reactions. This can entail accelerating a reaction, by decreasing the activation energy of reactants or promoting selectivity in multi-product reactions. The latter is of great interest to the chemical industry, as catalysts can be used to reduce the production of waste and pollutants [18]. Although they share basic characteristics with other forms of catalysts, catalytic materials present their unique advantages and limitations. While catalytic gases and liquids will generally present higher efficiencies, solid catalysts are reusable and environmentally friendly [19].

Heterogeneous catalysis is understood as the chemical catalysis process where the phase of the catalyst differs from the physical state of the reactants or products. In contrast, in homogeneous catalysis the reactants, products and catalyst are in the same liquid or gaseous phase. Solid-state catalysis takes place in the catalytically active sites of the material. Therefore, its

functionality will depend on its capability to create new active sites while still being exposed to reaction conditions. The morphology of the catalyst is of vital importance, as it will determine the accessibility of the active sites. Finally, the chemical composition of the catalyst must be such that the thermodynamic equilibrium between the materials is maintained, as to avoid further unwanted products or the catalyst being consumed [20].

2.1.1 The state-of-the-art in catalytic materials

The chemical industry relies on catalysis to a great extent for efficiency and sustainability. In Figure 2.1, Behrens [21] summarises the prevalence of catalytic processes across industrial applications, where up to 85% of processes include at least one step of catalysis. Out of these, 80% employ heterogeneous catalysts. These numbers are only expected to increase as the industry continues to adopt more green chemistry strategies. The selective nature of catalytic solids is central for the prevention of emissions, as well as for remediation processes such as wastewater treatment [22]. The environmental importance of developing efficient heterogeneous catalysts is therefore hard to overstate, and they are expected to play a central part in the transition to a carbon-neutral society.

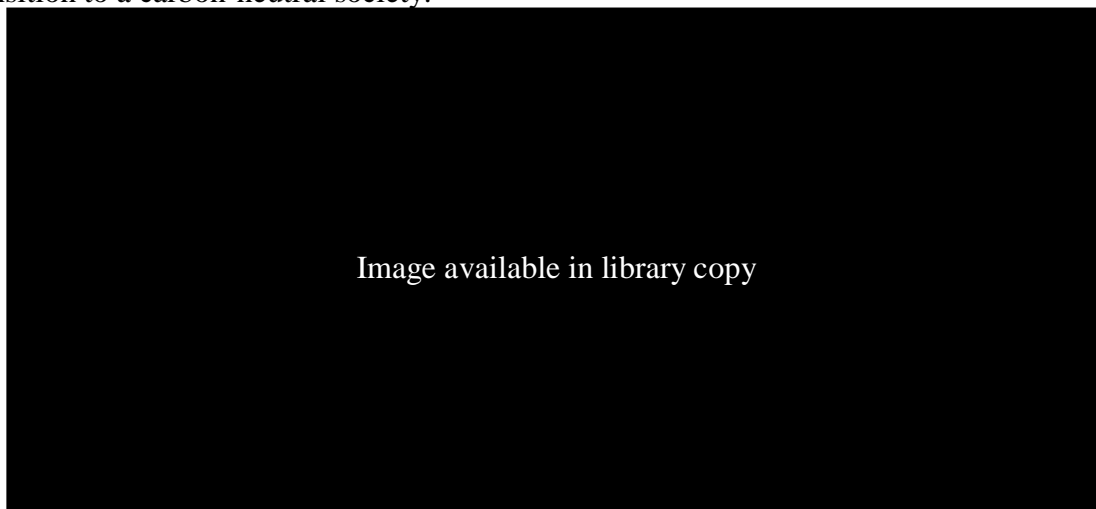


Figure 2.1 The utilisation of solid-state catalysts in comparison to other types of catalysts, and the prevalence of catalytic processes across the chemical industry [21]

Inorganic chemists have been attempting to develop a predictive model of catalytic activity for over 50 years [20]. This ‘standard model’ would allow researchers to develop catalysts with optimised combinations of structure, composition and chemical behaviour. However, their success has been very limited when compared to other members of the family of nanoscience, e.g. semiconductors [23], [24]. This disparity is unsurprising given the dynamic aspect of catalysis.

To draw on the same example, researchers can predict the behaviour of a semiconductor material when they understand the activity affecting its electronic structure, while the chemistry and geometry of the semiconductor remain unchanged under normal conditions [25], [26].

In contrast, catalytic action not only alters the electronic structure of material but simultaneously changes its geometry and chemistry during every cycle with varying degrees of reversibility. This challenge has driven catalytic research towards a more empirical approach, with the number of publications on conceptual catalysis steadily declining since the early 1990s [27]. The widespread trend, therefore, is to focus on the development of catalysts with desirable properties, without placing much emphasis on theoretical or experimental justification at a molecular level [20].

A variety of materials have found established uses as heterogeneous catalysts, and more are continually being developed. Notable examples are metals (including multi-metal systems) [28], graphene and carbon supports [29], carbides [30] and sulphides [31]. Metallic catalysts constitute a particular point of focus for industry and research alike. Liu et al. recently published a comprehensive review outlining the variety of applications which benefit from catalytic metals [28]. These include organic reactions, electrocatalysis, photocatalysis, selective hydrogenation and CO oxidation. Their review also highlights the research efforts devoted to understanding the factors driving metallic catalysis, which range from atomic geometry and electronic structure to the interactions between the metal and selected solvents. Nanostructured metals can be expected to remain a major topic in research, as well as to prevail across a great number of catalytic applications.

However, amongst this ever-expanding catalogue of catalytically active materials, metal oxides continue to be central to most applications [32]–[35]. Over 60 years ago, they were found to catalyse a diversity of acid-base, hydrothermal and oxidation reactions, which led to their extensive use in the energy sector [36]. Today, their capabilities are still massively relied upon for petrochemical uses [18], plus emerging applications in pharmaceutical chemistry [37], specialised synthesis and environmental processes [38]. Furthermore, the catalytic activity of metal oxides has continued to improve as researchers learn more about them [39].

2.1.1.1 Nanostructuring of metal oxides for catalysis

Early studies on metal oxide catalysts explored the enhancement of activity per unit weight by reducing the particle size to the nanoscale. The reduction in particle diameter would increase the surface-area-to-volume ratio (SA:V), thus improving reactivity. Similarly, porous materials and other non-compact solids exhibit higher chemical activities than their monolithic counterparts, owing to higher SA:V values. This knowledge was accompanied by developments in preparation methods, as well as additives and related technologies [40]. However, the research

objectives soon shifted from exploring the effect of particle size to a more careful consideration of the products of different preparation methods, i.e. morphology at the nanoscale [41].

Today, catalytic performance is not only understood as regulated by particle size but also as highly dependent on the shape of the nanoparticles. This discovery has triggered the need for a shape-selective synthesis of catalytic oxides. Additionally, because metal oxides are typically crystalline, studies have emphasised the facets favoured by different morphologies and, subsequently, the structural selectivity of catalytic reactions. Section 2.2 will discuss further the publications on the relationship between morphology, crystallinity and catalytic activity for the particular case of CeO_2 and related materials.

Catalytic metal oxides are regularly employed in most industrial processes that involve acid-base or oxidation reactions [42]. This width of applications has brought about the development of a great variety of compositions to suit different purposes. Some simple oxides such as alumina and zeolites, play an important role in acid-catalysed reactions, including fluid-catalytic cracking and isomerisation [43]–[47]. Mixed oxides like molybdates, tungstates or antimonates are used in the ammoxidation of propylene to produce acrylonitrile, which is necessary to produce a large number of polymers from rubber to carbon fibres [38], [48], [49]. Significantly, there are many multi-component mixed oxides composed of MO_6 octahedra like vanadyl pyrophosphate or VSbO rutile phase across a wide range of high-performance catalytic applications like hydrotreating, hydrogenation and selective oxidations [18].

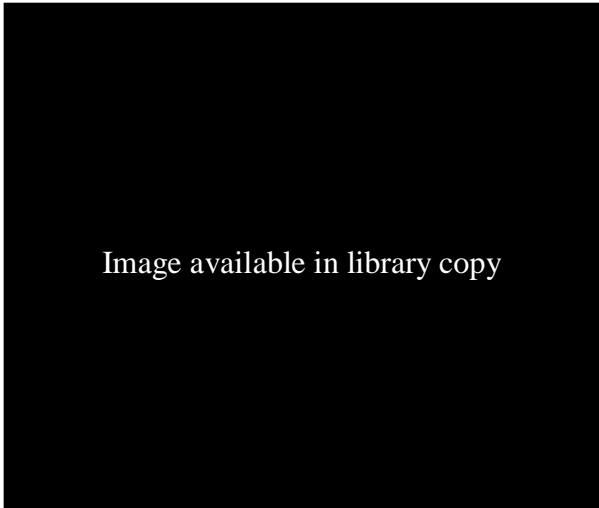


Image available in library copy

Figure 2.2 MO_6 octahedra-derived structures used in partial oxidation of alkanes: a) Vanadylpyrophosphate, b) rutile-phase VSbO, c) M1-phase MoVTe (Sb) NbO, d) Keggin molybdophosphoric acid [50]

In his 2016 review [50], Jacques Védrine compares the most studied MO_6 -derived structures for their use in oxidation catalysis, shown in Figure 2.2. More broadly, he discusses the economic importance of partial oxidative and oxidative dehydrogenation processes. As will be detailed in Section 2.2, ceria and its suboxides have attracted particular interest due to their high oxygen storage capacity and redox capabilities, which are valuable for noxious-gas-neutralisation applications like deNO_x and deSO_x reactions [51]. In addition to these applications, metal oxides prevail as supports for other active materials [52]. The synergistic interactions between the catalyst and the support have a great influence on the thermal and electron conductivities of the active phase, which in turn alters their catalytic performance.

The performance and versatility of metal oxides for catalytic applications have encouraged researchers to develop a large number of preparation methods. Common examples include pH-dependent co-precipitation, sol-gel processes and hydrothermal synthesis [53]–[56]. Researchers have extensively optimised each method in the search for higher selectivity, better energy efficiency or complex structures for particular applications like hierarchical nanoporosity [57]. These methods will normally produce precursor materials which need activation before catalysis applications. Thermal treatment is the most common way to achieve this, which converts inorganic anions like sulphates, chlorides and nitrates into the oxide phase of interest [58]. Heat treatment after this step is generally considered detrimental, as sintering can destroy the catalytically active features like edges and corners.

2.1.1.2 Economic and environmental importance of metal oxide catalysts

Alternative eco-friendly technologies for activation have ensued, which do not require an external source of heat [59], [60], as shown in Figure 2.3 [18]. Some of these methods provide the energy necessary for the conversion of the precursor in the form of mechanical force (e.g. ball-milling), electric field or through the action of ultrasonic waves, while others use radiation to generate the heat required *in situ* [60]. The development of selective, energy-efficient and sustainable methods of preparation can be expected to continue to grow an area of focus in catalysis research, as the applicability of new materials hinges on the development of fabrication strategies, which can expand to an industrial scale.

Clean-air strategies are an established priority for many organisations and governments seeking to reduce the number of substances hazardous to human health and wildlife [61]. Industries and regulators rely upon a large number of catalytic processes for the achievement of these objectives, including desulphurisation, treatment of wastewaters, vehicle exhaust catalysis and removal of volatile compounds [18], [62]. Several of these tasks have historically relied on noble metals like platinum or palladium [63]. However, metal oxides are frequently a more

financially viable alternative. A notable example is the catalytic oxidation of volatile hydrocarbons from solvents, households, car exhausts and the petrochemical industry, where nanostructured ceria has shown potential to replace bulk supported Pd [64]. Metal oxide solid catalysts are also effective for the oxidation treatment of other noxious gases generated by automotive exhausts like CO, SO₂ and NO_x [65]. Titania and zirconia have found significant environmental applications as photocatalysts in the treatment of soil and wastewaters from chemical plants[66]. By developing more accessible materials for the treatment of major toxic chemicals, their benefits can become more widespread across societies.

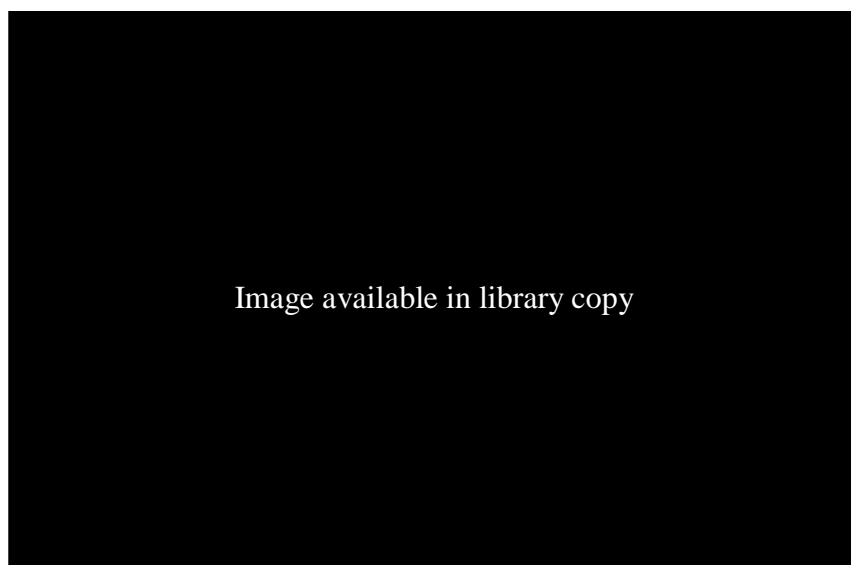


Figure 2.3 Activation methods for solid catalysts that do not require external heating [18]

2.1.1.3 Metal oxide nanostructures in catalysis

Metal oxide heterogeneous catalysts have increasingly become an area of priority in different research areas. Improvements have been made at all levels from the chemical engineering of catalytic reactors to molecular modelling [48]. New synthesis methods aiming for 100% selectivity are constantly in development, and they rely on advances in characterisation. Physisorption and different forms of spectroscopy are extensively used to identify active phases, while X-ray and neutron scattering can provide information on defects and surface geometry. As presented in Section 2.3, transmission electron microscopy (TEM) has made numerous contributions to the field of catalysis.

Some of the unprecedented information gained from TEM analyses include identifying the atomic structure of active phases, investigation of chemical compositions at the nanoscale, and imaging of electronic structure with atomic spatial resolution [67]. As mentioned above, a lot

is still unknown about the mechanisms of catalytic activity, and scientists are still trying to develop standard models to predict catalytic behaviour. The in-situ capabilities of TEM, combined with its resolution, make it a promising technique to understand the yet-unexplained chemical and structural dynamics of solid-state catalysis [20]. The importance of the applications of heterogeneous catalysts has motivated the development of new complex nanostructured materials. Some of the nanomaterials that have sparked interest for their catalytic applications include magnetic nanoparticles, micro/nanobubbles, layered double hydroxides, semiconductor quantum dots and catalytic nanomotors [68]. However, porous nanomaterials have particularly attracted a great deal of attention.

In particular, mesoporous oxides tend to have properties that are desirable for catalysis, e.g., large surface area, support capabilities and tuneable structure [69]. As mentioned above, the most common application of porous materials in catalysis is as support for active nanoparticles. However, there is an increasing interest in the standalone catalytic capabilities of porous materials. The following sections discuss the topic of porosity concerning heterogeneous catalysis, and the role that porous oxide materials play in catalysis, both as support and functional materials.

2.1.2 Catalytical activity in porous oxides and other materials

Porous metal oxide catalysts hold many advantages over their predecessors, which has inspired researchers to develop materials that can deliver both the structure and the chemistry necessary for catalysis in one single material. Nature displays a perfect example of such materials, where enzymes show the necessary bio-catalytic chemistry and structure in a single macromolecule [69]. Before elaborating on the developments found across the literature regarding porous catalytic metallic oxides, it is useful to briefly outline other major categories within porous catalysts, as they often share challenges and applications. Their major chemical composition separates porous materials into organic, inorganic and hybrid. This classification can be found in the comprehensive review by Nasrallah and Hierso [70], as shown in Figure 2.4.

Organic porous materials mostly consist of porous organic polymers (POPs). Their fabrication mostly consists of a directed assembly of functional organic units [71]. Depending on their building blocks, POPs classify as microporous organic polymers, hyper-cross-linked polymers, porous aromatic frameworks or covalent organic frameworks (COFs). The latter has attracted particular attention due to their high crystallinity and tuneable porosity [70]. Hybrid materials consist of organic functional groups which drive the assembly of metal precursors, resulting in a coordination polymer (CP). Some of these materials share similarities with the composites mentioned in the previous section consisting of a support and an active phase [72], [73]. How-

ever, a specific type of CPs known as metal-organic frameworks (MOFs) constitutes a widespread research area within functional porous materials. The literature hosts a large number of reviews regarding their development and applications [74]–[78]. However, their applications are often limited by their low thermal stability, which coincides with the challenges of silica-based materials [79].



Figure 2.4 Classification of chemically active porous materials by composition [70]

Nanostructured transition and inner transition metal oxides are ideal for many catalytic uses, as the diversity of their properties and electronic configurations makes them relevant to many industrial applications [38], [70], [80]. While most of them can assemble into catalytically active porous nanostructures, their chemical behaviour will still depend majorly on their composition [81]. This dependency means that the cation, or cations, in the oxide will determine the main characteristics of the catalyst and its subsequent application.

Firstly, the charge-to-ionic radius ratio will govern the acid-base strength of the catalyst [20]. Secondly, the hydrothermal stability of metal oxides is generally very high. However, for applications in particularly harsh environments, mixed oxide compositions (e.g. $\text{CeO}_2\text{-ZrO}_2$) have exhibited higher stability than their pure metal oxide counterparts [82]. Finally, the composition of a metal oxide can influence its concentration of oxygen vacancy defects, which can,

in turn, influence its activity [83]. However, oxygen vacancies are also largely associated with the morphology, crystallinity and porosity of the catalyst.

2.1.2.1 *The influence of porosity on the catalytic behaviour of oxides*

In the more general sense, porosity affects catalytic behaviour by increasing the surface area and exposing more active sites to the reactants. This correlation immediately makes them more efficient than their bulk counterparts. However, when researchers have explored the catalytic properties of porous materials, they have discovered shape-selective mechanisms that make the activity of these materials significantly different from that of other nanostructures with similar surface area [84]. This discovery has led to a great body of theoretical and practical research aiming to understand and apply these pore-specific phenomena.

Still, the most basic way of classifying pores is by their size, which divides them into three wide categories: Macropores are any pores larger than 50 nanometres, mesopores have sizes between the sizes of 2 nm and 50 nm, and micropores are pores smaller than 2 nm [85]. Some sources will refer to a special category within micropores of so-called ultramicropores with dimensions below 0.7 nm [86], [87]. Depending on the preparation methods, catalysts can exhibit pores of two or more size classes. The texture of pores, i.e. size and shape, is largely determined by the origin of the pore, which can be the preparation or modification of the material.



Figure 2.5 Common pore geometries [85]

Small changes in the dimensions of pores have been shown to have considerable effects on the performance of the material in catalysis. As an example, biomass upgrading is a crucial environmental application which involves mass transport of complex viscous molecules [84]. The efficiency of this conversion relies entirely on the porosity of the metal oxide catalyst. If the pores are too small, they are likely to be blocked by the macromolecules, causing low conversion rates and eventual deactivation of the catalyst. On the other hand, if the pores are too big, the selectivity of the catalyst will be poor, resulting in low-quality reaction products. These demands for fine-tuned porosity have made the synthesis of porous catalytic oxides a very active area of research. Researchers aim to develop preparation methods with better porosity control at the nanoscale [88]. Furthermore, specialised applications like biomass upgrading, have created an increased interest in hierarchically porous materials, which unify the catalytic activity of separate porous phases into a single material [84].

Different preparation methods not only result in different pore sizes but also generate a wide variety of regular and irregular pore shapes. Some common shapes are schematically represented in Figure 2.5 by Leofanti et al. [85]. The most common regular pore geometries include cylinders, slits and voids between connected spheres. Cylindrical pores can happen on the surfaces of MgO and Al₂O₃. Slit shapes are common to clays and activated carbons, and voids between spheres can result from solids obtained from gels and most silica-based materials. These geometries can be useful for describing some porous structures.

However, it is well established that pores are more likely to have irregular shapes [89]. That is, they do not have a uniform size along their length. It is usual for pores to be ink-bottle shaped, where the body of the pore is wider in diameter than its mouth. Alternatively, they can be funnel-shaped, with the mouth of the pore being wider than its body. Consequently, reported values of pore sizes could be deceitful, as they will significantly vary according to the method of measurement. Another important aspect of pore morphology is the location of a pore in relation to the surfaces of the containing material. In general terms, authors describe pores as closed (if they do not connect to the surface), blind (if they are only accessible from one surface but finish inside the body of the material) or through (if they connect two surfaces of the material). Additionally, pores can be isolated, or they can connect with one or more other pores to form a porous network.

2.1.3 Mesoporous materials for catalysis

According to IUPAC nomenclature, a mesoporous material is a solid containing pores between 2 and 50 nm [90]. Within catalysis, silica-based mesoporous materials are of great importance. Since their discovery, 25 years ago [91], [92], mesoporous silica (MPS) catalysts have already

substituted mineral acids and chloro-containing compounds in the majority of their long-established industrial applications [79]. They present several advantages, such as reduced biohazard, improved selectivity and yield of reactions, as well as reduced energy consumption. These impressive results have attracted the attention of researchers who seek to expand their uses by developing new pore architectures and framework topologies. Mesoporous materials share many physical and chemical similarities with microporous zeolites, both natural and synthetic. This resemblance is exemplified in Figure 2.6, which shows the structures of a zeolite and mesoporous silica with typical structures and compositions [93].

The main differences between the families of zeolite and mesoporous materials are crystallinity and pore dimensions. Zeolites exhibit a crystalline matrix and a limited pore size, which rarely exceeds 2 nm [94]. On the other hand, MPS materials are amorphous at the nanoscale and can have pores as big as 50 nm [79]. This trade-off of structural characteristics constitutes the main challenges for these materials, which researchers still seek to overcome. The crystalline silica network of zeolites has the advantages of high thermal and hydrothermal stabilities, accommodating for catalytic applications above 800 °C. However, this crystallinity only allows infiltration by elements with tetrahedral coordination geometries. Common infiltrates include Ca, Na, K, H₂O and NH⁴⁺ [95].

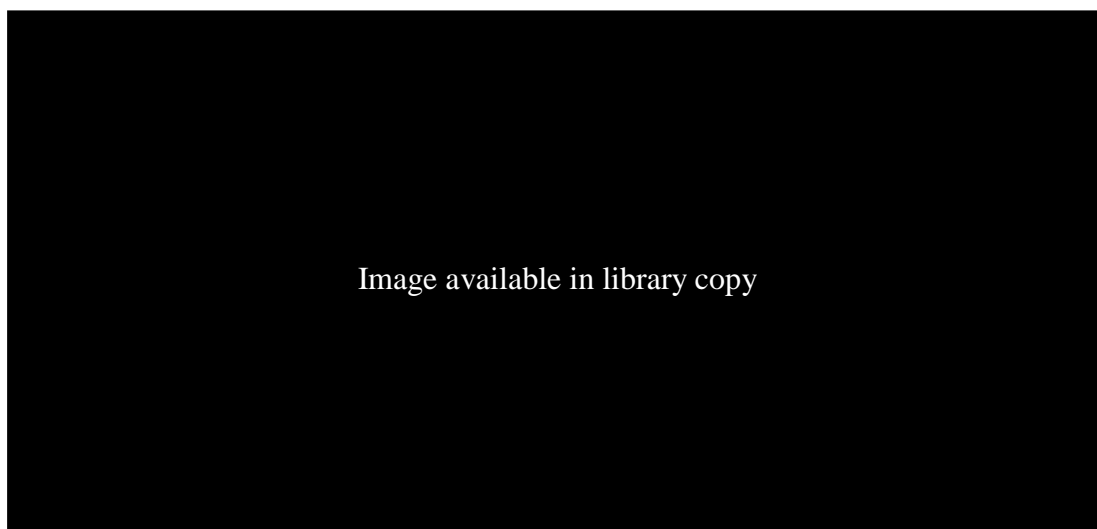


Figure 2.6 Typical structures of a) zeolite (ZSM-5) and b) MPS material (MCM-41) [93]

In contrast, the amorphous network in MPS has been used to accommodate a great variety of elements. The wider pore dimensions also allow oxides to form within the structure. This infiltration capabilities mean that MPS are not only useful in acid, basic or oxidation catalysis but as carriers for dispersed metal and oxide phases [96], [97]. Furthermore, they can present

a high concentration of silanols throughout their structure, which allows the grafting of complex organic and organometallic compounds [98]. Despite these advantages, the amorphous silica continues to limit the applications of MPS at higher temperatures [79].

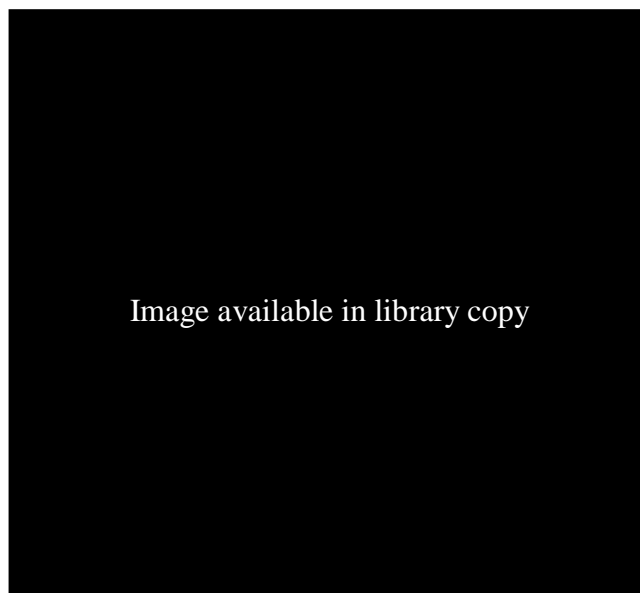


Figure 2.7 Sketch of the mesoporous hierarchy in FCC catalyst mixtures [79]

The ability of silica-based mesoporous materials to be combined with such a wide variety of elements and compounds has brought about applications far beyond heterogeneous catalyses, such as drug delivery [99] and bone tissue engineering [100]. As for heterogeneous catalysis, there are promising studies of the performance of MPS in all major catalytic environments [101]. Within the petrochemical industry, which relies majorly on solid-state acid catalysis, the MCM-41 family of mesoporous materials have shown to improve the yield of a reaction in the alkylation of benzene with olefins and propylene [102].

The transformation of vacuum gas-oil into valuable products via fluid catalytic cracking (FCC) is one of the highest priorities within the industry. The most common catalyst in use today is a complex mixture of clays, binders and micro/mesoporous materials, as schematically shown in Figure 2.7 [79]. The incorporation of MPS with hierarchical pore structures has resulted in higher conversion rates and better selectivity toward diesel production [103]. These applications bring back, however, the issue of thermal and hydrothermal stability, as FCC catalysts often operate at temperatures above 750 °C in the presence of steam, which results in limited performance and short life for the catalyst [104].

The Al content in mesoporous silica materials makes them obvious candidates for acid-catalysed reactions. However, several studies have explored the effect of loading the preformed MPS with alkaline ions like Na⁺ or Cs⁺, The resulting compounds combine the high dispersion

of MPS with the chemical activity of the alkali phase, giving highly active and selective basic catalysts [105]–[109]. Some of the most promising catalysts of this type include $\text{La}_2\text{O}_3/\text{Cs}_2\text{O}$ -impregnated MCM-41 for the production of biodiesel [107], SBA-15 supported CaO and fumed silica for the transesterification of castor and vegetable oils [110], and CeO_2 supported on SBA-15 for the synthesis of diethyl-carbonate [111].



Figure 2.8 Schematic representation of the typical preparation methods of a) a zeolite, ZSM-5 and b) mesoporous silica, MCM-41 [93]

As mentioned in the previous section, oxidation catalysis plays a major role in the environmental applications of heterogeneous catalysts. Hence, researchers have tried numerous combinations of mesoporous silicas with active oxides, in the search for catalysts that will selectively oxidise compounds under mild conditions. Titania-containing MCM-41 has found particular application in the oxidation of large organic molecules, where their zeolite predecessors could not be used [110]. Experimental results suggest that ceria-containing SBA-15 is effective in the industrial oxidation of carbon monoxide and hazardous volatile organic compounds (VOCs) in air and water [112].

The preparation of MPS materials is closely associated with that of zeolites [93], where a silica or aluminosilicate precursor is templated using a complex, typically organic macromolecule known as SDA or structure-directing agent. The silica or aluminosilicate polymerises around the SDA, forming the mesoporous structure. Finally, the SDA vacates the structure by

calcination or dissolution. The result is an open structure with long-range periodicity, which can be easily infiltrated by other molecules or ions. Lehman and Larsen have sketched this process in Figure 2.8 while highlighting the similarities between the preparations of ZSM-5 zeolite and MCM-41 mesoporous silica [93]. By varying the physical parameters and the chemical compositions involved in these reactions, researchers have been able to create a wide variety of recognised frameworks. This diversity of pore architectures and dimensions continues to expand, facilitating new applications for mesoporous silica materials.

2.1.3.1 Outstanding challenges in MPS technologies

The potential applications of mesoporous materials in catalysis have sparked significant interest in overcoming their inherent challenges. Widespread research is still underway seeking to improve their hydrothermal and thermal stabilities, as well as to control the dispersion and behaviour of active sites within the MPS structure [79]. Novel strategies generally aim at conferring the crystallinity of zeolites to mesoporous materials while retaining the versatile structure of the latter [113]. This combination of features results in hierarchical micro-mesoporosity, where the mesostructure provides mass transport capabilities and the microporous crystallinity gives better control of the active site structure and, more importantly, makes it possible to use the materials at higher temperatures.

Some promising examples of such novel materials include the successful syntheses of Ti-Beta/SBA-15 [114] and mesoporous TS-1 [115]. The fabrication of these materials usually consists of modified versions of the templating method for preparing MPS, as described above. A notable exception is the so-called *destructive* methods, where a preformed zeolite is periodically demetallised to obtain the desired hierarchical porosity. There have been successful applications across the literature from the early works of Ryoo et al. over 20 years ago [116], who used a sacrificial carbon template to achieve a nanocrystalline mesoporous structure, to the more recent dealumination procedure implemented by Na et al. [117]. Although promising, these results require costly preparation methods, which has naturally limited their application.

2.1.4 Synthesis and characterisation methods of porous catalytic materials

Advanced methods of preparation have been developed to obtain predictable pore morphologies. The anodisation procedures of aluminium metal have been finely tuned to obtain cylindrical pores in a so-called *honeycomb* configuration. The parameters of electrodeposition determine the width and depth of these generally uniform blind pores [118]. Blind pores can also occur during heat treatment, which causes vacancies in the oxide to reposition, resulting in a

nanostructure where the surfaces of the material show recesses, pits or concavities. This phenomenon occurs in a variety of catalytic oxide materials [1], [119], [120].

For the case of through-pores, like the one shown in Figure 2.8, they can appear in metal oxide catalysts as curved wormholes or straight nanochannels travelling between opposite faces of the rod. Such defects are commonly observed in systems like Vycor glass or during dealloying of Au/Ag [50], [121]. The formation of the channels happens via microscale heat treatment, where a low stability precursor forms the one-dimensional features inside a high stability phase before being leached or removed, leaving through-holes behind. This mechanism has also been considered for other oxides like cerium (IV) oxide nanorods [13], where the hydroxide phase could template the channels inside the oxide rods. This type of channels creates a high surface area, which provides oxide nanomaterials higher redox capacity compared to their non-porous counterparts.

Pore sizes smaller than 2 nm have been observed in a variety of heat-treated oxides and can appear as a random speckle covering the entire structure of the catalyst when observed in TEM [3], [4], [122]–[124]. Their shape is not well defined, but they generally appear to tend towards a spherical symmetry [4]. Researchers working with a variety of metal oxide nanomaterials have reported that further steps of heat treatment allow the conversion of these smaller pores into negative nanoparticles with well-defined faceted geometry [3], [125], [126]. There is still limited information on these negative nanoparticles, but they appear as three-dimensional cavities occurring only inside the body of the structure and never reaching the surfaces.

2.1.4.1 Nanocasting

An important application of MPS materials is as templates for the fabrication of other mesoporous materials via *nanocasting*, wherein the MPS functions as a structural matrix for other materials, such as oxides, metals or carbon. A precursor of the material of interest infiltrates the pores of the mesoporous silica. Common precursors include nitrates and chlorides for metal oxides [127], or sucrose for carbon [128]. There are several methods to obtain a successful impregnation.

Some systems favour incipient wetness impregnation (IWI), which consists of adding small amounts of highly concentrated precursor solution to the MPS [129], other groups have achieved good results using ultrasonication [130], dip-coating [131], and more sophisticated methods like chemical vapour deposition [132]. Once the precursor has successfully infiltrated the mesoporous structure, it is converted into its respective product, typically by heating. The cycle of infiltration/conversion is usually repeated a few times to ensure that the mesoporous structure is completely full. The silica matrix can then be removed by chemical etching using hydrofluoric acid or a strong alkaline solution. Structurally, the final product is *negative silica*.

Finally, a second infiltration/inversion process can be done on this product to obtain *positive silica* [133], in which the oxide presents an identical structure to the original MPS. For these cases, the intermediate infiltration is usually done using a carbon compound like CMK-3, which can later be eliminated by slow combustion [127].

Nanocasting has been extensively used to obtain mesoporous oxides, which can be used as supports with high thermal stability or as standalone catalysts. Their open structure and crystalline walls provide excellent conditions for catalytic activity. Some of the mesoporous oxides prepared in this way include Al₂O₃ [134]–[137], CuO [138], MgO [133], [139], [140], ZnO [141]–[145], TiO₂ [137], ZrO₂ [146], and CeO₂ [133], [147]–[149]. These products are just some examples of a wider trend in the research of catalysts. The vision of a catalyst is evolving from a composite consisting of a support and an active phase into a functional solid that has both the relevant chemistry and the desired porous structure. These materials provide opportunities not only in catalysis but also in fields like optical sensing and drug delivery [69]. The following section dives into these new developments and explores the challenges and opportunities presented by porous catalytic oxides.

2.1.4.2 Characterisation of nanoporous materials

The complexity and low dimensionality of pores in catalytic nanomaterials present interesting challenges when it comes to characterisation. Classic characterisation techniques are still widely used to obtain bulk properties like BET surface area, pore size distribution, total pore volume and average pore size [150]. Such established techniques include low-temperature adsorption of N₂ or Kr, Ar, He, Hg porosimetry, and permeametry. Appropriate use of these techniques and their respective measurement methods can provide valuable information on porous oxide materials. However, state-of-the-art catalytic materials rely on their characteristics at the nanoscale for their performance. This correlation is especially true for porous nano-oxides, whose intricate morphology creates active sites in ways that are not yet fully understood [20]. For this reason, transmission electron microscopy (TEM) and its related techniques have become a vital instrument for the development of these promising materials [151]. Metal oxides also have the advantage of being resistant to electron beam damage, which makes it possible to analyse them for extended periods using even high-voltage sources [152].

The most prominent application of TEM in catalysis is the study of nanomaterials *in vivo* or *in situ*. This is due to the limited information that the traditional *post-mortem* methods often provide. In similar fashion to other advanced TEM techniques, the application of *in situ* has been dependent on the developments in other TEM technologies. Particularly, *in situ* techniques have benefited from the implementation of micro-electro-mechanical systems (MEMS) [153], [154] and aberration-corrected microscopy [155]–[157]. Regardless of the experimental

challenges and the need for specialised microscopes, the number of related publications has shown significant growth over the last decade [158]–[160].

In their recent review, Taheri et al. have identified four main scientific challenges that have motivated the use of in situ TEM in materials science research [160]. First, the ability to capture phenomena in real-time and identify intermediate phases makes it a powerful tool to explain materials synthesis routes in detail. Secondly, by subjecting materials to different sources of energy and chemical environments, in situ TEM enables researchers to determine the chemical reactivity of nanoparticles. Thirdly, by exploiting the high-resolution capacities of the transmission electron microscope, researchers have been able to understand solid-state phenomena at the nanoscale. Finally, a great number of publications have utilised this technique to record and analyse failure mechanisms at the atomic scale.

Robert Sinclair classified in situ TEM methods into seven experimental categories according to the source of energy supplied to the specimen [161]. These categories are electron-irradiation momentum transfer, heating using a thermal source (i.e. heating holder), laser stimulation experiments, electrical biasing, controlled gas environment, liquid cell environments and nanoscale mechanical loading. The final section of this review will continue to discuss the most relevant developments in TEM for the fields of nanomaterials and catalysis.

Environmental concerns and energy requirements continue to increase the demand for new catalysts. Metal oxide catalysts are versatile and can provide high efficiency, selectivity and hydrothermal resistance. In turn, porous oxide nanomaterials have reported catalytic capacities up to 5 times higher than their non-porous equivalent [13]. These favourable characteristics are attracting the attention of researchers, and the field will continue to grow. A lot of questions remain unanswered, mainly regarding the mechanisms involved in the generation of active sites and the relation with the presence and characteristics of pores and similar defects. Nevertheless, the empirical development of materials that exploit these features has already shown great promise for heterogeneous catalysis and is expected to persist.

2.2 Catalytic potentials of porous ceria nanomaterials

For over 20 years, the number of publications on ceria-containing materials has seen a steady increase across disciplines, as shown by Montini [162] in Figure 2.9. Their impact continues to grow with new developments in materials preparation, advanced characterisation, as well as the environmental demands for solid-state catalysts. Most applications of ceria rely on its ability to switch between the oxidation states of the cerium cation without compromising the structure of the material [163]. However, there are other properties of ceria that make it one of the

most promising materials for catalysis, particularly at the nanoscale [14]. In support applications, for example, ceria can stabilise metals at a higher temperature, preventing them from sintering and maintaining single-atom configurations. It also enhances the performance of noble metals via oxygen transfer.

The advancement of ceria applications has only been possible through the collaboration of theoretical and experimental research. For example, in the early 1990s, Sayle et al. predicted that oxygen vacancy formation in cerium oxide depended highly on the properties of the surface [164], i.e. ceria nanoparticles (NPs) with different exposed lattice planes could have very different oxidation behaviours. This relation highlighted the need to develop new preparation methods since the conventional coprecipitation techniques normally result in polycrystalline materials with ill-defined heterogeneous shapes [14]. This section summarises the most impactful applications of ceria, the research advances that have propitiated them, and the probable future of ceria-related nanomaterials.

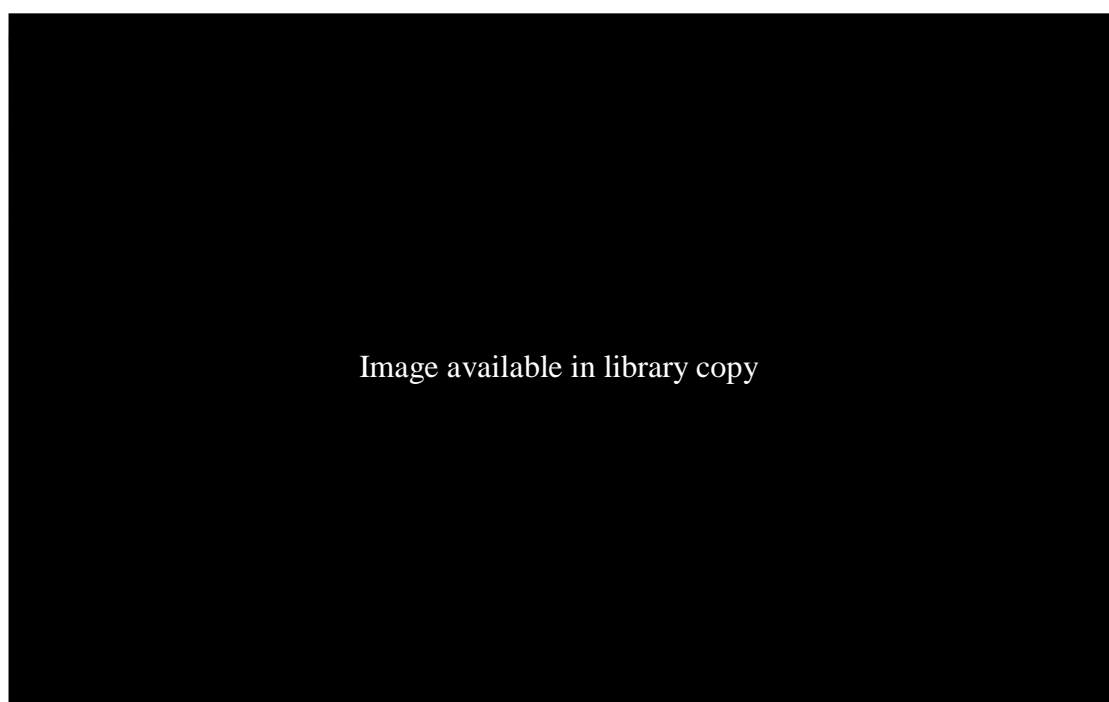


Figure 2.9 Chart summarising publications on ceria and its catalytic applications [162]

2.2.1 The significance of CeO₂ for industrial catalysis

Ceria has three main properties that make it desirable for catalytic applications, both as support and active component: reversible redox chemistry, thermal/hydrothermal stability and great

oxygen storage capacity (OSC). These advantages have made ceria and its suboxides an attractive component for many catalytic processes [13]. Different areas of application vary in requirements of catalyst chemistry and structure, which results in a wide variety of cerium dioxide nanostructures and composites.

This section highlights well-established catalytic applications of ceria and related materials, emphasising the nanoscale properties that make them suitable for each application. The role of ceria in the industrial processes is a particular point of attention, such as CO oxidation, CO₂ conversion and organic transformations. The final section introduces some of the promising uses of ceria that are still under development.

2.2.1.1 *The use of ceria in CO oxidation*

Carbon monoxide (CO) is a common by-product in many everyday sources like vehicle exhaust, heating systems and organic fumes. Exposure to high levels of CO can kill a human in less than two hours or cause long-term complications in survivors [165]. Environmentally, CO also contributes to the formation of hazardous ground-level ozone [166]. CO is removed from specific atmospheres by oxidation in a three-way catalyst (TWC) system. TWC devices normally consist of a noble metal deposited on ceria support.

The metal particles are responsible for oxygen activation, while the support carries oxygen atoms to the reaction sites on its surface converting CO into CO₂. This ability of the support to store and release oxygen under reaction conditions is known as oxygen storage capacity (OSC) and is the determining feature of the catalyst [51]. The particular working conditions of each application can have negative effects on the OSC performance of the ceria support. Some challenging environments include complex gas mixes, high working temperatures and high-frequency oscillatory systems [167]. Several dopants and solid solutions have been developed to overcome the challenges of pure ceria, and have become established TWC components. E.g., ceria-zirconia [168], gadolinium-doped ceria [169], cerium-praseodymium oxide and others [170].

As described above, the catalytic oxidation of CO occurs primarily on the surface of the TWC ceria supports. For this reason, the surface properties of CeO₂ have been extensively researched [13]. Beyond increasing surface area, CO-oxidising ceria has been improved by escalating the concentration of surface defects and controlling the crystallography to amplify oxygen mobility and lower the formation energy of vacancies [171]. Over the last ten years, different research groups have tested the effect that different exposed lattice planes have on the CO oxidation activity of ceria. The influence is notable across all different nanoceria morphologies: nanotubes, nanospheres, nanocubes, nanorods, nanooctahedra, nanospindles and nanowires [172]–[175]. Their results conclusively predict that those materials with {100} and

{110} exposed planes are more active in CO oxidation. The following sections discuss the research on the surface properties of ceria nanostructures in more detail.

The removal of CO is not only necessary in atmospheres where it could be damaging to humans and wildlife, but also within confined industrial processes. Particularly in the production of hydrogen gas by the reformation of hydrocarbons. This process generates CO, which is mostly oxidised via the water-gas shift (WGS) reaction. However, the product of this reaction generally still contains some amounts of CO which poison the metal-based catalyst used for the reformation process [13], [176]. Ceria has proved effective as a second stage oxidiser reducing the levels of CO below 8 ppm [177], [178]. This role in the WGS reaction also positions ceria as a relevant material for the future hydrogen economy [179].

2.2.1.2 *The role of ceria in CO₂ conversion*

The capture and storage of carbon dioxide (CO₂) by physical or chemical means, as well as its conversion into useful products, constitute a major area of priority for multidisciplinary research [180]. Therefore, it is necessary to overcome the challenges posed by the chemical inertness of CO₂ and its high bond energy. Cerium dioxide has proved effective in trapping CO₂ molecules on its surface under mild conditions [181]. The redox chemistry of ceria also allows it to activate CO₂ and promote its conversion in different catalytic processes in gas and liquid phase. The main strategies of conversion of CO₂ can be summed up into the production of carbonates and reduction into fuels. Ceria has been identified as a suitable catalyst for both processes, with its activity improved by the concentration of defects on its surface [180].

The catalytic synthesis of carbonates is a promising way to reutilise CO₂ by using it as a building block for the production of green reagents like dimethyl carbonate (DMC) [181]. The fabrication of DMC from CO₂ and methanol presents significant challenges due to the low reaction yield (<10%), the abundant production of water and the low chemical selectivity (60–90%). Furthermore, the reaction requires an intricate apparatus that integrates steps of dehydration and product separation [182], [183]. In recent years, Tomishige et al. have published several studies on the introduction of a catalytic bed of ceria nanoparticles as a reaction site promoter [184]–[186]. Their apparatus still requires dehydration agents and stoichiometric addition of reactants but has reportedly achieved conversion efficiencies above 95% with a DMC selectivity 99%.

Reduction processes convert captured carbon dioxide into useful hydrocarbon fuels like methanol or methane. This conversion can be achieved via thermochemical or photocatalytic reactions, both of which benefit from the properties of ceria [13]. The redox capacities of ceria, high oxygen diffusivity and tuneable surfaces are determining characteristics for the efficiency

of photocatalysts. In terms of surface defects, photocatalysis has presented an important challenge for materials preparation: the absorption of visible light is aided by the presence of surface defects, but if the defects are too abundant, they will trap the photogenerated charges reducing the efficiency of the reaction [187].

Researchers have sought to optimise the surface of ceria nanoparticles to produce the best possible rates of CO₂ conversion [188]. As for thermochemical conversions, samarium-doped ceria has been used to convert CO₂ and water into CO and hydrogen gas [189]. Unfortunately, the endothermic nature of the reaction means that a lot of energy is required, making the process infeasible at an industrial scale. A promising alternative is the use of a solar-thermal reactor, which benefits from a functionalised porous CeO₂ catalyst to create an abundance of thermochemically active sites [189].

2.2.1.3 Applications of ceria in organic catalysis and biomedical research

Beyond its significance in the treatment of gases as described above, ceria also plays a major role in the production of organic derivatives. Comprehensive reviews can be found on the extensive uses of ceria in a large number of organic reactions like oxidation, hydrolysis, coupling, addition, substitution and others [190]–[192]. These applications rely on the versatility and stability of ceria under reaction conditions. Particularly, organic reactions rely on the reversible redox capacity and the generation of surface Lewis acid/base reaction sites. Here is described the role of ceria in three major catalytic processes: hydrolysis, oxidation and hydrogenation. Emphasis is placed on the surface properties and modifications that provide the catalytic performance.

Hydrolysis and dehydration processes rely on the ability of a catalyst to absorb water and dissociate it into protons and hydroxyls. The catalyst must then be able to liberate the acid/base ions as required by the reaction and rapidly regenerate the active site. If the acid/base capacity of the oxide is too strong, the reaction sites become blocked, and the catalyst performance decreases until its deactivation [192]. The reaction conditions will vary according to the reactants and catalysts will behave differently depending on thermal/hydrothermal conditions. This limitation means that it is impossible to find a universal catalyst for organic hydrolysis. However, Wang et al. have shown that ceria nanoparticles exhibit water resistance and high acid-base activity in the production of 1,3-butanediol by catalytic hydrolysis, which is a high priority component for biomedical applications [190].

As aforementioned, the redox and oxygen storage capacities of ceria make it a prime candidate for catalysing oxidation reactions. Organic oxidations present the challenge that they mostly occur at temperatures below 100 °C. In spite of this limitation, ceria has been shown to oxidise benzyl alcohol into benzaldehyde in-air at 60 °C [190]. An evaluation of the oxidation

of aromatic anilines into aromatic azo compounds showed that the impregnation of the ceria catalyst with gold NPs resulted in oxidative capacity up to 10 times higher than pure CeO_2 [190]. Lv et al. have reported a novel catalytic system with high selectivity for the oxidation of toluene into benzaldehyde [190]. The material consists of highly regular ceria nanocubes covered in oleic acid. This coating facilitates the self-assembly of the cubes, which results in the preferential exposure of active $\{100\}$ planes.

It is worth to examine the crystallisation structure of cerium (IV) oxide, as it provides relevant information regarding its reactivity and oxidation mechanism. The unit cell structure is shown in Figure 2.10.

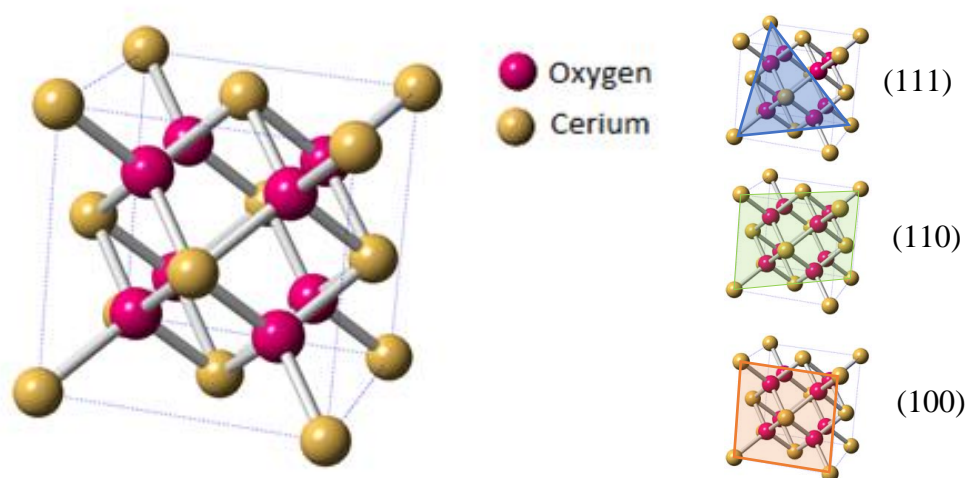


Figure 2.10 Model of a single unit cell of CeO_2 and schematic representations of relevant Miller indices (Model generated using Crystal Maker®)

As can be observed in the model, every cerium atom is coordinated with eight oxygen atoms forming a cube, and every oxygen atom is coordinated with four cerium atoms in a tetrahedral array. The unit cell has a cubic close packed or face centred cubic shape ccp/fcc. The structure can be defined as having a space group Fm-3m , with a cerium cation in its origin $(0,0,0)$, and the first oxygen anion at $(0.25,0.25,0.25)$ and a cell parameter $a=5.41134 \text{ \AA}$. This leads to a cubic unit cell as the one shown in Fig. 2.10 with cerium atoms at the corners and faces, and oxygen atoms in between filling the tetrahedral sites. This structure is commonly known as fluorite structure, because CaF_2 crystallises into the same geometry. The fluorite crystal structure is characterised by having a cation-anion ratio of 1:2, as well as the cation and anion coordination of 8 and 4 respectively.

By looking at the expanded crystal shown in Figure 2.11, it is easily observed that cerium atoms, when fully coordinated, are occupying only half of the octahedral sites. These empty

spaces are of great significance as they provide room for defect activity through oxygen diffusivity. An expanded study of ceria crystallography is explored in section 2.2.4.

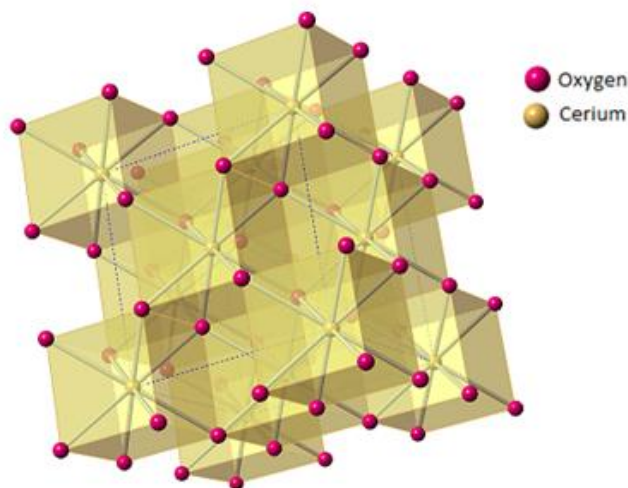


Figure 2.11 Expanded model of CeO₂ crystal structure.

Cerium ions have been rendered in order to display the empty octahedral sites.

(Model generated using Crystal Maker®)

Although the chemical behaviour of pure ceria is preferentially oxidising, it has also found extensive use as a stabiliser and promoter in reductive hydrogenation. The abundance of surface defects makes it a potent adsorbent for organic molecules compared to pure metallic NPs [193]. A large number of applications have benefited from this metal/ceria combination. Notable examples include the hydrogenation of unsaturated compounds by CeO₂-supported Au and Cu [194], [195]. A recent study by Zhang et al. utilised the highly active surface of porous nanorods to anchor sub-nm Pd clusters, resulting in a highly effective and selective hydrogenating agent [196]. The complex mechanisms of catalysis which combine the active metal nanoparticles with the crystallography and surface defects of ceria are not yet fully understood [13].

In recent years, the biocompatibility of ceria has expanded its applications from the industrial and environmental interests into biological and medical uses. CeO₂ has been found to successfully mimic the behaviour of biocatalytic enzymes such as oxidase, catalase, peroxidase and superoxide dismutate (SOD) [197]–[199]. The development of synthetic nanozymes is directly associated with important applications in drug delivery, biosensing, antioxidants and diagnostic tools [200], [201]. These applications are expected to improve as more fabrication methods are developed which facilitate the surface control and reactivity of CeO₂ catalysts.

2.2.2 The effects of nanoscale morphology on the activity of nanoceria

As explained in previous sections, despite the continued relevance of bulk catalysts in industrial applications, most of the efforts in catalytic material research are devoted to the development of nanomaterials. This prioritisation is particularly true for ceria, which has been the subject of over 25,000 publications since the 1950s [162]. Over the last ten years, however, most of the original publications on ceria concern materials that exhibit nanoscale magnitudes in at least one external dimension [202]. Accordingly, the present review does not comprise the fundamentals or developments of macroscale ceria. This section introduces the main nanoshapes of ceria, their preparation methods and the link between shape and chemical activity. The fcc crystal structure of cerium dioxide promotes crystallisation into characteristic polyhedral geometries. Under thermodynamically stable conditions, the facets of ceria nanoparticles will be mainly of the $\{111\}$ family, followed by the $\{110\}$ and $\{100\}$ planar geometries [14]. These features correspond to the best-known shape for ceria nanoparticles; the cuboctahedron [51], which exhibits eight stable $\{111\}$ octahedral facets capped by six $\{100\}$ faces. A schematic representation is shown in Fig. 2.12, as published Castell et al. in their work on UO_2 nanoparticles [120], which is a well-known analogous material to CeO_2 . This $\{100\}$ -truncated $\{111\}$ -octahedral geometry is observed in CeO_2 nanocrystals synthesised by a variety of methods. By controlling the experimental conditions, this initial shape can be extensively changed in all dimensions, resulting in (i) zero-dimensional structures (confined in 3 dimensions) like nanopolyhedra, nanocubes, nanospheres; (ii) unidimensional (confined in two dimensions) such as nanorods, nanowires, nanotubes and nanobelts; and (iii) two-dimensional structures (confined in one dimension), like nanosheets and nanoplates. Beyond these nanoshapes, it is possible to obtain nanomaterials which extend in three dimensions. They are still considered nanomaterials because their functionality and active features happen at the nanoscale [14].

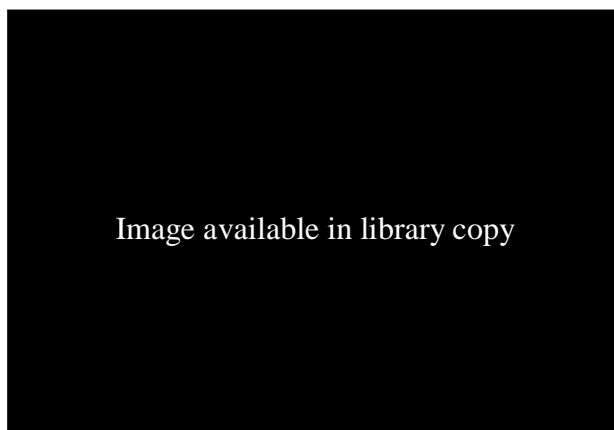


Figure 2.12 Sketch of a cuboctahedron or $\{100\}$ -truncated $\{111\}$ -octahedron [120]

2.2.3 Selective preparation methods of ceria nanomaterials

As explained in the first part of this literature review, different forms of catalytic activity rely on separate mechanisms and therefore benefit from different nanoscale characteristics of nanomaterials. Hence, there is a significant motivation to develop more selective preparation methods, which can allow researchers to tailor the morphology of ceria to the intended application. However, for the sake of simplicity, many studies of catalytic performance rely on CO oxidation as a good indicator of the general potential of a material or device for heterogeneous catalysis [203]–[205]. This process also happens to involve the reaction that uses CeO₂-based nanomaterials as active components most widely [51], as they are desired for their OSC and activity at lower temperatures. In general terms, CO oxidation has been enhanced by CeO₂ nanomaterials that exhibit a larger surface area. For example, ceria nanotubes have both external and internal surfaces which can host active sites. Correspondingly, their catalytic performance ranks amongst the highest of ceria nanomaterials [173]. This would suggest that nanoparticles with smaller sizes and very high surface area per volume would have the highest catalytic potential. However, their CO oxidation performance is poorer than most other CeO₂ nano-morphologies [206].

On the other hand, nanorods have particularly strong catalytic abilities regardless of their lower surface area. Studies have suggested that their performance improves as their diameter increases, even at the expense of their surface area [173], [207]–[209]. These seemingly contradictory findings can be explained by the catalytic mechanism. CO oxidation is normally carried out by the continuous reduction of Ce⁴⁺ to Ce³⁺, and subsequent oxidation of Ce³⁺ to Ce⁴⁺ using gas-phase oxygen. It can be deduced from this mechanism that the efficiency of the material will depend on the speed at which it can generate oxygen vacancies and replenish them, i.e., interstitial oxygen mobility [210].

The energy of oxygen vacancy formation is higher in (111) planes than any other and varies further for all the plane families present in the crystal structure of ceria [14], [211]–[213]. Section 2.2.3 will explore the published investigations into this relationship. For now, it is relevant to emphasise that the low performance of ceria nanoparticles is due to all their enclosing planes being (111)-type facets. The higher performance of nanorods and nanotubes alike is explained by the presence of more active (100) and (110) planes.

Furthermore, nanorods made from ceria differ from other materials in their non-cylindrical cross-section [211]–[213]. The cross-section of ceria nanorods has been investigated through 3D imaging [4] and atomistic modelling [214]. They have been shown to have a pseudo-hexagonal shape with sharp edges and corners. These under-coordinated sites are known to be

preferentially occupied by Ce^{3+} ions [215], which can adsorb gas-phase carbon monoxide making it easier to oxidise with the active interstitial oxygen [202]. This combination of factors, namely, exposed (100) and (110) planes, as well as the prevalence of edges and corners, make ceria nanorods one of the most promising catalytic nanostructures within the present context.

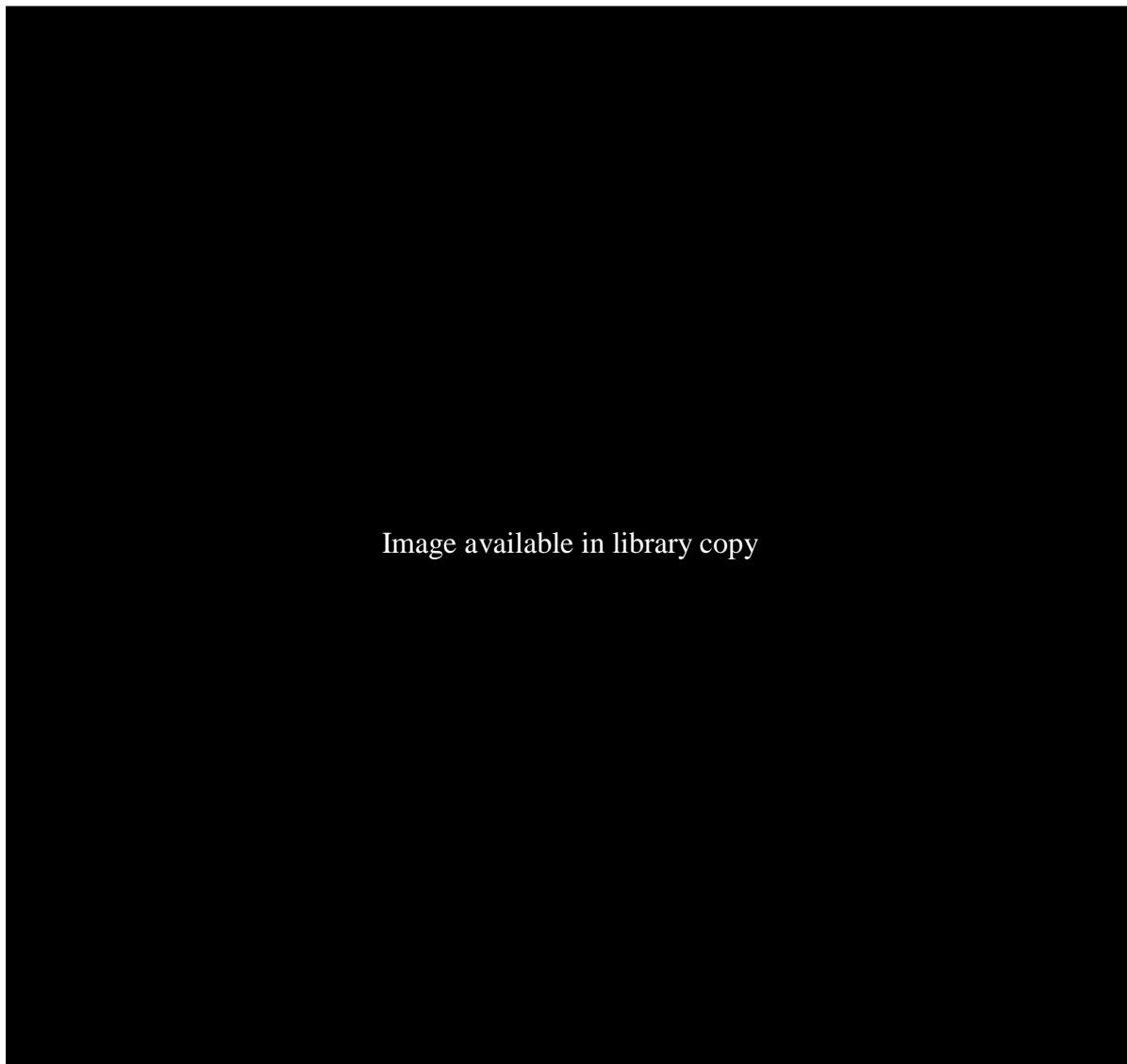


Figure 2.13 Summary of CeO_2 nanomaterials preparation methods [13]

Another subject of widespread interest is the aforementioned three-dimensional ceria nanomaterials, such as the templated porous materials obtained via nanocasting, where the growth of the crystal is normally dictated by a template. Widespread template materials include silica, polystyrene and poly(methyl methacrylate) (PMMA) [216]. In many cases, the composite ceria/template will have the desired properties without further processing. However, the template

is more commonly removed after the ceria has crystallised into the desired structure. As aforementioned, silica can be removed by etching with hydrofluoric acid or highly concentrated sodium hydroxide. Polymer templates are usually removed by calcination. For the particular cases where this extra removal step causes difficulties and to make the fabrication more efficient, template-free routes have also been investigated [217]. These methods rely on fine-tuning the parameters of conventional synthesis methods such as the hydrothermal/solvothermal process to achieve controlled dimensionalities and growingly complex structures [218]. These 3D nanostructures are the subject of widespread investigations due to their unique properties and potential applications. Their porosity confers catalytic capabilities several orders of magnitude superior to their bulk counterparts [219]. Additionally, molecular dynamics simulations have predicted that nanoporous ceria possesses yield strength almost twice that of its source bulk material [220].

Generally, most known shapes of CeO₂ nanomaterials can be achieved by more than one preparation method. Given that the variety of frequently published morphologies is wider than the number of prevalent synthesis processes, this section is simplified by categorising the literature below according to the preparation methods instead of using a geometrical classification. Firstly, this review takes a look at what are still the most common methods within bottom-up preparation approaches, i.e., emulsion and crystal-growth methods. These are directed only by the thermodynamic stability of the geometric facets. Afterwards, follows a brief presentation of the so-called ‘capping’ methods, which use organic or inorganic reagents which interact preferentially with either the {111}, {110} or {100} facets, thus inhibiting the growth of the material along that plane. Then, ‘templating’ methods mentioned above are presented in further detail. The section finishes with a brief mention of other methods which do not fit into the above catalogue, as well as the ceria nanoshapes associated with them. The reagents and reaction conditions for established preparation procedures are summarised by Ma et al. in Figure 2.13 [13].

2.2.3.1 *Crystal-growth directed methods*

The crystallographic structure of CeO₂ can direct the shape of crystals when there are no other interfering factors [202]. Two approaches are generally observed: precipitation and hydrothermal/solvothermal methods. Precipitation methods rely on water or organic compounds as solvents combined with a basic compound, such as ammonium carbonate, to precipitate a cerium salt such as cerium (iii) chloride. The following calcination step converts the cerium salt into oxide [51]. The simplicity of this method makes it very versatile and allows the introduction of dopants, which can be co-precipitated with the cerium salt and converted into solid solutions upon calcination or oxidation [21].

Controlled morphologies have been achieved by regulating the parameters of reaction such as the precipitating agent, the precipitation and oxidation reaction temperatures, pH values and concentration of the original aqueous or organic solution [221], [222]. Chen et al. published an extensive study of the factors that drive the morphology of final products in precipitation and highlighted the importance of oxygen availability and reaction temperatures [223]. It is important to mention that precipitation methods still have very limited selectivity, and the products generally have a wide distribution of shapes and sizes [202].

Another widespread method that relies on the crystallographic properties of ceria to direct the growth of the products is the hydrothermal/solvothermal treatment. This approach can be found across a large number of inorganic nanomaterials synthesis [224]. The process comprises the use of an autoclave to create the desired pressure and temperature conditions to promote the reaction in solution. The confined space produces reflux of solvent vapour, which raises the temperature inside the autoclave until the solution has reached vapour saturation pressure. The internal pressure is indirectly controlled by the temperature of the system and the amount of liquid compared to the capacity of the autoclave. There exist a variety of physical and chemical parameters used to generate ceria nanomaterials with specific properties [223]. Effective reaction solvents include $\text{Na}_3\text{PO}_4 \cdot (\text{H}_2\text{O})$ [225], [226], NH_4OH [227], [228], H_2O_2 [229], [230] and urea [231], [232], the most common being an aqueous solution of NaOH [233]–[235], which has been shown to predictably produce high-quality nanopolyhedra, nanocubes and nanorods. Mai et al. identify the main driving conditions to be the temperature and time of reaction and the concentration of NaOH in water [236].

The aforementioned alternative solvents are interesting for specific applications. For instance, Yan et al. reported the successful preparation of ceria nano-octahedra and nanorods in Na_3PO_4 [237]. Their work also provides unprecedented insight into the formation mechanism of nanorods, which grew by self-assembly of the octahedra. Altogether, the products of hydrothermal synthesis have markedly high crystallinity, which is greatly beneficial for catalytic applications. However, the size distribution is normally very wide and difficult to control [202]. The complexity of the synthesis mechanisms generally means that the preparation strategies for materials of a certain size and shape have to be developed empirically [224].

2.2.3.2 *Surfactant-assisted methods*

Capping reagents are generally organic surfactants which form micelles that prevent a certain type of crystalline face from growing, forcing a constraint on the material in the dimension of the face. Once the desired faces are inhibited, crystalline growth can be promoted to produce a higher dimensionality product such as nanorods [238], nanowires [239], [240], nanoplates [241], [242] and nanosheets [243]. This family of processes are also known as organic- or

surfactant-assisted methods. The most common capping agents used in the preparation of ceria nanomaterials are octadecylamine [239], cetrimonium bromide (CTAB) [238], [243], among others. By controlling the reaction times and temperatures, as well as the surfactant/Ce³⁺ ratio, capping methods can produce a wide variety of nanostructures with high crystallinity and size uniformity [202]. The main downsides to this method are that the use of organic surfactants can often increase the operation price of the synthesis and can leave behind residues or impurities [244].

2.2.3.3 *Template-assisted methods*

The third major approach to synthesising ceria nanomaterials consists of template-assisted methods, which are of particular interest for the preparation of hollow and porous CeO₂ with a high surface area. These methods can be broadly separated into three types: self-templating, soft-templating and hard-templating. Self-template synthesis has been largely favoured for the fabrication of CeO₂ nanotubes [233], [245], [246]. At first, a ceria nanocrystal is used to direct the growth of the desired volume. Later, the hollow structure is achieved via oxidation or alkaline washing. The soft-template synthesis relies on the Ostwald ripening of small crystals being promoted by the action of a surfactant [202]. This mechanism has been successfully utilised to produce ceria morphologies like nanospheres, nanorods, nanoplates, spindles, flowers and others [247].

A distinction is made between soft-templating and capping methods in that, by control of temperature and concentration, the surfactants are being allowed to assemble with the ceria crystals to form a compound structure. Once the desired structure has been achieved, the surfactant is calcinated, leaving behind a highly porous structure with low dimensional tolerances in three dimensions. Finally, the use of hard templates is also popular for the preparation of hollow structures. In this method, a ceria precursor is normally mixed with a hard template such as ZnO nanorods [248], [249], carbon nanotubes [250], polyacrylamide [251] or colloidal crystals made from polystyrene or silica spheres [252], [253].

Once the hard template and the ceria precursor have been mixed, it is proceeded to remove the template by chemical or thermal action, which may also convert the Ce³⁺ to CeO₂. The removal of the template can sometimes result in shrinkage and the collapse of the hollow structure, which has been overcome using a dual template method [202]. The resulting products from hard-template fabrication have highly controllable dimensionality and very high surface area. However, thermally stable templates can be hard to remove completely and may influence the properties of the resulting CeO₂ product by blocking the structure, thus reducing the surface area or pore accessibility [254].

2.2.3.4 Alternative preparation methods

Other methods that have proved very effective in producing a variety of ceria nanoshapes are electrochemical deposition, microwave-assisted synthesis and ultrasonic irradiation. Electrochemical deposition is one of the most promising techniques for scaling up ceria nanomaterials production. It is simple, low-cost, environmentally friendly and allows fine control of the product by controlling the electric current in the cell and the pH-value of the solution. Ceria nanorods and nanoctahedra have been prepared using this method [255]–[257].

Microwave-assisted preparation can significantly reduce the heating times compared to the more conventional methods mentioned above [258].

In combination with self-templating methods, microwave synthesis has been used to prepare hollow ceria nanospheres [259], nanorods [260] and other nanomaterials [261]. Sonochemical activation methods rely on ultrasonic irradiation to enhance the surface reactivity of nanocrystals, promoting their assembly into more complex structures [262]–[264]. Other more specialised techniques for the preparation of ceria nanomaterials are flame spray pyrolysis [265], supercritical solvothermal [266] and chemical vapour deposition [265]. The growing applications of ceria nanomaterials will continue to encourage the development of specialised techniques with better shape and size selectivity, tuneable crystalline features, and scale-up and functionalisation capabilities.

2.2.4 Crystalline defects, vacancies and cavities in ceria nanomaterials

Further to the dependency of catalytic behaviour on the morphology of the active and support materials, there is a direct relationship between the crystalline features of the contact surface and the performance of the CO oxidation or other catalytic processes. As mentioned before, the performance of nanorods is much higher than that of nanoparticles, despite their much lower surface area. Early studies of CeO₂ crystallography published by Conesa et al. in the 1990s established the most thermodynamically stable surfaces in ceria to be the {111}, {110} and {100} [267]. Further studies corroborated these findings [267], [268], as well as the existence of metastable surface {211}, which rapidly converts to a 'stepped' version of {111} planes to lower its energy state. Even less stable surfaces include {310} and {210}, which are rarely found in actual materials [267].

Unsurprisingly, the vast majority of studies concentrate on the three most stable planar families {111}, {110} and {100}. In Figure 2.14, Trovarelli and Llorca summarise the main energy characteristics of these main planes [14]. The values of relaxed and unrelaxed surface energies have been obtained by Nolan et al. using density functional theory (DFT) calculation [269].

The same group also published separately the predicted values of energy formation of oxygen vacancies, which they obtained using first-principles DFT, combined with on-site electronic correlations (DFT+U) [270]. The stability of CeO₂ surfaces can be predicted from the energy values in the table. Both the relaxed and unrelaxed surface energy values are lowest for {111}, followed by {110} and {100}. This relationship is consistent with {111} planes being the most common throughout ceria nanomaterials [271]. Another indicator of stability are the coordination numbers for cerium and oxygen atoms in each surface family. Higher coordination numbers generally mean that the surface is more stable. The coordination numbers for bulk ceria is Ce(8) and O(4), which would be the highest found for the material [14]. The reduction in coordination numbers is consistent with the predicted stability values and the calculated surface energies.

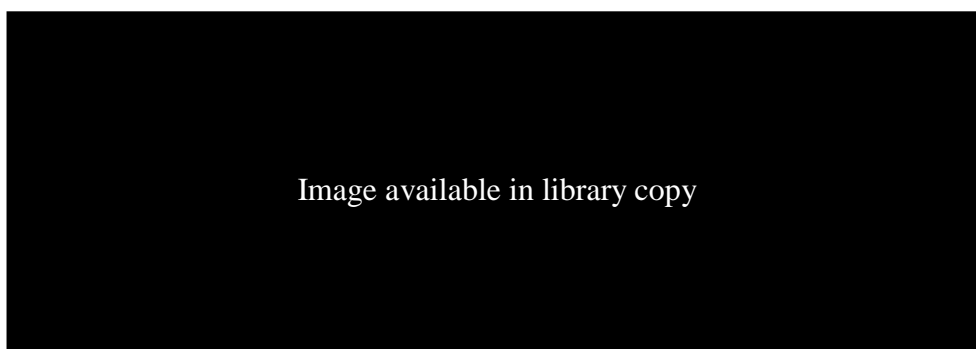


Figure 2.14. General characteristics of stable CeO₂ surfaces [14]

Figure 2.15 shows schematic representations of different views of the three stable ceria surfaces [14]. These sketches highlight the differences in activity and stability of each crystal structure. The {100} consists of repetitive O-Ce-O-Ce blocks, which generate a net dipole moment. It has the highest number of uncoordinated oxygen and cerium atoms, two available sites each, which explains why it is the most active of the stable surfaces [272].

The atomic interactions within the {100} surface are still a subject of debate, and several mechanisms have been proposed for its self-stabilising behaviour, particularly the location of oxygen atoms on the relaxed surface [14]. All different views of the {110} crystal structure show a termination in a coordinated network of cerium and oxygen atoms in a seemingly flat layer. This last point has been the subject of debate with modelling studies suggesting that the structure could be expected to relax by displacing the cerium atoms inwardly [273]. Lastly, the {111} terminates in a layer of oxygen atoms and has a limited activity corresponding with having only one coordinative unsaturated site per ion [273].

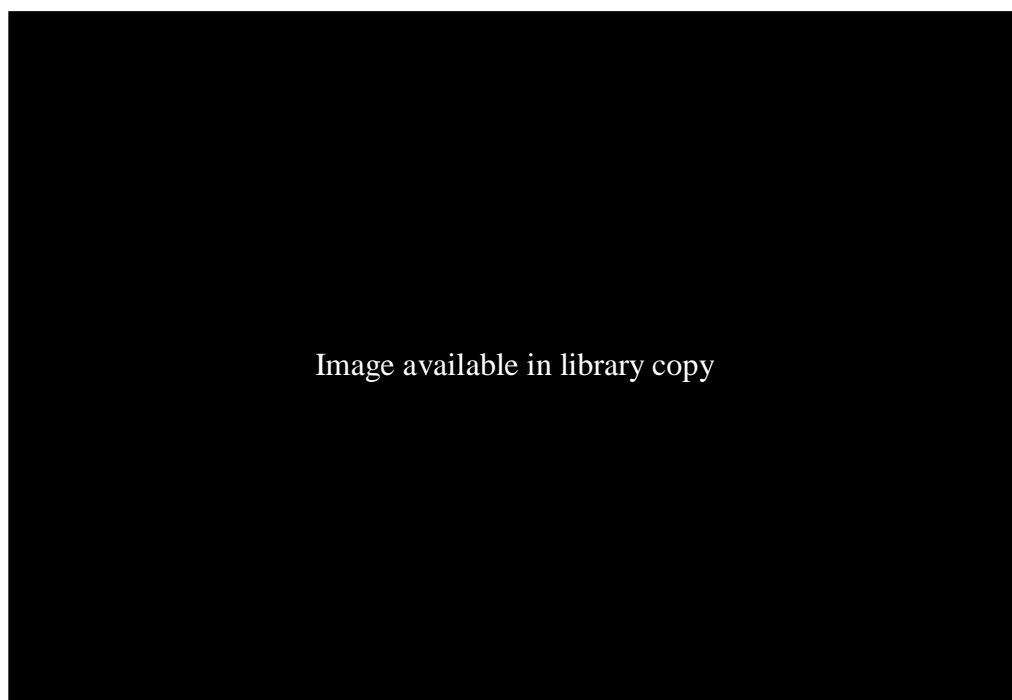
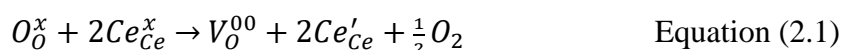


Figure 2.15. Views of (100), (110), and (111) ceria surfaces. O (red), Ce (grey) [14]

Vacancy defects play a central part in oxygen storage capacity. As mentioned previously, OSC is a vital feature for ceria applications and the driving force for its catalytic performance. The formation energy of vacancies presented in Figure 2.15 is consistent with the activity hierarchy of stable crystal surfaces in ceria. As {111} surfaces are the most compact, it is more difficult to accommodate a vacancy defect [274]. The formation process of vacancies in ceria has been established as follows [51]:



Where electrons travel from an oxygen atom to two adjacent cerium atoms reducing them to Ce^{3+} and generating an oxygen vacancy, this is consistent with the higher activity in redox reactions of nanomaterials with the exposed {110} planes, which are most prone to vacancy formation [274]. Vacancies are not only reactive, but they also exhibit variable mobility. Several studies have highlighted the behaviour of vacancies in crystalline nanoceria under different conditions of irradiation, chemical etching and heat treatments [119], [275], [276].

Figure 2.16 summarises several types of vacancy-related defects that occur in ceria nanorods. Fig. 2.16 (a) shows a solid rod with a high concentration of vacancies or point defects occupying its volume and surfaces. This type of structure is commonly achieved via irradiation and lattice swelling [277] and is closely associated with the case 2.16(b) in the figure, where

the same type of vacancies occurs, but they arrange to form clusters. Inside these clusters, vacancies retain their punctual dimensions by having residual lattice atoms in between vacancies. This phenomenon has been consistently observed in ceria nanorods [4], [119], [278].

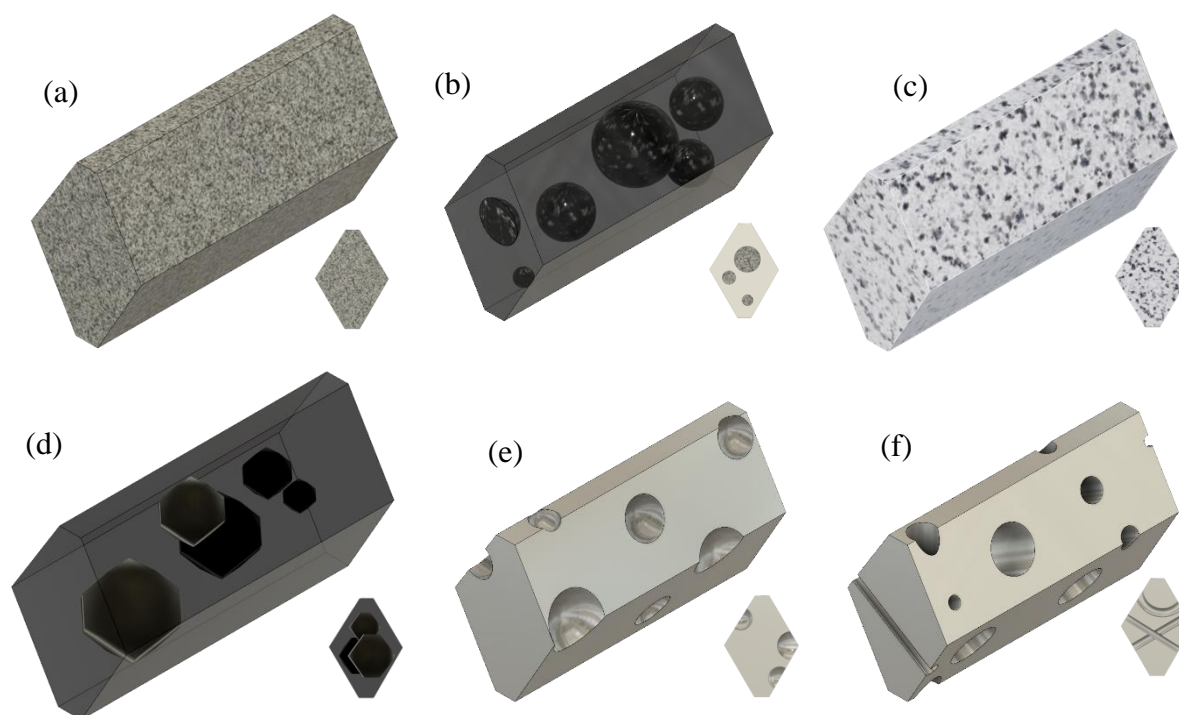


Figure 2.16 Schematic representation of different propositions of porous structures found in the existing literature: (a) point defects/vacancies; (b) vacancy clusters, (c) micro-voids, (d) mesopores with “negative particle” facet shape, (e) Surface pores, etch pits, concavities, (f) through-holes, nano-channels, wormholes.

Vacancy clusters are regularly a further product of irradiation experiments, where vacancies may start at random locations as in Fig. 2.16 (a), and then assemble into larger voids via dislocation loops [276]. It is also possible to obtain vacancy clusters via atomic-scale heat treatment. This process implies removing individual hydrogen, oxygen atoms or hydroxyl ions to create localised groups of vacancies [4], [278]. Upon heat treatment, these defects have been shown to evolve into small pores (<2 nm). Their shape is not well defined, but they generally seem to tend towards a spherical symmetry [4]. Heat treatments can also cause residual vacancies to reposition, resulting in a nanostructure like the one shown in 2.16(e) where the surfaces present with recesses, pits or concavities [12], [119], [120], [279].

Of particular interest is the occurrence of so-called 'negative nanoparticles', which reportedly evolve from the smaller pores/vacancy clusters[3]. These are three-dimensional cavities

with morphologies that correspond to that of ceria nanoparticles, namely octahedra and cub-octahedra. The activity of these defects, as well as their precise nature and formation mechanisms, are still majorly unexplored. The limited amount of information has created a significant contrast in theories. Sakthivel et al. first published the finding of these defects and proposed the inverse or negative nanoparticle theory consistent with previous studies on titania performed by Zhu et al. [125] and Han et al. [126]. Soon after that, similar defects were obtained by Li et al. [2], who observed that the presence of these defects improved the catalytic performance of the nanomaterials almost by a factor of four. However, they proposed a different explanation to Sakthivel in terms of the expected morphology in three-dimensions and the formation mechanism of the defects. This disparity is a significant gap in the literature, which could benefit from advanced characterisation studies.

2.3 The capabilities of advanced TEM for the study of porous nanocatalysts

In its most traditional form, transmission electron microscopy (TEM) allows a detailed morphological analysis of nanoscale features. This ability is of utmost importance in nanomaterials since morphology at the nanoscale is responsible for the properties that drive their state-of-the-art applications. Conventional TEM has been instrumental in the characterisation of a variety of functional morphologies like nanotubes, core-shell, nanorattles, matches, janus, stars, octopodes, dumbbells, as well as larger-scale materials with nanoscale characteristics in three dimensions like zeolites and mesoporous materials [280]. Some simpler structures also benefit from conventional TEM for the determination of defect mechanisms and nanoheterogeneity characteristics.

The importance of these developments is difficult to overstate, as nanomaterials constitute a core research interest in the fields of energy, environment, electronics, health and other major fields of study [281]. However, the capabilities of the transmission electron microscope extend far beyond morphological characterisation. This section of the review explores the literature concerning the different modes of TEM and the answers they have provided to imperative chemical and structural questions. Particular attention is placed on the contributions of TEM with tomographic and analytical capabilities to the field of nanoporous oxide catalysts.

2.3.1 The role of TEM in nanomaterials research

Over the last 30 years, nanomaterials and nanostructured materials have revolutionised the capabilities of a multitude of applications [280]. In the health sector, biocompatible nanomaterials have been used as sensors, microfluidic devices [282], cosmetics [283] and drug carriers [284]. In the domain of energy, nanomaterials are found in thermoelectric devices, photovoltaic cells, batteries, different types of fuel cells and photoelectrochemical devices [281], [285]. Famously, nanomaterials have made possible the modern information technology industry [286], [287], with nanoscale components being central to the optic and photonic devices, microelectronics, smart displays and countless more. In environmental applications, the efficiency of most devices is enhanced by the inclusion of nanomaterials [288]. Some examples are photocatalysts, protective and functional coatings [288], electrocatalysts [289] and sensors [290]. Given such a variety of applications, the study of nanomaterials and nanostructures benefits multiple fields beyond the domain of materials science.

The capabilities of TEM to determine nanoscale morphology, as well as compositions, makes it an authoritative complement for theoretical studies. For instance, TEM imaging plays an important role in systematic nanoscale composition diagrams [291], [292]. In these studies, researchers seek to predict changes in morphology and reactivity based on changes, generally, in the preparation [293]. For the cases of chemical preparation, chemists and materials scientists often rely on TEM for the understanding of construction mechanisms [294]. The analytical capabilities of TEM play a central part in nanomaterials preparation. This role continues to grow with the range of compositions found across nanomaterials. Currently, the major compositions of interest at the nanoscale include multicationic and multianionic species, mixed oxides, complex alloys, borides, phosphides, fluorides, phosphates, chalcogenides, carbon-based structures like nanotubes and graphene [67]. Additionally, there are a great number of organic nanomaterials, such as liposomes, micelles and block-copolymers. Scientific journals often feature comprehensive reviews outlining the application of transmission electron microscopy to a great variety of complex morphologies and compositions [295]–[300].

While there exist a great number of techniques that have characterisation capabilities at the nanoscale, TEM and its related techniques continue to provide the best opportunity to overcome the challenges associated with the characterisation of structures and physicochemical properties at the nanoscale and atomic scale. To name some examples, atomic force microscopy (AFM) and scanning electron microscopy (SEM) routinely achieve sub-nanometre resolution [301], [302]. Additionally, atomic force microscopy (AFM), scanning tunnelling microscopy (STM) and other types of scanning probe microscopy (SPM) techniques have proven potential for in-situ experiments without the constraints of high-vacuum conditions necessary for electron microscopy [303]. However, these techniques have very limited depth sensitivity. Therefore, they can only analyse surfaces or surface features. This limitation is important in nanomaterials applications, as most complex structures will occur beneath the surface. Somani

and Umeno published a review where they emphasise the importance of TEM for the study of carbon nanostructures [304]. Given the infinite amount of allotropes of carbon, nanostructures can be difficult to distinguish from each other when using surface analysis techniques. For example, multi-walled carbon nanotubes look almost identical to carbon nanofibers when imaged using SEM.

Meanwhile, transmission electron microscopy and scanning transmission electron microscopy (STEM) hold an important advantage by their very nature. TEM and STEM techniques generate by definition a transmitted image of the entire structure, including any features found under the surface, as well as surface properties. Transmission techniques facilitate the distinction of multi-walled carbon nanotubes and nanofibers. The review concludes that, without the use of TEM characterisation, it is almost impossible to make conclusive determinations of carbon nanostructures.

Transmission electron microscopy techniques routinely achieve sub-Angstrom resolution. To achieve this, they are operated at 100 – 300 keV [305], [306]. This high-energy beam can damage a wide range of materials. TEM groups have done multiple studies on the mechanisms involved in electron-beam damage. These complex phenomena vary according to the material. They primarily include heat transfer, radiolysis and knock-on damage [307]–[309]. TEM scientists have explored different ways to reduce the effects of beam damage or protect the materials against it. Zhang et al. have published a computation-assisted approach to protect metal-organic frameworks (MOFs) from the electron beam damage [310]. In it, they use computational methods to achieve precise alignments and focus values. Their atomic-resolution imaging has provided unprecedented insight into the structures of MOFs. This knowledge is directly beneficial for the applications of MOFs, which are materials of great interest to the catalysis community for their functional porosity, tuneable composition and high surface area, as detailed in Section 2.1.

Counteracting the effects of electron-beam damage in TEM constitutes a very active line of research [311]–[313]. A common approach to solve the knock-on damage effect is to reduce the energy of the electron beam. This compromise usually results in poor resolution and significant loss of electron penetration [314]. Cryogenic TEM is a very popular technique to avoid heating damage, at least to some extent. However, it does not counteract other types of beam damage [315], [316]. A promising solution to these collective effects comes from the development of direct-detection electron counting (DDEC) cameras, which can capture images with a low signal-to-noise ratio at extremely low doses of electrons [317]. These cameras are increasingly popular for biological applications but are still rare in the materials community, owing to practical difficulties [310]. This case is a typical example of the significance that digital image acquisition and related technologies have had on the advancement of TEM. It is worth noting

that the effects of the electron beam are not always undesirable, as irradiation-induced phenomena can be of significant interest.

2.3.2 Advanced TEM techniques and their use in heterogeneous catalysis

The nanoscale spatial resolution of TEM has established it as the most powerful tool for characterising the structure of nanomaterials. By combining imaging and spectroscopy, TEM is capable of obtaining a wide range of information at the nanoscale. This section will outline the most widespread modes of operation of the transmission electron microscope. Given the versatility of these techniques, named examples focus on the characterisation of solid catalysts at the nanoscale. However, most analytical methodologies are transferable across the diverse fields of application of TEM [318]. It is also worth mentioning that the techniques described below are far from the totality of TEM capabilities. They are also not the only TEM-techniques used for the study of heterogeneous nanocatalysts [67]. This section aims to underline the versatility of TEM, as well as to exemplify the acumen employed by researchers in the cited literature to favour a specific TEM mode.

2.3.2.1 High-resolution transmission electron microscopy (HRTEM)

HRTEM is a widespread and robust technique for the study of nanoparticles. It is commonly used for nanometrology of particles, as well as morphological analysis. It is a reliable tool for the crystallography of exposed surfaces and interfacial features. These characteristics are central to the catalytic performance of materials, as detailed in section 2.2.3. Some of the main catalytic materials that have been characterised using HRTEM include metal nanoparticles like Pd, Pt, PtFe_x and PtNi_x [319]–[321], as well as metal oxides and carbides such as IrO₂, RuO₂, CoFe₂O₄, LiCoO₂, Mo₂C and W_xC [322]–[325]. As a way of illustration, Zhang et al. recently published an HRTEM characterisation of PtNi_x nanoparticles heat-treated in different gas atmospheres [326]. High-resolution images showed the presence of corners and step defects in the exposed surfaces of their samples heat-treated in CO. These features were less marked in NPs heated in Ar, as seen in Figure 2.17. These results allowed them to correctly predict the influence of the heat-treatment atmosphere on the electrocatalytic performance of PtNi_x nanoalloy in the oxidation of methanol.



Figure 2.17 HRTEM and EDX results of PtNix NPs before heat treatment (a-c), and after treatment in Ar (d,e) and CO (f) [326]

2.3.2.2 High-angle annular dark-field scanning TEM (HAADF-STEM)

By the effect of mass-thickness contrast, the majority of modes of TEM imaging will present changes in contrast associated with the atomic weight of the material. However, this can be very unpredictable in cases with three-dimensional bodies, as the contrast could come from a change in thickness at constant chemical composition. HAADF offers a reliable solution to this problem with a high atomic-number sensitivity. More significantly, this technique suppresses incoherence artefacts originated by Bragg scattering. Other significant advantages of the technique are a lower dependence on sample thickness and focus value, all while maintaining high spatial resolution [318]. HAADF-detection is particularly useful for selective imaging of high-Z components of multiphase materials. Figure 2.18 shows a pair of images of the same sample region to compare the results of HRTEM and HAADF imaging [327]. The HRTEM image shows Pt nanoparticles (1-2 nm) suspended in the Vulcan Carbon (VC) film.

On the other hand, the Vulcan carbon film is nearly invisible in HAADF mode, while improving the visibility of the Pt NPs. More importantly, this image also allowed Ephsteyn et al. to resolve concentrations of Ta atoms in the VC film region. This case is an example of the

capabilities of HAADF for selective imaging by favouring high-Z elements over thickness features. Similarly, HAADF has been used to map Pt [328], Co [329] and Fe [330] single atoms for electrocatalysis.

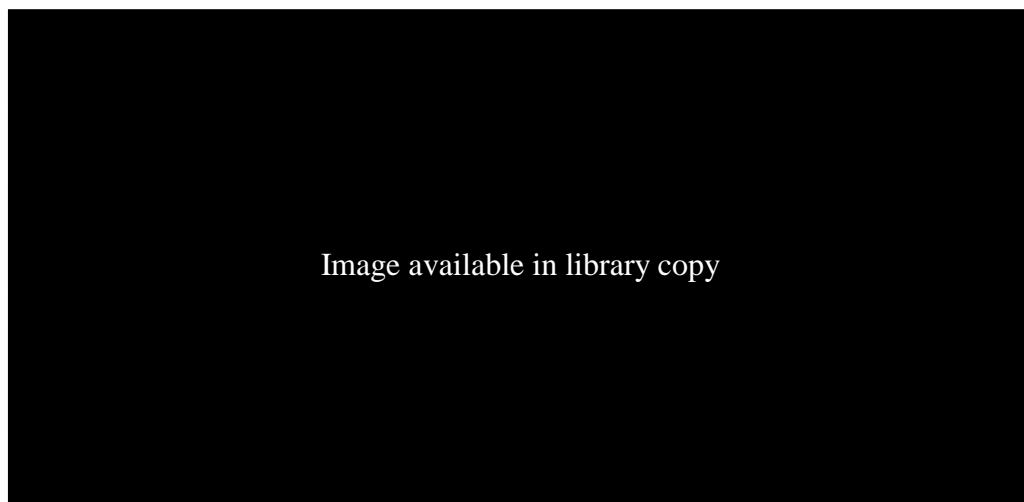


Figure 2.18 (a) HRTEM and (b) HAADF-STEM images of the same area [327]

2.3.2.3 Energy-dispersive X-ray spectroscopy (EDS)

While HRTEM can reveal the morphology of nanostructures with high spatial resolution, it is often necessary to complement this knowledge with the distribution of chemical species in the sample. EDS is the most common and simple way to achieve qualitative and quantitative elemental identifications in modern electron microscopes [67]. The capabilities of this technique will depend on the instrumentation (X-ray detector, electron source) and the species intended for identification. EDX works especially well on heavy elements that have a high fluorescence yield, for example, Au, Ag, Pt or Pd [331], [332]. The operation is normally done in one of three modes: point mode, line scan or mapping. Particularly of interest are the line scan and mapping techniques, especially when working with composite nanomaterials. EDS mapping provides information on the spatial distribution of elements in a selected area. This mode has provided fundamental knowledge of complex systems like heteroatom-doped graphenes [333], multi-metallic nanoparticles [334] and Fe,Co-nitrogen-carbon structures [335], [336] down to atomic resolution.

A clear example of the capabilities of EDS mapping can be found in work mentioned above of Zhang et al. with PtNi_x nanoalloys [326]. They complemented their HRTEM analysis with 2D X-ray spectroscopy to reveal the spatial distribution of platinum and nickel within the na-

noparticles. EDS mapping showed a significant increase in superficial Pt atoms after CO treatment compared to Ar (Figure 2.17). These results revealed not only that CO-treated NPs were more electrocatalytically active, but that Pt atoms played a central part in the mechanism of methanol oxidation. Line scan mode presents some advantages over EDS maps. Mainly, the limited area of analysis allows for longer acquisition times, which results in lower noise-to-signal ratios and more precise quantifications. This technique is particularly suitable to analyse the cross-sectional elemental distribution of nanostructures. Such application can be seen in the work of Li et al., who used EDX as the main tool in their extensive study of the formation of PtNi nanowires from a Pt/NiO core/shell precursor [337].

2.3.2.4 *Electron-energy-loss spectroscopy (EELS) and energy-filtered TEM (EFTEM)*

A more sophisticated form of spectroscopy than EDS is achieved by measuring the energy of the electrons after they have travelled through a transparent sample. This technique allows much more precise identification of the elements present in the sample, compared to X-ray spectroscopy. While EDS is mostly sensitive to heavy elements, EELS can identify much lighter atoms such as oxygen, carbon or boron [67].

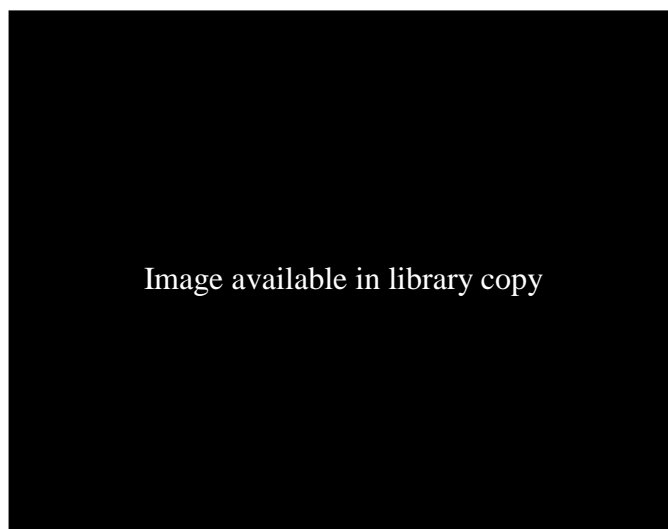


Figure 2.19 Cerium M4,5-edge spectrum from Pt-CeOx [338]

Furthermore, it can be used to reveal the electronic structure of the atom. These capabilities have proven very useful for the field of catalysis, which widely employs transition metals as supports and active components. EELS has been used to characterise their oxidation states and chemical bonds. The superior analytical sensitivity and spatial resolution have even allowed studying the mechanics of charge transfer between catalytic nanoparticles and oxide supports

[319], [325], [339]. A great example of the capabilities of this technique can be found in the work of Chauhan et al., who used EELS to study the electronic structure of cerium atoms in CeO₂ nanowires [338]. Figure 2.19 shows the EELS spectrum of cerium with two distinct peaks, CeM₄ and CeM₅. The ratio between the intensities of these two peaks was used to identify the most prevalent oxidation state of the cerium atoms. These results led them to conclude that an addition of 5 wt% platinum nanoparticles resulted in a much higher concentration of Ce³⁺ and, therefore, a higher oxidation capacity.

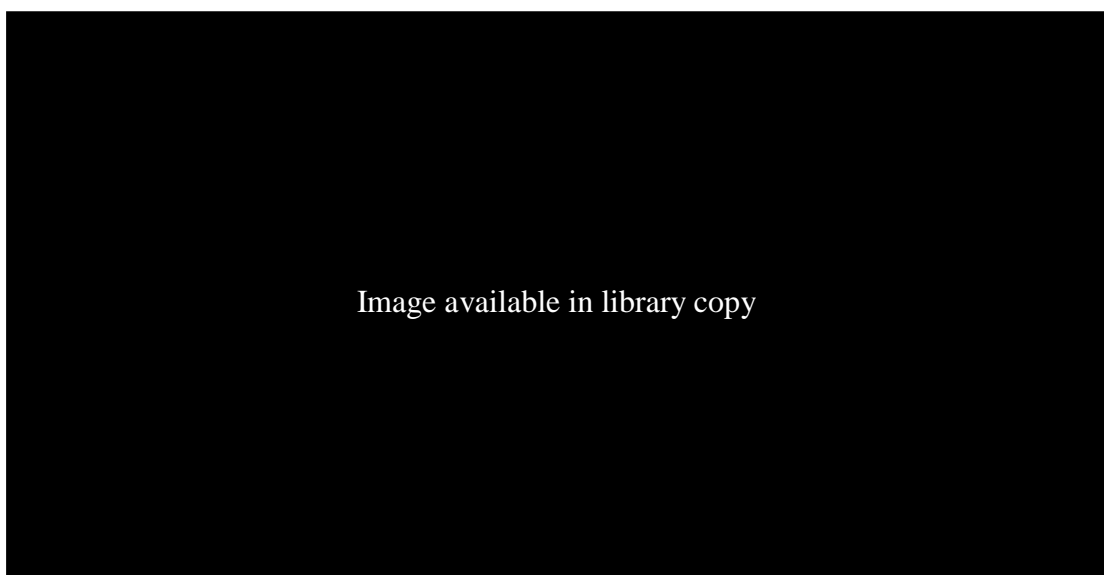


Image available in library copy

Figure 2.20 EFTEM study of SN-doped carbon nanotubes [340]

In metal-free nanomaterials, EELS has been used to identify the coordination and hybridisation state of carbon and heteroatoms, e.g. S, P, N, B [341]–[344]. Similarly, as EDX, EELS can be used to obtain chemical composition maps of a selected area. Elemental images are formed by selecting a specific energy loss (eV) and filtering out all other signals. This technique, usually called EFTEM, holds analogous advantages over EDS mapping as EELS does over EDS point spectra. That is, the ability to identify the spatial distribution of all elements, except for lighter elements like H, He or Li, with superior spatial resolution and lower noise-to-signal ratio. Figure 2.20 shows the EFTEM results reported by Shi et al., who studied the effect of sulphur and nitrogen doping in carbon nanotubes [340]. Their studies showed that nitrogen appeared preferentially along with the intersecting 'bamboo' structures of the nanotubes. On the other hand, oxygen and sulphur show a homogeneous distribution throughout the structure. This distribution is associated with a better catalytic oxidation performance than their N-doped counterparts.

2.3.3 Electron Tomography (ET)

Electron tomography, also called 3D-TEM, is a useful tool for characterising nanostructures and nanomaterials in three dimensions. The principle of the technique is the same as that of other forms of tomography: Capture one- or two-dimensional information at multiple angles and use computational methods to obtain information of higher dimensionality. The shorter wavelength of electrons compared to X-rays, neutrons, light, and other waves used for transmission gives electron tomography one of the highest resolutions of any 3D analysis techniques available today [151].

Moreover, TEM scientists combine electron tomography with other abilities of the transmission electron microscope to obtain analytical and structural information of nanoobjects in three dimensions [345], [346]. The first materials science publication using electron tomography date back as far as 1988, when Spontak et al. successfully reconstructed a block copolymer microstructure [347]. However, the use of ET for materials science has never become as widespread as for cell biology. This is due to the inherent technical difficulties associated with 3D-TEM, as described below. Developments in different areas of digital imaging and TEM technologies have enabled researchers to gradually surmount the challenges which limit the use of electron tomography.

In the biological sciences, electron tomography has been used to obtain three-dimensional reconstructions of cell organelles for over five decades. The 1982 Nobel lecture by Aaron Klug is a first-hand description of the history of 3D imaging in electron microscopy [348]. The works of Klug and De Rosier provided historical breakthroughs in the characterisation of the morphology and inner structures of living cells [349]. Early studies by Hoppe et al. also contributed to show the potential of electron tomography in the fields of biological sciences [350].

The first applications of electron tomography to materials characterisation were the successful 3D reconstructions of polymeric nanostructures and other soft materials, which exhibit complex three-dimensional architectures, and which greatly benefitted from the quantitative capabilities of electron tomography [351], [352]. Since then, polymeric structures continue to be a common field of application of 3D-TEM, expanding its capabilities to increasingly complex block copolymers and nanocomposites [353]–[356]. It was not until the early 2000s that inorganic nanomaterials began to benefit from electron tomography, with the pioneering works of Koster et al. who employed HRTEM tomography to reconstruct a porous zeolite [357]. These results attracted significant interest from the catalysis research communities who saw the potential of electron tomography as a tool to elucidate catalytic mechanisms at the nanoscale [151].

Besides its powerful resolution, another important advantage of 3D-TEM over other forms of tomography is the variety of image acquisition modes available in the TEM. For example,

energy-filtered imaging can be used in combination with electron tomography to obtain three-dimensional analytical maps of multiphase materials [346], [358], [359]. The multiple advantages of coupling electron tomography with analytical and z-contrast imaging modes are outlined by Midgley and Weyland in their milestone publication [15], where they first proved the capabilities of this type of approach.

To obtain relevant information, the choice of imaging mode is of utmost importance. Researchers make this decision based on two major factors; the type of material, and the feature of interest. As seen in the previous section, different imaging modes will be adequate for a study depending on whether the material is conducting, insulating, inorganic, organic, amorphous or crystalline. Likewise, researchers will choose different techniques according to the properties they seek to characterise, be it morphology, elemental composition, meso- or atomic structure, and so on. The most common technique found in the electron tomography literature is bright-field imaging (BF-TEM).

In comparison with other techniques such as EFTEM, BF-TEM is fast and easy to implement, which can be very important in 3D-TEM, since the acquisition of a tilt series can last up to several days [360]. However, the capabilities of the technique often outweigh the experimental challenges. As a result, there is a vast literature of three-dimensional studies of nanomaterials, which benefit from advanced TEM acquisition modes including EDX mapping, plasmon EELS spectroscopy [346], [361], electron holography [362] and other state-of-the-art imaging modes [151]. The complexity of certain materials may require a combination of imaging modes to be employed at each tilt angle in the tomographic series [363]. The publication by Xu et al. provides a useful reference for the limitations and advantages of the most common techniques used in conjunction with ET [16]. In there, they compare reconstructions of the same object from tilt series acquired using EFTEM, BF and HAADF-STEM.

The application of electron tomography to a wider variety of materials has required modifications to the technique to suit the experimental challenges of each object of interest. For example, the majority of publications use the conventional approach of 'quantitative tomography' [151]. This method relies on the intensity of each point of the sample to be a function of the signal of interest in that point across the thickness of the specimen. While this is the case in amorphous materials, crystalline and polycrystalline materials do not follow this rule. In this case, the coherent scattering of electrons produces stronger contrast than the mass-thickness contrast which quantitative tomography relies on for the reconstruction of volumes. In other words, Bragg-diffraction contrast in crystalline materials will cause the intensity of a point of constant thickness and composition to vary significantly at those recording angles which coincide with coherent elastic scattering.

Given the prevalence of crystals in materials science, researchers have had to find ways around the problem of coherency artefacts. Common workarounds across the literature use

energy-filtered imaging or high-angle annular dark-field (HAADF-STEM), which significantly reduce the effects of Bragg diffraction in the images [364]. However, this requires a microscope with STEM capabilities, as well as a more intricate experimental setup. A third approach is found in the work of Saghi and Möbus, who proposed a method of 'geometric tomography', wherein the reconstruction uses only binary information [9], [365]. This approach eliminates the undesired imaging artefacts of crystalline materials, as well as the mass-thickness contrast associated with the specimen thickness and atomic number. Regardless of this loss of information, geometric tomography has proven effective in reconstructing the morphology of crystalline materials using conventional bright field imaging. A gap in the literature can be seen here, as the field could benefit from expanding the use of geometric tomography to reconstruct the inner structure of materials as well as their morphology.

2.3.4 The capabilities of TEM in studying nanoporous materials

As discussed in previous sections, porous materials continue to grow in interest for a wide range of applications. Their relevance has resulted in a great number of research efforts devoted to the synthesis of new nano- and mesoporous materials, as well as studies into their characteristics and capabilities [366]. Their functions result from the periodicity of pores as well as the defects found on the surfaces of the connecting walls [79]. The continuity of the enclosing crystalline structure and the morphology of the material in the larger scale are also contributing factors to their behaviour. This morphological and structural complexity has encouraged the development of new tools and methods for the characterisation of porosity and porous materials.

As evidenced in the review by Liu et al., TEM was not a popular method of choice for the study of porous materials before the last decade [8]. One of the reasons is the sensitivity of many porous structures to collapse under the electron beam. Beyond this, the three-dimensional complexity of porous materials can render intricate results, which do not resolve the structure of individual pores. However, the development of new microscopy technologies, as well as the implementation of three-dimensional characterisation methods have resulted in unprecedented knowledge of porous materials at the nanoscale.

A particular advantage of electron microscopy over most techniques used for the study of porous structures is the ability to characterise non-periodical information. Meanwhile, most gas-based techniques only provide average information on bulk characteristics, e.g., pore size, shape, wall thickness [85]. Important information such as structural defects and terminal structures can only be obtained by electron microscopy. Additionally, transmission techniques, i.e., TEM and STEM also enable the characterisation of pores beneath surface barriers, which is not a possibility in SEM and other surface techniques [367].



Figure 2.21 MOF terminal structure identification by HRTEM[8]

Figure 2.21 shows the HRTEM characterisation of a metal-organic framework, Nickel-doped metal catecholate (Ni-CAT-1). In this study, Liu et al. presented the unprecedented characterisation of the terminal structure of a crystalline MOF, as indicated by the white arrows [8]. This information allowed them to develop better-informed theories relating to the activity of Ni atoms throughout the structure and develop a theoretical model shown in the Figure. MOFs are known to collapse under the electron beam easily. Hence, these results could only be obtained by utilising a reduced electron beam density with overlapping acquisitions, which reduced the signal-to-noise ratio. Additionally, they employed a post-specimen spherical aberration corrector. This study serves as an example of the challenges that porous materials present during TEM characterisation, as well as the important benefits to overcoming those challenges.

There are other non-periodical characteristics of porous materials beyond their terminal structure. These include incommensurate modulation, quasi-crystalline regions and inter-growths. These structural deviations can play an important role in the activity of the material and are, therefore, a relevant subject of study. The challenges presented by these characteristics often means they cannot be fully understood by microscopical or imaging methods. Instead,

TEM analysis is often used in conjunction with theoretical modelling. This challenge is presented by a lot of non-conventional crystals, which lack periodicity at the nanoscale but are classified by crystals according to their diffraction pattern.

The literature contains countless examples of the synergy between transmission electron microscopy and theoretical modelling. Some of the porous materials which have been studied using this strategy have been zeolites [368], MPS materials [366] and polymers [369], [370]. Of particular relevance to the present work are the atomistic models of ceria nanomaterials performed by the groups of Sayle et al. [188], [371]. These studies have not only allowed the morphological characterisation of nanomaterials but provided unprecedented insight into their formation mechanisms, as well as reliably predicting their behaviour [215], [372]. There exists an important gap in the literature, as the porosity found in ceria nanorods by Qu et al. [2] and others [3] has not been scrutinised under this type of collaborative approach.

Chapter Three

Experimental Methods

The present chapter covers the methodology utilised to achieve the objectives of the present work. The experimental results reported in chapters 4-6 concern investigations into various porous materials. Due to this diversity, the preparation of each material is presented in detail at the start of each relevant section. Nevertheless, a significant amount of methods is common to all experimental work in this project. These overarching methods are the focus of this section. All the studies reported in the present work rely on some form of electron microscopy to reveal the microstructure and formation mechanisms of a particular object of study. Additionally, a majority of electron microscopy results have been analysed, processed or in some way transformed by the use of specialised software. The present chapter describes the microscopy instrumentation and software packages used to study the materials of interest throughout this project.

The research design of this project aims to elucidate the formation and structure of selected porous nanomaterials by exploiting characterisation capabilities across electron microscopy. To this end, the present report combines the results obtained using a variety of SEM and TEM equipment. The choice of instrumentation for each task across the experiments in this work was based on the suitability of an instrument for the intended experiment, as much as its availability.

Far from hindering the production of novel research outcomes, the limited availability of advanced TEM instrumentation throughout the project was a significant driving force for the development of innovative image processing methods. The success of this approach is especially notable in Chapter 5, where a new form of geometric tomography is proposed, which made it possible to overcome the limitations posed by the instrumentation.

3.1 Electron microscopy instrumentation

All of the electron microscopy characterisations presented in this work were performed within the Sorby Centre for Microscopy and Microanalysis in the Faculty of Engineering at the University of Sheffield. The main objective of the centre is to provide high-resolution imaging and

analysis of inorganic materials. The facility consists of fourteen microscopes, eight SEMs and six TEMs, which range widely in their capabilities and access requirements.

The electron microscopes used throughout the present work were selected based on their imaging resolution, analytical capabilities and their availability during the experimental periods of the project. These criteria are detailed below with the specifications of each instrument, emphasising their relevance to the work reported here, as well as their capabilities and limitations.

3.1.1 JEOL JEM-2010F

This transmission electron microscope was considered a promising instrument for the experimental objectives of this work due to its multiple novel accessories and state-of-the-art capabilities. Significantly, this microscope has an EDX detector, EELS/EFTEM capabilities and a dedicated accessory for STEM and HAADF imaging. The high-resolution and analytical capabilities of this microscope made it particularly relevant to the experimental requirements of composite materials reported in Chapter 6. This microscope became available halfway through the experimental period of the project and was unavailable for the last year of experiments for reasons not connected with this work.

This instrument is located inside a purpose-built laboratory below ground level. For vibration isolation, the microscope sits on a large concrete block cast directly onto the bedrock. A 5 mm air gap isolates the concrete block from the rest of the floor. All four walls of the laboratory are covered in heavy curtains to reduce acoustic vibrations. Additionally, a field cancellation system (Oxford Instruments) is fitted inside the room to make the ambient magnetic field suitable for the electron microscope.

The field emission gun in the 2010F presents several advantages over the standard tungsten filaments, such as the one found in the JEOL JEM-3010 and the Philips 420EM. Specifically, FEG allows focusing the beam to a small probe, which is beneficial for analytical methods, such as EELS or EDX. The gun also contributes to the imaging capabilities of the instrument, as the superior coherence of the FEG beam decreases the information limit in HR-imaging to just over 1 Å, according to the manufacturer.

The 2010F provides accurate control over the location of the specimen due to its incorporation of a piezo-stage, as opposed to a more conventional hand-controlled stage or one with electric motors. The piezo-stage is particularly advantageous during tomography tilt-series acquisitions, as the object of study can easily shift its lateral position. This feature is also beneficial to compensate for the effects of specimen drift.

This TEM can carry out electron energy loss spectroscopy (EELS) using a Gatan imaging filter located under the camera chamber. This capability was beneficial for the present work in

characterising the composition of an MSU-F/CeO₂ composite at the nanoscale, as seen in Figure 6.24. Further analytical capabilities rely on the ultrathin-window EDX detector (Oxford Instruments), which was extensively used throughout the investigations of composites reported in Chapter 6. Throughout this work, a JEOL Beryllium double-tilt specimen holder was occasionally used to improve the accuracy of analytical results by avoiding spurious element signals corresponding to the material of the holder.

Figure 6.26 shows an unaccounted signal of Al, which is most likely resulting from an undesired by-product in the silica sample or from the carbon film used as support for TEM specimens.

Finally, the 2010F microscope features STEM capabilities, which rely on an advanced scanning imaging device. This instrument enables to control beam parameters to generate an electron probe as reduced as 20 Å. By using the high-angle annular dark-field detector, this hardware allowed the acquisition of high-resolution Z-contrast transmission images, as seen in Figure 6.24.

3.1.2 JEOL JEM-3010

This transmission electron microscope features ultrahigh resolution capabilities with a point resolution of 0.17 nm and a lattice resolution of 0.15 nm. This microscope has a standard LaB₆ thermal emission filament electron gun, which significantly reduces its throughput compared to the 2010F. As described above, a significant factor for the selection of this microscope for the present work was the 4.5 mm pole-piece gap, which could accommodate the rotation of a tomography specimen during tilt-series acquisition. This TEM was the only high-resolution instrument available for the majority of the experimental period of this project. The difference in availability is the main reason the electron tomography work in this project was performed using 3010, instead of the 2010F.

3.1.3 Electron tomography instrumentation

The higher imaging resolution of the 2010F would normally make it more desirable for electron tomography than the 3010. However, the 2010F poses a significant mechanical limitation that the pole-piece gap is only 2 mm wide. This design feature aims to improve the resolution of the microscope. However, it poses a significant downside for electron tomography. The 2 mm gap is too narrow to allow the high-tilt-angle rotation of a standard-grade 3 mm TEM specimen grid. This limitation is overcome by an in-house preparation method developed specifically for the preparation of samples suitable for tilt-series acquisition in the 2010F TEM.

After a suspension of nanomaterials has been applied onto the standard-grade carbon-coated TEM grid, a scalpel is used to cut the grid into two sections. The cut is made across a chord of the circular grid, which is at least 0.5 mm smaller than the diameter of the grid. This operation produces a semi-circular segment no more than 1 mm wide, which still contains a significant section of carbon film hosting the nanomaterials. This procedure is done with caution to avoid inflicting damage to the carbon film that could render the specimen unusable. Once a suitable segment has been produced, it is mounted onto a purpose-built titanium rod using a low-vapour-pressure epoxy resin. Specifically, the titanium rod features a J- or C-shaped flattened tip designed to hold the continuous section at the rim of the reduced TEM grid. A small amount of high-vacuum sealant (Torr Seal ®, Kurt J. Lester Company) is prepared according to the manufacturer instructions, and two small drops are applied to the tip of titanium rod at the points of contact with the TEM grid.

Finally, the specimen glued to the rod is allowed to dry for two hours before attaching it to a specialised tomography holder (Gatan, Inc.). The holder is then inserted into a table-top vacuum pump, where the prepared specimen is kept overnight. This step is intended to reduce the risk of introducing volatile products associated with the sealant into the microscope. This preparation method was used to produce the samples studied in sections 5.2 and 6.2.1.1. In contrast, the 4.5 mm pole-piece gap of the 3010 allows the full rotation of a standard-grade 3 mm TEM grid without the need for intricate sample preparation.

3.1.4 Philips EM-420

This instrument is a conventional transmission electron microscope with no high-resolution capabilities and is thus unsuitable for atomic-lattice imaging. Nevertheless, its high availability and high throughput made it a valuable addition to the instrumentation used for this work. Also, this instrument was available during the entirety of the experimental period of this project.

Numerous factors can affect the production of desirable materials at the nanoscale. For this reason, the preparation of high-quality TEM samples can be a reiterative process. The application of this microscope for the present work mainly focused on exploratory characterisations. These sessions aimed to assess the quality of a sample before moving on to a more sophisticated instrument for its detailed characterisation.

The Philips EM420 has a thermionic tungsten electron source like the 3010. However, the low-acceleration voltage operation gives this microscope a significantly higher throughput than the 3010. It operates at low-acceleration voltage, from 60 kV to 120kV, making it suitable for imaging of materials that are sensitive to electron-beam damage. For this reason, this TEM was valuable for the initial explorations of polystyrene materials, as presented in section 6.1.2.3. The low-magnification capabilities of this microscope made it suitable for surveying colloidal

crystal samples to assess their long-range ordering properties, as seen in Figures 6.10 and 6.11. According to the manufacturer, this TEM has 0.34 nm and 0.3 nm of point and lattice resolutions, respectively.

3.1.5 JEOL JEM-F200

This instrument is a high-throughput TEM with high-resolution imaging and analytical capabilities. The cold-field-emission gun incorporated in this microscope gives it a significant advantage over the conventional Schottky FEG in the 2010F. This microscope features an automated sample-holder transfer system (SpecPorter®), which makes it easy and efficient to load samples. The high efficiency of this microscope made it suitable for the characterisation of multiple TEM specimens of nanomaterials heat-treated at different temperatures, as reported in Chapter 4. This TEM only became available during the final three months of the experimental period of this project.

3.1.6 Scanning Electron Microscopes Inspect F/F50

Surface imaging and compositional analyses were carried out using a field-emission gun (FEG) scanning electron microscopes. The application of these instruments is particularly prominent in the characterisation of opal materials presented in section 6.1. The high-brightness FEG in these microscopes enabled surface imaging of polystyrene opals at low kV-values, which allowed the samples to be characterised without the need for conductive-carbon-coating. In addition, these microscopes can make column adjustments automatically based on the user selection of kV and the spot-size setting. This feature makes these SEMs particularly efficient, which allowed the characterisation of multiple samples prepared under different conditions. Therefore, these SEMs were instrumental to the optimisation of colloidal crystal fabrication, as presented in section 6.1.2.1.

These microscopes provide characterisation flexibility by virtue of their multiple detectors, which can be used in combination. For example, Figures 6.17 and 6.36 relied on the comparison between high-resolution secondary and back-scattering images to highlight the Z-contrast in composite materials. The analytical capabilities of the Inspect F50 were particularly valuable for the characterisation of composite materials in this project, as reported in Chapter 6. The ability to combine surface images and compositional maps enabled the accurate characterisation of SBA-15/CuO composites, as reported in section 6.2.1.2

3.2 Digital image analysis and processing

The characterisations involved in this project relied on a diversity of digital image processing methods to draw significant information from the electron microscopy results. The software packages described below were used for different grades of transformations. These ranged from the simple calibrations, assigning pixels with a dimensional value, to the different back-projection operations presented in Chapter 5, which use imaging results to produce higher dimensionality information. The selection of the following software packages was based on their capabilities and availability. The availability of specialised open-source image processing software made it possible to achieve the objectives of the project without the need to develop new image-processing codes.

3.2.1 ImageJ

This program was used extensively throughout the project for a wide range of image processing applications. In addition to being available at no cost, ImageJ is built with an open architecture, which allows ample extensibility. This has encouraged the development of a plethora of user-written plugins available in online repositories. Such custom plugins were also used extensively during this work, as outlined below. The hardware requirements ImageJ are minimal, but it can be used to perform heavy operations involving multiple images, which are potentially limited only by memory availability. Further details regarding the background, development and applications of ImageJ can be found in the 25th-anniversary article by their developers at the National Institutes of Health, Schneider et al. [373].

The basic capabilities of ImageJ, i.e. without third-party plugins, were used to perform a majority of the essential operations presented throughout this report. Such applications included: image calibration, line and area measurements, fast-Fourier transform (FFT) calculations, intensity thresholding, as well as contrast manipulations. Furthermore, ImageJ was used to create density diagrams based on pixel value calculations, as seen in Figure 5.2(a). The filtering capabilities of ImageJ are often a valuable tool when processing electron microscopy images, which often contain speckle associated with the carbon-film. This effect can be removed using a median filter prior, which facilitates particle detection and measurement, as seen repeatedly throughout Chapter 4.

The ability of ImageJ to display, analyse, edit and print multiple image file formats allowed results to be transferred between EM-lab machines and other computers. This compatibility is particularly important for the present work given the variety of electron microscopes used. Each electron microscope is paired with a software package, which often produces results in company-specific formats that can be difficult to display, analyse or process in other PCs. The

ability of ImageJ to work with image stacks was particularly valuable for the handling of tomography results. Image stacks are a series of images that share a single window. A significant application of this ability is seen in Figure 5.8, which shows a Z-projection of a tilt-series modified using a new segmentation process.

3.2.2 TomoJ

Electron tomography is significantly more popular across the life sciences than for materials science applications, as discussed in section 2.3.3 of the literature review. TomoJ, like most other transmission electron tomography software, has been developed for applications across cellular biology. This software is an ImageJ plug-in developed by Chemistry, Modelling and Imaging for Biology (CMIB) at the Curie Institute, which developers make available free of cost along with relevant articles and tutorials [[374]].

Due to its development background, TomoJ is configured to assist in the tasks involved in the reconstruction of subcellular components. Therefore, special considerations had to be taken for the reconstruction of inorganic oxide nanomaterials performed in the present work. For instance, the automated alignment algorithms integrated into TomoJ proved unsuitable for the signals processed in the experiments here reported, as discussed in section 5.3.2.1. This and other limitations are presented in detail in the relevant sections across Chapter 5.

TomoJ was a valuable tool for the tomographic calculations performed in this project. Particularly, TomoJ provides the option to carry out non-weighted back-projection calculations, which is not a facility in all tomography software. Both BP and WBP were utilised during the present work, as reported in sections 5.1 and 5.2.2. Besides, the availability of multiple algorithms such as algebraic and simultaneous-iterative reconstruction techniques made it possible to test the suitability of different methods before selecting geometric tomography as the most suitable method for the reconstruction of mesoporous ceria nanorods from conventional bright-field images.

3.2.3 Chimera

UCSF Chimera was used for the visualisation of tomograms as three-dimensional objects. The majority of tools in this software are aimed for the analysis of molecular structures. It is made available for free for non-commercial use by its developers at the Resource for Biocomputing, Visualization and Informatics (RBVI), alongside relevant tutorials and articles [375].

The ability of this software to visualise multiple 3D-objects simultaneously, as well as to overlap their bounding boxes, was essential for the reintegration of segmented single-object

reconstructions, as seen in Figure 5.14. This feature made it possible to apply a different threshold to each object, and then insert a calibrated scale bar to perform 3D-nanometrology, as seen in Figure 5.12. The extensive customisation options in Chimera made it possible to present each pore in a different colour for identification, as well as giving the rod surface a mesh-appearance. This produced highly illustrative 3D objects that facilitated the study of the 3D characteristics of the mesoporous nanorods.

3.2.4 Adobe Creative Cloud

The image-editing capabilities of ImageJ were complemented with packages from the Adobe Creative Suite. Particularly, Adobe Photoshop (Ps) and Illustrator (Ai) were used for specific tasks within the pre-processing steps of tomography experiments.

Photoshop does not share the capabilities of ImageJ to work with stacks of multiple images inside the same window. However, Ps provides scripts that allowed loading multiple images into a single file comprised of multiple one-projection layers. A significant advantage of working with Ps layers over ImageJ stacks is that Ps does not require all images to be the same size. Once images have been loaded into a Ps file, it is easy to align them by laterally displacing one layer at a time. After a satisfactory alignment, rotation and translation transforms were applied to the whole series simply by selecting all layers in the file. Finally, individual layers were exported into image sequences, which were successfully pre-processed, as shown in Figure 5.6.

Illustrator was used for the steps involved in the segmentation of objects from the same image, such as in Figure 5.7. The facility of Ai to draw and edit vectors that tracked the shape of a defect at a given projection was essential for the novel GT method presented here. The drawings representing the precise shape, size and relative location of each feature were finally exported into Ps format to apply the necessary transformations for the reconstruction, as detailed in section 5.1.2.2.

3.3 Further experimental methods

Several procedures employed in this work are not considered established experimental methods but still belong to ongoing international research. Accordingly, such methods are presented in Chapter 2. Examples of such methodologies include the infiltration of nanoporous materials and the fabrication of colloidal crystals, both detailed in Chapter 5. As mentioned at the beginning of this chapter, the descriptions of materials and preparation methods, which are specific to a single section of results can be found in the corresponding chapter.

Chapter Four

Ageing of Metastable Ceria Nanomaterials

This chapter presents the most relevant findings of the project in regard to the ageing of metastable ceria nanomaterials. Below are summarised the main motivations for these experiments.

Catalysis groups would generally consider any type of heating to be undesirable for catalytic nanomaterials, as it tends to reduce surface/volume ratio, removes regions of high activity like defects or metastable facets, and, in the particular case of ceria, it oxidises Ce^{3+} to Ce^{4+} . However, catalytic materials are routinely exposed to high temperatures in operation [18], which justifies their study under these conditions. On the other hand, an increasing number of researchers are defying this preconception by exploring the effects of heat treatment on a number of catalytic nanomaterials, including ceria [11], [376], [377]. The present work highlights the role of TEM characterisation in exploring the effects ageing at the nanoscale. Each of the chosen ageing temperatures is motivated by a gap in the literature.

Firstly, air-stored or room-temperature ageing for seven years was encouraged by collaborators seeking to identify room-temperature alterations. Nanocubes and nanorods are metastable materials, which makes them prone to transformations at room temperature. This type of test can be found in modelling literature but has never been performed experimentally. Given the nanoscale dimensions of the materials, there exist the possibility that atmospheric air could change the surface oxidation levels. This would cause diffusion of the surfaces in the order of several nanometres, which would significantly alter the morphology of materials of this scale. Furthermore, the characterisation of samples aged at room temperature provides a reference for any transformations in heat-treated samples that may be due to air-storage time as opposed to the heating.

The second temperature of 800 °C can be found in the works of Sakthivel et al. [3] and Li et al. [2]. The latter performed catalytic performance tests and found that nanorods were four times more active after the heat treatment. This temperature also appears significant in the transformations studied via thermo-mechanical analysis (Fig. 4.1), as it appears to be the final temperature before the onset of the sintering stage of bulk ceria. Researchers have attributed this enhancement to heat-induced porous defects in the nanorods. However, the structure of these novel materials has remained relatively unresolved.

The highest temperature employed in this work is 950 °C. This practical maximum was set based on the transformation diagram shown in Figure 4.1, which shows that the sintering of

bulk ceria begins at 800 °C. Heating above this temperature would destroy the nanomaterials and form bulk powder ceria. There is no precedent in the literature of heat treatment of nanorods or nanocubes at such a high temperature.

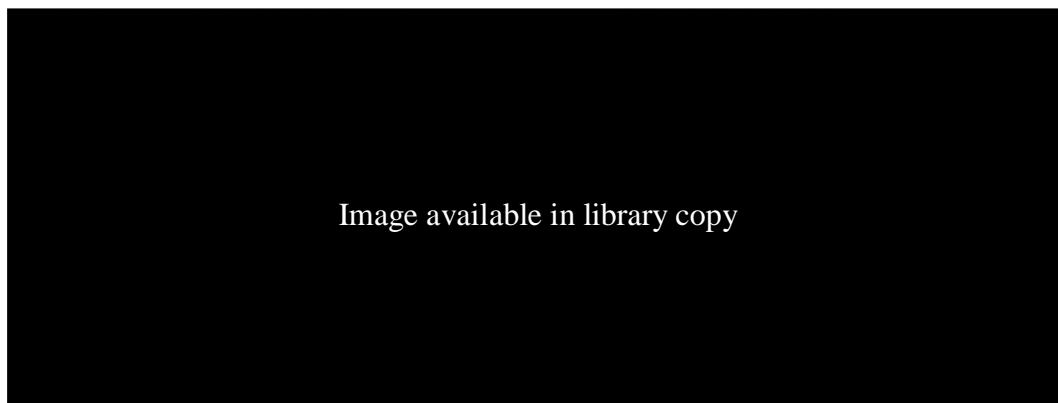


Figure 4.1 Thermomechanical behaviour diagram of bulk ceria [378]

Ceria nanorods and nanocubes were prepared by collaborators by optimising the parameters of a conventional hydrothermal synthesis. The procedures are found in detail in their publication [214]. In brief, ceria nanomaterials were obtained by reacting aqueous solutions of Ce(NO₃)₃·6H₂O and NaOH inside an autoclave. The morphology of the products was predicted by controlling the concentration of sodium hydroxide, the reaction temperature and the time of reaction. Nanocubes were obtained by reacting the ceria precursor with a [22.5 M] NaOH solution at 180 °C for 24 hours whereas nanorods were obtained by using NaOH [22.5 M] at 120 °C for 24 hours.

4.1 Effect of room-temperature storage

The syntheses of ceria nanocubes and nanorods were performed seven years prior to this experimental work, during which period the materials could undergo structural and morphological transformations. For this reason, it is useful to perform an in-depth TEM characterisation of the materials. The results obtained are compared to those obtained by collaborators when the materials were originally fabricated. Chapter 3 presents the details of the equipment and resources employed in this work.

4.1.1 Sample preparation of air-stored nanocubes and nanorods

The dry CeO₂ nanocube- and nanorod- powders were separately stored in 1.5 mL polypropylene centrifuge tubes for seven years after their original fabrication. The powders appeared fine and compact, occupying a volume of approximately 200 microlitres in the centrifuge tubes. Both showed a pale yellow colour, which is typical for cerium(IV) oxide. To prepare the TEM samples, the tubes were filled with deionised water to their full capacity, and the caps were snapped back on and examined for leakage. The solution immediately became cloudy, consistent with the dispersion of nanoparticles, while most of the powder remained visible at the bottom of the containers. Subsequently, the tubes were immersed in an ultrasonic bath for 25 minutes. At the end of the ultrasonication, there were no visible powders at the bottom, and the suspensions were evenly cloudy. A 500 μ L volume of each suspension was transferred to an empty 2.5 mL centrifuge tube, previously rinsed with deionised water. Each suspension was diluted with deionised water to a ratio of 4:1. Each liquid was handled using disposable micropipette tips to avoid combining the suspensions. The molar concentrations of cerium oxide in the suspensions were not considered relevant as the aim was simply to obtain a translucent homogeneous suspension, which would produce well-dispersed TEM samples with enough amount of material for adequate analysis. It is for that same reason that the original powders were not weighed or measured in any way.

The final suspensions were added onto standard grade carbon-coated square copper grids (3.05 mm, 200 mesh). The copper grids were first laid on clean flat surfaces with the carbon film side directed upward. Using new disposable micropipette tips, a volume of 50 μ L of each suspension was poured on top of each copper grid. The suspensions formed small drops and were allowed to dry at room temperature for one hour. Once dry, each sample was examined using a visible light microscope to verify the integrity of the carbon film. Each copper grid was stored in a clear gelatine capsule to avoid contact with hard surfaces, which could damage the carbon film. Each gelatine capsule was transferred to a glass vial and clearly labelled.

4.1.2 TEM of air-stored ceria nanorods

High-resolution TEM was used to characterise the sample at different magnifications. Images taken at lower magnifications, such as the one shown in Figure 4.2 can be useful to show the general contents conforming the sample. The section shown in the image is typical of the sample, and it initially allows the evaluation of the adequacy of the sample preparation. A great number of particles are visible, but they are dispersed well enough that the system is still transparent to electrons. The carbon film appears to be in good condition with no tears or holes. Additionally, this large section of about $2 \times 2 \mu\text{m}$ is consistently in focus throughout its area.

This relates to the integrity of the copper grid, which has remained flat after preparation and handling. Image (a) in Figure 4.2 shows an agglomerate of nanorods, which extends over several micrometres. The image is in bright-field acquisition mode, which means that contrast directly correlates to the thickness and atomic number if diffraction contrast is suppressed and can be ignored. I.e., darker sections can indicate a thicker region of the sample or the presence of a heavier element. The edge of the agglomerate has been selected for imaging, since it is more likely to be electron transparent and have more isolated particles, which are generally easier to image. This low-magnification image of an area crowded with nanoparticles can be used to identify features of interest for further analysis. Several features of interest in the image have been annotated.

Feature A consists of an elongated shape of constant diameter with lighter contrast along the middle, as seen in the digital close-up Fig. 4.2 (b). This is unexpected in a solid rod which thickness remains constant throughout the structure. A lateral view of a nanorod would show constant grey values, whereas inclined projections may show a darker region along the middle of the rod as an effect of thickness. Since the contrast in feature A does not follow either of those cases, it would be reasonable to interpret this feature as a nanotube. However, given the lack of similar features across the sample, the tube-like appearance is more likely associated with two rods of very similar diameters attached along their edges. Profile analysis is shown in the plot in Fig. 4.2 (b). The lateral axis of the plot represents the position along the arrow annotated in Fig. 4.2 (b). The vertical axis represents the intensity value of the pixels. As expected, the background produces the lightest regions of the graph. The grey value of the pixels is not constant across the diameter of the rods, which would reflect as steep rectangular variations of grey value. Instead, the graph in Fig. 4.2 (b) shows two curves with clear minimums representing the thickest region of each rod projection. It is important to note that the peak in-between the two rod sections is very pronounced and virtually reaches the grey value of the background. This corroborates the hypothesis that features A is not a nanotube, but two rods attached by their lateral edges. Further study, e.g., electron tomography could determine whether there is a gap in between the rods, or if they constitute a continuous body. The latter could indicate a parallel growth mechanism.

Feature B is the shortest rod found in the present system with a length of 169.7 nm and a diameter of 13.5 nm. Feature C consists of a dark faceted shape. This feature appears consistently throughout the sample. The shape is 26.7 nm along its sides, which is consistent with the diameter of many of the rods. As the chemistry of the sample is constant, the darker appearance of these features can be attributed to a thickness much larger than their lateral dimension. For example, Feature E is much wider than C while its grey value is visibly lower. This suggests that these faceted features do not have a different geometry but are in fact nanorods oriented along the direction of the electron beam.

Feature D is the longest rod present in the image, which is 230.7 nm in length and 23.26 nm in diameter. The nanorods visibly vary significantly in length while their lateral size remains relatively consistent throughout the sample. Table 4.1 summarises the average dimensions of 25 nanorods in Figure 4.2.

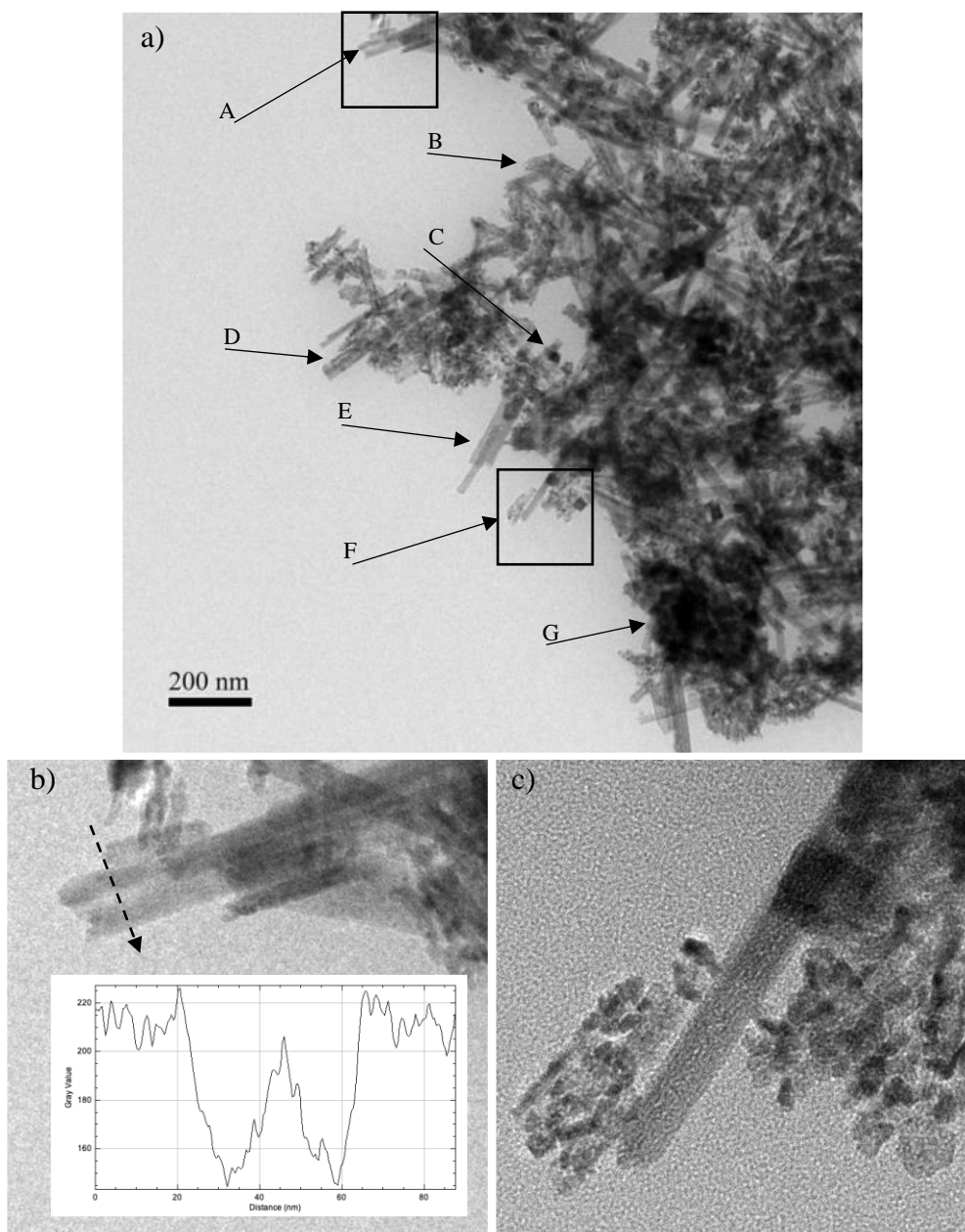


Figure 4.2 Low-magnification TEM image of ceria nanorods after seven-year ageing (Image (a) acquired using JEOL F200 TEM at 200 kV sampling=0.42 nm/pixel. Images (b) and (c) are subsets of (a) as indicated)

Feature E consists of an agglomerate of rods aligned along their lengths. This region has been chosen for further imaging owing to its electron transparency and its suitable representation of the sample. It also shows the terminal geometry of its nanorods, which can be an important feature in structural studies. Finally, feature G is identified as an example of a region that is too thick for transmission imaging. Feature F was also chosen for further imaging as it contains an agglomeration of small particles, which are common throughout the sample. The digital close-up image shows that the crystalline nanoparticles have self-organised into a rod morphology.

The diameter and continuous edges of this cluster make it recognisable as a half-formed nanorod. This information supports the theory of “oriented attachment”, as introduced by Penn and Banfield [379]. This theory has been accepted as the formation mechanism of a diversity of 1D-nanomaterials, including ceria nanorods [271]. The growth of the nanomaterial is dictated by the attachment of nanocrystals into a common crystallographic orientation. This self-organisation is followed by consolidation of the system, resulting in the nanorod morphology. The fact that individual precursor nanoparticles are still visible suggests that the nanocrystals were able to attach during the synthesis, but that the conditions were not sufficient for the consolidation to happen.

Table 4.1 Summary of nanorod dimensions throughout figure 4.2

	Min	Max	Mean	Standard deviation (σ)
Length (nm)	131.9	230.7	176.6	31.9
Diameter (nm)	13.5	23.3	17.3	3.1
Aspect ratio	7.8	12.2	10.4	2.1

Figure 4.3 presents an image of the features annotated in figure 4.2 as E and F at medium magnification. A number of rods appear to be orientated along the direction of the electron beam and appear as dark faceted features. This allows estimating some characteristics of the cross-sectional geometry of the nanorods, which appears enclosed by straight parallel sides. It is not possible, however, to determine the precise geometry of the cross-section at this stage, since any small variations in the inclination of the rod with respect to the electron beam axis would change the projected geometry.

Feature 4.3(a) shows a group of three rods attached along their lengths. The outermost particle is of particular interest for its transparency and isolation and was chosen for further analysis. The image also shows the terminal morphology of the rods. The three rods marked as a feature 4.3(b) appear to finish in a straight cap whereas the continuous rod highlighted as feature 4.3(a) ends in an angled point. These terminations have been previously reported in the literature [3], [4], [271] in as-synthesised rods and are therefore not an effect of air-storage.

Furthermore, the corners forming these terminal morphologies do not appear rounded or deformed after the seven-year period.

Annotation 4.3(c) highlights the presence of particles under 10 nm across, which appear to vary in shape and size. These particles could be precursors, which have not self-organised into nanorods. As described above, nanoparticles are expected to occur as precursors in the mechanism or oriented attachment. The fact that the nanocrystals appear as localised clusters, instead of being scattered throughout the structure suggests that they were in the process of self-organising into nanorods. Furthermore, a feature such as the one denoted F in figure 4.2 could also be present in these clusters, but in such an orientation that is not evident in the present projection.

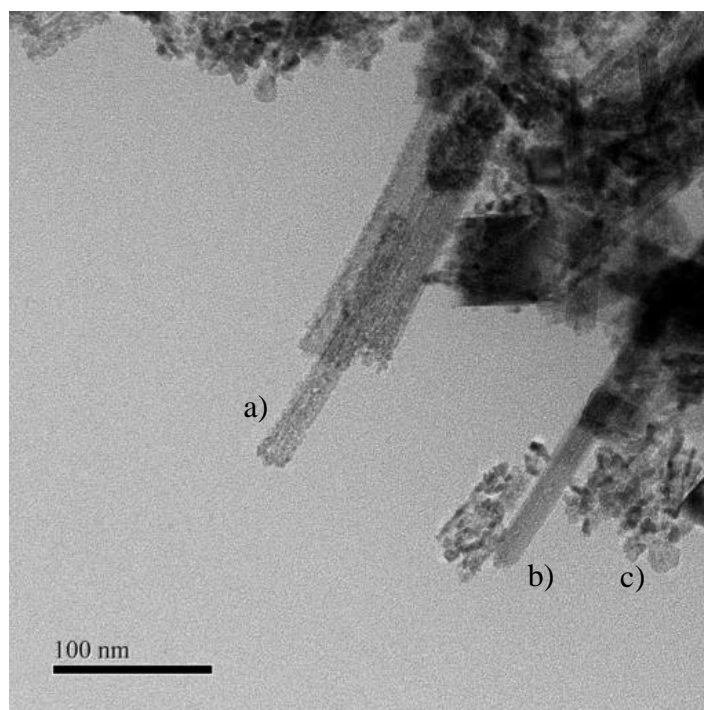


Figure 4.3 Medium-magnification image of ceria nanorods (Image acquired using JEOL F200 TEM at 200 kV, sampling=0.108 nm/pixel.)

The examination of a nanorod at higher magnifications allows studying their internal structure beyond their projected morphology. Figure 4.4 shows a high-resolution image of the rod selected as feature (a) in figure 4.3. The figure also contains a digital close-up of a selected area to highlight the typical crystallinity of the rods. The close-up image was calibrated using the scale bar and its fast Fourier transform (FFT) obtained using Image J. The FFT shows two distinct sets of diffraction peaks forming two concentric circles, which correspond to two values of atomic plane spacing. The six peaks forming the inner circle have a planar distance

of 0.31 nm, while the four peaks located on the outer diameter correspond to a measurement of 0.28 nm. According to the literature on ceria crystallography, a spacing of 0.31 nm corresponds to the $\{111\}$ -plane family, and 0.28 nm is the d-spacing of $\{200\}$ planes [14]. According to this identification, the growth direction of the rod is $[211]$.

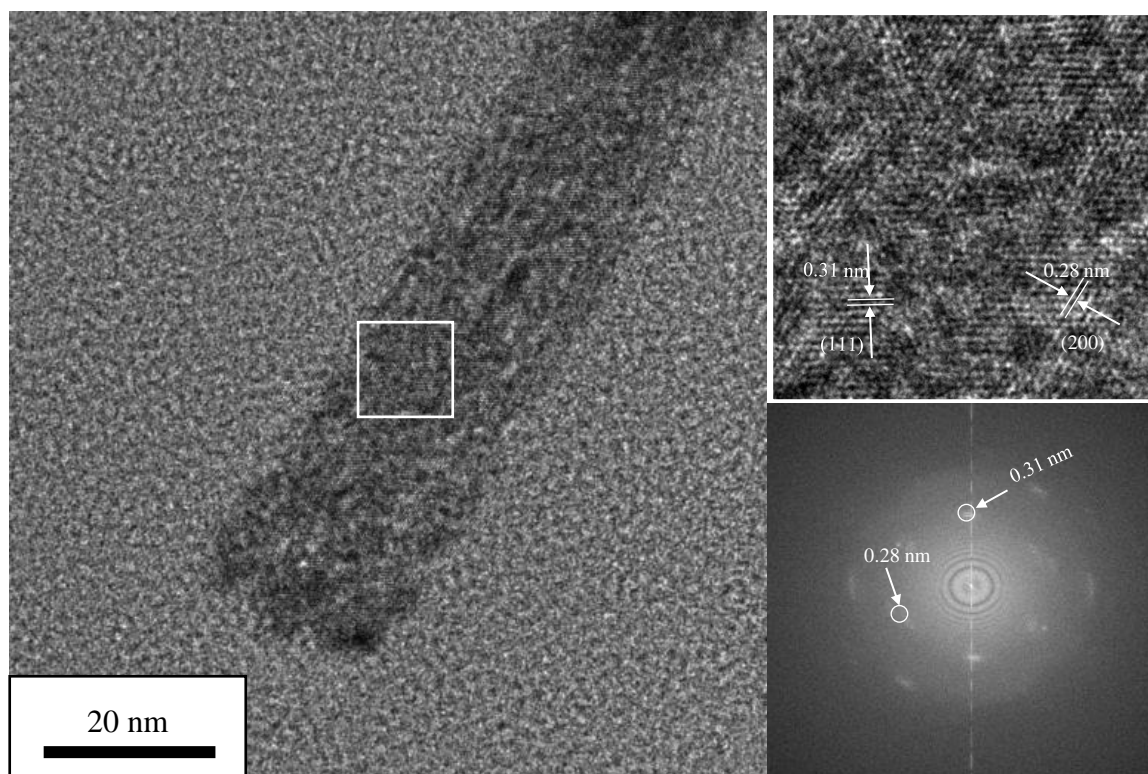


Figure 4.4 High-magnification HRTEM image of selected ceria nanorod with digital close-up and fast-Fourier transform (Image acquired using JEOL F200 TEM at 200 kV, sampling=0.021 nm/pixel)

The digital close-up shown in Figure 4.4 allows distinguishing a significant discontinuity in the crystal structure of the nanorods. The $\{111\}$ and $\{200\}$ planes appear to remain consistently exposed throughout the surface of the nanorod. However, the direction of the lattice fringes changes repeatedly in units of 1 to 1.5 nm. Other groups have reported this type of structure in ceria nanorods [4]. However, the literature suggests that it is more common to find a homogeneous monocrystalline structure [236], [271]. It is unclear what the mechanism is, that gives rise to this high-strain disordered structure. At this stage, however, it can be reported that it has not changed in the seven-year period between characterisations of this material.

Figure 4.5 summarises the main features of ceria nanorods before and after seven years of storage. This characterisation shows that the nanorods have not changed in any noticeable manner in their morphology nor in their structure. The most important features that suggest that the

nanorods were unaffected are the sharpness of the corners, the consistent crystalline structure and the continuity of the walls.

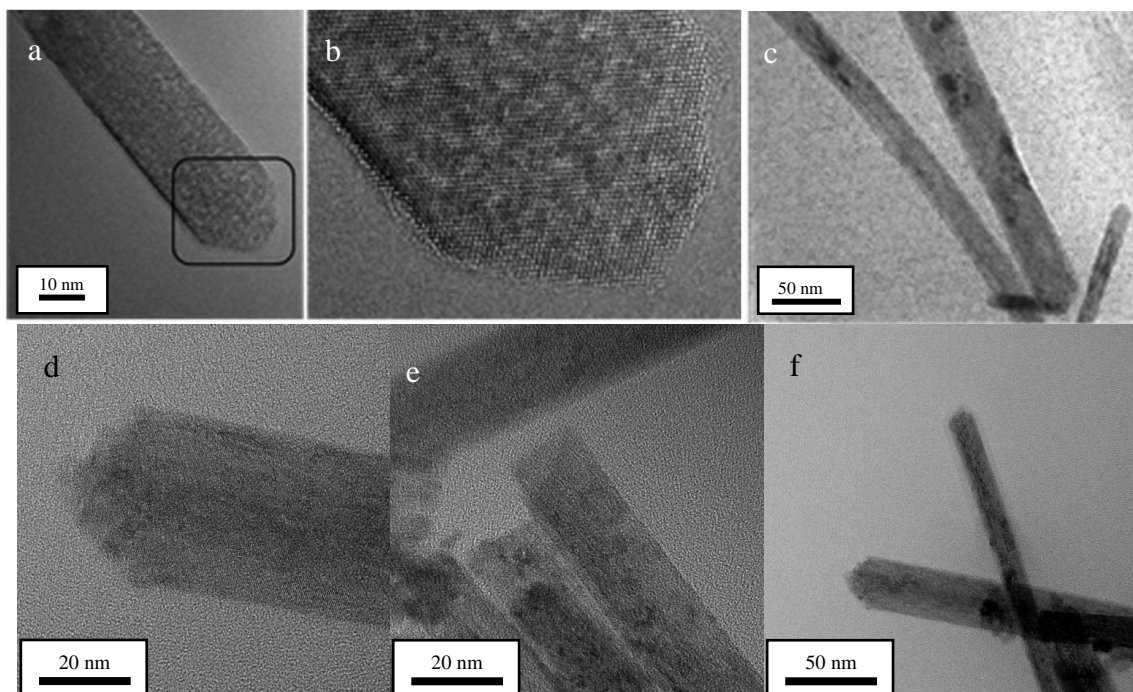


Figure 4.5 Time-ageing of ceria nanorods. Ceria nanorods before (top) and after (bottom) seven years of storage under ambient conditions. BEFORE images were acquired by collaborators Bhatta et al., as reported in their publication [3]. AFTER images were acquired using JEOL F200 TEM at 200 kV, samplings: (d)=0.016 nm/pixel, (e)=0.026 nm/pixel, (f)=0.052 nm/pixel

4.1.3 TEM imaging of aged ceria nanocubes

An in-depth characterisation of ceria nanocubes was performed after seven years of storage at ambient conditions. Figure 4.6 shows a collection of images obtained using high-resolution TEM. This initial exploration allows assessing the adequacy of the sample preparation procedure, as well as gauge the overall contents of the sample. A number of cubic nanoparticles can be observed as well as a continuous carbon film. Across the sample, a wide distribution of sizes of nanocubes is observed, with lateral dimensions ranging from 2 to 60 nm. The nanocubes appear to agglomerate into smaller clusters than those observed in the nanorod sample above. Paradoxically, it is easy to find isolated nanorods, while cubes always appear attached to small agglomerates. These differences in behaviour could be due to sample preparation. However, the dilution processes for both materials were the same, which suggests that the forces between

nanorods and cubes are actually different. The attachment behaviour of the nanocubes could be weaker owing to them having a smaller surface area per volume than rods. Cubes may also find it more difficult to attach given their wider size distribution. Figure 4.6 suggests that cubes attach to others of similar size with the smaller cubes forming into particularly close-packed agglomerates.

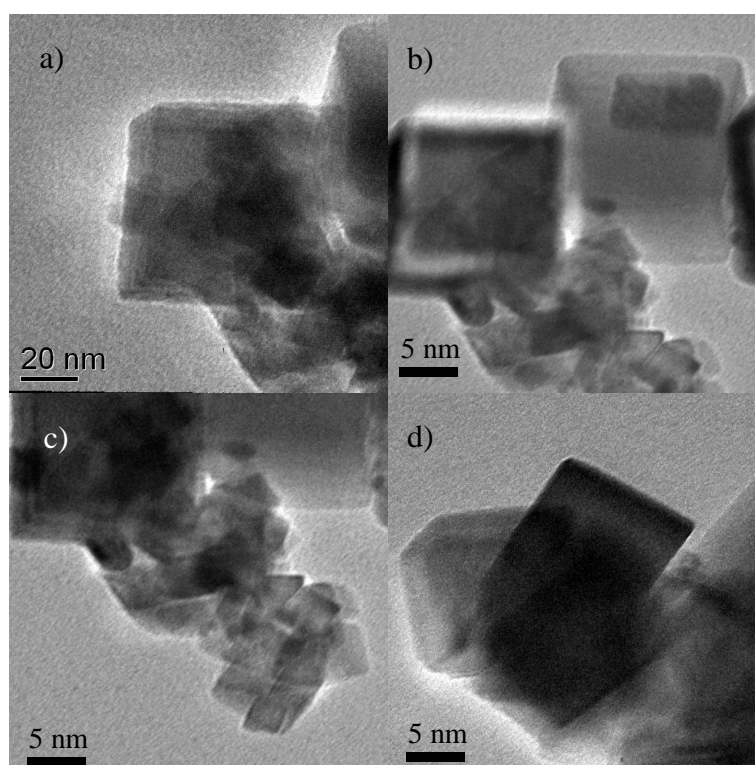


Figure 4.6 TEM imaging of time-aged ceria nanocubes (Images acquired using JEOL 2010F TEM at 200 kV, samplings: (a)=0.26 nm/pixel, (b-d)=0.058 nm/pixel)

The images shown are in the bright-field mode, which means that the thicker regions of the sample appear darker. Variations of grey values are observed in images 4.5b and c, which can be expected from three-dimensional bodies such as cubes. The particularly dark cubes also have the longest lateral size, consistently with thickness-contrast. Similarly, the agglomerate of small cubes shown in Fig 4.6c shows a darker contrast along its middle axis. This is an important feature, as it indicates that the cubes attach strongly to each other and not to the carbon film. The latter case would create a monolayer of cubes of constant thickness. Figure 4.6d shows a corner with a peculiar hexagonal shape. This feature appears commonly across the sample. While it could suggest a different shape from the cubes seen in other images, this feature has been identified as an effect of the two-dimensional projection of a rotated cube.

This is a common occurrence in transmission imaging and is only possible to avoid the introduction of three-dimensional techniques like electron tomography.

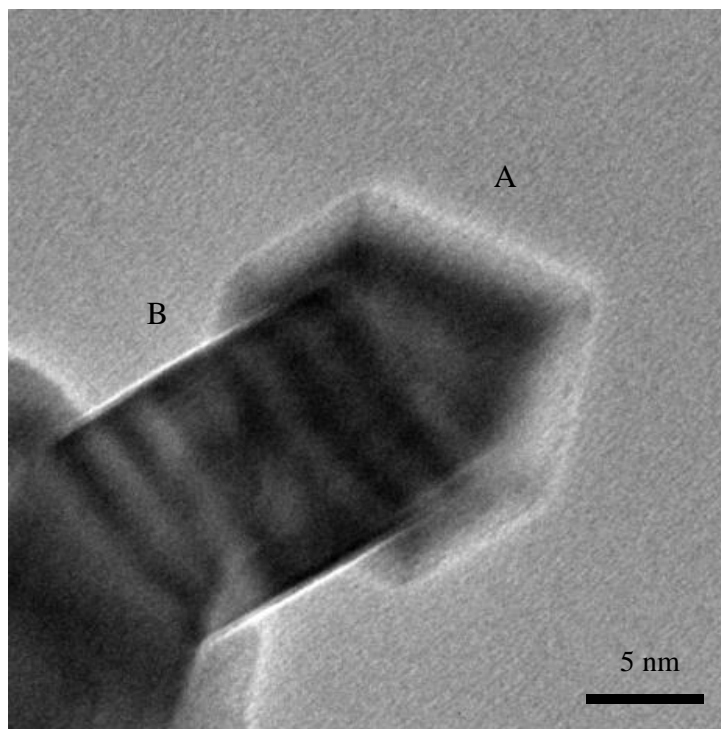


Figure 4.7 TEM emphasising geometrical features of RT-aged ceria nanocubes (Image acquired using JEOL 2010F TEM at 200 kV, sampling=0.058 nm/pixel)

Figure 4.7 shows a cluster of nanocubes at medium magnification. This image particularly shows the straight sides of the cubes, as well as the sharp corners. The changes in grey value across the objects can be used to estimate three-dimensional features of the cubes. For example, there is a visible 2-nm wide ribbon running along the edge of the outermost cube, annotated as feature A. This is indicative of electrons passing through a thinner volume than the core of the material.

The angles and constant width of this feature suggest that the cube has no imperfections in its edges or corners. As for the second cube, identified as feature B, a number of thin dark bands parallel to its sides can be seen crossing its body, which corresponds to thickness fringes. The continuity of these features, as well as their straight orientation, suggests the cube to be perfect in three dimensions. The images shown in Figure 4.8 are the highest in magnification of the present study. Both images emphasise the terminal structure of ceria nanocubes, which consists of continuous edges and sharp corners.

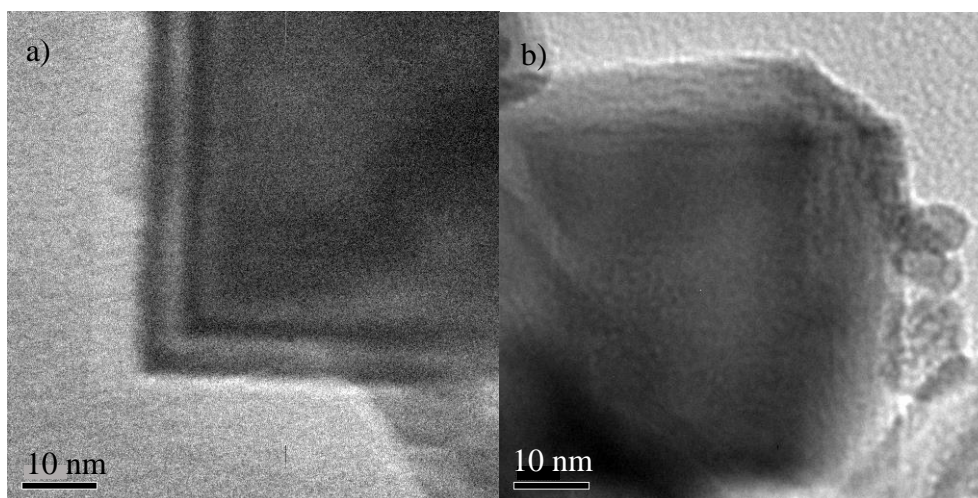


Figure 4.8 High-magnification TEM of the terminal structure of ceria nanocubes (Images acquired using JEOL 2010F TEM at 200 kV, sampling=0.058 nm/pixel)

The contrast variations in figure 4.8 are as expected from the morphology resolved throughout the previous images. This is a significant difference with the nanorods, which show variations in contrast along with their entire structure, e.g. Fig 4.4 (e). This suggests that the nanocubes have a more homogeneous crystalline structure than the rods. In catalysis, this is associated with a less reactive material. Finally, the existence of 2 nm-diameter nanoparticles in Fig 4.6(c) can be associated with the formation mechanism of ceria nanocubes.

Figure 4.9 summarises the main features observed in ceria nanocubes stored at room temperature. The top row features images acquired when the materials were first synthesised. The seemingly flat corner in image 4.9 (d) relates to the aforementioned projection effect and not to the geometry of the particle, as seen. Here it is reported that the period of storage does not have a significant effect on the morphology or structure of the material. However, when viewed in direct comparison to the BEFORE sample images (Fig. 4.9 a,b), the air-stored samples appear to show a small but finite curvature in the corners (Fig. 4.9 c,d). This could suggest a deformation mechanism as predicted by some theory groups [380]. The radius of the rounded corner in Figure 4.9(c) has been estimated at 1.7 nm. Further examination of such features at higher resolutions could expand the knowledge of their ageing mechanisms.

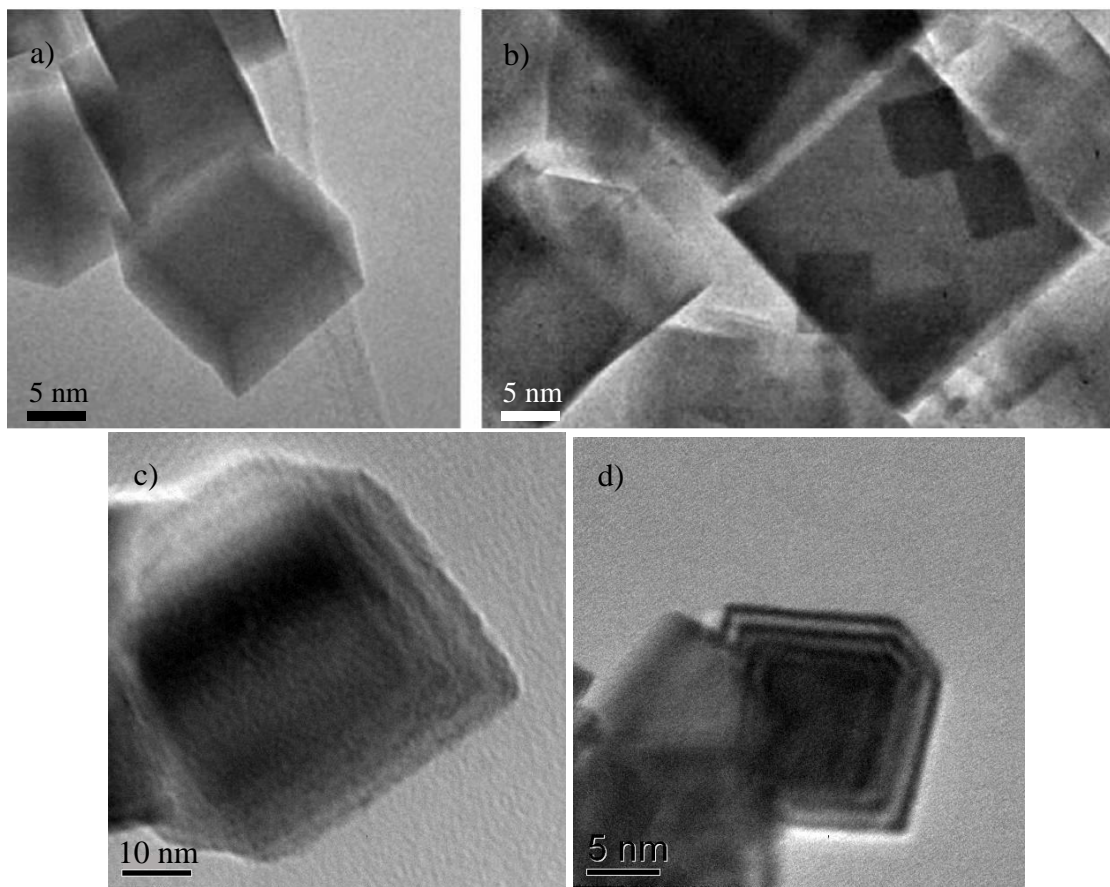


Figure 4.9 Time-ageing of ceria nanorods. Ceria nanorods before (top) and after (bottom) seven years of storage under ambient conditions.

BEFORE images were acquired by collaborators Bhatta et al.

(Image acquired using JEOL 2010F TEM at 200 kV, sampling=0.058 nm/pixel)

4.2 Near-sintering heat-treatment ageing

This section presents the experimental design of a heat-treatment procedure for ceria nanomaterials, as well as the advanced characterisation of its products. This experimental work seeks to learn further aspects of the transformation of ceria nanomaterials by exposing them to temperatures higher than any reported in the literature. The heat-treatment procedure used in this work is assessed by heating a sample at 800 °C and comparing its transformations at the

nanoscale with the TEM results reported by Sakthivel et al. for the same temperature [3]. Afterwards, it is presented an in-depth TEM characterisation of the materials after near-sintering heat treatment at 950 °C.

4.2.1 Heat-treatment procedure

Using a stainless-steel spatula, the ceria nanocubes and nanorods were transferred into standard TGA aluminium oxide 600 µL crucibles, which have high purity and can withstand temperatures of 1600 °C (Mettler Toledo). Three specimens were prepared in this way, two containing ceria nanorods and one containing ceria nanocubes. A novel preparation method for a heat-resistant TEM sample is also proposed, as described below. The heat-resistant sample was submitted to the heat-treatment step along with the powdered samples of CeO₂ nanorods and nanocubes. This innovative experimental design is of interest to the processing of nanomaterials processing, as the amounts are often limited.

The preparation of TEM samples requires a very small amount of material. However, experimental methods in nanomaterials often report amounts of substances larger than would be necessary for their characterisation. This is due to the practical aspects of handling powders or liquids, which can become stuck to glassware surfaces, or be absorbed into ceramic crucibles and mortars. By suspending the nanomaterial onto an electron-transparent film prior to processing, it is ensured that the sample can survive the processing steps while minimising waste.

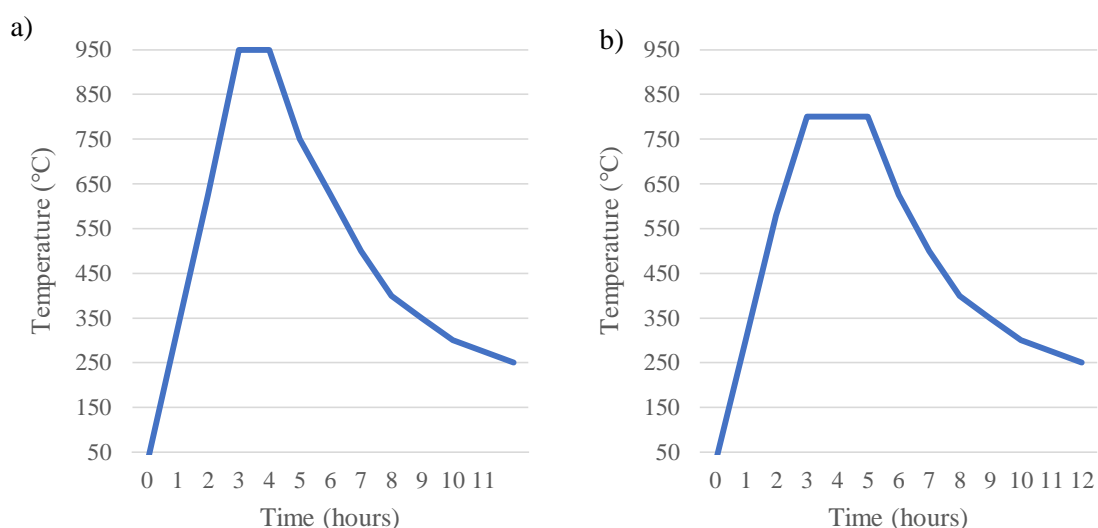


Figure 4.10 Heat-treatment schedules for ceria nanocubes and nanorods

The heat-resistant TEM sample was prepared using a silicon nitride TEM window grid, which the manufacturer suggests for use in *in situ* experiments of up to 1000 °C. The sample

preparation was identical to the procedure described in Part I for loading nanoparticles onto carbon-coated copper grids. After allowing it to dry at room temperature, the specimen was placed in a porcelain crucible and heated alongside the powdered samples. Figure 4.10 shows a graphical representation of the heating schedules. The heating atmosphere was air, and there were no forced convection or cooling.

As shown in diagram 4.10 (a), the heating ramp was set to 5 °C/min for three hours. Then, the final temperature of 950°C was held for one hour, to finally allow the samples to cool down inside the furnace. This annealing process was used to treat three samples: one powder sample of ceria nanorods, one powder sample of ceria nanocubes and the aforementioned heat-resistant TEM sample.

Table 4.2 Sample characteristics and nomenclature

Sample No.	Nanomaterial	Annealing temperature	TEM substrate
1	CeO ₂ nanorods	800 °C	C-coated Cu grid
2	CeO ₂ nanorods	950 °C	C-coated Cu grid
3	CeO ₂ nanorods	950 °C	Si ₃ N ₄ -coated Si
4	CeO ₂ nanocubes	950 °C	C-coated Cu grid

The second heating schedule, seen in Figure 4.10 (b), was used to treat one sample of powder ceria nanorods. This curve consists of ramping up at 5 °C/min for 2.5 hours, holding the final temperature of 800 °C for two hours and allowing to cool down inside the furnace. The heat transfer of the furnace normally slows down below 500 °C, so the samples were allowed to cool overnight before opening the furnaces. After heat treatment, the powdered samples were prepared for TEM characterisation using the same suspension, dilution and mounting procedure described in Part I. The heat-treated ceria nanorod sample mounted on Si₃N₄-coated silicon grid was used for TEM characterisation without further processing. The heating and sample preparation conditions of the samples are summarised in Table 4.2. All samples were heated, starting at room temperature. Sections 4.2.1 to 4.2.4 present the TEM results of the annealed samples.

4.2.2 TEM imaging of ceria nanorods after heat treatment at 800°C

An in-depth TEM study has been performed of the sample heated at 800 °C. The cited literature contains accounts of other groups who have performed similar experiments [2], [3], [11]. Therefore, it is useful to observe the results obtained working with this holding temperature, before proceeding to parameters, no other group has reported on before.

Initially, images are presented at low and medium magnifications. Figure 4.11a shows agglomerates of rod-shaped nanoparticles forming close-packed colonies. It can be deduced that these agglomerates are three-dimensional from the dark contrast at the centre of each, suggesting the overlap of numerous nanorods. In the same way as the sample of rods before heat treatment, a number of small dark objects can be distinguished, which correspond to the two-dimensional projection of rods oriented along the axis of the electron beam. In addition to the three-dimensional aggregates, Figure 4.11a also shows several nanorods appearing in isolation. This is beneficial to TEM analysis, as they are more likely to be electron-transparent than three-dimensional clusters.

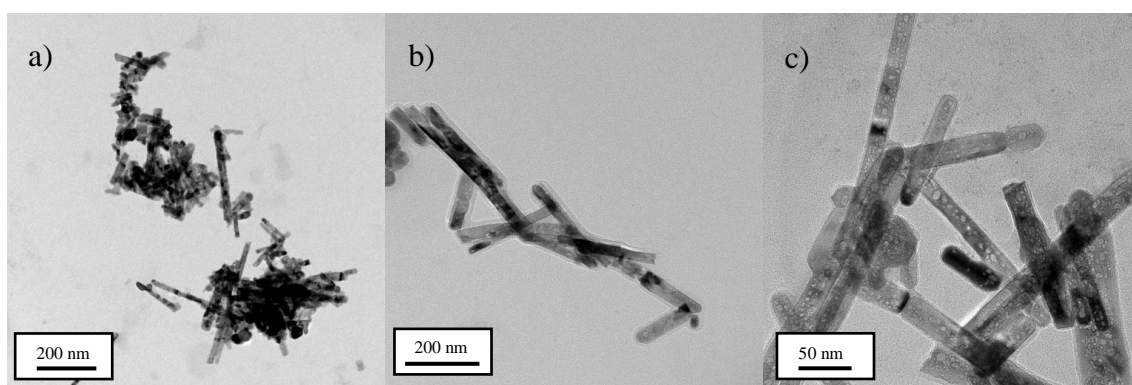


Figure 4.11 Low- and medium-magnification bright-field images of typical ceria nanorods after annealing at 800 °C (Images were acquired using JEOL F200 TEM at 200 kV, samplings: (a)=0.26 nm/pixel, (b)=0.32 nm/pixel, (c)=0.052 nm/pixel)

Figure 4.11b emphasises a coating-like feature surrounding the group of nanorods. This feature is found across several images at different magnifications. This is not an effect of imaging, as it does not disappear by changing the microscope settings. Instead, this feature can be attributed to the effect of carbon contamination. This phenomenon consists of deposition of nanoscale carbon on the sample around the materials produced by the cracking of hydrocarbons in the chamber, the specimen and the holder. This was tested by focusing the beam on an empty area of carbon film for a few seconds. The irradiation produced a dark ring of deposited carbon, as expected. In the case of this sample, the analysis could proceed regardless, since the layer of carbon surrounding the nanoparticles had good electron-transparency. Furthermore, the contaminant has an amorphous nanostructure, which makes it easily distinguishable at high magnifications from the crystalline nanoceria (e.g. Figure 4.12b). In cases where carbon contamination needs to be eliminated, this can be achieved by use of plasma cleaning to a high efficacy as demonstrated in [381].

Figure 4.11c shows a mostly transparent group of nanorods. At this magnification, it is possible to evaluate the morphological integrity of nanorods after heat treatment. Comparing with the nanorods sample in Part I, heat-treated nanorods at 800 °C appear to preserve their straight walls and continuous diameters. However, it is also possible to observe the prevalence of bright features throughout the structure. These features appear similar to those reported by other groups after heat treatment [3], [13].

Figure 4.12 shows two images at different magnifications of a group of several nanorods with parallel orientation. Image (a) emphasises the strong attachment of the rods with no visible gap between them. Several regions of dark contrast can also be identified occupying the body of the rods. Some of these dark areas correspond to overlapping particles, as indicated. However, some of these dark patches actually arise from the Bragg diffraction of the material, which can cause strong contrast artefacts dependent on the orientation of the crystal lattice with respect to the electron beam. Image 4.12(b) highlights the crystalline structure of the nanorods.

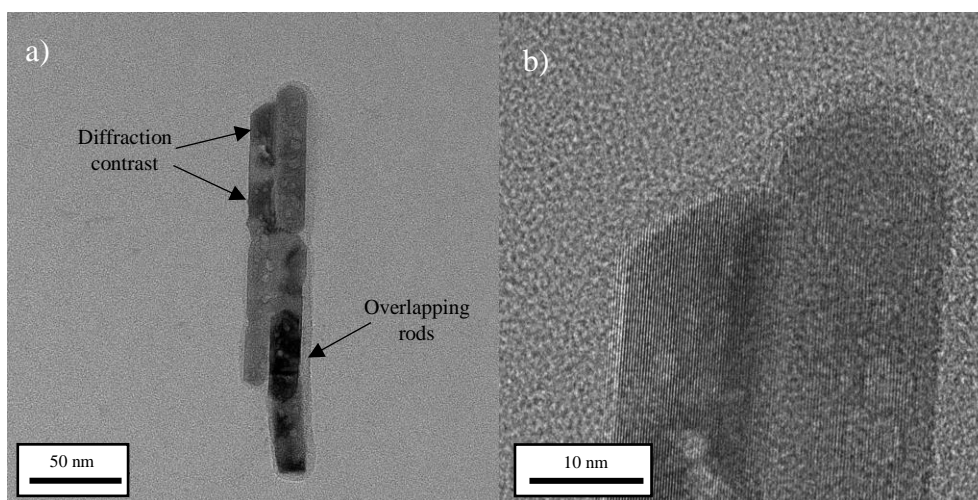


Figure 4.12 Medium- and high-magnification bright-field images of a nanorod aggregate (Images were acquired using JEOL F200 TEM at 200 kV, samplings: (a)=0.056 nm/pixel, (b)=0.026 nm/pixel)

Continuous lattice fringes can be observed travelling along with the structure. When comparing this image to the crystal structure shown in Figure 4.4, a significant structural difference can be seen. The annealed samples consistently present a continuous monocrystalline structure absent from as-synthesised nanorods. Another important feature of Figure 4.12b is that this magnification shows the aforementioned bright features in more detail. It can be seen that they appear preferentially along the middle of the rods and that they are more or less symmetrical in shape. They appear to range between 2 and 6 nm in diameter. Additionally, the lattice fringes

cross the area of these features uninterruptedly, which suggests that the crystalline walls of the rod are enclosing these heat-induced features.

Figure 4.13 summarises the results of the crystallographic study of three rods from the heat-treated sample. By increasing the magnification of the microscope, it is possible to resolve the atomic lattice fringes, as seen in images (a-c). The distance between fringes correlates with the unit cell parameter of the crystal. This is a reliable method to perform elemental identification, as well as for characterising the particular crystallography of nanoparticles. As detailed in Chapter 2, the catalytic activity of ceria nanomaterials varies significantly with the crystallography present in their surfaces. The image processing shown in Figure 4.13 d-f was performed using ImageJ, a popular open platform for scientific image analysis. A more detailed description of the software packages employed in this work is detailed in Chapter 3. At first, the images were calibrated using the scalebar which is printed by the microscope. This establishes a scale of pixels per nanometre. Then, using ImageJ, the Fast-Fourier transform (FFT) of the image was calculated to obtain a digital diffraction pattern (d-f). The FFT images show annotations of the d-spacing value represented by each peak.

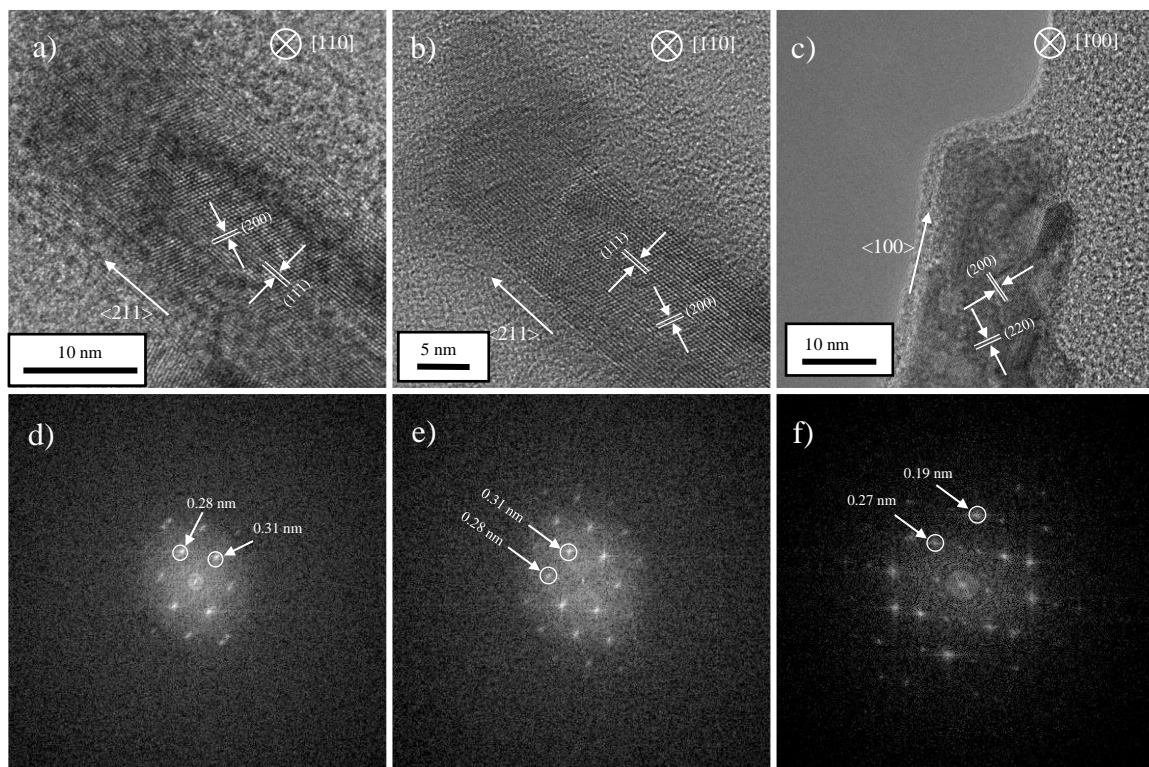


Figure 4.13 Crystallographic analysis of ceria nanorods annealed at 800°C
 (Images were acquired using JEOL F200 TEM at 200 kV, samplings: (a)=0.026 nm/pixel,
 (b)=0.032 nm/pixel, (c)=0.028 nm/pixel)

Although there are peaks that appear unidentified, their d-spacing values are factors of other peaks, which means that they represent the same family of planes. In total, six sets of lattice fringes were identified in this crystallographic study, obtaining three different d-spacing results: 0.19 nm, 0.28 nm and 0.31 nm. According to the literature, these values of d-spacing correspond to the {220}, {200} and {111} plane families, respectively [271]. The annotations in figures (a-c) correspond to plane identification. Unsurprisingly, the most common plane family exposed across the sample is the {111}, which the literature has identified as the most stable. However, two measurements of 0.28 nm are visible corresponding to the {100}-plane family, which the literature reports as the least stable [14]. The analysis shown in Figure 4.13 suggests that the exposed planes remain unaltered after annealing at 800 °C. This is important since there are other visible changes in the structure, such as the emergence of defects and the consolidation of a single-crystal structure (Fig. 4.8). In order to facilitate the interpretation of the crystallographic measurements above, as well as to relate them to the growth mechanisms of the nanorods, figure 4.14 shows a schematic representation of the formation of ceria nanorods along both directions [211] and [100], as published by Du et al. [271].

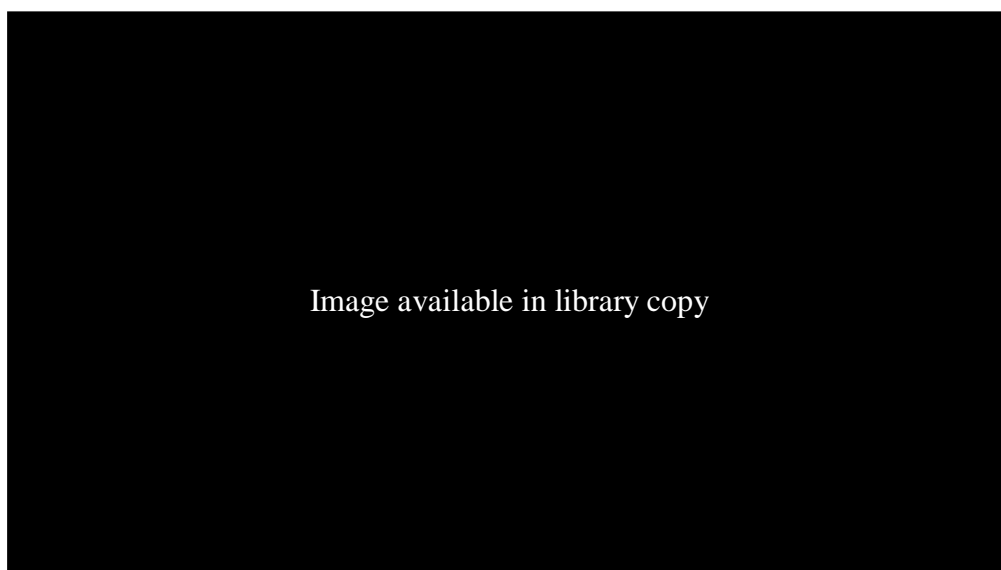


Figure 4.14 Schematic diagram for the self-assembly of ceria nanocrystals into ceria nanorods by oriented attachment and subsequent Ostwald ripening [271]

4.2.2.1 Integrity of the terminal morphology of nanorods after annealing at 800 °C

Another common effect during ageing processes is the rounding of corners. Figure 4.15 shows that the tips of the nanorods continue to exhibit sharp facets. Du et al. identified two different types of terminal structures in as-synthesised ceria nanorods [271]. This parameter relates to

the crystallography of the rod. Rods which exhibit (111) planes along their axis, have a growth direction [211] and terminate in a (200) plane, such as the rods (a) and (b) of Fig 4.15. The second type of rod seen in the literature terminates in a (111) plane, like the one shown in Figure 4.15c. This corresponds to a [110] growth direction.

The occurrence of these planes at the corners of the sample indicates that the terminal structure of the nanorods prevails after heat treatment. Fig. 4.15 (c) also shows a particularly clear resolution of the porous defects, which has been used to identify the alignment of the pore facets with the atomic planes of the rod. As shown in the inset, the facets of the pore align completely with the prominent [111] planes inside the rod. This result supports the finding stated throughout this work, that the growth of the pores is directed by the crystallography of the rods.

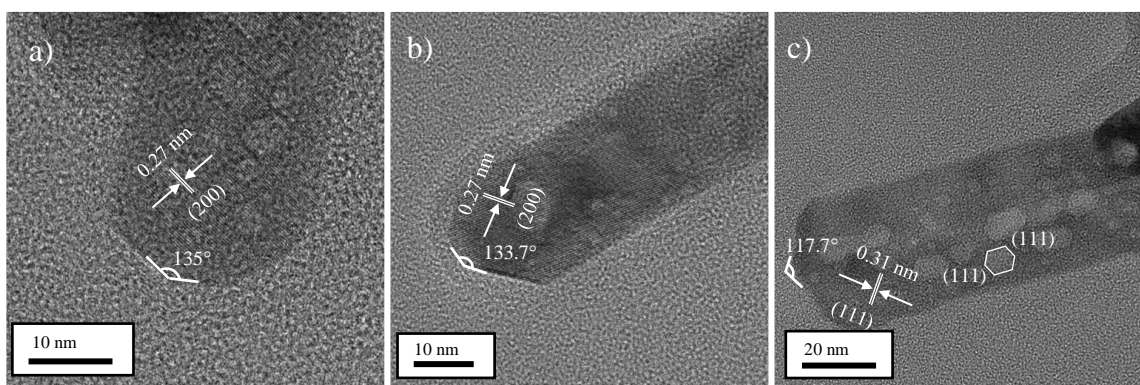


Figure 4.15 Terminal structures of ceria nanorods after annealing at 800 °C (Images were acquired using JEOL F200 TEM at 200 kV, samplings: (a)=0.028 nm/pixel, (b)=0.024 nm/pixel, (c)=0.039 nm/pixel)

4.2.2.2 Discovery of negative-rod defects

Sample 1 presented with a new type of defect, which is so far absent from the literature. It consists of elongated pores extending along the growth direction of the rod. Figure 4.16 presents three examples of this novel heating-induced feature.

In all three instances, pores connect, forming an enclosed channel of roughly constant diameter. In the same way as the other defects found in the sample, the elongated pores do not reach the lateral walls of the nanorod. It is also observed that the lattice fringes cross the area of the elongated defect, which suggests that they are also enclosed by walls perpendicular to the viewing plane. These defects show the potential to transform the rods into ceria nanotubes without the use of templates. Across the sample, these channels present lengths from 10 to 50 nm and widths of 3 to 5 nm, corresponding to the diameter of the symmetrical porous defects.

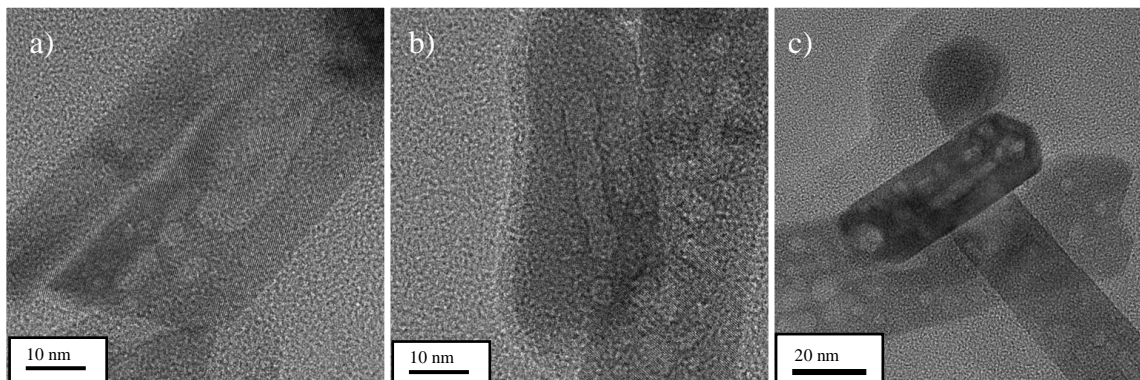


Figure 4.16 Examples of *negative-rod* defects (Images were acquired using JEOL F200 TEM at 200 kV, samplings: (a)=0.032 nm/pixel, (b)=0.032 nm/pixel, (c)=0.058 nm/pixel)

4.2.3 TEM of ceria nanorods annealed in powder form at 950 °C

The TEM results reported in section 4.2.1 are consistent with those obtained by Sakthivel et al. for ceria nanorods annealed at 800 °C [3]. This consistency suggests that the proposed heat-treatment methodology is adequate for annealing ceria nanomaterials. As mentioned above, there are no previous studies of the behaviour of ceria nanorods annealed at temperatures above 800 °C. TEM sample was prepared by suspending and diluting the annealed powder as described in 4.1. Figure 4.17 shows the initial explorations of the sample at low magnifications. Figure 4.17a shows an area crowded with nanoparticles of diverse shapes and sizes. The presence of electron-transparent areas indicates that the materials have not sintered into bulk particles and are suitable for TEM analysis.

Furthermore, image 4.17 (a) shows a number of elongated features, which suggest the survival of a number of nanorods. Image 4.17(b) shows an area containing several isolated particles. This image emphasises the diversity of shapes and sizes in the annealed sample. The deformation is apparent when the image is compared to a non-heat-treated nanorod image like Fig. 4.2. Medium magnification images are shown in Fig. 4.17 (c) and (d) emphasise the deformation of nanorods, which have flowed into morphologies with lower surface area. The temperature range of this transformation can be placed between 800 and 950 °C.

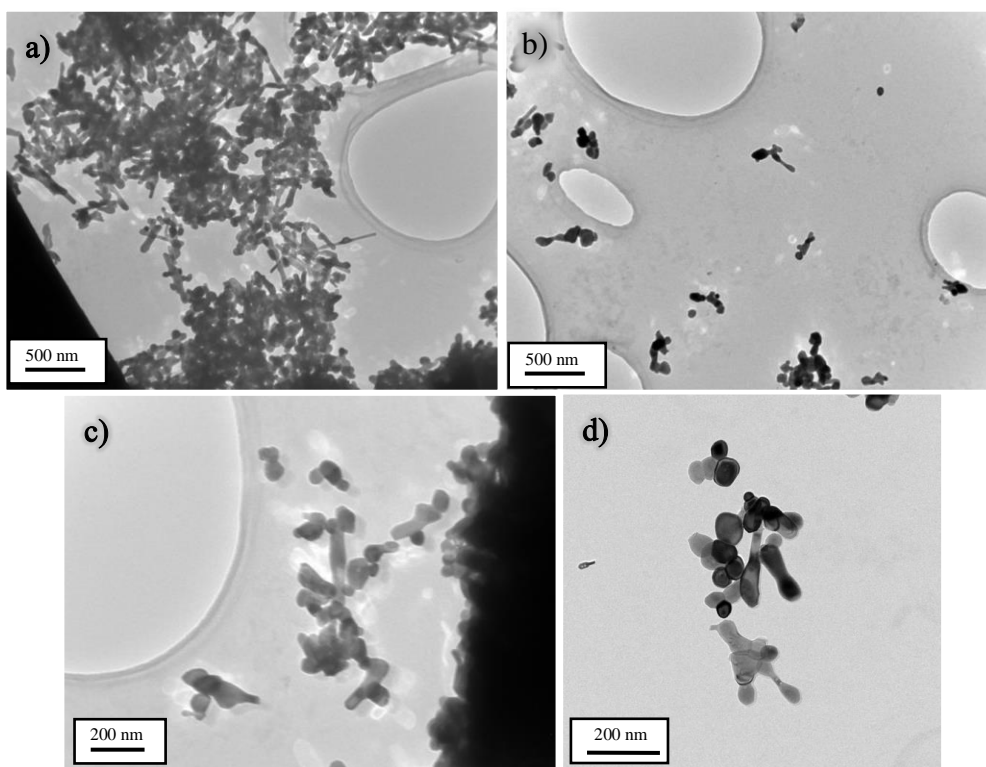


Figure 4.17 HRTEM bright-field imaging of ceria nanorods annealed at 950 °C
 (Image acquired using JEOL 2010F TEM at 200 kV, samplings:
 (a)=0.86 nm/pixel, (b)=0.86 nm/pixel, (c)=0.45 nm/pixel, (d)=0.41 nm/pixel)

This can be assumed since the images of sample 1 annealed at 800 °C preserved their rod morphology, as seen in Figure 4.11. Another important feature of the images shown in Figure 4.17 is that the material has retained a nanoscale particle size. Image 4.17(d) shows several particles forming clusters, but retaining their individual shape. This is an indication that the annealing temperature of 950 °C was adequate and the material did not sinter. However, the changes in the morphology of the particles suggest that the sample has begun the sintering process.

Figure 4.18 presents TEM images taken at medium magnification. These images allow for resolving the shape of individual particles. Image 4.18 (a) shows several features of interest. Firstly, by measuring the lateral size of the different regions of several nanorods, as annotated in feature A, the deformation mechanism was estimated. The end sections have a lateral dimension of 50-80 nm, while the thinner middle section exhibit diameters between 15-25 nm. The latter measurement is recognisable as the original diameter of the nanorods, as shown in Table 4.1. These results indicate that the flow of material has occurred from the ends of the nanorod toward the middle. This distinction is important, as the opposite case could also be true. In such a case, the material would flow from the middle section to the ends of the nanorod.

This would result in the middle section of the nanorods presenting a lateral size smaller than the non-heat-treated rods measured in table 4.1.

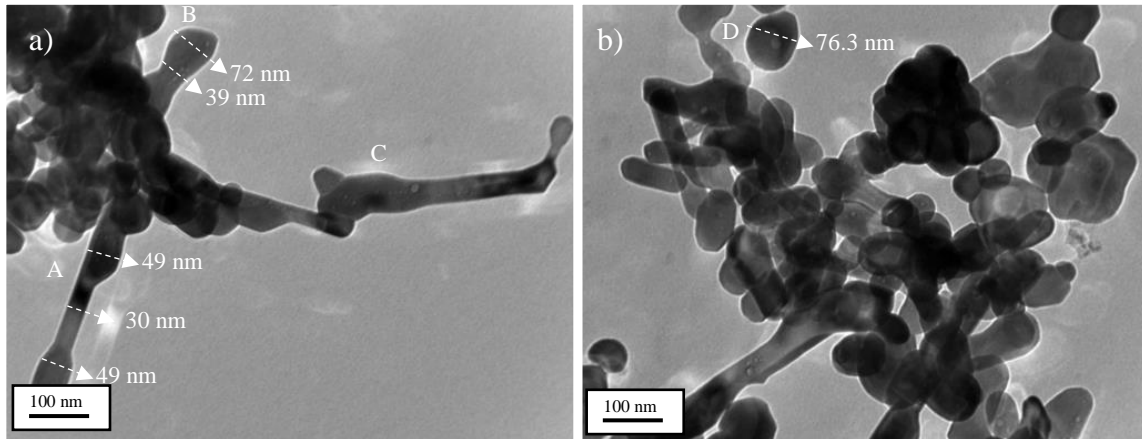


Figure 4.18 Agglomerates of ceria nanorods after heat treatment at 950 °C
(Images were acquired using JEOL F200 TEM at 200 kV, samplings:
(a)=0.027 nm/pixel, (b)=0.027 nm/pixel)

Feature B consists of a shorter nanorod, which as deformed similarly to feature A, with the end section growing to a diameter of 72 nm, and the middle section presenting a diameter of 39 nm. Interestingly, this rod appears to have been too short of forming a continuous middle section like the one present in feature A and others. Feature B has instead formed into a peanut-like shape with only a small portion maintaining its original diameter. Feature C presents a lateral deformation similar to the ones in A.

However; the rod appears to have attached to other particles as an effect of heating. This behaviour is studied in further detail in subsequent images. Feature D in image 4.18(b) shows a particle with a shape that is typical across sample 2. The particle shows a nearly spherical symmetry with a minimum diameter of 76.3 nm. This diameter is greater than those presented in table 4.1. This particle has lost its rod-like features as an effect of heat treatment. The analysis of these images suggests that the longer nanorods have preserved their diameter along their middle section. Meanwhile, the shorter nanorods have deformed into roughly spherical geometries.

Figure 4.19 shows two views of a cluster of nanoparticles at different magnifications. These images highlight the prevalence of pores in the structure of the nanomaterial. The pores appear to be smaller and less frequent than the ones observed in sample 1 after annealing at 800 °C.

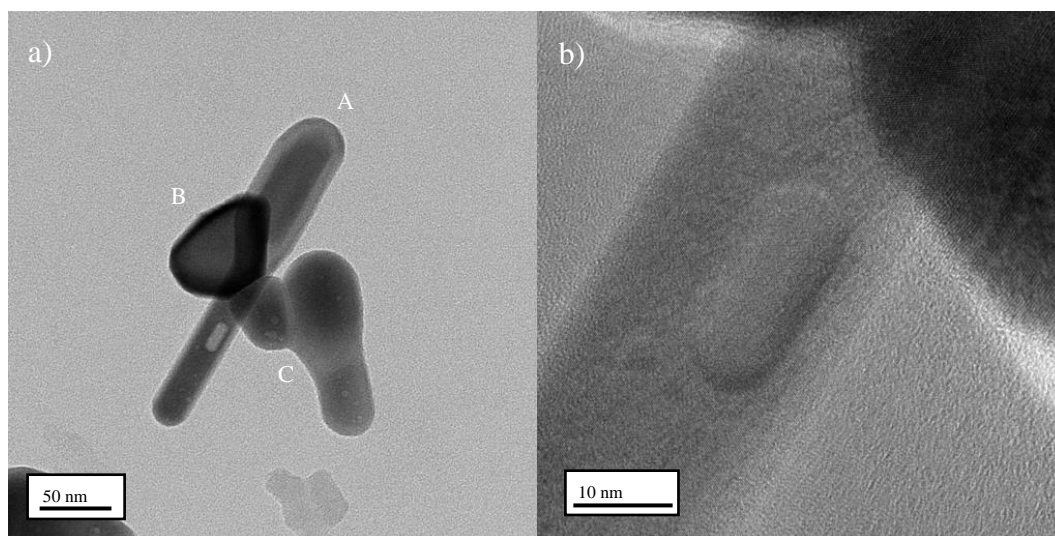


Figure 4.19 Particle shape and porous defects after annealing at 950 °C
(Images were acquired using JEOL F200 TEM at 200 kV, samplings:
(a)=0.012 nm/pixel, (b)=0.009 nm/pixel)

Consistently with sample 1, pores appear to be enclosed by the walls of the particle. This characteristic was estimated from the fact that the walls of the particles are continuous. If the pores were located on the surfaces of the particles, the walls would be expected to present with dents. The cluster in image 4.19 (a) contains a variety of morphologies, representative of the most prevalent geometries across the sample. Feature A is still recognisably a nanorod, with continuous sides of constant diameter. However, this rod presents prominent deformation at one end, which has a lateral size twice as wide as the rest of the nanorod. The wider end appears to have a lighter coating-like feature surrounding the body of the rod. This type of feature is common throughout the sample and has been resolved as an effect of thickness contrast, and not a variation in composition. This inference has been confirmed by EDX analysis shown below (Figure 4.23).

Feature B consists of a non-porous particle with no recognisable traits of a nanorod. The particle appears enclosed by six straight edges, which suggests a faceted three-dimensional geometry. This particle joins at one end with feature C. The two particles have formed a straight joint, thus reducing the surface area of the system. This type of behaviour can also be observed between the two particles forming feature C. These particles also present with a number of pores while having lost their rod morphology. This suggests that the porous structure can be maintained by the particles beyond the changes in morphology. Image 4.19(b) shows a higher magnification image of particle A, which draws attention to a prominent pore running along the body of the nanorod. The pore appears to be enclosed within the body of the nanorod. This can be deduced from the fact that the lattice fringes run uninterruptedly across the region of

the pore. This phenomenon indicates that the pore is enclosed by solid material. The morphology of the pore is similar to that of the “negative rods” shown in section 4.2.1, with the larger diameter of the pore being parallel to the growth direction of the rod. Significantly, this pore has a straighter and better-defined shape than similar features found in sample 1. However, the feature appears more rarely across sample 2. It is also observed that the “negative rod” in Figure 4.19b has a much shorter length than those observed in sample 1.

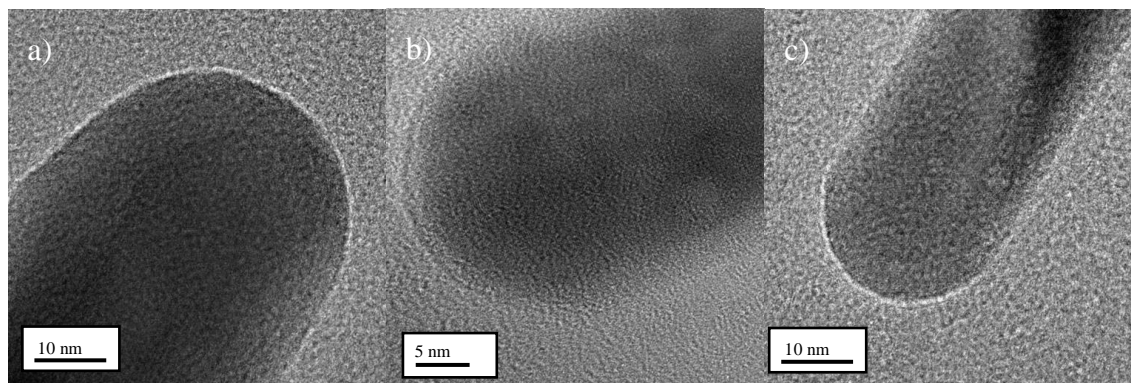


Figure 4.20 Terminal morphology of nanorods after heat-treatment at 950 °C
(Images were acquired using JEOL F200 TEM at 200 kV, samplings:
(a)=0.011 nm/pixel, (b)=0.007 nm/pixel, (c)=0.011 nm/pixel)

Figure 4.20 shows high-magnification images of three different nanorods emphasising their terminal morphology. These can be compared with the terminal morphology of non-heat-treated nanorods in Figure 4.3, as well as those in Figure 4.15, corresponding to nanorods annealed at 800 °C. It is evident that the nanorods have lost their sharp corners, and facets are no longer discernible at the tip of the rod. The temperature range of this phenomenon can be inferred to be between 800 °C and 950 °C, as the rods in sample 1 presented with very sharp corners, as seen in Figure 4.15. This process is accompanied by the oxidation of surface Ce³⁺ to Ce⁴⁺, and the subsequent reduction in catalytic capabilities [123].

Figure 4.21 contains two images, which highlight the presence of pores and the joining behaviour of the particles. Image 4.21 (a) shows a variety of particle shapes, consistent with those observed in previous figures. Namely, the shorter rods have deformed and increased in lateral size, while the longer rod has maintained the projected width along the middle section of its length. Notably, the particles exhibit pores of similar characteristics to the ones observed in sample 1 after annealing at 800 °C. The pores range in diameter between 6 and 15 nm. These dimensions are consistent with the pore diameters observed in sample 1, e.g., Figure 4.16. Furthermore, the higher magnification of image 4.21(b) shows that the pores have the same faceted

geometry as the ones obtained after annealing at 800 °C. These similarities are especially significant when considering the transformations in the size and shape of the nanorods.

Image 4.21(b) shows a region where two particles are in the process of coalescing into a single solid. The particles exhibit rounded edges and corners and have attached along their length, thus reducing the surface area significantly. The rounded corners and edges result in a reduction in active sites for catalysis. However, the surviving pores still exhibit faceted geometry, e.g., sharp corners and edges, which could host catalytically active sites.

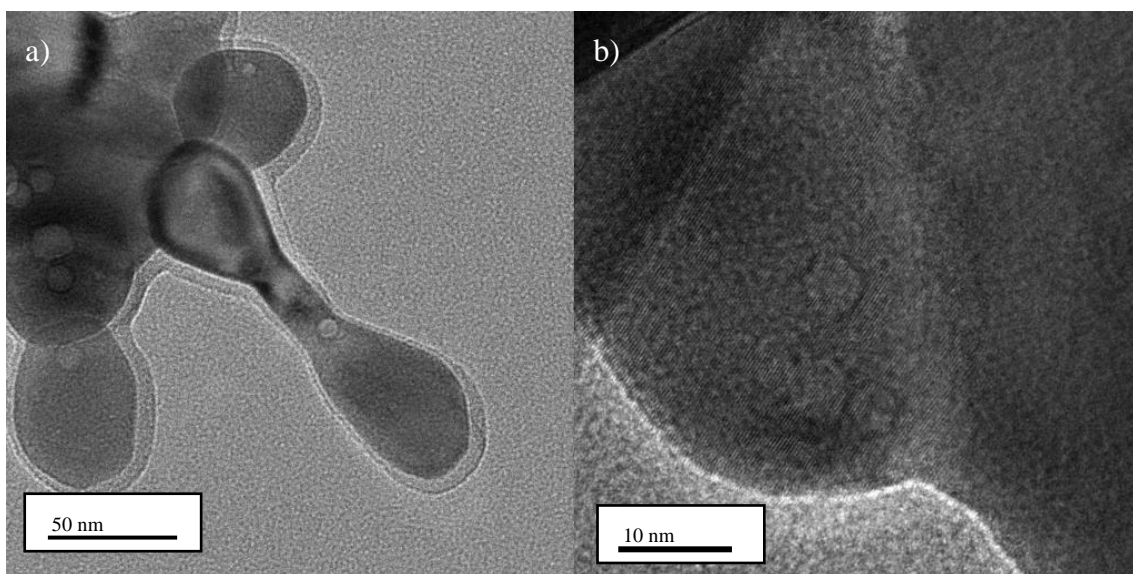


Figure 4.21 TEM at medium and high magnifications of sample 2
(Images were acquired using JEOL F200 TEM at 200 kV, samplings:
(a)=0.071 nm/pixel, (b)=0.022 nm/pixel)

A small number of particles can be found across sample 2, which have retained the sharp corners and edges of the nanorod morphology. An example of such a feature is shown in Figure 4.22. This rod is 45 nm in length and exhibits sharp corners. While the sample contains plenty of particles of similar length, the vast majority of them have distorted into rounded geometries during heat treatment. The most notable deviation from the nanorod geometry is the presence of two different diameters joined by a symmetrical neck, which gives the particle a distinct “bottle” shape. It is possible to resolve in image 4.22 (a) that the crystallography of the particle is constant, which makes it improbable that the feature consists of two particles joined during sintering. Instead, the feature was more likely formed from a single distorted nanorod.

The terminal morphology of the particle shows a corner with a shape consistent with the rods observed in sample 1 (see Fig. 4.15). The effect of projection can account for the small variations in the observed terminal angle of the rod. The particle also exhibits pores similar to

those found across sample 1 and elsewhere in sample 2. The pores have a diameter of 7 nm, which is consistent with the pores found in much larger particles. This corroborates the previous statement that the dimensions of the pores are significantly less variable than the size of the particles. Furthermore, the pores exhibit distinctly faceted geometries consistent with those observed in sample 1, as well as those reported by Sakthivel et al. [3]. The results shown in Figures 4.21 and 4.22 suggest that the 950 °C heat-treatment does not result in observable changes to the pore structure in comparison with samples annealed at 800 °C, in spite of the significant deformations to the size and morphology of the particles. The main difference in the porous structure is the concentration of pores, which is significantly lower in the sample heated at 950 °C than the sample annealed at 800 °C.

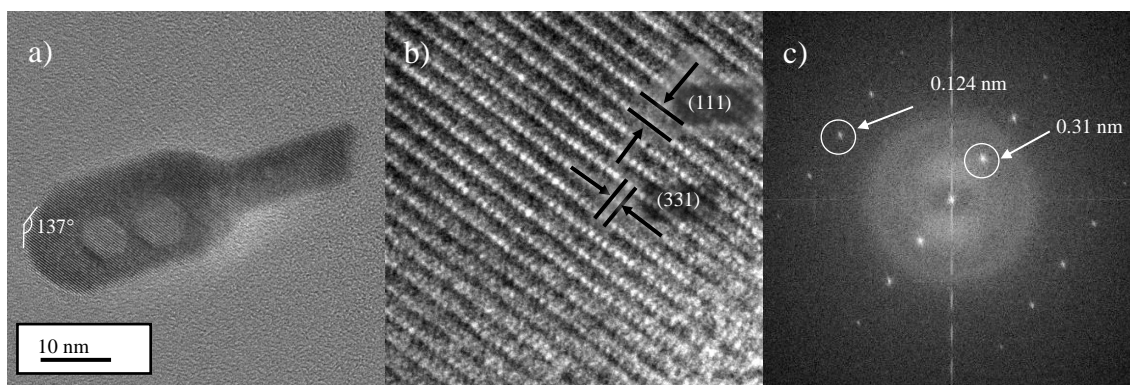


Figure 4.22 HRTEM study of a bottle-shaped nanoparticle in sample 2
(Image was acquired using JEOL F200 TEM at 200 kV, samplings=0.043 nm/pixel)

Images in Fig 4.22 (b) and (c) highlight the crystallography of the nanoparticle, which presents two sets of lattice fringes. The first set corresponds to the {111}-plane family, which appears consistently throughout this work. However, the second set of fringes corresponds to the {331}-plane, which is rarely found. Therefore, this crystallography is associated with an unusual viewing direction of the CeO₂ nanostructure, identified as [321].

Figure 4.23 shows an energy-dispersive X-ray (EDX) line scan of sample 3, identifying the elemental distribution of the sample. The analysis was performed along the annotated line, which crosses through four distinct particles of different shape and thickness. The spectrum at the top indicates the presence of carbon. Its prevalence is expected as the sample is suspended on a carbon film. The green and red lines at the bottom of the image vary in a parallel fashion, indicating a continuous composition of ceria.

The most significant observation in this study is the prevalence of ceria signal across the section containing a pore, as annotated in the figure. The lack of any variation in the signal is an indicator that the pores are not through-holes as suggested by Li et al. [2], but are enclosed

within the nanoparticles, as suggested by Sakthivel et al. [3]. This evidence is not conclusive since a through-hole oriented in a different direction to that of the electron beam could produce a similar result, as shown in 4.23.

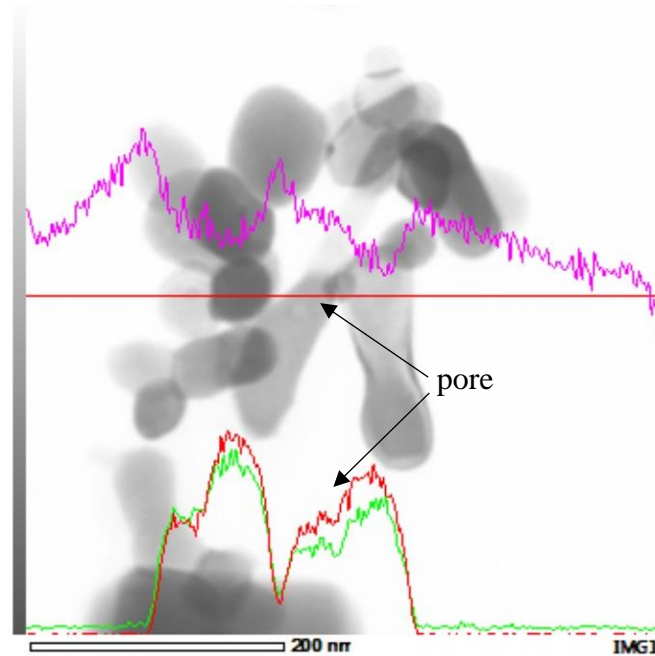


Figure 4.23 EDX line scan of sample 2. Carbon (magenta), Cerium (red), Oxygen (green)
(Image was acquired using JEOL F200 TEM at 200 kV, samplings=0.31 nm/pixel)

Further study of the sample was performed using scanning transmission electron microscopy (STEM). Figure 4.24 shows a set of two acquisitions of the same area in bright-field 4.24(a) and dark-field 4.24(b) mode. By comparing the two images, it is possible to discern if contrast is caused by differences in thickness or in composition across the sample. In this particular case, each image shows a dark feature at the top left corner of the panel.

This feature appears in image 4.24(a) as much darker than the deformed rod. This contrast could suggest that the dark feature corresponds to a large crystal of ceria formed by sintering of the nanorods. However, the same feature in image 4.24(b) also appears dark but exhibits enough electron transparency to be able to resolve the end of the overlapping nanoparticles. The fact that the top-left feature in question appears nearly transparent and not the same brightness in dark-field mode as the deformed nanorod indicates that it does not consist of ceria, but of a lighter composition, most probably carbon.

A feature of relevance to this study are the four pores located along the middle of the deformed nanorod. These appear bright and well-defined in bright-field mode, image 4.24 (a). However, in image 4.24a(b) they seem obscured with less-defined edges and a lower contrast

with the body of the rod. This behaviour supports the aforementioned hypothesis that the pores occur with the body of the rod and not as through-holes. By reducing the effect of contrast-thickness, high-angle annular dark-field (HAADF) emphasises the high-Z contrast of ceria, which appears to surround the pores. However, this result does not exclude the possibility that the pores are surface pits, which could virtually produce similar results to image 4.24.

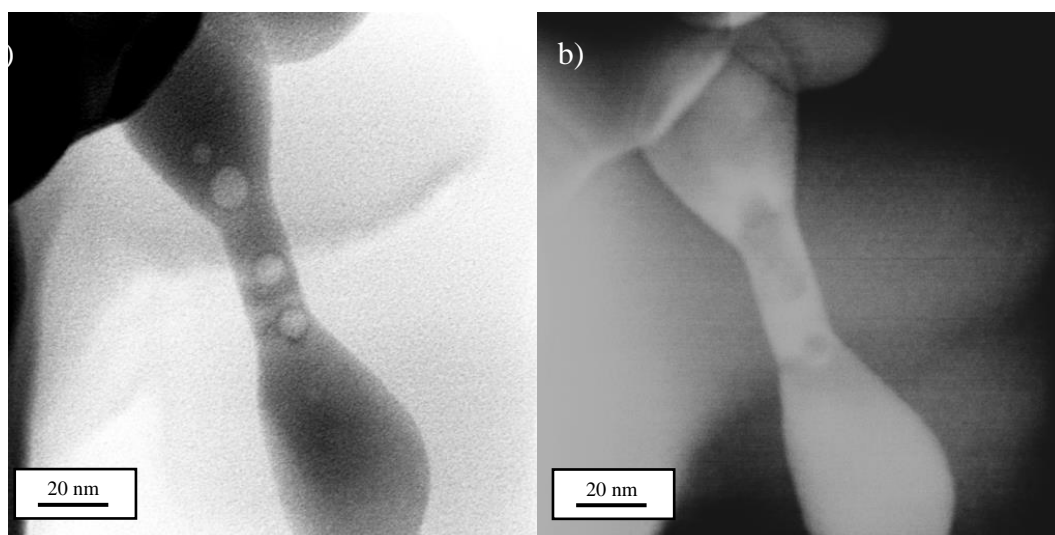


Figure 4.24 BF- and HAADF-STEM images of sample 2 (Images were acquired using JEOL F200 TEM at 200 kV, samplings=0.03 nm/pixel)

4.2.4 TEM of ceria nanorods annealed in a heat-resistant sample at 950 °C

As mentioned above, the handling of nanomaterials during experimental procedures entails a number of practical complications. In the case of heat-treatment, powders of nanomaterials can easily be lost or contaminated during the process. This challenge is often overcome by preparing greater amounts of powder than would be necessary for analysis, resulting in waste of product. The results herein seek to evaluate the adequacy of a heat-resistant TEM sample as an alternative to conventional heat-treatment of powders. As described in previous sections, a heat-resistant sample was prepared by suspending non-heat-treated ceria nanorods onto a Si₃N₄-coated Si substrate. After drying at room temperature, the sample was annealed at 950 °C alongside samples 2 and 4.

An initial exploration of the sample was conducted in order to assess the suitability of the preparation methods. Figure 4.25 shows a set of low-magnification images acquired in bright- and conventional dark-field mode. Image 4.25(a) allows resolving extensive agglomerates of particles. Mainly, the Si₃N₄ film appears to have survived the heat-treatment procedure. The

film shows good electron-transparency, and there are no visible holes or tears in the film. The nanoparticles have not sintered into a bulk solid and seem dispersed enough for TEM characterisation. Image 4.25(b) shows a dark-field imaging, where the nanoparticles appear bright, and the supporting film appears dark. This result confirms the amorphous nature of the Si_3N_4 film while emphasising the high crystallinity of the ceria nanoparticles. An important finding from this result is that the small round features annotated in image 4.25 (a) are absent from image 4.25(b), which indicates that they are amorphous. Hence, the features can be attributed to the background film and ruled out as ceria nanoparticles. This feature appears consistently throughout images of sample 3 while being absent from all other samples. This difference also supports the statement that these small round features are a characteristic of the Si_3N_4 film.

As the suitability of the preparation method for a heat-resistant sample has been established, this section continues the exploration of sample 3. The following results seek to expand on the effects of 950 °C-ageing on ceria nanorods.

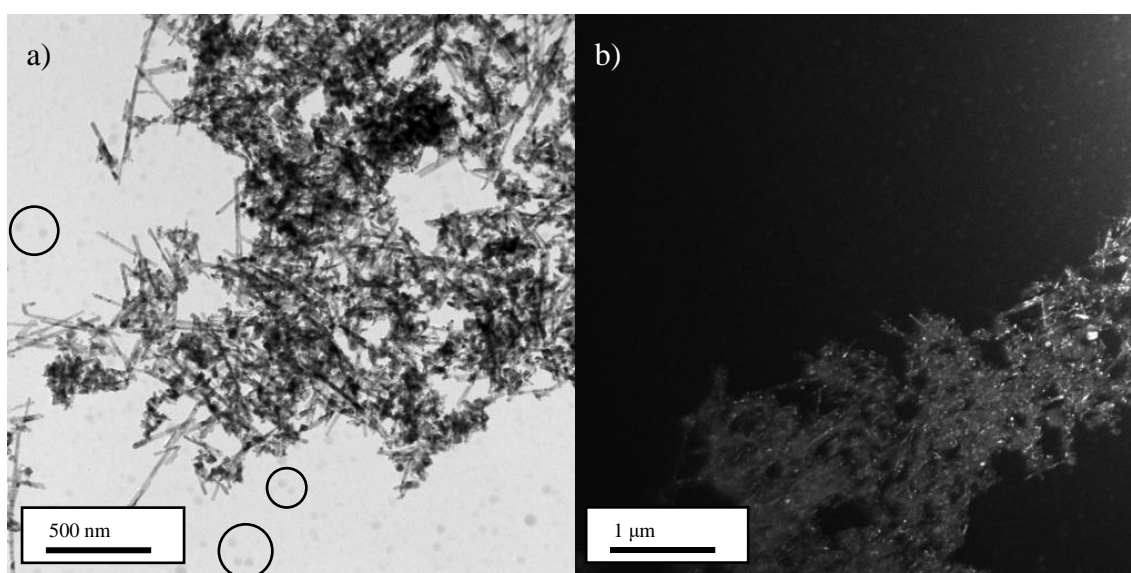


Figure 4.25 TEM Bright-field (a) and dark-field (b) images of sample 3
(Images were acquired using JEOL F200 TEM at 200 kV, samplings:
(a)=0.52 nm/pixel, (b)=0.23 nm/pixel)

Figure 4.26 shows a set of images at low and medium magnifications of sample 3. Image 4.26 (a) shows several rod-shaped objects forming an electron-transparent cluster. At lower magnifications, sample 3 appears similar in contents to sample 1 and the time-aged sample. However, closer examinations in images 4.26 (b) and (c) reveal that the sample does not consist solely of rod-shaped objects. Nanoparticles of different shapes and sizes are visible consistently

with sample 2, which followed the same heating procedure. Image 4.26(b) particularly highlights the deviation from the rod morphology, as most objects in the image appear to have round edges.

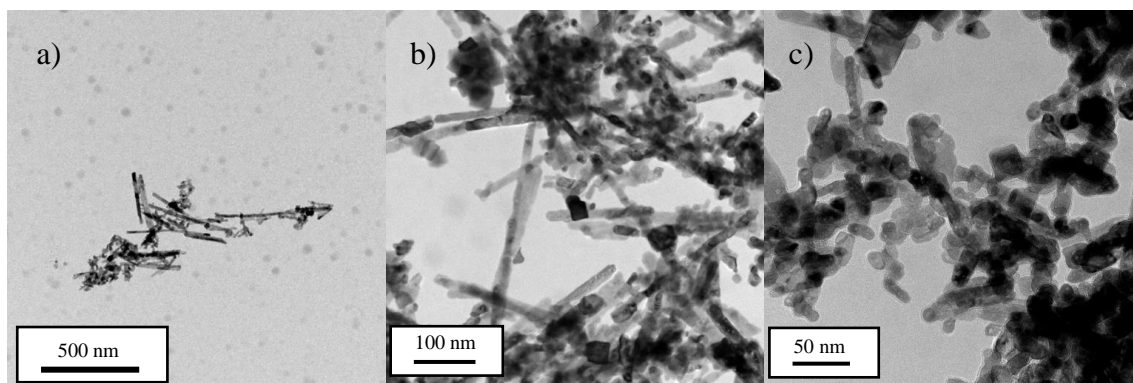


Figure 4.26 HRTEM Bright-field images of sample 3 at medium magnification (Images were acquired using JEOL F200 TEM at 200 kV, samplings: (a)=0.52 nm/pixel, (b)=0.21 nm/pixel, (c)=0.15 nm/pixel)

There are observable differences in the contents of samples 2 and 3. This can be seen by comparing images 4.26c and 4.18b. The rods in the heat-resistant sample appear to have deformed to a lesser extent. Features such as peanut-shaped nanoparticles are absent from sample 3, while they were prevalent throughout sample 2. The differences between these samples could suggest that the suspension of the nanorods prior to heat treatment affected the nanoparticles making them more resistant to the exposure to near-sintering temperature. This finding suggests that the proposed methodology for preparing heat-resistant TEM samples is not only advantageous for the reduced waste but can also improve the heat-resistance of the nanoparticles.

The higher integrity of sample 3 suggests that heat treatment at higher temperatures could potentially be performed. The pore defects are more prevalent in sample 3 than in its powder-form counterpart. This could be associated with the improved thermal stability of the nanorods. Both facts are visible in Figure 4.27, which shows arrays of nanorods. The particles have lost their straight edges and sharp corners during heat treatment but continue to have a recognisable rod morphology. Symmetrical pores can be observed in almost all the nanorods in both images. Consistently with previous samples, the pores do not reach the edges of the rods. Consistently with sample 2, pores are less frequent throughout the nanorod structure after annealing at 950 than at 800 °C.

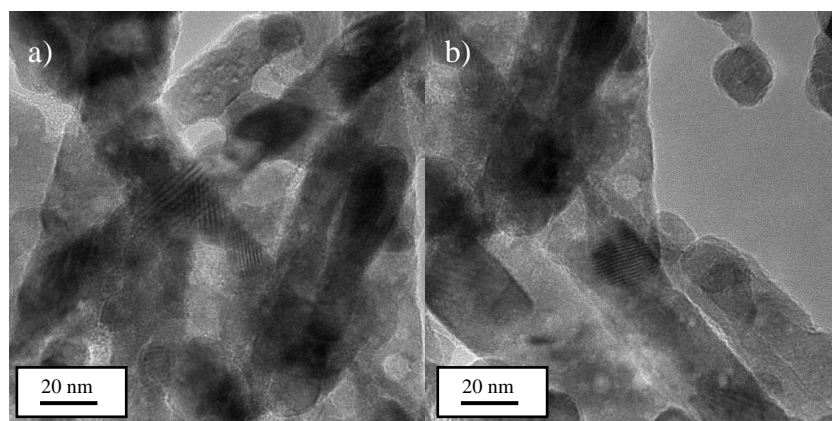


Figure 4.27 TEM images of sample 3 showing the prevalence of pores (Images were acquired using JEOL F200 TEM at 200 kV, samplings: (a)=0.43 nm/pixel, (b)=0.45 nm/pixel)

Although sample 3 exhibits fewer heat-induced morphological changes than sample 2, the effects of sintering are still evident. The set of images in figure 4.28 highlight these effects. Image 4.28(a) contains a number of nanoparticles of different shapes forming a loose cluster. In similar fashion to previous samples, the particles attach to others of similar shape and size. Images 4.28(b) and (c) highlight the formation of a joint between two parallel nanorods. These further demonstrate the significant differences in sintering behaviour between sample 2, in powder form, and sample 3, suspended on Si_3N_4 film. These differences are especially remarkable since the samples were prepared from the same materials and underwent the same heating schedule.

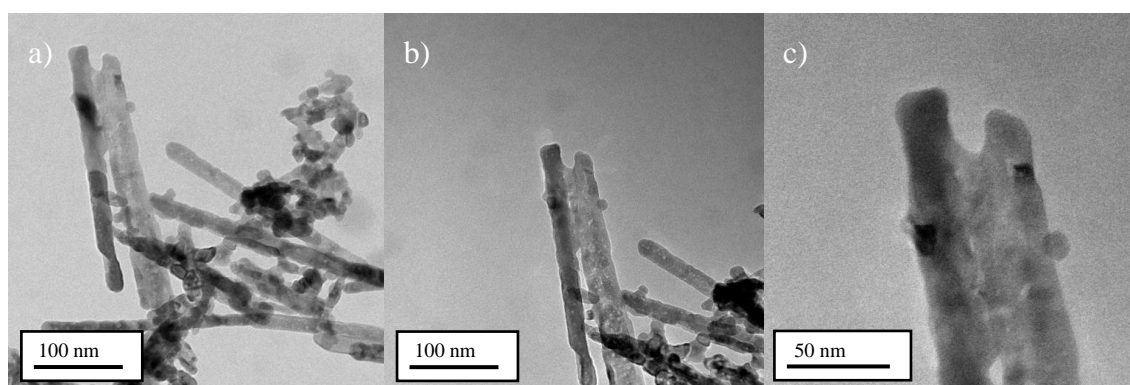


Figure 4.28 TEM images of rod/particle cluster with sintering effects (Images were acquired using JEOL F200 TEM at 200 kV, samplings: (a)=0.025 nm/pixel, (b)=0.025 nm/pixel, (c)=0.015 nm/pixel)

A crystallographic study of sample 3 is summarised in figure 4.29. At first, rods were selected which were oriented in such a way that the end of the rod could be characterised. Additionally, these rods present exposed planes and visible pores. The rods selected for this study are shown in images 4.29 (a), (e) and (i). Then, high-magnification images were obtained covering the terminal morphology of the rods, as seen in 4.29 (b), (f) and (j). The angle at the end of the rod shows little variation between particles. The angle at the end of the rod is dependent on the growth direction of the rod, as established by Du et al. [271]. In this case, all three rods have the same growth direction, as described below. Additionally, the variations in the angles at the end of the rods are small enough that they can be attributed to each rod having a slightly different orientation with respect to the electron beam. Most significantly, these images show a significant difference in structure to the ends of rods in sample 2, seen in figure 4.20.

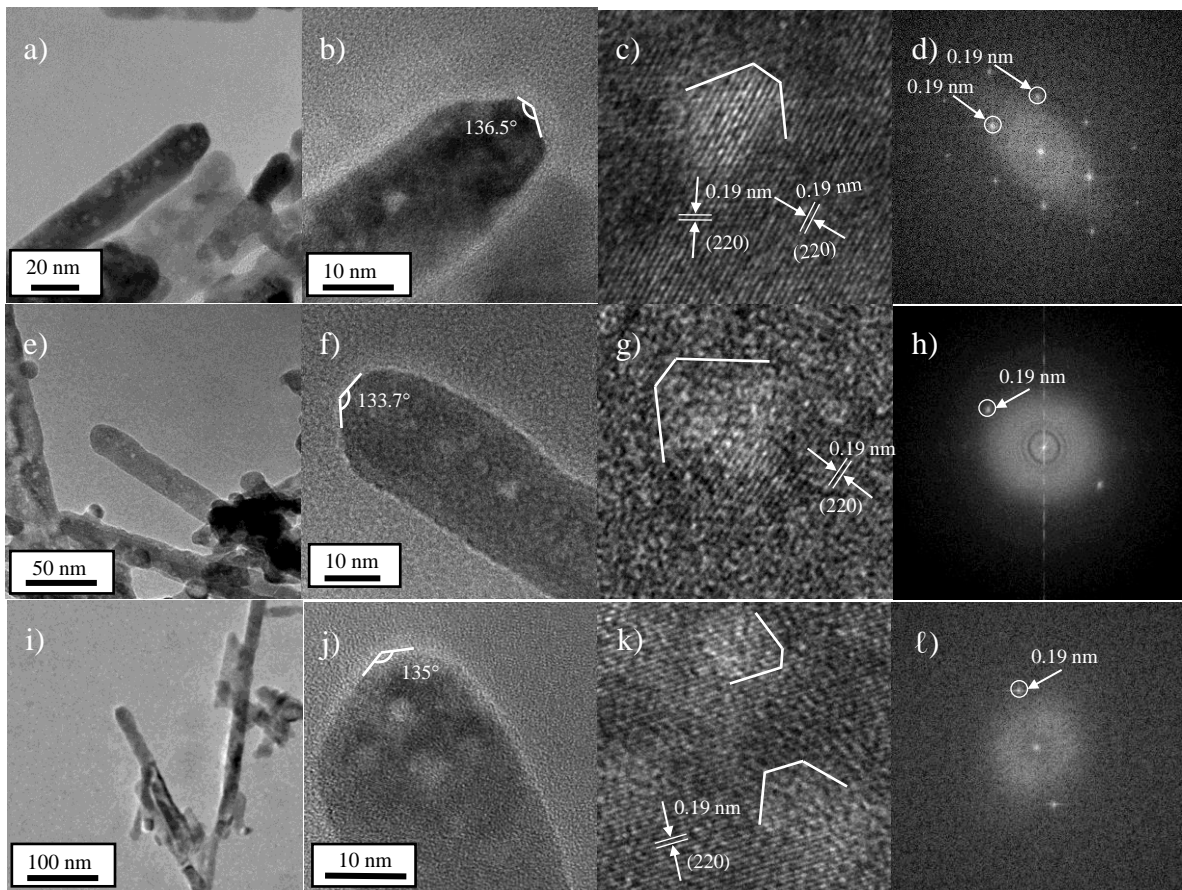


Figure 4.29 Structural and crystallographic analysis of nanorods in sample 3

(Images were acquired using JEOL F200 TEM at 200 kV, samplings:

(a)=0.052 nm/pixel, (b)=0.021 nm/pixel, (e)=0.112 nm/pixel,

(f)=0.025 nm/pixel, (i)=0.154 nm/pixel, (j)=0.012 nm/pixel)

The rods in figure 4.29 all present with sharp ends which allow consistent angular measurements. This corroborates the statements above that the heat-resistance of the particles is enhanced by the suspension onto a Si₃N₄ film. The next set of images, 4.29 (c), (g) and (k), show digital close-ups of each rod emphasising the structure of the pores and annotating the lattice fringes found in the image. Consistently with samples 1 and 2, the pores are crossed by lattice fringes which suggests their location within the body of the rod. Furthermore, the pores exhibit facets consistent with a truncated octahedron, as annotated across the images. This was reported by Sakthivel et al. for samples annealed at 800 °C [3]. Here it is demonstrated that the cuboctahedral geometry of pores persists after annealing at 950 °C. The exposed planes are determined using fast-Fourier transform measurements, as shown in images 4.29(d), (h) and (l). The prevalence of {220} planes is noted. These are not unexpected in the structure, although the {111} family is reportedly more common [236]. It is a possibility that the annealing process has helped to stabilise the {220} facets. This would be of great significance, as these planes provide higher catalytic performance than the {111} [14].

4.2.5 HRTEM of ceria nanocubes annealed in powder form at 950 °C

Sample 4 consisted of ceria nanocubes annealed at 950 °C. This sample was heat-treated in powder form like sample 2. Figure 4.30 displays several views presenting the main characteristics of the sample. Image 4.30 (a) shows that the particles form clusters in the order of several micrometres, but the edges of these appear grey, suggesting they are thin enough for transmission imaging. The carbon film used for this sample was not continuous but holey, which can be seen in some of the images. Images 4.30 (b) and (c) concentrate in areas with a lower density of particles to resolve the shape of individual particles. Mainly, the materials conforming the sample have lost their original cubic morphology and have developed into irregular shapes with a spherical aspect ratio.

The particles appear to have a combination of round and sharp corners, especially when compared with their non-heat-treated equivalent in section 4.1.1. The attraction between particles has grown stronger during heating, resulting in areas of high density like 4.30(d) and (e). The range of individual sizes can be estimated from this collection of images to be between 45 and 215 nm in diameter. This range of diameters is consistent with the original cubes, but with the absence of smaller nanoparticles like those seen in Figure 4.8.

Nanoparticles are thought to have coalesced into larger solids during heating. Image 4.30(f) is taken at a higher magnification and shows the presence of round and sharp edges. This transformation is significantly different to sample 2, where the vast majority of particles developed round edges. At the centre of the image, there is a particle with regular sides and seemingly sharp corners. The resulting geometry contains more sides and corners than the original cube.

This phenomenon is observed repeatedly throughout sample 4. Closer examination of the edges and corners of the particles demonstrates that the material preserved the sharpness of cubic corners and edges after annealing at 950 °C, as seen in Figure 4.31.

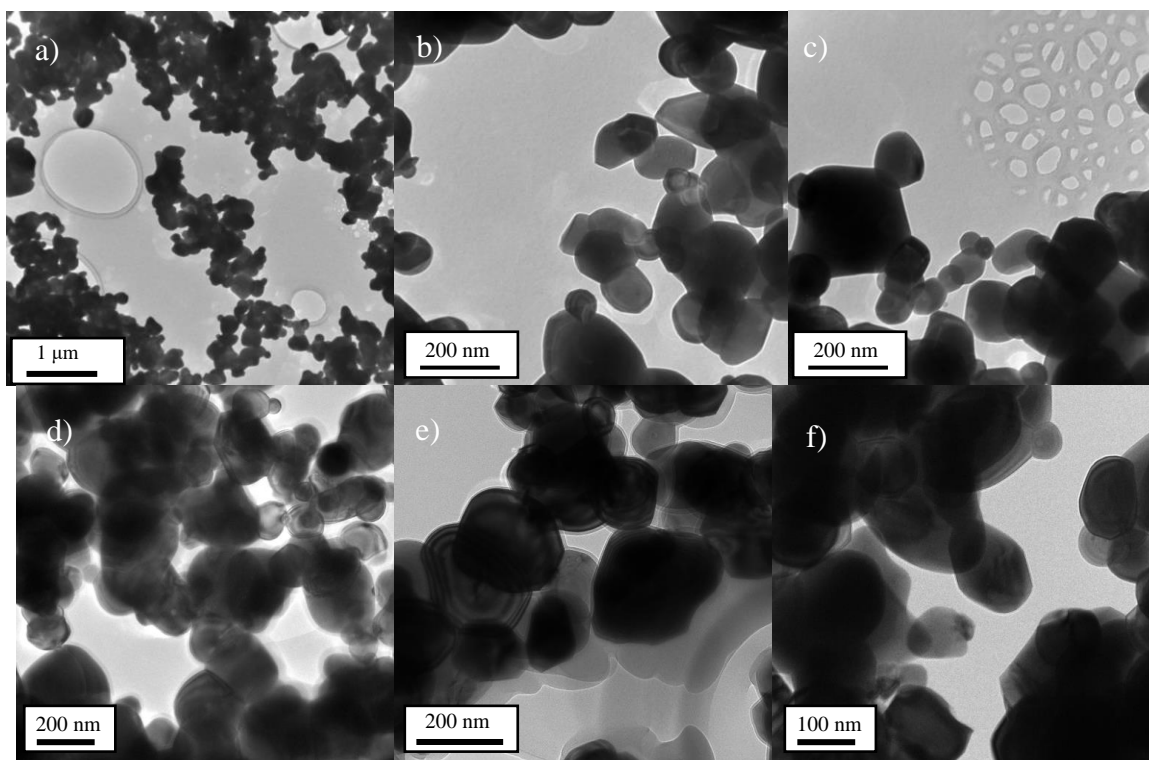


Figure 4.30 HRTEM images of sample 4 at low and medium magnifications

(Images were acquired using JEOL 2010F TEM at 200 kV, samplings:

(a)=1.2 nm/pixel, (b)=0.85 nm/pixel, (c)=0.82 nm/pixel,

(d)=0.95 nm/pixel, (e)=0.84 nm/pixel, (f)=0.52 nm/pixel)

Images (a-c) show examples of sharp corners. These terminations do not have a cubic geometry but have developed into a new shape with more corners. The higher concentration of corners would normally increase the catalytic capabilities of the individual particles. Secondly, the sides of the cubes have remained straight for the most part while shortening and multiplying, as seen in images (d-f). Potentially, this transformation also increases the reactivity of the nanocubes due to an accumulation of defects in the corners and edges of the material. The development of sharp edges and corners is a significantly different product of heat treatment to the results exhibited by samples 1-3. Particularly, the cubes showed more stability than the nanorods in sample 2, heated too in powder form. This difference in behaviour suggests that nanocubes have higher thermal stability than nanorods. In spite of the occurrence of sharp

edges and corners in sample 4, the surface area and density of the sample reduced significantly during heat treatment.

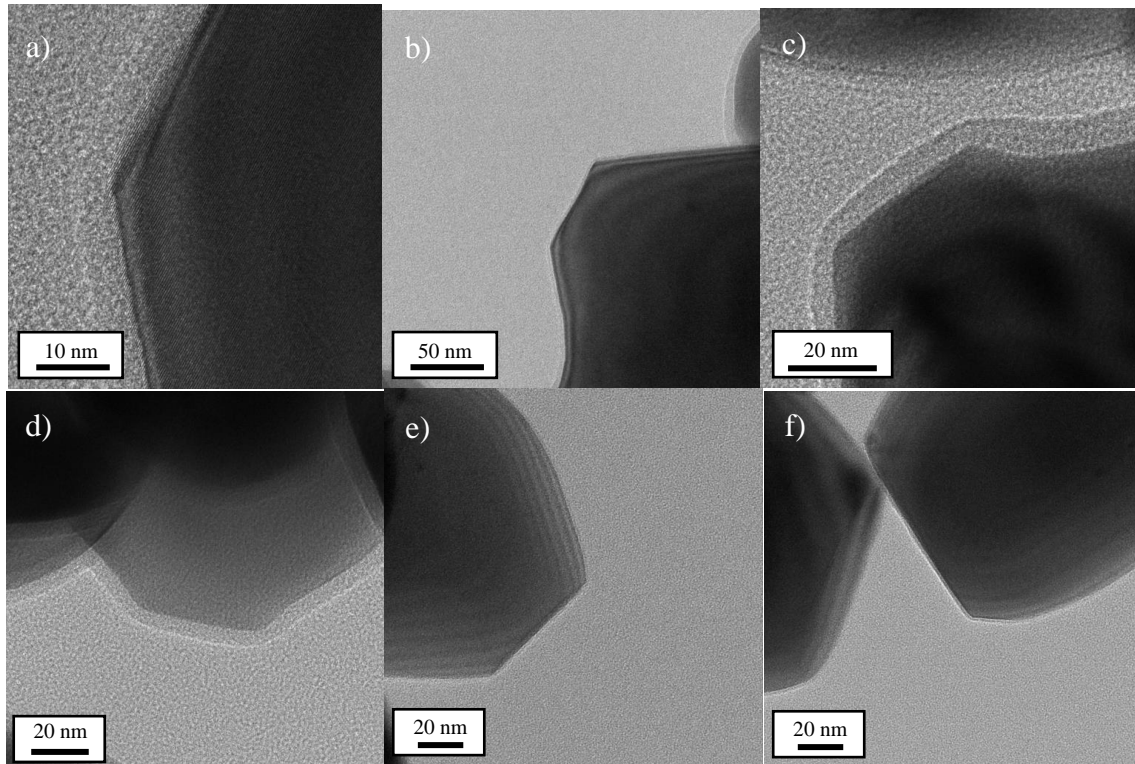


Figure 4.31 TEM of sample 4 highlighting straight sides and sharp corners (Images were acquired using JEOL F200 TEM at 200 kV, samplings: (a)=0.012 nm/pixel, (b)= 0.041 nm/pixel, (c)=0.024 nm/pixel, (d)=0.02 nm/pixel, (e)=0.032 nm/pixel, (f)=0.032 nm/pixel)

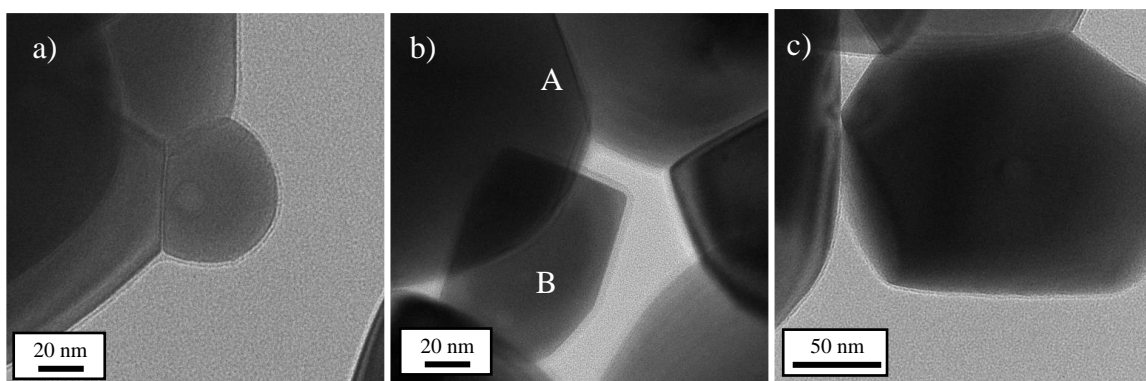


Figure 4.32 Mid-magnification images of sample 4 emphasising sintering deformations (Images were acquired using JEOL 2010F TEM at 200 kV, samplings: (a)=0.032 nm/pixel, (b)=0.032 nm/pixel, (c)=0.073 nm/pixel)

The effects of sintering can be observed at the nanoscale in Figure 4.32. Image 4.32 (a) focuses on three particles which have deformed into a single volume, while the individual particles continue to be discernible. Image 4.32 (b) also shows a cluster of three nanoparticles. Except, these have sintered into an open solid, which consolidates empty space between them. Another important feature in sample 4.32 (b) is the particle annotated as B, which retains a near-cubic geometry after heat treatment. This is a rare occurrence across the sample. Image 4.32(c) shows a particle over 200 nm in diameter, attaching to another by one side. The particles appear to have attached by their shorter sides, which appears to be the most common case in sample 4. These and other similar types of deformations associated with sintering are prevalent across the sample. However, most clusters continue to expose sharp corners and edges from deformed nanocubes, such as that in image 4.32(c).

The crystallographic characterisation of sample 4 is summarised in Figure 4.33. The high-magnification images 4.33(a) and (d) show sharp corners and straight edges. Image 4.33(a) also includes the deformations of cubes associated with sintering. The digital close-ups of these images allow the resolution of atomic lattice fringes. In both cases, the particles have remained monocrystalline, and seem to terminate consistently with their crystalline structure, despite their deformations. The crystal planes present in the sample were identified using fast-Fourier transform measurements. The measurements of individual peaks are annotated in images 4.33(c) and 4.33(f). The particle in 4.33(a) presents peaks at 0.16 nm and 0.27 nm, which correspond to $\{131\}$ and $\{200\}$ planes, respectively. These correspond to the unusual viewing direction $[013]$, as annotated on the FFT in image 4.33(c). The particle in 4.33(d) shows prominent peaks at 0.19 nm, which relates to the $\{220\}$ -planar family. Therefore, this particle can be deduced to terminate in (110) surfaces.

As observed in section 4.2.3, nanorods annealed at 950 °C also presented a high concentration of (110) planes. This increase is discernible when comparing images of materials annealed at 950 °C (Figs. 4.29 and 4.33) with those of rods annealed at 800 °C (Fig. 4.13), or before any heat treatment (Fig. 4.4). Materials without heat-treatment and materials annealed at 800 °C also present (110) planes, but these appear less commonly than the (111) . Planes of the $\{111\}$ -family have not been observed in samples 3 and 4.

The disappearance of a particular type of planes would result in the morphologies seen in samples 2-4, with a combination of rounded and angular features seen across each sample. The disappearing planes would give way to rounded features, while those planes that are more stable at higher temperatures would result in the material retaining certain, sharp corners and edges. This relationship can be observed in Figure 4.33, where the sharper terminations of the particles are parallel to the planes annotated in the digital close-ups. The results from samples 3 and 4 are surprising, considering that planes of the $\{110\}$ family are said to be less stable

than the $\{111\}$ [14]. A possible explanation would be that, although (111) surfaces are more prevalent at room temperature, (220) planes have a higher thermal stability. Thus, the (110) not only become the most common at high temperatures but direct the morphological transformations. The prevalence of (220) planes at higher temperature can be directly linked to their apolarity. I. e., (220) planes are the only ones that contain both Ce and O atoms in the exposed surfaces. This is made evident by their schematic comparison as seen in Fig 2.15.

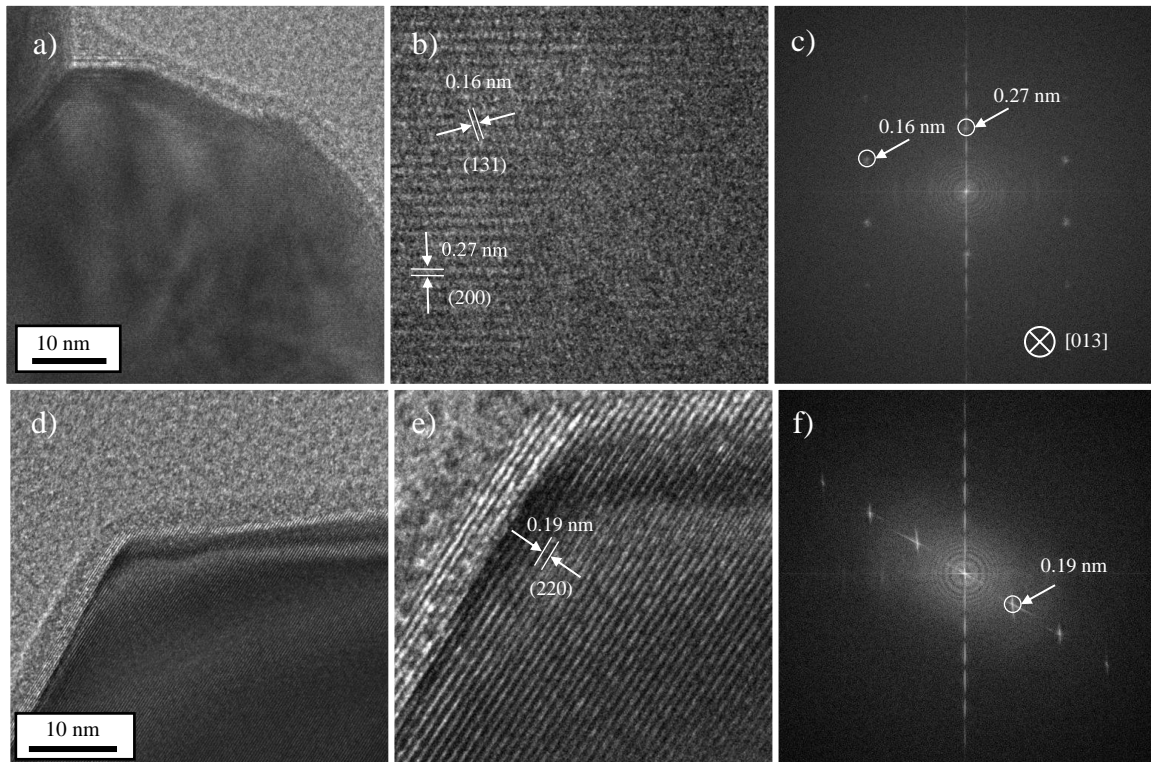


Figure 4.33 Crystallographic analysis of nanocubes annealed at 950 °C
(Images were acquired using JEOL F200 TEM at 200 kV, samplings:
(a)=0.012 nm/pixel, (d)= 0.014 nm/pixel)

4.2.5.1 Discovery of porosity defects in annealed nanocubes

Nanocubes exhibited pore defects after annealing at 950 °C. This feature repeatedly appears throughout sample 4, as seen in Figure 4.34. The pores present similar characteristics to those found in nanorod samples 1-3. For instance, pores present a symmetrical geometry and appear to be enclosed within the body of the particle. On the other hand, the pores observed in nanocubes have less pronounced facets than the pores presented in nanorods. The sizes of the pores observed in this work ranged from 7 to 25 nm, making them significantly larger to the pores in nanorods. This could be due to cubes having larger cross-sections than rods, which

could allow more growth of the pores in three dimensions, whereas the formation of pores in nanorods could be potentially limited in directions different to the growth or the rod.

Nevertheless, the size of pores does not increase in larger nanocubes. This disassociation between the size of pores and the containing particle is also consistent with the behaviour of pores in nanorods. The occurrence of pores in nanocubes is illustrative of the formation mechanism of these defects in all nanomaterials. Authors have suggested that the pores grow from internal defects produced during oriented-attachment formation of nanorods [379]. However, the formation mechanism of CeO_2 nanocubes is established as dissolution/recrystallization, which is credited for their higher stability than nanorods. Therefore, the results here presented indicate that oriented attachment is not the cause of mesopores in ceria nanomaterials.

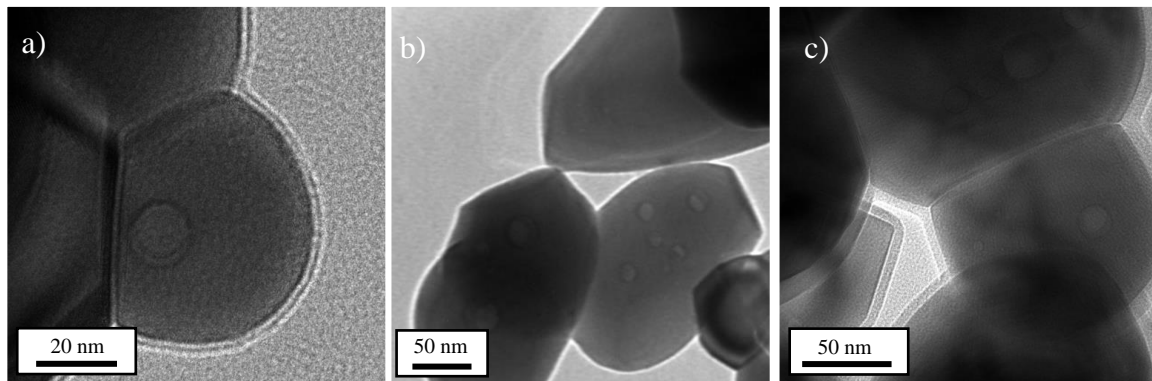


Figure 4.34 Porosity defects in nanocubes annealed at 950 °C
(Images were acquired using JEOL F200 TEM at 200 kV, samplings:
(a)=0.011 nm/pixel, (b)= 0.031 nm/pixel, (c)= 0.027 nm/pixel)

Chapter Five

Electron Tomography of Mesoporous CeO₂ Nanorods

The experiments reported in this section continue the work presented in Chapter 4, which established reproducible annealing methods for the production of defect patterns in CeO₂ nanorods. This section seeks to resolve the unanswered questions regarding the structure and morphology of the heat-induced defects. As mentioned before, these defects have been credited with improving the catalytic capabilities of ceria nanorods. There are a small number of publications that employ TEM to image the structure of porous CeO₂ nanorods in two dimensions [2], [3] which are complemented and expanded by the results in chapter 4. Additionally, Florea et al. have reported successful electron tomography reconstructions of solid nanorods. However, there have been no reported explorations into the 3D morphology and distribution of defects in heat-treated ceria nanorods. A study of the 3D structure at the nanoscale is necessary to understand the formation mechanism of heat-induced defects and facilitate the design and applications of these promising new materials [13]. Furthermore, the findings in Chapter 4 that the heat-induced defects can appear in other morphologies beyond nanorods make the present exploration all the more relevant to the field of catalytic nanomaterials.

Figure 2.16, found in Chapter 2, Literature Review, shows several possible internal structures of defective ceria nanorods found across the literature. This myriad of proposed explanations is used as the starting point for the present study. Briefly: 2.16(a) presents patches of high concentrations of point defects with possible lattice deformation [277]; 2.16(b) shows clusters of ordered point defects, which do not result in empty space [276]; 2.16(c) shows a widely reported structure [4], [119], [278] consisting of sub-2nm sized voids with irregular shape spread randomly across the rods. The bottom row of sketches represent the most likely explanations for the structure of heat-induced pores in nanorods: 2.16(d) corresponds to mesopores of with defined geometries, as reported by [3], [125], [126]; 2.16(e) shows pores that connect to the surface, like those observed after chemical etching [12], [119], [120], [279]. Finally, 2.16(f) represents 1D-nanochannels through-pores or wormholes, as seen in [12].

It should be noted that the six structures described above could look very similar in two dimensions, even using high-resolution transmission electron microscopy. This uncertainty is a significant motivation for using electron microscopy to study such materials. However, as

discussed in section 2.3.3, electron tomography carries several limitations, which can be appreciated in the present study. As reported in the previous chapter, heat treatment of ceria nanorods resulted in enhanced quality of the crystal structure. In turn, these highly crystalline objects produce Bragg-enhanced contrast when imaged in TEM bright-field mode. These high-contrast features are detrimental to electron tomography, as ET uses the variations in grey values to reconstruct three-dimensional morphologies. Therefore, sources of contrast that are not associated with (thickness \times density) can result in distortions in tomographic reconstructions.

For this reason, ceria nanorods are good candidates for the experimental approach reported by Saghi et al. [9], which uses the principle of geometric tomography to reconstruct nanostructures based on binary information. However, there are several conditions that the input information needs to meet for GT to be applicable. Namely, the object being reconstructed should be axially convex. This is often true for isolated nanoparticles and solid nanostructures, but not for materials with empty space, which are not strictly convex by definition. Secondly, GT is not recommended for multi-object systems where objects overlap in one or several views across the tilt series. This is due to the elimination of contrast in GT, which merges all overlapping objects into one, resulting in distortions to the reconstructed volume. For non-porous materials, this limitation is easily overcome by selecting isolated particles during imaging. However, in a system such as the mesoporous nanorods in the present study, pores are almost sure to overlap with each other in several views across the tilt series. These limitations have motivated the successful attempt in this study to develop a novel modified version of the geometric tomography algorithm, which will be detailed in the following sections.

The tomographic reconstructions obtained in this work are reliable 3D models of the mesoporous nanorods and can be used to obtain statistical measurements of their shape and size in three dimensions. Also, the tomographic reconstructions reported here are a reliable tool to establish the location of the pores with respect to the surfaces of the rod, which is a point upon which authors have not reached a consensus so far. Sakthivel et al. proposed that the defects occur inside of the structure, as sketched in Figure 2.16(d). On the other hand, Li et al. concluded that the pores appear as recesses or concavities on the surface of the rod, such as the ones in Fig 2.16(e). Thirdly, Gao et al. suggested a growth mechanism, which results in pores travelling across the structure and connecting opposite surfaces of the rod, as represented in Fig 2.16(f). Furthermore, the development of a new approach that overcomes the experimental limitations of geometric tomography can open the doors for the 3D characterisation of other porous systems in the future.

The materials used in this study were prepared by collaborators at the University of Central Florida, as detailed in their publication [214]. In brief, CeO_2 nanorods were obtained by optimising the parameters of a typical hydrothermal synthesis. At first, a solution of $Ce(NO_3)_3 \cdot 6H_2O$ was used as a cerium precursor and NaOH as an activating reagent to induce

nucleation and growth of the nuclei. These experimental conditions were used to produce different morphologies of ceria nanomaterials. Expressly, parameters were set to synthesise rod-shaped nanomaterials selectively. High selectivity was achieved by a concentration of NaOH of 22.5 molL⁻¹ and maintaining the reaction temperature of 120 C for 24 hours. Further heat treatment of the rods was carried out at 800 °C in an oxidising environment for with a holding time of 3 hours. The materials used in this work could not have been prepared at the experimental facilities of the University of Sheffield, as the Department of Materials Science and Engineering does not incorporate an autoclave that can reproduce the hydrothermal synthesis conditions described above.

5.1 Tomography of porous rods

This section describes the procedure used to reconstruct a mesoporous ceria nanorod. The objective of this experiment was to obtain a reliable three-dimensional model of the mesoporous ceria nanorods. The main experimental stages of the study are outlined, starting with the parameters used for the electron microscopy, to the computational processing of the images. Finally, a detailed interpretation and metrology of the tomographic results are presented.

5.1.1 Image acquisition

The TEM specimen was prepared using a standard-grade 3.05 mm copper grid coated in holey carbon film. The holey carbon film was selected for this experiment as the holes could facilitate faster alignment of the electron beam. Furthermore, particles could potentially be found in the edges of holes, which could be good candidates for tomography objects, as the contrast of the carbon film is eliminated. The annealed nanorod powder was suspended in deionised water and deposited on the C-coated Cu grid. Subsequently, it was allowed to dry at room temperature. The sample was mounted onto a Fischione tomography sample holder and allowed to sit in a table-top vacuum pump overnight. Imaging was performed under a JEOL 3010 electron microscope. Details of the equipment used are described in Chapter 3.

An initial exploration of the specimen was performed to locate a suitable tomography object. The first condition that the object should meet to be suitable for tomography is to be representative of the rest of the sample. In this case, the object should be a nanorod that presented heat-induced defects like the ones seen in Section 4.3.1. Secondly, the object should be isolated in the directions perpendicular to the rotation axis. This condition prevents the object from being obscured by overlapping objects upon rotation. One-dimensional materials such as nanorods present a challenge in tomography. This is due to the projected thickness they can

achieve when rotated perpendicularly to their axis. Therefore, the third condition for the nanorod to be studied was for it to be oriented along the rotation axis, or as close to it as possible.

Figure 5.1 shows the initial (0°) views of the object selected for tomography. The object consists of a single nanorod with several well-defined defects along its length. The two magnifications shown were selected for the tomography as they highlight different characteristics of high interest for the study. The image at medium magnification seen in Figure 5.1 (a) emphasises the morphology of the nanorod. The image shows a section of the rod 140 nm long. This broader view shows the continuity of the walls, which can be an early indicator of the porous structure of the rods. There are no visible indents or missing regions of material. This could support the idea that defects happen within the body of the rod and do not reach the surface. Furthermore, the preferential location of the defects can be observed, which mostly seem to occur within the central 4/5 of the rod diameter, as suggested by Sakthivel et al. [3].

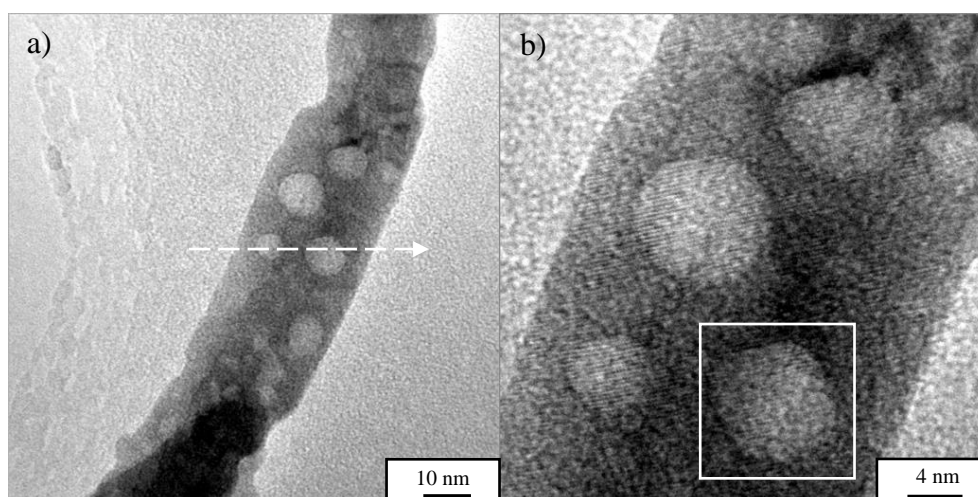


Figure 5.1 HRTEM images of the object selected for electron tomography
(Images were acquired using JEOL 3010 TEM at 200 kV,
samplings: (a)=0.41 nm/pixel, (b)=0.006 nm/pixel)

The image at high magnification, Figure 5.1 (b), highlights the internal structure of the nanorod rather than its morphology, showing a homogeneous monocrystalline structure with visible lattice fringes. The nanorod shows five distinct bright features enclosed by straight lines with a well-defined faceted geometry. Figures 5.1 (a) and (b) show a dark stripe of constant width running along the longitude of the rod. This is consistent with the pseudo-hexagonal cross-section of the rod and can be attributed to the thickness of the material [4]. However, some dark patches can also be seen encircling the defects, which are more likely associated with high crystalline lattice strain than with the morphology of the material. The dark areas of strain appear to be located next to the sharp corners enclosing the defects. These dark patches

only seem to appear in the solid rod material and grow weaker as they move away from the defect area until they are no longer visible 1.3 nm, or six atomic lattices, away from their origin. These regions of dark contrast are more visible at some tilt angles than others, which is expected of certain crystallographic features.

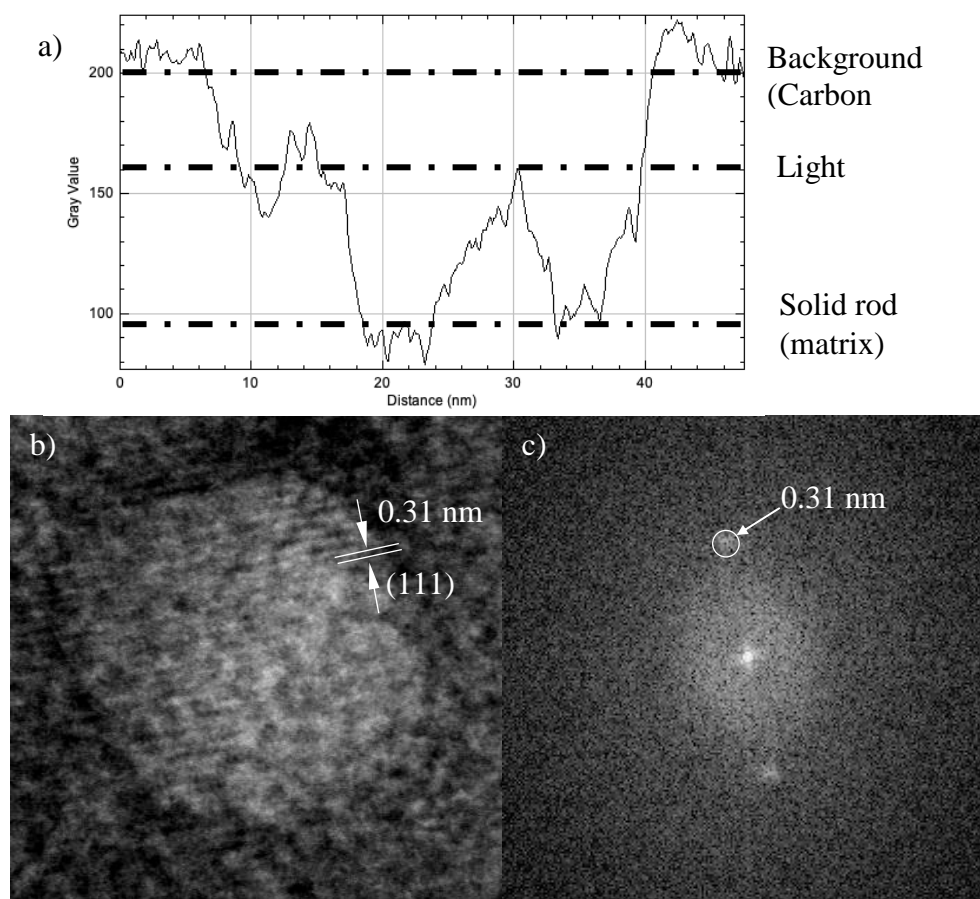


Figure 5.2 (a) profile analysis of the annotated length in Fig 5.1(a). (b) shows a digital close-up of the inset in Fig 5.1(b). (c) FFT of image (b) with annotated measurements (Scale bar in Figure 5.1)

Figure 5.1 (a) presents a high contrast between the body of the rod and the bright defect areas. This observation could support the theory that the defects are channels or through-holes, as suggested by Gao et al. [12]. Such defects would run across the entire lateral section of the rod communicating the front and back faces, as shown in Figure 2.16 (f). In order to investigate this, a profile was taken at different sections of defect-containing material, which rendered results consistent with the plot shown in Figure 5.2 (a). The section of the rod corresponding to the plot is annotated in a light arrow. The profile shows that the intensity of the bright features is, in fact, higher than any other area in the rod, but never reaches the intensity of the

Carbon film in the background. Another possibility could be that the defects were indeed channels, but they were at an angle with respect to the electron beam. The beam would still be travelling across a lot of heavy rod material, which would reduce the intensity in the profile. However, the rod shown in the images contains defects of up to 11 nm within a lateral section of 35 nm. For this reason, a channel-like structure would be expected to show at least a small region of the defect transmitting the same intensity as the background.

The digital close-up presented in Figure 5.2 (b) allows resolving lattice fringes corresponding to the {111} exposed plane, as measured using the FFT pattern in the image 5.2 (c). It can be seen that, when these fringes enter the brighter regions, they are not interrupted. This behaviour suggests that the single crystalline structure is continuous despite the defects. There are also no visible instances of Moiré pattern in this or other bright defect areas, which suggests that the patches correspond to a region of missing material, like a pore or cavity, as opposed to a region with a different crystalline structure like the one pictured in Figure 2.16 (b).

Although the shape of the defects in Figure 5.1(b) appears to vary slightly. This is expected for most 3D features, as the projection will make specific shapes appear elongated or shortened. However, regardless of this effect, there is consistency in the orientation of the features, with the upper and lower sides of each defect maintaining parallelism with the exposed {111} atomic planes, while the shorter sides remain parallel to the growth direction of the rod.

5.1.1.1 Tilt-series acquisition

The tomography holder potentially allows a complete 180° rotation of the sample, since it is significantly smaller than the lens gap, as explained in Chapter 3. However, due to the effects of self-shadowing, it is impossible to acquire such a tilt series in practice. Furthermore, there is no practical way to position an object of interest at the exact centre of the TEM grid and, therefore, the acquisition will always happen off-centre. Naturally, as the distance between the object of interest and the centre of the grid increases, the volume of the material causing the self-shadowing also increases, thus reducing the span of the acquired tilt series. Given these fundamental limitations, a tilt series was obtained across 120° for each of the selected magnifications, as limited by the geometrical constraints of the sample, which self-shadowed upon further rotation. Images were taken with 5° increments in rotation angle. The acquisition was performed using a single tilt sample holder, which rotates the specimen around a single axis. Initial assessment of the suitability of tomographic tilt series should consider the main difficulties of electron tomography, i.e., electron-beam damage and geometric constraints. Figure 5.3 shows the full tilt series at medium magnification. The object of interest remains visible across the entire series. A large perforation is observed in the carbon film in the images between -60° and -35°. As mentioned above, this study was performed on a specimen suspended on a holey

carbon film. While the edge of the hole overlaps with the nanorod of interest, it has good electron transparency, and the main features of the object are still resolved. The inclination of the rod in the field of view varies as the specimen is rotated. This is expected as any rod is unlikely to be inclined at the same angle as the rotation axis of the goniometer. However, there is not a significant difference between the two axes, and the series is deemed adequate for tomography. In other words, the difference between the rotation axis and the axis of the rod has not been neglected during further computational operations, but their proximity has benefitted the imaging results.

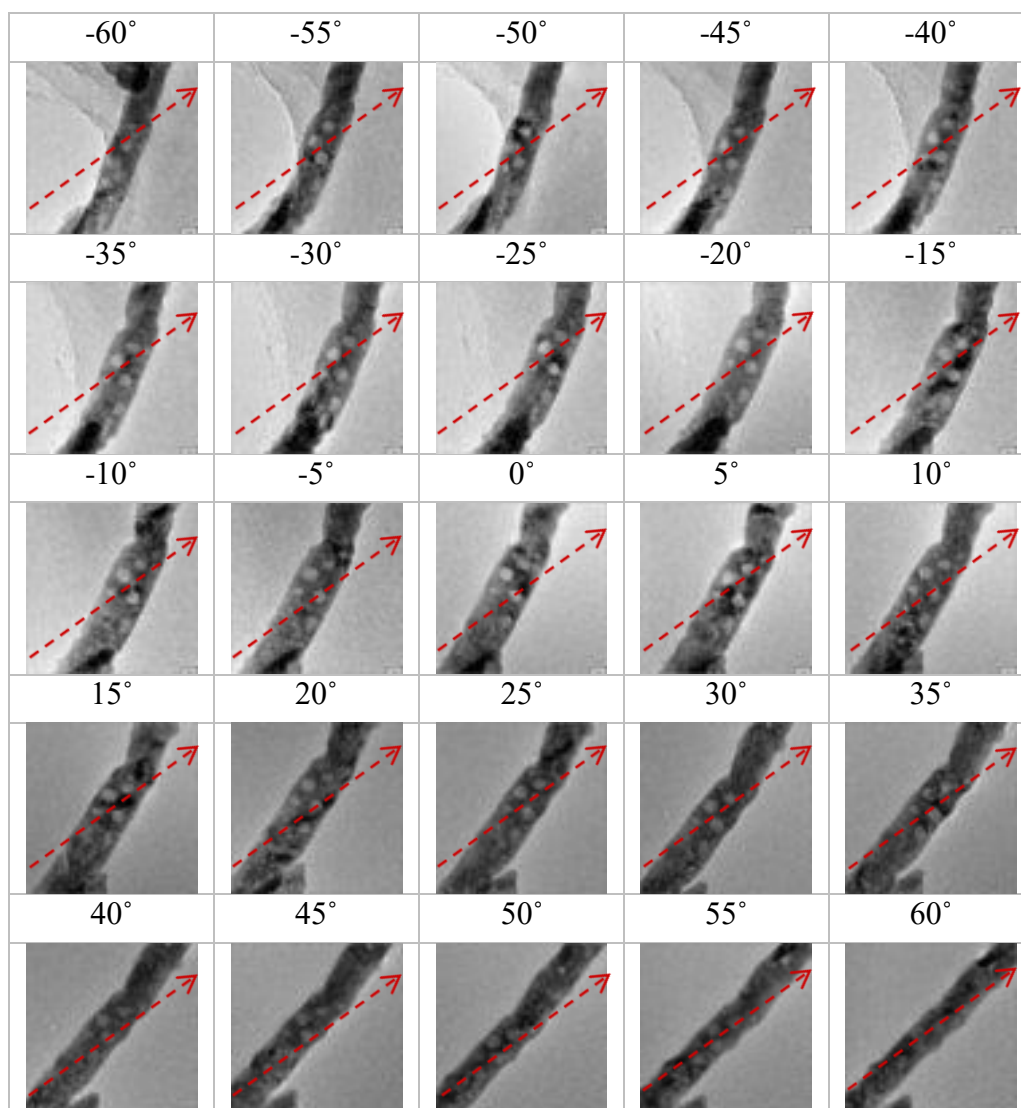


Figure 5.3 TEM tilt series of an annealed ceria nanorod at medium magnification. Instrumental tilt-axis orientation calculated at 35.75° and represented by the arrows (Scale bar in Figure 5.1). Images obtained at nominal magnification 200kX and the plane of the detector camera located at negative plate level. Note: the arrows represent the direction of the tilt axis, but not its lateral location, as the latter is unknown prior to alignment.

The rod appears to vary in diameter between 35 and 25 nanometers. With its width increasing as it rotates from -60° to 0° and decreasing again as the specimen is rotated towards 60° . This variation in diameter is expected for a non-cylindrical rod and supports the cross-sectional morphology published by Florea et al. [4]. Another essential feature observed across the images in Figure 5.3 is that the sides of the rod remain continuous throughout the rotation with no recesses or indents appearing at their sides. This supports the estimations in the two-dimensional studies presented in Chapter 4, that the defects do not rest on the surface, as has been suggested by Li et al. [2].

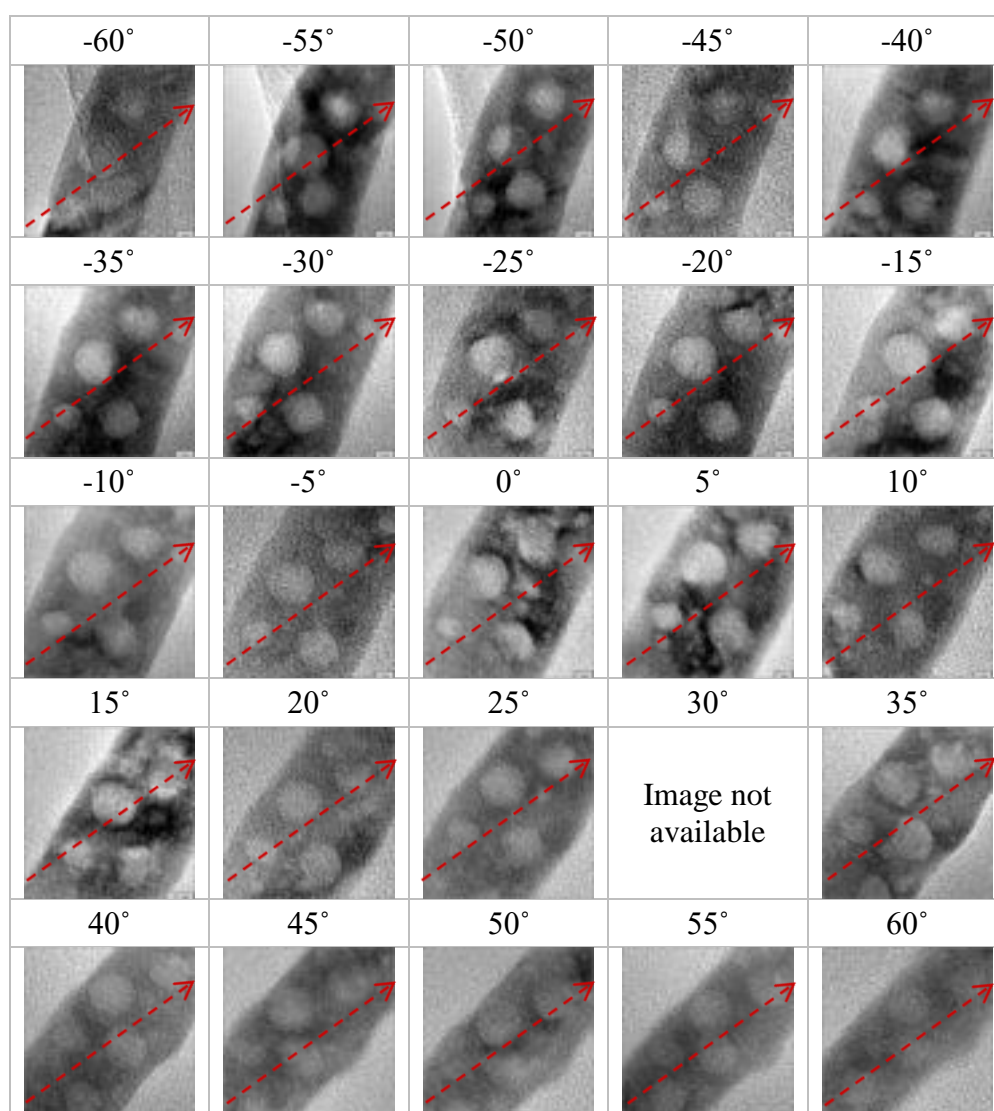


Figure 5.4 HRTEM tilt series of an annealed ceria nanorod at high magnification. Instrumental tilt-axis orientation calculated at 35.75° and represented by the arrows (Scale bar in Figure 5.1). Images obtained at nominal magnification 600kX and the plane of the detector camera located at negative plate level. Note: the arrows represent the direction of the tilt axis, but not its lateral location, as the latter is unknown prior to alignment.

The tilt series obtained at high magnification is shown in Figure 5.4. This series seeks to highlight the shape of the internal defects of the rod in three dimensions. There are several defects, which can be traced across the entire series, which is favourable for their reconstruction. The background feature observed in the series above is also visible at the lower angles and overlaps with the defects. At this magnification, the grainy appearance of the carbon film is more noticeable and causes blurring of the edges of the defects in the images at -60° and -55° . This effect is unavoidable without the use of aberration correction instrumentation. For the present study, however, this feature can be suppressed by applying pre-processing steps before the reconstruction.

The image taken at 30° has not been possible to retrieve and is not available for the tomographic study. However, this does not impede the reconstruction, as the angle can be skipped, or the image can be replaced with a digital close-up of its medium-magnification counterpart.

The series is considered adequate since the general shape and location of the defects can be discerned across all images in the series. Nevertheless, there are significant artefacts of Bragg diffraction visible in most of the images. As mentioned in the sections above, this type of feature can cause significant distortions to the reconstructed volumes. The presence of these artefacts is a significant motivation to use the method of geometric tomography, as described in the following sections.

5.1.2 Image alignment and pre-processing

This section presents a description of the steps of computation that precede the application of tomographic reconstruction algorithms. Mainly, this section describes the criteria used in the alignment and binarising of the tilt series. Also, a method of segmentation is presented, which has been implemented to make the object suitable for the geometric tomography algorithm. Overall, the steps presented here aim to prepare the images for the reconstruction algorithm and are instrumental for the successful production of a reliable three-dimensional result. The steps of alignment, binarisation and segmentation have been applied to all images in each series. However, for the sake of conciseness, only a representative number of images are shown in each figure of this section.

5.1.2.1 Image alignment

Image alignment is a necessary step in all experiments involving electron tomography. Since there is no way to ensure that the object of interest is sitting on the rotation axis of the instrument, the object is bound to move across the field of view between images. This is minimised by re-centring the region of interest between images. It is often also necessary to adjust the

focus of the objective lens and the z-height of the specimen between images since the displacement occurs in three dimensions. The main aim at the moment of imaging is to keep the object of interest in view and focus, relying on the steps of lateral alignment, as shown here.

Several semi-automated methods can perform a lateral alignment. For example, markers consisting of gold nanoparticles are often used in biological samples. This is generally inapplicable for experiments involving nanomaterials, where tilt series are acquired at high magnifications. Commercially available Au markers range in size from 1 to 100 nm. Unfortunately, even a 1-nm would occupy around 50 pixels in an image like those used for this experiment (256×256 pixels). This would not only obstruct features of interest from view but would be unlikely to be helpful in computer-assisted alignment. A second widespread semi-automated method for the alignment of stacks of images for tomography is the application of a cross-correlation algorithm. This algorithm recognises a small segment of the object, which it can trace across the entire stack, and aligns the images by placing that segment in a consistent place throughout the stack. Nevertheless, the nature of the sample, as well as the electron-microscopy parameters employed, result in images with many artefacts. These features are indistinguishable from morphological features for the algorithm, which renders it unusable. A third possibility could be to align the object during the acquisition. The instrument used for these acquisitions JEOL JEM-3010 incorporates an auto-alignment Tietz ® software, which can compensate the lateral displacements during the acquisition of a rotational series of a three-dimensional object which does not match the eucentric rotation geometry. However, this software has proven ineffective for the type of samples studied in the present work.

Since the computer-assisted alignment methods available could not be used for the present study, the alignment has been done manually. This method implies the superposition of images in the stack by pairs and the translation of each image to match the location of a determined feature. The feature selected had to be such that it was visible across all 25 images in each series, and be small enough that its location could be pinpointed to an area represented by a few pixels, thus reducing displacement errors. Preferably, the feature selected for alignment would appear along the central axis of the rod, which produces a smoother alignment with the object to be reconstructed rotating around a centred axis. For the case of the tilt series shown in Figure 5.3, acquired at medium magnification, the bright patches along the body of the rod showed a consistent geometry throughout all the images, and at least one of them occurred along the axis of the rod. More importantly, the defects appear small enough at this magnification that they are suitable to be used as a point of reference for lateral alignment. Figure 5.5 shows a selection of images aligned by this method. The frame surrounding each image represents the area of the original image. The image taken at 0° is arbitrarily used as a starting point, and all images are translated to match the position of the selected region. The images were aligned with respect to the geometric centre of the annotated feature.

Potentially, it would be better to use multiple features for alignment. However, the series presented in figure 5.4 shows significant variation in the resolution of different features. The selection of such features for the alignment presented here would be detrimental to the accuracy of the lateral position of the overall object. Therefore, the selection of a single feature which appears as the clearest or most visible across the series is a reasonable compromise to obtain the best possible alignment.

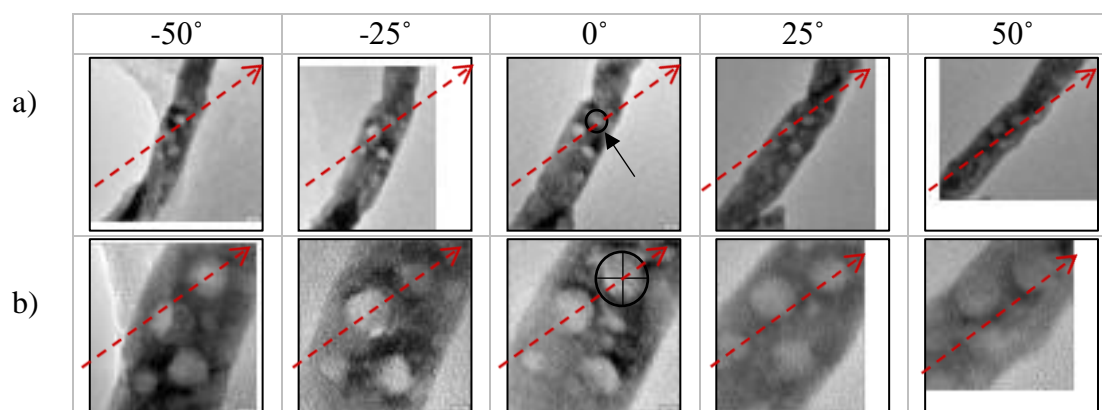


Figure 5.5 Selected views of (a) medium-magnification and (b) high-magnification aligned images showing the lateral displacement from the original frame of the images. Instrumental tilt-axis orientation calculated at 35.75° as indicated by the arrows. The reference point for alignment annotated on both 0° projections

The resolution of three-dimensional objects is influenced by a number of factors. Firstly, the lack of information between rotations. This is the reason early tomographic works in materials science used over 100 images per series[382]. Evidently, this does not solve the problems of artefacts caused by the missing wedge or the presence of Bragg-enhanced contrast in the images. A reduced number of images such as used in the present experimentation does make it more difficult to align the images with precision, as any form of automated or manual alignment is easier to perform when the images are more similar. An unsuccessful alignment would cause distortions such as ‘moon-shaped’ particles and other 3D-artefacts. The quality of any alignment process, manual or otherwise, can be assessed using a Z-projection like the one shown in Figure 5.8 which, as discussed below, exhibits a successful alignment result.

Since manual alignment is performed by visual approximation, it is necessary to consider the associated error when interpreting the resulting tomograms. It is only possible to align two images within one pixel relative to each other. Therefore, after consecutively aligning 25 images, the last image is offset from the first one by approximately $\sqrt{(25-1)}$ or 4.89 pixels. Since the size of a pixel varies according to the image sampling and the TEM magnification, the

absolute uncertainty will be different for each tomographic series. Table 5.1 summarises the uncertainty values for the four tomographic series reconstructed in the present work. Since all images are the same size when fed into the back-projection algorithms (256x256 px), the relative uncertainty remains constant at 1.92%.

Table 5.1 Absolute and relative uncertainties caused by manual alignment

Tomographic series	Sampling (nm/px)	Lateral size of each image	Absolute uncertainty	Relative uncertainty
Fig. 5.3	0.41	104.83 nm	±2.01 nm	±1.92%
Fig. 5.4	0.139	35.62 nm	±0.68 nm	±1.92%
Fig. 5.16	0.7	179.37 nm	±3.429 nm	±1.92%
Fig. 5.20	0.34	86.71 nm	±1.659 nm	±1.92%

The alignment of images at high magnification presents a more difficult challenge than those at low magnification. Notably, it is less likely to find a small feature appearing across the entire series since a feature of such size as would appear small at high magnification would most likely disappear from view into the structure of the rod. Hence, it was necessary to employ a different approach for the lateral alignment of the high magnification series. First, a rough alignment was performed using the same feature annotated in Figure 5.5. Then, a more delicate alignment was achieved by superposing a circle consistent with the widest diameter of the annotated pore in each view. This was necessary since the pores do not appear spherical at high magnifications, as was reported in Chapter 4. Figure 5.6 shows a selection of images from the aligned high-magnification tilt series. Consistently with the previous step, the image at 0° was used as the starting point for the manual alignment of images by pairs.

Following the lateral alignment of individual images, the image-stack was rotated to make the direction of the rotation angle parallel to the horizontal. This step simplifies the reconstruction algorithms by establishing a constant tilt axis angle of 0°. The rotation axis of the object can be found by repeatedly scrolling through the aligned tilt series and tracing the trajectory of each feature across the tilt series. This step also serves to corroborate the suitability of the alignment procedure, since a successful alignment will result in features travelling in a straight line upon rotation. That line is perpendicular to the rotation axis. Naturally, the feature used for manual alignment will rotate in its place without lateral displacement.

Although the angle of the tilt axis is determined by the goniometer, it may vary between experiments, regardless of using the same TEM instrumentation. A rotation of the specimen

may occur especially when working at different magnifications. Therefore, it is significant to perform both lateral and rotational alignment procedures for every tilt series. A historical record of successful tomographic reconstructions performed with the same equipment can be used as an initial guideline to approximate the orientation of the tilt axis but should then be verified and fine-tuned for every new tilt series. For the present experiment, each stack of aligned images was summed to generate a visual overlap of all images in each tilt series. By tracing features visible across the entire series, several parallel lines were drawn, normal to the rotation axis. The direction of the rotation axis was measured at 35.75° . All images were rotated clockwise by that measure. Then, for the reconstruction algorithm to work, the images had to be translated downwards by 46 out of 256 pixels to place the rotation axis at the centre of each frame. This transformation is distinguished from the first step of alignment as the location of each image relative to each other is maintained by displacing the images as a stack. Therefore, the objects are only moving with respect to their containing frames. The canvases containing each of the images were enlarged to avoid the loss of information during these transformations.

In order to take advantage of the information obtained from each of the tilt series at different magnifications, both series were integrated into one. This way, the resulting reconstruction would show the morphology of the rod from the images at medium magnification, as well as accurate information on the structure and morphology of the defects, as provided by the tilt series acquired at high magnification. This step required an empirical alignment of the two magnifications, by overlapping corresponding images at each tilt angle and expanding the mid-magnification image to match the dimensions of the features visible in the high-magnification counterpart. This process was repeated for the images with the best visibility, and a correlation close to 1:3 was found, which meant low magnification images needed to be expanded symmetrically in height and width by 303% in order to match the dimensions of the features in the high-magnification images. Initially, both series of images were of the same size. By integrating both series, a joint series is obtained, which has the structural information of the high magnification images, as well as the external geometry information from the low-magnification images. This method of combining information is only applicable here because of the implementation of segmented geometrical tomography.

Figure 5.6 shows a selection of images from each series before (a, b) and after integration 5.6(c). It can be appreciated that the limited amount of geometrical information provided by the high-magnification series (row b), is complemented by the overlap with the mid-magnification. Notably, the images in the row 5.5(a) were large enough that the final frame barely includes signs of the rotation and translation steps described above. Mainly, all the images in the row 5.5(a), as well as the rest of the mid-magnification series show a section of the rod finishing in parallel sides, which favours the appearance of the final reconstruction.

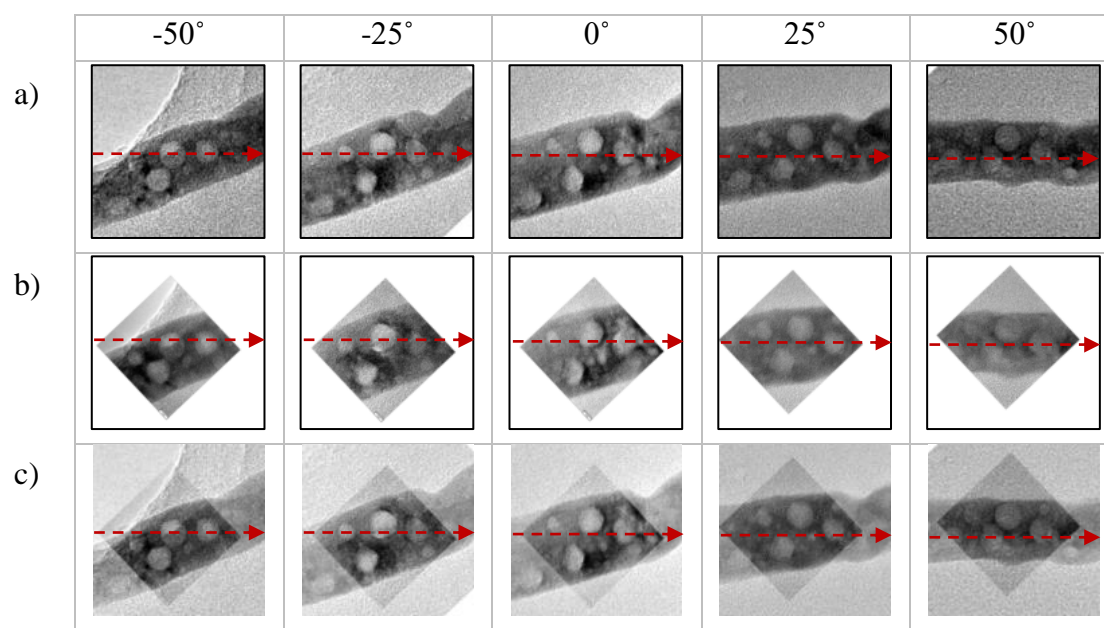


Figure 5.6 (a) Selected views of medium-magnification after enlargement. (b) High-magnification images showing the rotational and lateral displacement from the original frame. (c) Superposed images at medium and high magnifications to complement structural and morphological information. Instrumental tilt-axis orientation adjusted to 0° and centered, as represented by the arrows

5.1.2.2 Image pre-processing

Following the series of alignment steps shown in the section above, the images were used to produce simple delineations of each feature of interest. The result was a full-tilt series of each feature in isolation. Selected images of each series are shown in Figure 5.7. The requirements of geometric tomography algorithms justify this method. Firstly, by isolating the outline of the rod, its morphology can be reconstructed without difficulties, since it complies with the principle described above, that each object is equal to its own convex-hull.

As can be seen in Figure 5.7, each structural feature, or pore, was also isolated to generate individual tilt series. The main reason for this is to avoid the effect of overlap of pores. While overlapping pores can be differentiated in the original images, this becomes impossible once the images have been binarised for tomography. An essential parameter in this process was the size of the frames containing the isolated features, which needed to remain constant. This measure ensured that the isolated features would return to their original position when all the individual tilt series were integrated. Each single-feature series was generated by manually tracing the feature of interest in each image across the aligned tilt series. By preserving only the shape

and relative location of each feature, all the artefacts caused by diffraction and inelastic scattering of electrons in the carbon-film are eliminated.

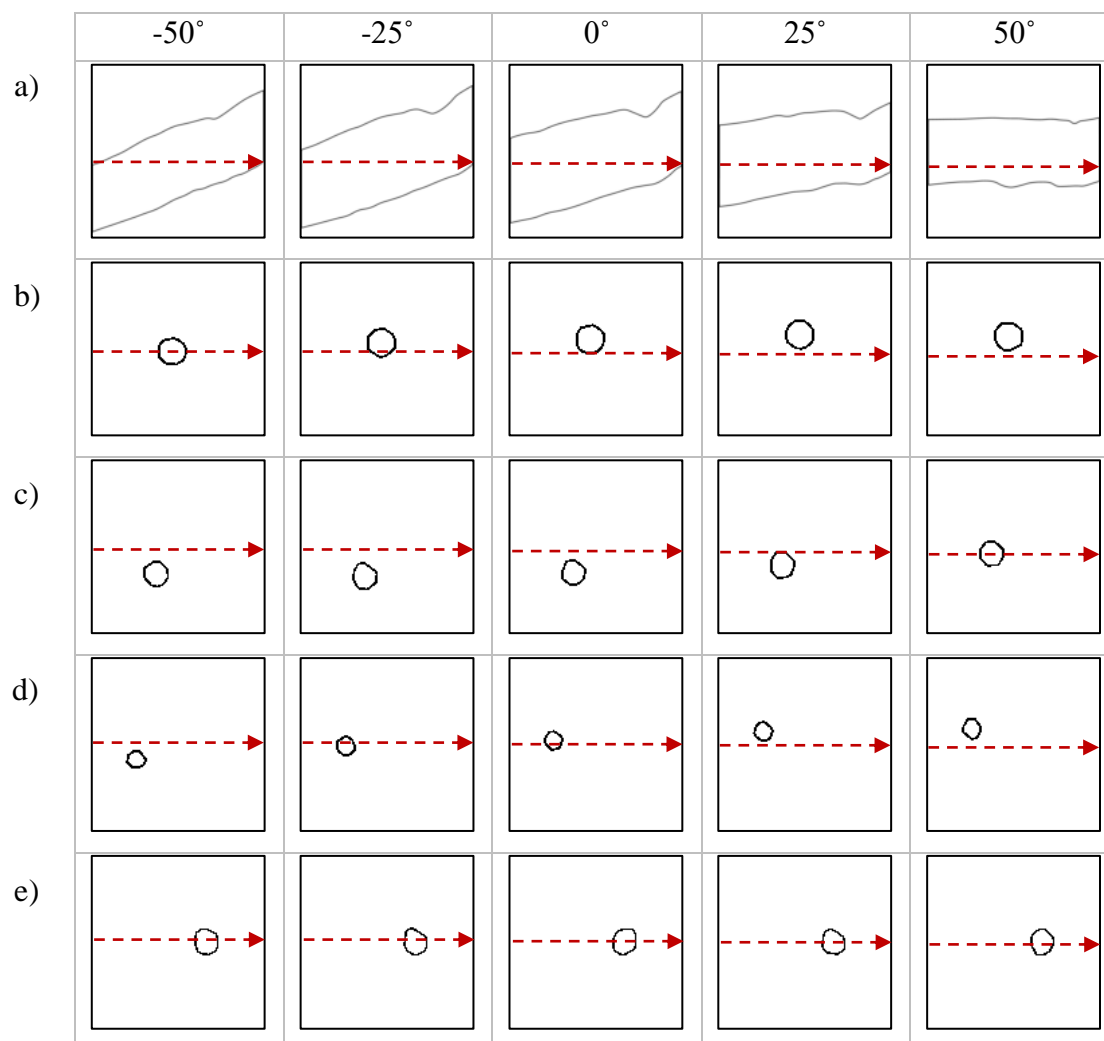


Figure 5.7 Selected images from single-feature tilt series showing the rod (a) and four defects identified as (b-e). Instrumental tilt-axis orientation adjusted to 0° and centered, as represented by the arrows

After segmenting the images into individual features, each series was suitable to be used in geometric tomography. A unique aspect of the method presented here is that it results in five individual tilt series, as shown in Figure 5.7, all of which share the same alignment and, therefore, the same location of the rotation axis. However, as a product of the segmentation, all single-feature series except for the one shown in Fig 5.6 (e) rotate around a feature which is hidden from view, since the feature delineated in 5.7(e) was the original point of reference for the alignment. Figure 5.8 illustrates this fact by stacking all the five tilt series into one image.

The rotation axis and the rotation centre have been annotated. This image also highlights the effect of lateral alignment with the features travelling in straight vertical lines across the series.

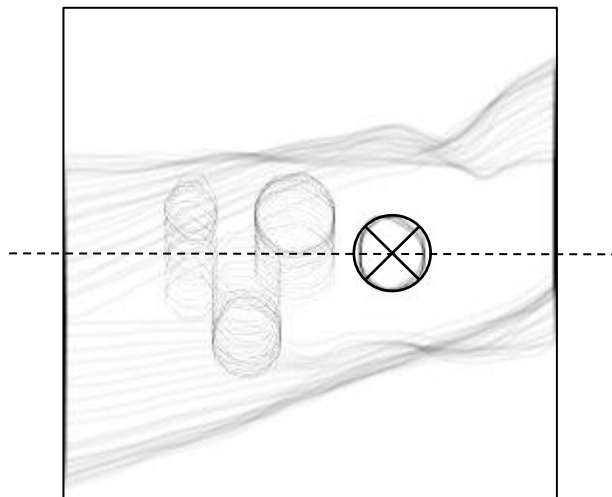


Figure 5.8 Z-projection of segmented features highlighting the location of the rotation axis and the alignment centre. The projection shows that the rod runs diagonal to x, y, z axes

The final step of pre-processing was to assign different grey values to the background and the feature. Since this experiment was performed using black and white 8-bit images, there exist a total of 256 grey values ranging from black=0 to white=255. Typically, a binarisation transform would apply values of either 0 or 255 to every pixel in the image. However, this causes an undesired effect of elongation as identified in early tomography attempts. A theoretical experiment is shown in figure 5.9 to illustrate this fact. Image 5.9(a) shows a theoretical cylinder reconstructed using black (0) and white (255) values. For comparison, image 5.9(b) is presented, which was reconstructed from a grey-on-black series consisting of the black background (0) and very dark grey feature (10).

When using conventional binary images (0 and 255), the grey values at most points become saturated upon reconstruction. For example, at the centre of the cylinder, the grey value would become 255×25 for 25 images. Since 255 is the maximum value of a pixel in 8-bit images, the region continues to appear white. However, outside of the body of the cylinder, it would be expected that the values suddenly would drop to zero, but image 5.9(a) shows a pair of distinct zig-zag features at the top and bottom of the cylinder. These can be explained by the same principle above, where several slices smaller than 25 presents a white region, which is multiplied by the number of slices and renders a value higher than 255 which is capped and shown as white. The result is the presence of white features in the final reconstruction, which does not correspond to solid volumes.

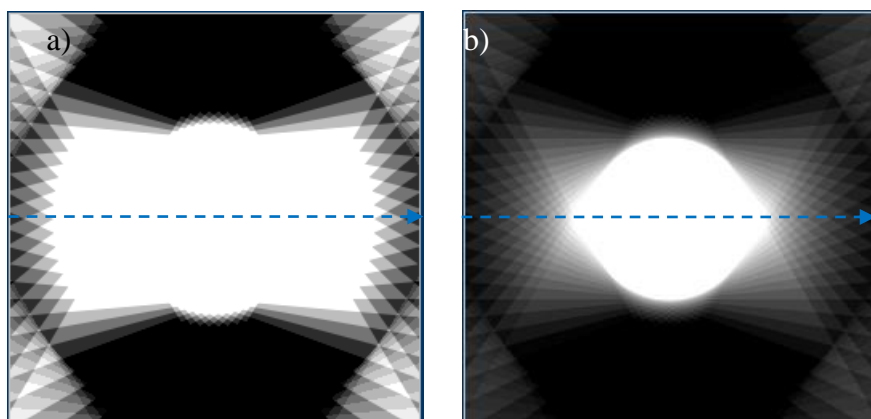


Figure 5.9 Cross-sectional views of reconstructed volumes of theoretical cylinders using (a) conventional binarisation (255/0) and (b) grey feature on a black background (10/0). Theoretical “Electron beam” direction is represented by the arrows

On the other hand, image 5.9(b) shows the successful minimisation of this undesired elongation. By assigning a value of 10 to the feature being reconstructed, the values in the final cross-section are significantly lower than in the case above. To draw on the same example, the centre of the cylinder will have a value of 10×25 for 25 images. This value remains constant across the cross-section of the cylinder where all 25 images present value of 10. However, the intensity drops rapidly at the ends of the diameter. The zig-zag feature mentioned above is still present, but it does not obstruct the interpretation of the volume and can be corrected by adjusting the threshold at the rendering stage. Another favourable product of the proposed method of binarisation is the reduction of the effect of the missing wedge, which will be reported on in the following sections.

In order to implement the elongation-correction method described above, each series of single-feature images was assigned the values of 0 for the background and 10 for the feature. A selection of images from each series is presented in Figure 5.10. It is noted that the images presented in the figure do not have the values used for reconstruction since a grey value of 10 is nearly indiscernible from black. Therefore, the grey value used in the figure has been chosen for illustrative purposes. The single-feature tilt series represented in Figure 5.6 are deemed suitable for reconstruction after the pre-processing steps.

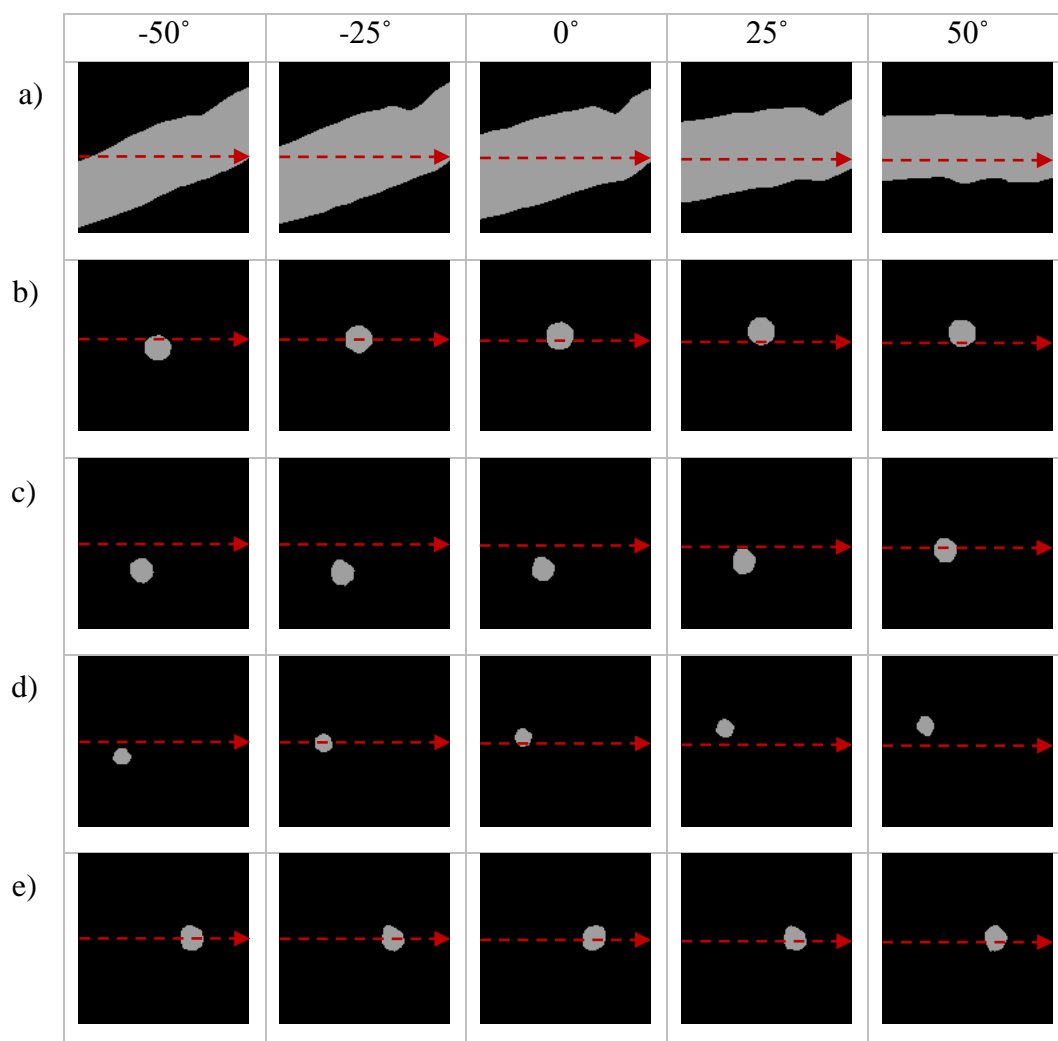


Figure 5.10 Selected binarised images from single-feature tilt series showing the rod (a) and four defects identified as (b-e). Instrumental tilt-axis orientation adjusted to 0°

Mainly, the HRTEM images have been successfully aligned, and the medium-magnification and high-magnification series have been segmented to make them suitable for a geometric tomography algorithm. There is a loss of information during the segmentation and binarisation of images, e.g., other defects besides (b-e), or contrast variations within the selected features. However, the main objectives of the present experiment were the reconstruction of a mesoporous rod showing the shape and distribution of heat-induced defects in three-dimensions. Consistently, shape, size and distribution were the only pieces of information left in the images at the end of the pre-processing stage.

5.1.3 Image processing

The selection of the reconstruction algorithm is usually based on the quality of the input images, the presence and type of imaging artefacts, and the information required from the tomogram. The computational demands that the available equipment can comply are also to be taken into consideration. As seen in the pre-processing steps, the present work sought to minimise the information fed into the algorithm in order to obtain simpler but clearer results than the traditional procedures would provide.

The simplicity of the binarised images used in geometric tomography allows using a back-projection operation to obtain the 3D object. Standard BP method consists of “smearing out” the 2D images into a 3D volume. Each TEM image, or projection, is put into the algorithm along with its direction (tilt-series angle). The result of the operation is a “back-projection body” for the particular direction of projection. Naturally, as more projections are added to the model, the 3D object generated becomes a closer approximation to the real object.

For tomography methods other than GT, back-projection operations need to be modified by Fourier weighting, which compensates unnecessary blurring and enhances the resolution of periodic features in the reconstructed object. However, the binarisation of the projections prior to the back-projection steps makes the weighing step unnecessary. Furthermore, weighting creates a tube-like effect in the reconstruction of rods. Geometric tomography is one of the few instances where the weighting filter can be neglected from the operations.

As described above, the input information of the tomography algorithm consisted of five series of 25 images; each image was 256×256 pixels in size. It was essential to maintain the ratio of the images constant across all single-feature series to avoid displacement of an object from its position relative to the others in the final 3D volume. The depth of a reconstruction is a variable parameter, which is written into the algorithm. For this experiment, the depth of each tomogram was set to 256 slices. Therefore the rod and each of the four selected defects was reconstructed as single 3D objects contained within a cube of 256×256×256 voxels. Most importantly, each reconstructed feature maintained its relative position in three-dimensions.

The back-projection operations were applied using open-access software TomoJ [374]. Each of the reconstructed stacks consisted of 256 slices. A selection consisting one out of every forty slices of each 3D stack is shown in figure 5.11. An initial observation of the back-projected results shows that each feature rendered a typical-looking tomogram. It should be noted that the blurring seen in the slices at the top and bottom of the series is symmetrical, although all objects except 5.7(e) were not placed along the rotation axis, as would be expected in a conventional back-projection operation.

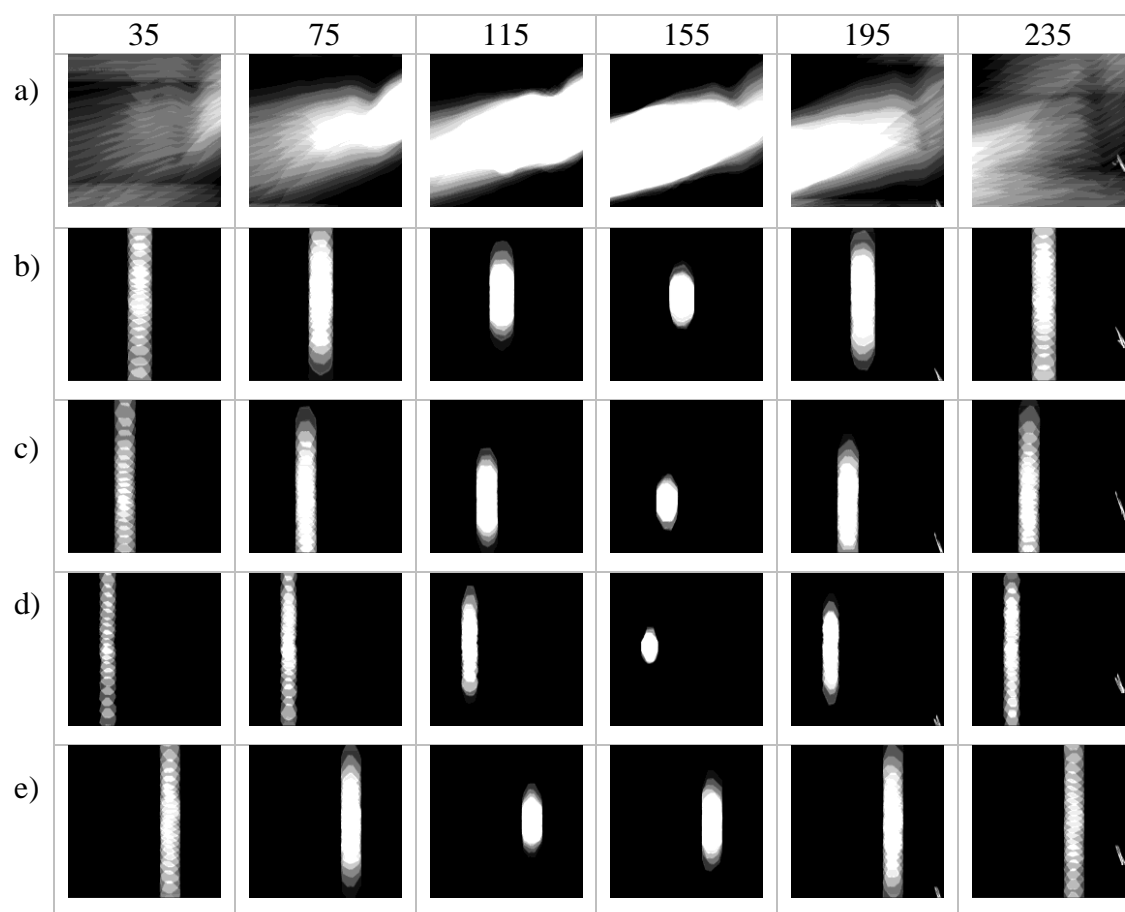


Figure 5.11 Selected slices from single-feature tomographic stack reconstructing the rod (a) and four defects identified as (b-e). The column headings correspond to the location of a slice within each 256-slices deep tomogram. Electron beam direction equal to viewing direction

The symmetry and straightness of the blurring feature across each tomogram also indicate a suitable alignment procedure, including the right placement of the rotation axis. When this condition is not met, the blurring usually presents a “banana” shape or other distortions. The numbers at the top of the figure indicate the depth out of 256 of each slice. It is noted that the cross-section of features (b-e), represented by the images with the lowest amount of blur, occurs between slice numbers 115 and 155. This feature is favourable as it indicates that all features have been reconstructed inside the body of the rod, which is reconstructed between slices 115 and 195. An unsuccessful attempt could have resulted in one or more of the features (b-e) being reconstructed outside the body of the rod, which would indicate that the relative position was not maintained throughout image processing.

Another relevant feature is that each of the defect series presented the cross-section at a different location within the body of the rod. This indicates that they were not artificially centred along the reconstructed 3D-space, which would have been another product of unsuccessful

segmentation. Finally, the lateral location of the features is easily associated with its location in the projections in figure 5.10. This is especially important for a feature such as 5.11(c), which occurs outside the alignment centre and rotation axis shown in figure 5.8. The reconstruction was deemed adequate considering the quality of the stacks generated and could be used to render a 3-dimensional object using visualisation software.

5.1.4 3D visualisation

The tomographic results have been visualised using open-access software, Chimera, which was employed to render surfaces corresponding to the bodies in the single-feature tomograms. High-value thresholds were applied to the 3D objects in order to minimise the artefacts generated by the back-projection operations, such as spurious intensities or ghost images which produce undesired elongation. The first step of visualisation consisted of assessing the reconstruction of individual features, which are shown in Figure 5.12. The nomenclature applied to each surface is maintained from previous steps. Row 5.12(a) shows the surface obtained by back-projection of the rod morphology. The 3D rod segment has a width of 45 nm and a length of 140 nm. These measurements are consistent with the dimensions observed in the projections shown in Figure 5.6. Row 5.12(a) contains two images captured along the length of the rod in the (y,z) direction.

These images emphasise the cross-sectional morphology of the ceria nanorod. The sharp corners and straight edges are consistent with a non-sintered structure, as estimated in Chapter 4. More importantly, these results coincide with the pseudo-hexahedral cross-sectional morphology of ceria nanorods reconstructed by Florea et al. [4] and calculated by Sayle et al. [215]. Therefore, the results presented here indicate that the cross-sectional morphology of ceria nanorods remains unchanged after heat treatment at 800 °C. The 10 nm scale bar can be used to verify the lateral dimensions of the rod, which is 35 nm wide by 45 nm tall with defined facets along the (110) and (100) planes, which can be extracted from Figure 5.1. The distance between the diagonal faces is 40 nm.

The three-dimensional visualisation of the reconstructed nanorod presents the usual artefact of the missing wedge. This feature will be elucidated using theoretical model reconstructions in further sections. At this stage, the missing wedge can be identified as an elongation of the reconstructed object in the direction of the electron beam, which is represented across Fig 5.6 as the z-axis. The primary consideration should be that this feature is an artefact of the back-projection, and it is in no way associated with the actual morphology of the projected object. Therefore, the estimations of terminal structures should be based on those edges and corners, which do not occur along the z-axis. Rows 5.12(b-e) shows the reconstruction of a single pore in isolation.

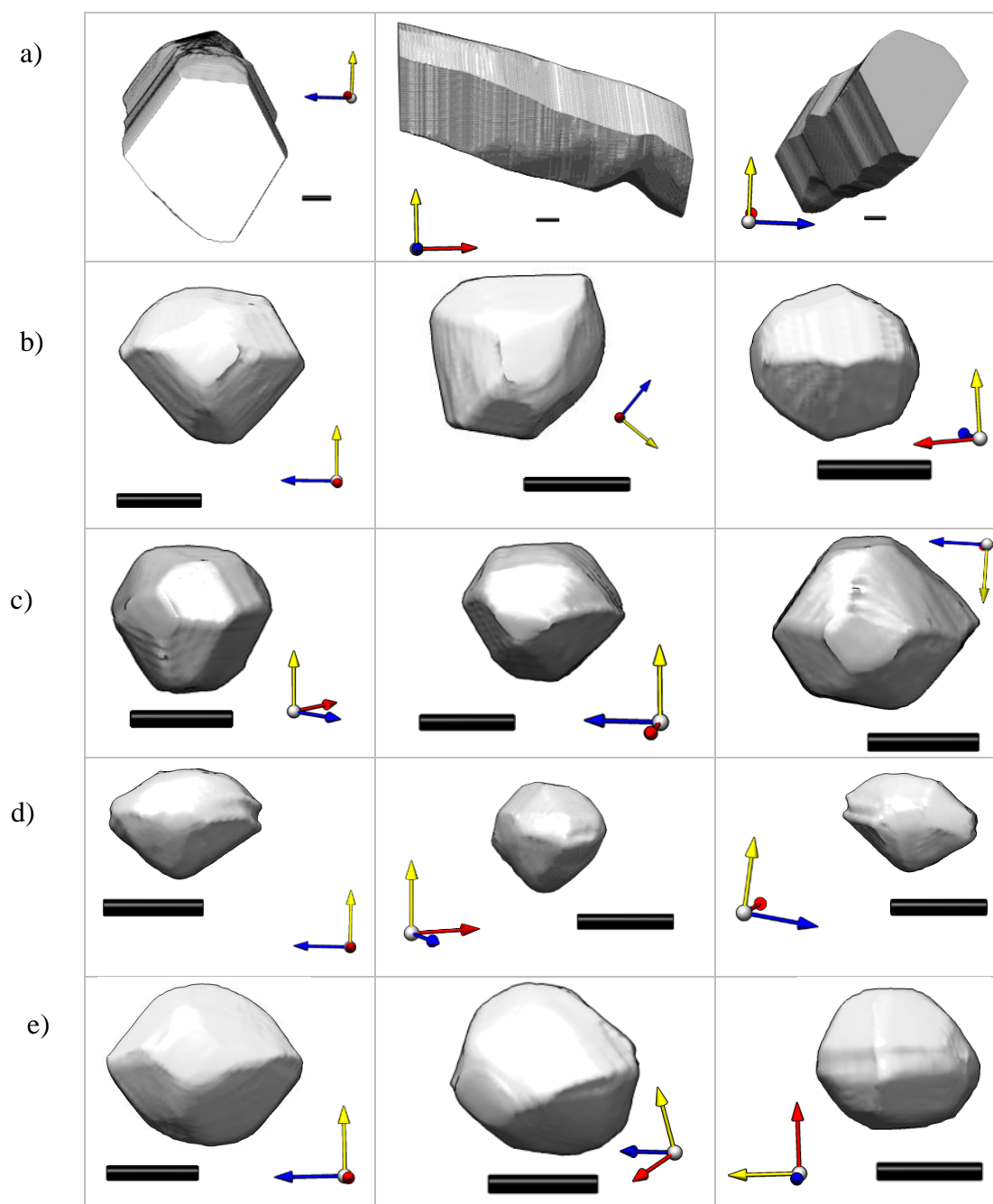


Figure 5.12 Selected views of 3D-visualisations of single-feature tomograms showing the shape of the rod (a) and the defects (b-e). All scale bars = 10 nm. Axes colour code x (red), y (yellow), z (blue). Electron beam direction indicated by blue axis

The geometry is symmetrical and is composed of smooth surfaces. The flat surfaces at the top and bottom of the pore, as well as at the front and back are shaped like squares and connect

forming the sides of eight irregular hexahedra. Similarly to row 5.12(a), each volume in rows 5.12(b-e) presents a missing wedge artefact, which appears as a cone of missing information along the z-axis. This causes the defects to appear elongated and distorted along their horizontal plane. These results indicate that the thermally induced defects are three-dimensional bodies and that their shape corresponds to a truncated octahedron. This type of defect has been recognised by Zhu et al. [125] and Han et al. [126] as ‘negative nanoparticles’, as the cuboctahedral morphology is established as the most common 3D shape of ceria nanoparticles.

Unsurprisingly, the smallest feature in Figure 5.12, shown in row 5.12(d), also presents the most pronounced reconstruction artefacts along the z-axis. This effect is associated with the fact that the feature only represented a small fragment of information within the 256×256 images in Figure 5.10 (d). A way to resolve this would be to reconstruct it on its own while disregarding its position relative to the rod. This would result in a better reconstruction of the morphology feature, but compromise the information on its distribution. Nevertheless, it is noted that the defects were reconstructed successfully regardless of their position relative to the rotation axis, defect 5.12 (e), which is situated on the rotation axis, presents a three-dimensional shape consistent with defects 5.12 (b-d). This is indicative that the novel process of segmentation is a suitable modification of geometric tomography for the reconstruction of individual features.

The next stage in visualisation entailed the integration of all the defect reconstructions into a single 3D object. This operation was only possible because the location and size of each defect were maintained throughout the process. Therefore, the bounding box of all series is the same size, and the defects appear in their real location as obtained from the projections. The visualisation of the integrated tomograms is shown in Figure 5.13. The defects have been colour-coded for identification.

The different views in the figure highlight the consistency in shape and orientation of the pores, which present flat surfaces at the top and bottom. There are essential characteristics to be considered at this stage. Mainly, the position of the defects relative to each other has been successfully maintained throughout the process of reconstruction. Furthermore, the implementation of a segmentation step has successfully avoided the distortions associated with the overlap of projected objects. Ostensibly, each feature has been reconstructed as an individual volume, as seen in image 5.13(c). The orientation of the defects does not appear to be random, but they all seem to align their shorter and longer sides in parallel, which can be resolved in the regions unaffected by the missing wedge (x-axis). In the case of ceria nanoparticles of the same morphology, the shorter and longer sides of the cuboctahedron would correspond to the (100) and (111) planes respectively. Analogously, the ‘negative nanoparticles’ present a marked alignment in three dimensions, where the (100) terminal facets align along the same axes for

all the individual particles. The same is true for the corresponding (111) terminal facets. These facet identifications do not correspond to the planes present in the sample but are based on the crystallography of a ceria nanoparticle, which shared the same morphology as the defects presented here, as identified by Du et al. [271].

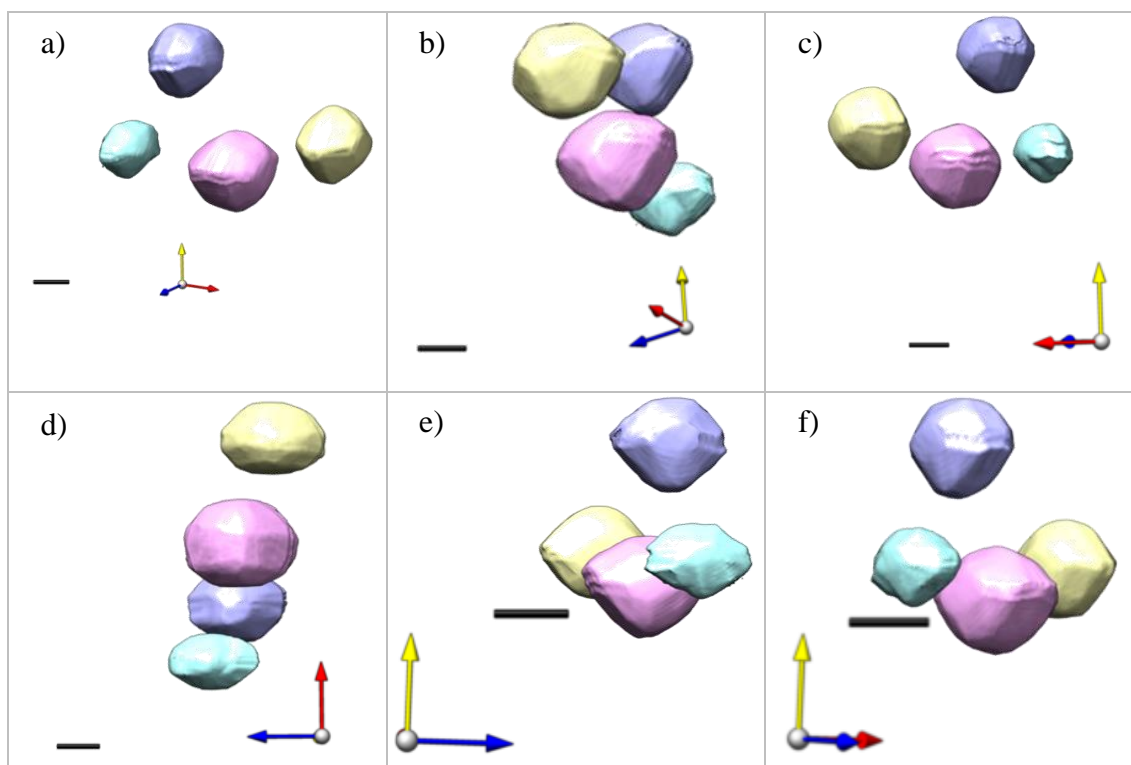


Figure 5.13 Selected views of 3D-visualisations of integrated tomograms showing the shape and relative position of defects (b-e). All scale bars = 10 nm. Defect colour code, as per previous figures: Purple = (b), pink = (c), blue = (d), yellow = (e). Axes colour code x (red), y (yellow), z (blue) Electron beam direction indicated by blue axis

Another essential characteristic that can be appreciated in Figure 5.13 is the lack of lateral distortion in the defects reconstructed outside of the rotation axis. As shown in figure 5.8, the rotation axis is located at a position central to defect 5.13(e), which makes the feature identified as 5.13(b) the most distant from the rotation axis, which can be appreciated in the view in Fig. 5.13(a). However, the volume reconstructed shows the same negative-particle morphology as the defects reconstructed along the rotation axis or closer to it. This result is indicative that the step of segmentation subsequent to the lateral alignment is appropriate for multi-object projections.

The volumes shown in Figure 5.14 correspond to the visualisation of all five individual series integrated into the same 3D object. The surface of the wall is presented as a mesh instead

of a continuous surface to facilitate the interpretation. Image 5.14(a) shows a view of the rod along the z-direction. That is, this view corresponds to the projection at 0° as seen in Figure 5.1. The dimensions, shapes and locations of the defects are recognisably the same, with no visible distortions. Upon rotation, the three-dimensional qualities of the rod become more apparent. Image 5.13(b) helps to make discernible the lateral elongation associated with the missing wedge. As expected, this feature runs parallel to the x-axis, which is close but not parallel to the body of the rod. However, it is still possible to distinguish the main facets associated with the pseudohexagonal cross-section of the rod. By complementing this three-dimensional morphology with the crystallographic identification showcased in Figure 5.2, the surfaces of the rod can be associated with the (110) and (100) planes, with a lateral distance of 45 nm between (110) faces and 40 nm between (100) faces. The pseudohexagonal cross-section of the rod is particularly emphasised in images 5.13(c) and (d), which show similar but not identical cross-sections. It should be noted that the missing wedge artefact is located at different positions respective to the top and bottom of the cross-section. This is due to the missing wedge always being perpendicular to the rotation axis, which is not strictly parallel to the growth of the rod. This effect is an experimental constraint in the tomography of predominantly one-dimensional materials like nanorods, as elaborated at the beginning of this chapter. When this artefact is considered, the cross-section of the rod can be considered continuous.

The results shown in Figure 5.14 elucidate the main question that the present study set out to answer regarding the distribution of the defects. The reconstructed volume reliably indicates that the defects appear exclusively within the body of the rod. This means that the defects can be accurately named cavities. As discussed at the beginning of this chapter, there have been conflicting propositions in the literature regarding the distribution and morphology of these heat-induced defects. The present study indicates that the defects are indeed three-dimensional cavities, as suggested by Sakthivel et al. [3], and sketched in Fig. 2.16(d).

In addition to highlighting the distribution of the pores in the system, the visualisations in Figure 5.14 showcase an ordered orientation of the pores with respect to the walls of the rod. This phenomenon is particularly visible in images 5.13(e) and (f), which show that the shorter sides at the top and bottom of the pores are parallel to the shorter (110)-sides of the rod. The remaining two square faces, which in the visualisations are nearly parallel to the y-axis, are oriented as regular planes to the growth direction of the rod. Consistently, the broader faces of the pores form planes which run parallel to the longer (100)-sides of the rod. These orientations suggest that the crystal structure of the rod dictates the growth of the pores.

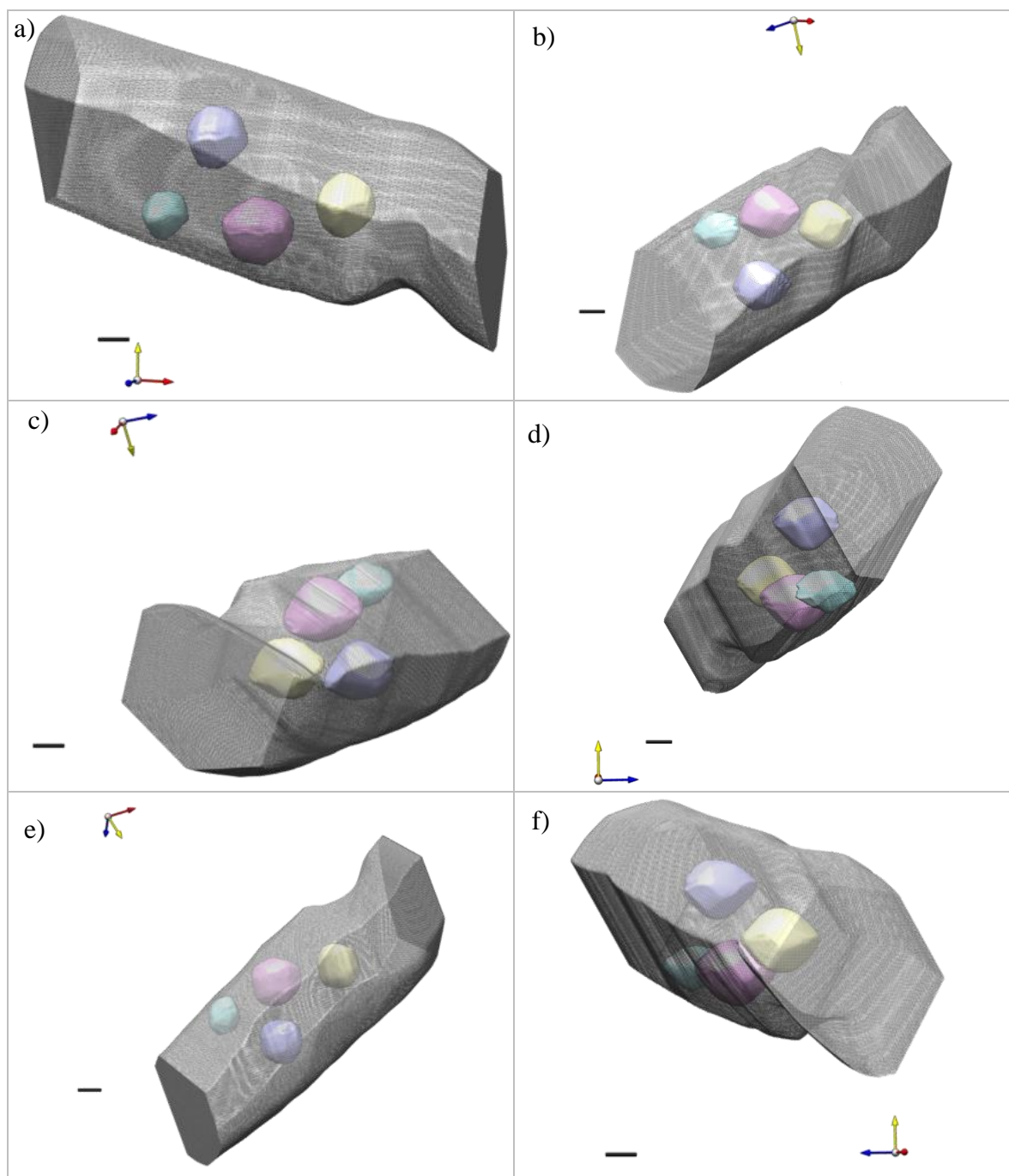


Figure 5.14 Selected views of 3D-visualisations of integrated tomograms showing the structure in three dimensions of a mesoporous ceria nanorod. All scale bars = 10 nm. Axes colour code x (red), y (yellow), z (blue). Electron beam direction indicated by blue axis

As established in Chapter 4, the crystallinity of the rods is significantly consolidated during heat treatment. Therefore, the high quality of the single-crystal structure is associated with the formation of negative-nanoparticle defects, which present facets defined by the crystal planes

in the rod. This behaviour supports the propositions presented in section 4.2.1.1 regarding the formation of negative-nanorod defects and their estimated transformation into nanotubes upon further heat treatment. Namely, since the crystal structure ostensibly dictates the growth of internal defects, the negative rods can be expected to continue growing along the body of the rod until a nanotube is formed. Were this not the case, the defects could grow in directions which exited the rod and connected with a lateral surface.

The results in figure 5.14 indicate that geometric tomography, hitherto only applied to solid bodies, can be used for the reconstruction of porous materials by introducing the steps of segmentation and pre-processing presented in this report. The distribution of the pores as exclusively interior features raises questions as to the mechanisms dictating the enhanced catalytic performance reported in the literature [13]. It is suggested that the walls separating the cavities from the surface of the rod can diffuse oxygen into the cavities, consistently with the established mechanisms of oxygen storage capacity [51].

The accessibility of internal defects in the pores via a diffusion wall would increase the concentration of reaction sites in two significant ways. Firstly, the absence of material inside the cavities creates internal concave walls, which increase the surface-area-to-volume ratio of the overall system. In the particular case of the porous rod used for this study, the surface area was measured to increase by 37% when compared to an identical but non-porous rod. Secondly, the faceted geometry of negative-nanoparticle pores results in a large concentration of corners and edges throughout the structure, which are reported to hold large concentrations of Ce³⁺ ions, as well as crystallographic defects which enhance the reactivity of the material [14].

Mainly, the results in this section have contributed the knowledge that heat-treated ceria nanorods develop internal pores of defined negative-nanoparticle geometries. The orientation of the pores is defined by the exposed crystal planes which define the geometry of the rod.

5.2 Supplementary tomographic studies

This section presents the results of three tomographic experiments, which complement the work presented in the previous section. A first experiment aids the interpretation of the visualisation results by creating models which emulate the effects of experimental conditions on known geometries. Then, the tomographic study of a non-heat-treated rod is presented, to observe any further differences from the annealed nanorods used throughout this work. Finally, the new method of geometric tomography is used to generate two-dimensional cross-sections from one-dimensional information of a porous system.

5.2.1 Theoretical missing-wedge reconstructions

Theoretical models were constructed which emulated the experimental conditions of the projections obtained in the tilt series acquisition described in 5.1.1.1. The geometries selected were a cylinder, to compare to the rod, and a sphere, which can be compared to the pores. 2D images were created and put into the back-projection algorithm with the same parameters as the experimental data. Namely, each series consisted of 25 identical 256×256 pixels 8-bit images, which represented the projected sphere and cylinder. The images were assigned a tilt angle corresponding to the series acquired experimentally, as shown in figures 5.3 and 5.4. Accordingly, there was a difference of 5° between images, and each series spanned over 120°, thus leaving 60° of missing information.

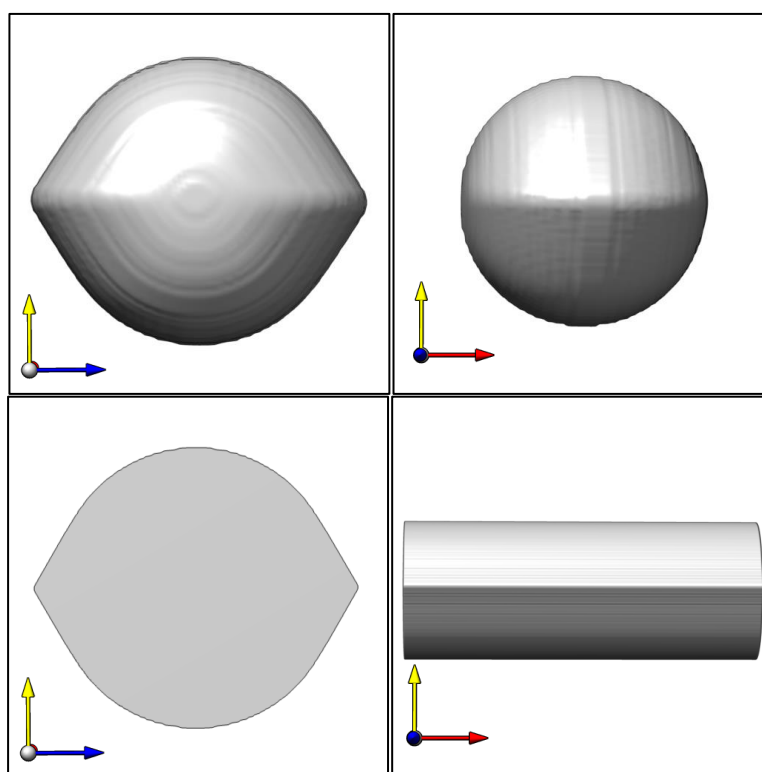


Figure 5.15 Visualisations of back-projected reconstructions of a perfect sphere (top) and cylinder (bottom) showing the effect of the missing wedge. Axes colour code x (red), y (yellow), z (blue). Theoretical “electron beam” direction indicated by blue axis

The reconstructions of a perfect cylinder and sphere shown in the figure serve to distinguish the effect of the missing wedge from the morphology of reconstructed samples. In particular, the top and bottom of the reconstruction present the expected circular cross-section, while the area of missing information appears elongated and distorted. The circularity of the sphere and

the cylinder in the areas outside of the missing wedge support the interpretation of the volumes shown in Figure 5.14. The experimental results show marked facets and angular corners, which are absent from the model and are therefore not a product of the back-projection. The results are shown in Figure 5.15.

As expected, the regions of missing information result in a ‘missing wedge’ artefact. Figure 5.15(c) emphasises the facet-like appearance of the artefact, which underlines the importance of correct interpretation of results. Mainly, the missing wedge is restricted to the two 60° symmetrical regions of missing information. Therefore, any features observed in those regions should not be attributed to the geometry of the object. For clarity, the missing wedge region has been annotated in two dimensions in Fig. 5.21(b). However, when facets or crystal deformations appear outside the limits of these missing-information regions, they can be safely attributed to the object being reconstructed. In the particular case of rods and voids, as objects of interest of the present study, only those facets appearing along the direction of the z-axis, as indicated in Fig. 5.13 are to be dismissed as by-products of the missing wedge. Facets appearing outside of this region, such as the distinctive flat faces containing the objects across the y-axis, can be safely assumed to be the real facets corresponding to the cuboctahedral morphology of the voids. Furthermore, such features have been confirmed by comparison to the 2D appearance of the void in Figure 5.2 (a). In general terms, all real-object features in the reconstruction should be visible in at least some of the input projections, and their location and dimensions should match those of the reconstructed object in the same projection.

On the other hand, the appearance of the missing wedge in both the sphere and cylinder, confirms that the elongations observed in the reconstructions of the rod and pores are not associated with their morphology, but a common effect of the back-projection algorithm. The elongations appear to develop in the same measure for both geometries. For the sphere, the distortion is also visible in front view. This distinction is also applicable when comparing the effect of the missing wedge on the visualisation of the rod and the pores, as shown in Figure 5.12, with a thin edge traversing the horizontal of the reconstructed pores. For the objects of this study, it can be said that any feature of elongation which appears along the horizontal and is not replicated at 90° for the top and bottom of the rod or pores, is associated with the missing wedge and does not represent the geometry of the object.

5.2.2 Tomography of a non-porous rod

A second assessment that aids the interpretation of results in section 5.1 is the comparison of the mesoporous nanorod reconstructed via modified geometric tomography with the results of a more conventional weighted-back-projected non-porous rod. The sample used for this test belongs to the same batch of nanorods fabricated via optimised hydrothermal synthesis, as

outlined at the beginning of this chapter and published by collaborators. The electron microscopy characterisation was carried out using a JEOL 3010 microscope equipped with a Fischione tomography sample holder. In other words, the experimental conditions of the tomographic characterisation of the sample of non-porous rods were in general terms the same as those used for the tilt-series acquisition of the mesoporous nanorod.

A selection of results of the image acquisition is presented in row 5.16(a) of Figure 5.16. Mainly, the images show a cluster of rods aggregated in parallel. The sample was selected, applying the same criteria described in section 5.1.1. Briefly, the object was representative of the overall sample; the object was isolated in the directions perpendicular to the rotation axis of the goniometer; and, the position of the rod was parallel or nearly parallel to the rotation axis. The tilt series were acquired using the same parameters as in section 5.1, resulting in a series of 25 images acquired between every 5° rotation, with the whole tilt series spanning 120°.

Manual image alignment was performed following the same steps as described in section 5.1.2. The feature selected for alignment was the visible corner at the end of the nanorod, which remained visible throughout the entire series. A selection of images showing the result of the alignment step is presented in row (b) of Figure 5.16. Images have also been rotated and translated in order to align the experimental rotation axis with the horizontal of the frame. A final preparatory step prior reconstruction consisted of cropping an area covering only the object of interest and inverting the grey values of the image. The inversion step was performed in order to create a direct correlation between thickness and intensity. The pre-processed tilt series ready for tomography operation is shown in row (c) of Figure 5.16. The images were not binarised but consisted of values of intensity between 0 and 255 with a positive correlation between thickness and intensity.

In a conventional tomographic computation, the series of pre-processed images were loaded onto open-access tomography software TomoJ [374] and applied a weighted-back-projection algorithm. The Fourier-weighted algorithm was selected based on the input images not being binary. Therefore, the procedure of reconstruction can be described as the more conventional quantitative tomography (CT), as opposed to geometric tomography. This distinction was proposed by Saghi et al. [365], who presented a continuous transition from GT to CT by using saturated or semi-binarised projections. A selection of representative slices of the tomographic stack is presented in Figure 5.17.

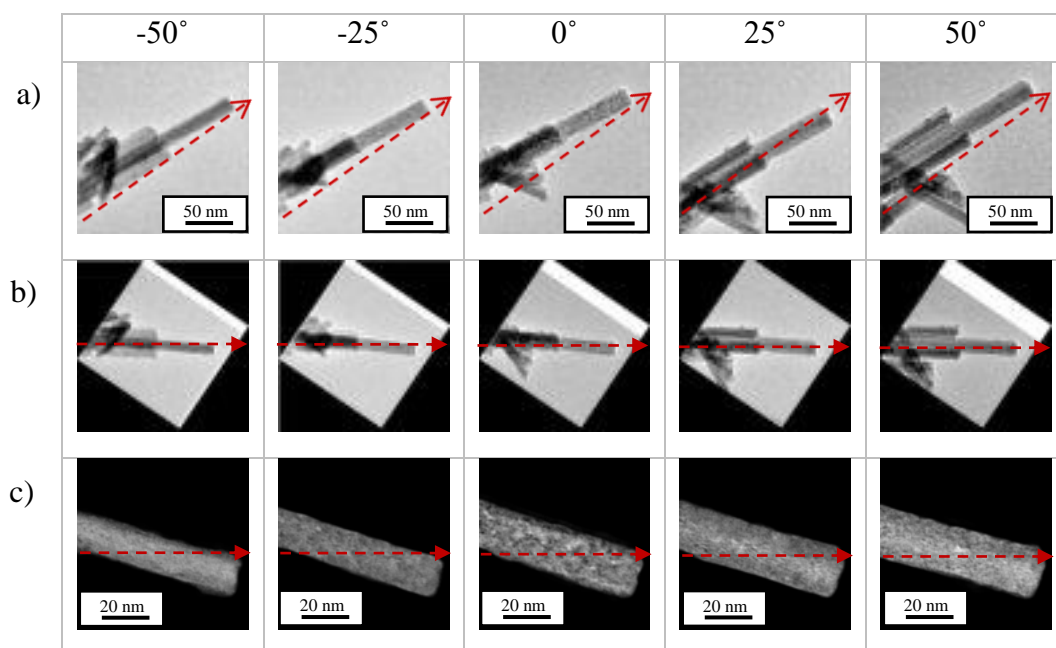


Figure 5.16 Selected images from the tilt series of a non-porous rod highlighting the main steps preceding image processing: (a) Image acquisition (Images obtained at nominal magnification 100kX and the plane of the detector camera located at negative plate level, sampling = 0.7 nm/px), (b) image alignment, (c) area selection and grey-value inversion. (a) Instrumental tilt-axis orientation calculated to 35.75° as represented by the arrows, and (b,c) corrected to 0° and centered as represented by the arrows. Note: In (a), the arrows represent the direction of the tilt axis, but not its lateral location, as the latter is unknown prior to alignment.

A similar evaluation can be performed as for the series reconstructed in section 5.1.3. Specifically, the blurring effect at both ends of the stack appears to travel symmetrically in perpendicular directions to the rotation axis. The thickest section of the rod appears between slice numbers 115 and 155, and the thickness reduces at both ends of the cross-section represented by ebbing away of the intensity in the slices around 75 and 195. Given the resolution of the original images shown in Figure 5.16 (a), the scale of the images can be defined as 4.5 pixels/nm. The depth of the reconstructed volume was set to 256 slices to match the lateral size of the original images of 256×256 pixels. Therefore, the scale of the final reconstructed cube can be defined as 0.22 nm/slice. By this scale, the rod can be said to have an average height of 28 nm and a width of 38 nm, which result in an aspect ratio of the cross-section equal to 1.35. This value is very close to the ratio of 1.28 calculated for the porous rod, which was, on average 45 nm tall by 35 nm wide.

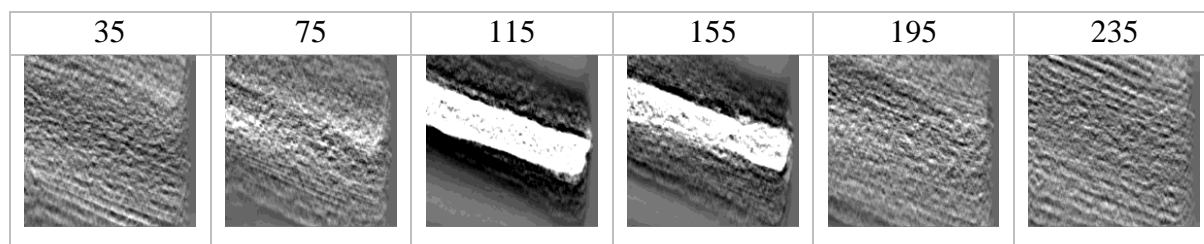


Figure 5.17 Selected slices from the weighted-back-projection stack of a non-porous rod.
Electron beam direction equal to viewing direction

Following the weighted-back-projection operation, the stack was visualised using open-access 3D visualisation software Chimera [375]. A high threshold was applied to the cube in order to suppress artefacts that generated distortion that was a by-product of the reconstruction algorithm and not associated with the morphology of the particle. These distortions include, but are not limited to, the missing wedge artefact. The radial artefacts associated with every back-projection calculation are only prevalent at low-thresholds and are therefore easy to eliminate. The missing wedge is minimised only to the 60° limit associated with the missing information in the projection acquisition. A selection of representative views is presented in Figure 5.18. These results can be compared with the visualisations of the reconstructed porous rod in Figure 5.14.

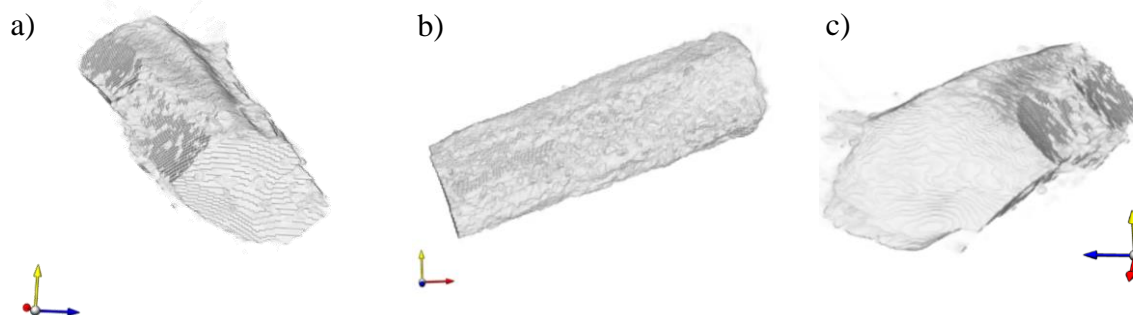


Figure 5.18 Selected views of a reconstructed non-porous rod.
Electron beam direction indicated by blue axis

The cross-sectional views in images 5.18(a) and (c) are particularly relevant for this study, as they support previous statements regarding the prevalence of the geometry of the rod upon heat treatment at 800 °C. Furthermore, the similarities between the 3D visualisation of the weighted-back-projection of a non-porous rod and the porous rod characterised via the novel methods proposed in this work reflect favourably on the assessment of the technique. By obtaining results, which are consistent with the more established techniques across the literature

on electron tomography, the method of geometric tomography after segmentation can be deemed an appropriate alternative for overcoming the challenges associated with the three-dimensional TEM characterisation of porous materials.

5.2.3 Further modifications of geometric tomography from one-dimensional information

A significant advantage of the geometric tomography algorithms is the possibility of reconstructing three-dimensional objects from a more limited amount of information than would be required for other forms of electron tomography. In the case presented in section 5.1, each three-dimensional object was reconstructed using a set of binarised two-dimensional projections. In the same way, tomography allows for two-dimensional images to be reconstructed from projected one-dimensional information. This section briefly explores the application of the modified geometric tomography algorithm to obtain cross-sectional views of porous materials from one-dimensional binary information.

In other words, the present study seeks to achieve reconstructions using the minimum amount of information possible. A number of applications motivated the development of such reduced-information algorithms. Namely, for a system such as the porous nanorods, the cross-sectional structure can be deemed the most crucial information. Normally, this information is extracted from a reconstructed volume generated using tomography. In this way, all forms of tomography are commutative between back-projection and slice selection. The method proposed here involves the pre-selection of 2D slices, each corresponding to a 1D section crossing the object in each projection. Therefore, this study incorporates a new methodology to produce significant information on the three-dimensional structure of a porous rod consuming minimum time and memory.

A tilt series of a porous rod was acquired following the same procedure as the experiments above. The object selected for tomography is shown in Figure 5.19. The rod complied with the requirements outlined for selection of a tomographic object, with no surrounding objects that could cause geometric constraints and an orientation close to that of the rotation axis. Three cross-sections of interest were identified and annotated as (i-iii) in the figure. The sections contain solid material and pores. To generate representative results, the three sections selected present with different relevant characteristics: (i) contains a wide pore close to the centre of the rod, (ii) contains a pore off-centre, and (iii) contains two pores, which overlap upon rotation.

Similar to other heat-treated rods, the enhanced crystallinity produced strong diffraction-related artefacts, which are visible in Figure 5.19. The rod has an average lateral size of 25 nm and presents pore sizes ranging from 2 to 7 nm. This rod appears to have a higher concentration of defects than the one characterised in section 5.1, although they belong to the same sample.

This difference in structure could be due to the rod in this experiment containing smaller defects. The initial observations of the rod before tilting suggest that the pores do not reach the walls of the nanorod and that they present faceted geometries. Therefore, the characteristics of this rod coincide with the materials of interest across this work. The selected object was characterised using a JEOL 3010 High-resolution transmission electron microscope, and a Fischione tomography holder was used to allow for the high-angle rotations necessary for tilt-series acquisition.

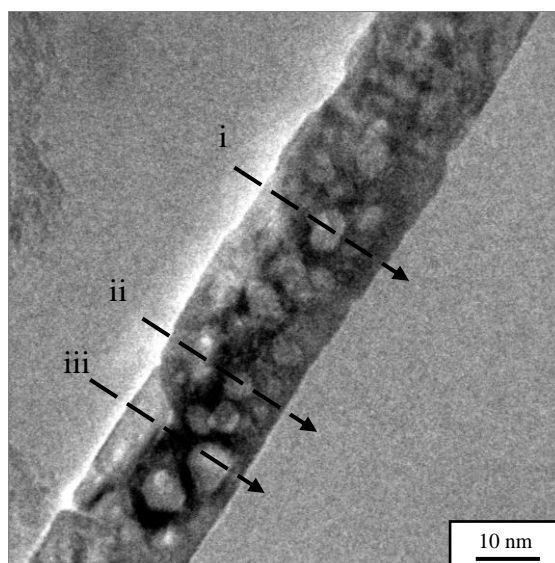


Figure 5.19 object selected for tomography with annotated cross-sections of interest.

Lines (i-iii) correspond to profiles (i-iii) elsewhere in this section.

(Images were acquired using JEOL 2010F TEM at 200 kV,
samplings: (a)=0.02 nm/pixel)

The tilt series was acquired by capturing 25 images between 5° rotations, producing a series of transmission images spanning 120° rotation. A selection of images from the tilt series is shown in Figure 5.20 (a). Following the acquisition, the images were manually aligned using the pore identified in section (i) as the reference feature for alignment. Images were then rotated and translated to situate the rotation axis along the horizontal of the images. Successful alignment of the tilt series resulted in each of the features of interest identified in Figure 5.19 moving in a straight direction that was perpendicular to the rotation axis.

5.2.3.1 Application of GT for cross-sectional reconstructions

A line was drawn along each the selected sections to extract the relevant information of each of the features. The lines consisted of binary information assigning a value of 0 to the pore and background, and a value of 1 to the solid rod. A selection of aligned images with the one-dimensional identifications marked is shown in Figure 5.20 (b). Row 5.20 (c) in the figure shows the extracted information from each of the images. The lines were one pixel wide by 256 pixels long but have been magnified for illustration.

Changes in the white and black segments of each line across images reflect the changes in the projected position and size of the features of interest. These lines cannot be used for electron tomography, as a region of the rod between a pore and the background would produce a concave body upon rotation. Therefore, the lines were segmented similarly to the images in section 5.1. Cross-sections (i) and (ii) were separated into two series each, consisting of rod and pore information. Line (iii) crosses a region with two pores and was therefore segmented into three series, one containing information on the rod and one for each pore.

Each of the three sets containing single-feature lines was inserted into the back-projection algorithm to construct a volume, using the same parameters specified in section 5.1.3. Then, the resulting volumes were visualised, adjusted for threshold and integrated as shown in 5.1.4. The resulting cross-sections are shown in Figure 5.21(a). The reconstructed cross-sections show in white the outer morphology of the rod, which coincides with previous tomography publications [4], as well as the other studies in the present work. This consists of a symmetrical 6-sided polyhedron with prominent straight sides cut by shorter lines. These intersections are credited to host most catalytically active sites [1].

The tomography results also show the pores as symmetrical with defined facets consistent with {100}-truncated {111}-octahedra. The geometry appears to align with the edges of the rod, coinciding in their shorter [100] sides and their more prominent [111] facets. As for the location of the pores, the reconstructions show them to be fully enclosed by the rod. They seem to appear at random lateral locations within its volume. However, they do seem to stay within the central 3/5 of the rod diameter, as previously suggested [3]. This could indicate the existence of a semipermeable diffusion wall, which could contribute to the high catalytic activity associated with these materials.

The images in Figure 5.21(a) show that the distribution of the pores is maintained after image processing. The cross-section identified as (i) shows the pore at the centre coinciding with the projected distribution seen in Figure 5.19 and across the tilt series. However, if the distribution of the pore was lost, it could appear at the centre of the image after processing. For this reason, the pore in (ii) was intentionally selected to be located off the middle axis of the

rod. The reconstructed cross-section shows the pore in a location consistent with the projections. Furthermore, the slice annotated as (iii) was selected to contain two pores of different size, both offset from the central axis of the rod. The successful reconstruction would preserve these three characteristics, as seen in Figure 5.21(a).

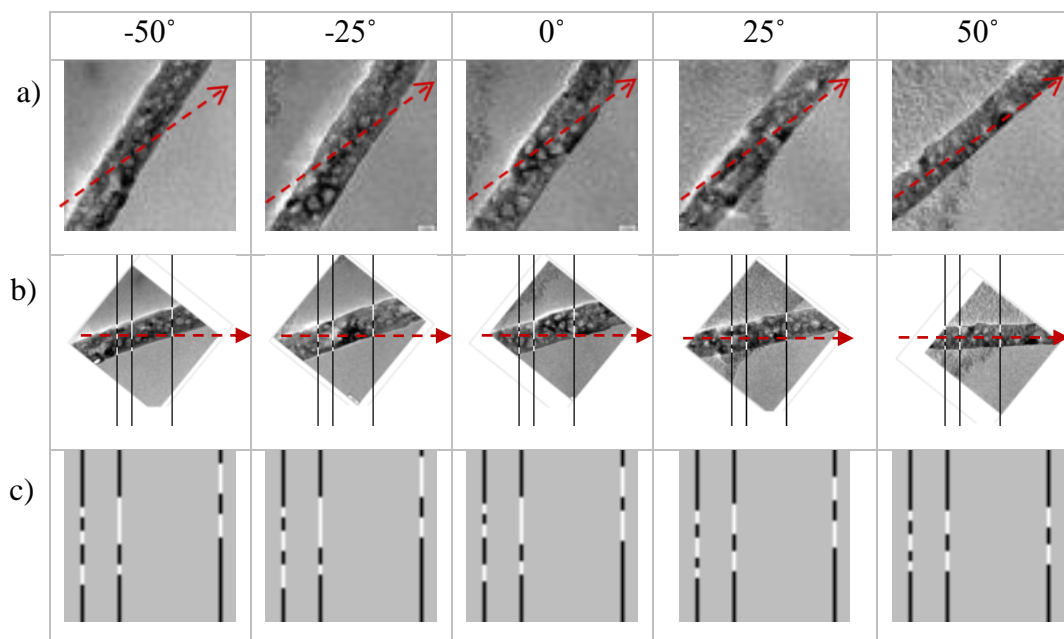


Figure 5.20 Conversion of tilt-series images into sets of 1D information showcasing: (a) images acquired at indicated tilt angles (Instrumental tilt-axis orientation calculated to 35.75° , as represented by the arrows). Images were obtained at nominal magnification 200kX and the plane of the detector camera located at negative plate level, (b) aligned images with the superposition of binary line (Instrumental tilt-axis orientation adjusted to 0° and centered, as represented by the arrows), and (c) magnified 1D-information before segmentation (Scalebar in Fig. 5.19) Note: In (a), the arrows represent the direction of the tilt axis, but not its lateral location, as the latter is unknown prior to alignment.

The original series had to be segmented into three single-feature series, in order to comply with the convexity requirement of geometric tomography. If this requirement were not met, the resulting cross-section would show two small cylinders reconstructed from the walls at the top and bottom of the reconstructed surface, in the location between the edge of each pore and the edge of the rod. The results of this experiment indicate that geometric tomography can be used for the reconstruction of porous cross-sections by using segmented one-dimensional binary information. Using binary information allows the selection of the features of interest and avoid artefacts in the final reconstructions, while still gaining reliable information on the internal geometry of the nanomaterial.

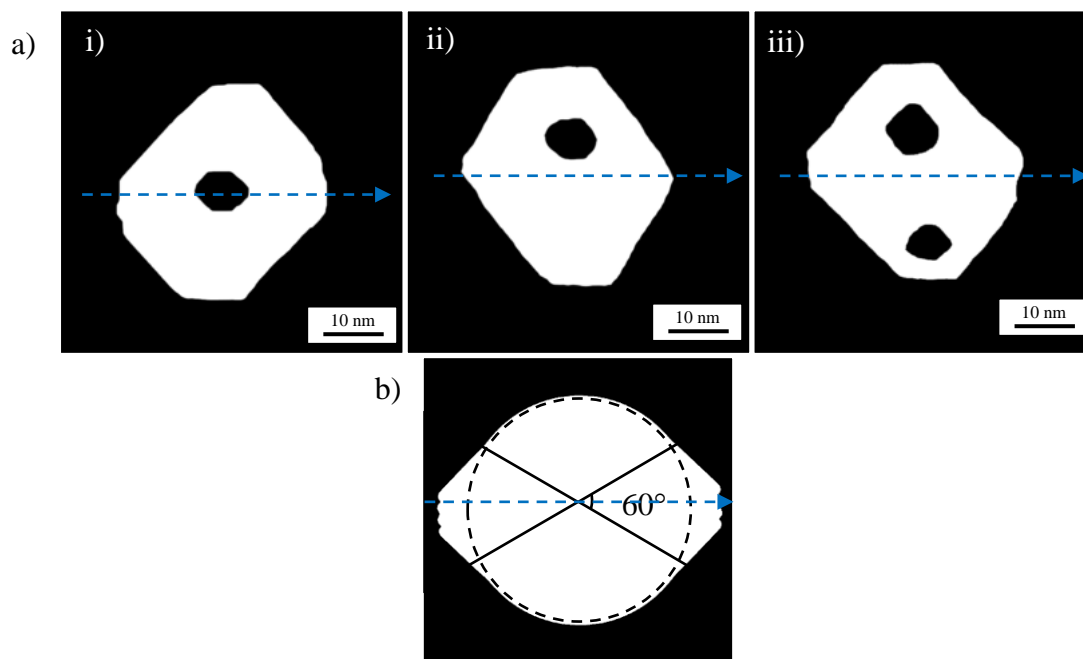


Figure 5.21 (a) Slices of a porous nanorod reconstructed using geometric tomography of a segmented one-dimensional tilt series. (b) Cross-section of a theoretical cylinder reconstructed to show the effect of the missing wedge.

Electron beam direction is represented by the arrows

In the same way as the reconstructed volumes in section 5.1, the back-projection in this experiment produced a missing-wedge artefact, which is not associated with the morphology of the rod or the pores. In order to distinguish the effect of the missing wedge from the morphology of the sample, theoretical reconstruction of a perfect cylinder is presented in Figure 5.21(b), which simulates the same imaging conditions as the experimental results, i.e., 25 images taken between 5° rotations. The model shows that the top and bottom of the reconstruction present the expected circular cross-section, while the area of missing information appears elongated and distorted. Therefore, the facets at the top and of the rod and pores can be attributed to their geometry and are not a by-product of the back-projection operation, since the missing-wedge artefact does not affect features on that plane. This has been reiterated by the theory demonstrations shown in section 5.2.1.

5.2.3.2 Shape-from-contour cross-sectional reconstructions

Throughout this study, the capabilities of geometric tomography have been explored to produce higher dimensionality results from data-reduced input information. To investigate this

concept further, Saghi et al. [9] also contrasted the binary reconstructions with a modified algorithm which reduces the information even further; the modified method was labelled shape-from-contour algorithm. Here it is reported the application of this method to the reconstruction of the tilt series above (Fig. 5.20). The results are shown in Figure 5.22, where the cross-sectional views of the back-projection have been generated for each feature. This is the first account of the shape-from-contour method being used to reconstruct a porous material.

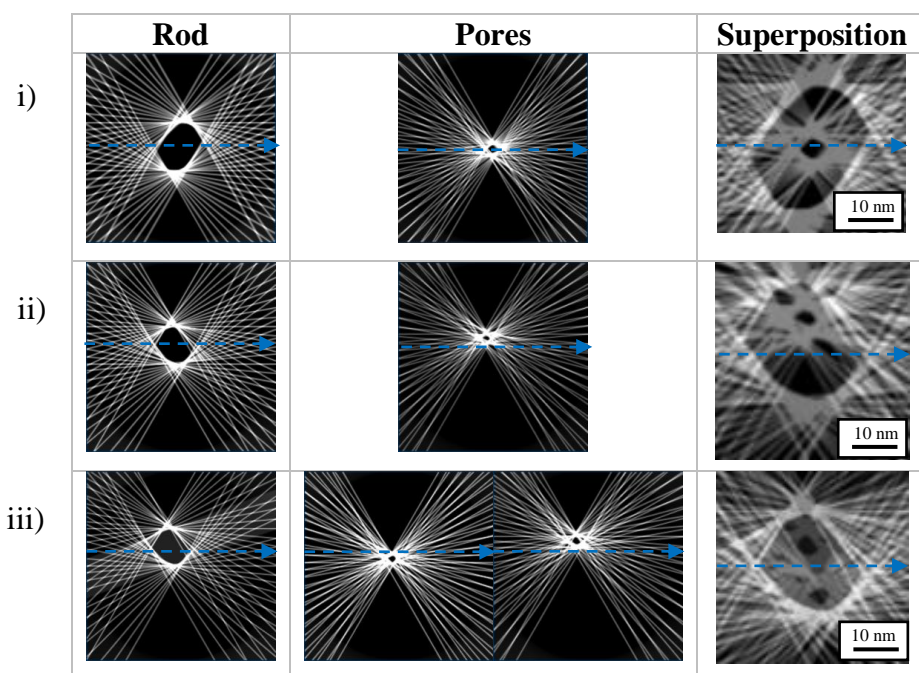


Figure 5.22 Shape-from-contour reconstructions of cross-sections of a porous rod
Electron beam direction is represented by the arrows in each reconstruction

For this method, instead of binarising the projections like in previous experiments, only the edge of each object of interest was retained. In other words, the one-dimensional tilt series are shown in Figure 5.20(c) was transformed from binary information to two isolated pixels for every feature of interest, marking the points of transition between the background and the rod and the rod and the pores. The back-projection operation successfully reproduced the cross-sections of interest hitherto identified as 5.19(i-iii). This is verified by comparing the results shown in figures 5.21 and 5.22. Also, the yz-views of the shape-from-contour slices in Figure 5.22 are illustrative of the back-projection operation. Each line with two pixels produced two parallel lines in the direction of the tilt-angle of their respective projection. The sum of all 50 lines corresponding to the 25 projections resulted in the construction of the feature in two dimensions. The regions corresponding to the missing wedge can be seen at either side of each

reconstruction. The lack of information at those tilt angles results in the rest of the lines extending until they encounter a line forming the opposite edge. The result is the familiar elongated distortion associated with the missing-wedge artefact. Regardless of the reduced-data used in the algorithm, the superposed images provide enough information to characterise the mesoporous rod, identify its morphology and the geometry of the pores.

Chapter Six

Formation of Functional Composites and Porous Materials via Nanocasting

The present work elucidates the behaviour of a selected variety of porous catalytic materials in a template-infiltration process. The general process of nanocasting and its major steps of infiltration, conversion and removal have been described in detail in section 2.1.4.1 of the literature review, which features a description of the state-of-the-art found across the literature. In cases where the template is removed, the end product is an inverse structure that is highly porous and has an accurate deliberate morphology. It is also essential for the inverse structure to have a controlled composition with no traces of unwanted template material or other substances involved in the fabrication. The present work comprises an exploration into the fabrication of porous composites based on three different templates: synthetic opals and two forms of mesoporous silica: MSU-F and SBA-15. The latest advances in fabrication, application and characterisation of these materials are expanded in sections 2.1.2-4 of the literature review.

The choice of the three templates for the present study has been motivated by the aim to cover a range of dimensionalities and pore sizes, as well as having both periodical and chaotic pore structures. Opals are expected to form a highly periodical uninterrupted network of spheres of 100 nm or larger. SBA-15 is also periodically ordered but contains small pores <15 nm separated by thin walls. MSU-F porous silicates have pores as small as 2 nm and up to 30 nm, with a narrow size distribution centred around 20 nm. Their distribution is chaotic, but they are expected to show connectivity. After a successful characterisation of the template materials, different methods of infiltration are tested for each template, in order to explore the compatibility of these techniques.

Nanocasting entails several methods of infiltration which seek to infiltrate the pores in the template with an active material. Different results can be expected from this process at the nanoscale, which would influence the performance of the composites in catalysis. A first scenario would entail the complete filling of the pores, with no empty space left and the infiltrating material forming a continuous solid across the porous structure. Another possibility would be for the infiltrating material to be deposited only around the edges of the pores, resulting in a product that is still porous, but the pores are smaller than those of the template, owing to the catalytic coating. Finally, the infiltration could result in the formation of small particles which

fill up the pores and leave spaces depending on their arrangement. These assembling possibilities have been summarised by Vradman et al. in Figure 6.1 [10]. The materials chosen for the infiltrations have been selected based on their relevance for catalytic applications, as reported in section 2.2. A detailed characterisation of the composite products can reveal the intricate interactions between the template and the catalytic material and elucidate the products of nanocasting employing three prominent templates. By elucidating the structure of nanocasting products, the present work provides a significant contribution to the field of porous nanomaterials.




Image available in library copy

Figure 6.1 Sketch of main types of infiltration products, as reviewed by Vradman et al. [10], showing: (I) assembled nanoparticles smaller than the pore diameter; (II) nanoparticles of similar diameter to the pores; (III) layer of infiltrating material; (IV) nanoparticles inside and on the surface of the pores

The present study uses a variety of techniques across electron microscopy to reveal the porous structures of these materials in unprecedented detail. Furthermore, by characterising the composites resulting from different infiltration conditions, this work brings to light the interactions of the template with the filling materials during the different stages of fabrication. A major objective of this study is to achieve an understanding of the pore structure and the template/replication process that is currently not found in the literature. The results shown in this chapter, contribute to understanding the formation of catalytic composites and other porous materials made by nanocasting, as described in section 2.1.4.1.

6.1 Study of opals and inverse-opal formation

Opal substrates were prepared by three different methods: colloidal vertical deposition, centrifugation and gravitational sedimentation. The colloidal crystals were characterised to compare the efficiency of each preparation method. Following the characterisation, the most ade-

quate method was selected to produce further samples. Furthermore, the colloidal crystals resulting from the self-assembly were used in the fabrication of catalytic composites prior to template removal steps to achieve a catalytic negative-opal structure. The first stage of investigations consisted of exploring the formation of colloidal crystals via self-assembly procedures seeking to define the boundary conditions of the self-assembly. As a result, the optimal conditions for the formation of colloidal crystals were defined. These results were used as a starting point to explore the suitability of different source materials for opal fabrication.

6.1.1 Self-assembly of colloidal crystals from PS beads

A comparison of different methods found across the literature was carried out to achieve polystyrene opals and to characterise them using visible-light microscopy and scanning electron microscopy. The preparation procedures are detailed below and summarised in Table 6.1. Finally, the characterisation of the opal samples is presented and examined in order to establish the most suitable method for preparing the intended structure.

6.1.1.1 Colloidal Vertical Deposition

All vials and glass slides were washed by rinsing with deionised water three times and one time with ethanol prior to use. 1 mL of ready-made colloidal solution of polystyrene spheres (Agar Scientific 400nm, 1.6088×10^{13} n/g) was poured into the 3 mL vials and labelled according to Table 1. 1.5 mL of ethanol were added to each vial. The solutions were ultrasonicated for 0.5 h to ensure dispersion of the particles in the suspension. Glass slides were inserted vertically or diagonally according to Table 6.1. The required size for the glass slides to be at 60° was worked out by measuring the internal diameter of the vial and dividing it by $\cos(60^\circ)$. The vials were left uncovered, and the liquid was allowed to evaporate at the temperatures indicated. Evaporations at 30 and 50 °C were carried out in a laboratory furnace to achieve better control than on a hot plate. Drying times were recorded and are presented in Table 1. Once the substrates were dry, they were removed from the vials and analysed using an optical microscope to find the areas where the crystals were deposited. The glass substrates were cut into adequate sizes and mounted on SEM specimen holders using conducting carbon adhesive tape.

6.1.1.2 Centrifugation

The ready-made colloidal solution of polystyrene spheres (Agar Scientific 400nm, 1.6088×10^{13} n/g) was poured into a 1.5 mL centrifuge tube with no further liquid added, and then subjected to 6000 rpm for 4 hours using a Spectrafuge Mini Centrifuge. Most of the liquid

in the tube was removed using a pipet while being careful not to touch the crystals visible at the bottom of the tube. The remaining liquid was allowed to dry at room temperature overnight. Once dried, the resulting product was scraped from the bottom of the tube and placed on an SEM specimen holder previously coated with conductive carbon adhesive tape. The sample was identified as P1-CENT.

6.1.1.3 Sedimentation

A 3 mL glass vial was washed by rinsing with deionised water three times and one time with ethanol prior to use. A volume of 1.5 mL of ready-made colloidal solution of polystyrene spheres (Agar Scientific 400nm, 1.6088×10^{13} n/g) was added to the vial, which was labelled P1-SED and allowed to dry at room temperature. The dry product was scraped from the bottom of the vial and placed on an SEM specimen holder previously coated with conductive carbon adhesive tape.

Table 6.1 Opal samples key

Name	Substrate position	Dispersant added	Drying temperature	Drying time
P1-CoVD-19 (V)	90°	Ethanol (1:1)	19 °C	1 week
P1-CoVD-30 (V)	90°	Ethanol (1:1)	30 °C	4 days
P1-CoVD-50 (V)	90°	Ethanol (1:1)	50 °C	2 days
P1-CoVD-19 (T)	60°	Ethanol (1:1)	19 °C	1 week
P1-CoVD-50 (T)	60°	Ethanol (1:1)	50 °C	2 days
P1-CENT	NA	Water	19 °C	4 hours
P1-SED	NA	Water	19 °C	1 week

6.1.2 Characterisation of polystyrene opals

The materials prepared were characterised using visible-light and scanning electron microscopy. Mainly, the materials were assessed based on the periodicity of the spheres. A perfect opal would be expected to present a continuous multilayer structure with a hexagonal close-packed (hcp) arrangement. Because all the opals were grown using the same source materials, the comparison between the results at this stage serves to select the most suitable method for the fabrication of opals. This comparison informed the choice of methodology for the preparations of opals utilised in subsequent experimental procedures as reported throughout this subchapter.

6.1.2.1 Visible-light microscopy (VLM)

The first stage of characterisation seeks to establish whether the materials have been deposited onto the glass substrate at all. To evaluate this fact, the opal samples on glass substrates were placed under a visible-light microscope. Because the beads used for the fabrication of the opals were 400 nm in diameter, they are not visible in VLM. Nevertheless, this step of characterisation can provide initial information on the sample at the macroscale. All visible light microscopy included in this section was performed in reflection geometry.

Figure 6.2 shows a pair of images of samples P1-CoVD-19(V) and P1-CoVD-19(T) captured under the visible-light microscope. The optical properties of opals allow distinguishing the thickness of a region based on the colour observed in the images. This is due to the optical properties of opal, which interacts with light based on the spacing between the spheres. Nevertheless, a second approximation can be made between the colour and the thickness. Therefore, based on such correlation to the wavelength values, the thinner regions appeared red or brown, and the colours approached blue and white as the thickness of the sample increased, the glass in the background appeared cream/yellow under low-light conditions.

Image 6.2(a) shows a significant amount of material deposited onto the glass substrate. Furthermore, a large proportion of the material exhibit colourations indicating significant thickness. Overall, there is no order that is immediately apparent at this magnification. Image 6.2(b) shows a much larger agglomerate than 6.2(a), which is much thicker than 6.2(a) across a wider area, based on the colouration. The results observed at the macroscale using visible-light microscopy are an early indication that the deposition of spheres in colloidal vertical deposition at room temperature is affected by the position of the substrate, with an inclined substrate producing a thicker material.

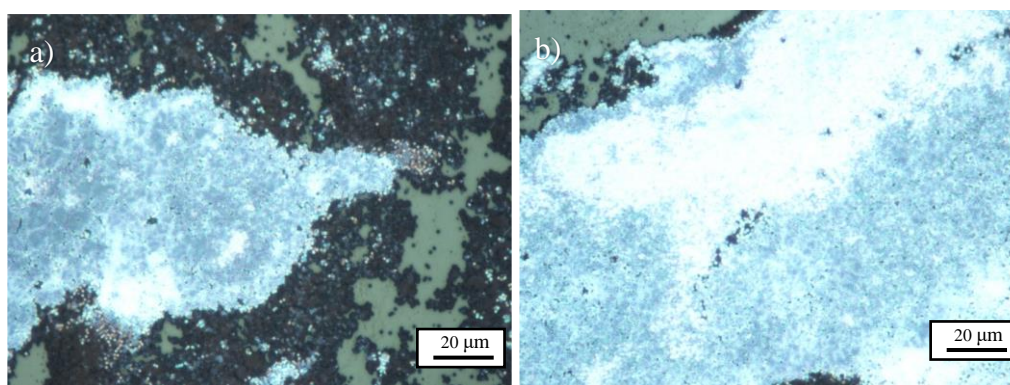


Figure 6.2 Visible-light microscopy images of samples (a) P1-CoVD-19(V) and (b) P1-CoVD-19(T) (Images acquired using Nikon Reflected Light Microscope Mag=500x)

The products obtained by crystallising above room temperature were dried significantly faster than those left to dry at room temperature, as shown in Table 6.1. The products are shown in Figure 6.3. The product obtained at 30 °C shows a wider spread of material with mostly thin regions, seen in red, and some regions of greater thickness, seen in white. An interesting difference is found between images 6.3(a) and (b). Both being the product or CoVD onto vertical substrates and the only variable being the drying temperature. The product obtained at 50 °C also shows mostly regions in red and a smaller proportion of white/blue than 6.3(a). However, the deposited material appears confined to a specific region, which has a distinctive elongated shape characteristic of the evaporation step. This characteristic is also present in the third image of the figure, which also corresponds to a sample crystallised at 50 °C, but onto an inclined substrate. Notably, the material deposited onto the inclined substrate at 50 °C exhibits significant white and blue regions indicative of thicker growth. This a significant finding for the methodology of colloidal vertical deposition. By comparing the images in figure 6.3, it is suggested that the use of an inclined substrate is more significant to the growth of a thicker material than the temperature at which the crystallisation occurs.

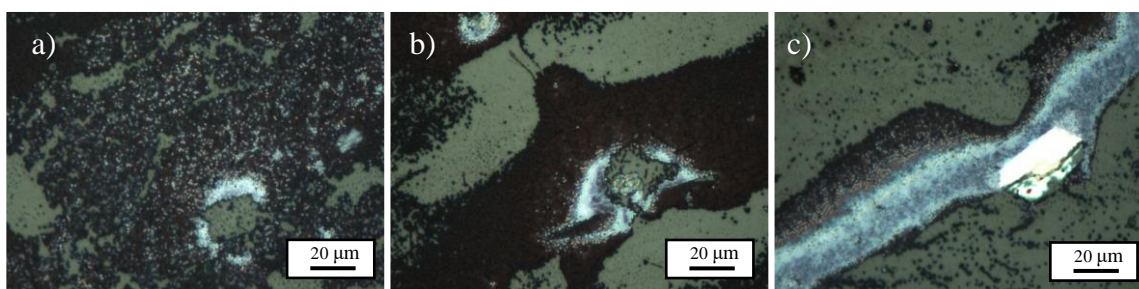


Figure 6.3 Visible-light microscopy images of samples
 (a) P1-CoVD-30(V), (b) P1-CoVD-50(V) and (c) P1-CoVD-50(T).
 (Images acquired using Nikon Reflected Light Microscope Mag=500x)

Furthermore, the effect of temperature can be traced across figures 6.2 and 6.3, suggesting that the area of the deposited material is increased by the slower low-temperature deposition but appears to have little effect on the thickness. On the other hand, the use of an inclined substrate produces a thicker material in spite of drying at a higher temperature. The images obtained by VLM; however, do not provide information regarding the quality of the crystals at the nanoscale, i.e., the ordering of the spheres.

The images shown in Figure 6.4 correspond to the materials obtained via gravitational sedimentation. This method would be expected to produce thicker materials. However, the results of visible-light microscopy observations suggest that most of the deposited material formed

thin layers similar in thickness to those obtained from vertical deposition using vertical substrates. Nevertheless, the deposits formed from sedimentation are larger in area and appear to show fewer patches of the uncovered substrate. The main features observable in the sedimented products is the occurrence of nearly circular regions of thicker material. The higher magnification in image 6.4(b) highlights the contrast between the thinner and thicker regions of the material. Particularly, the thicker region appears to vary in thickness following a concentric circular pattern formed during room temperature drying.

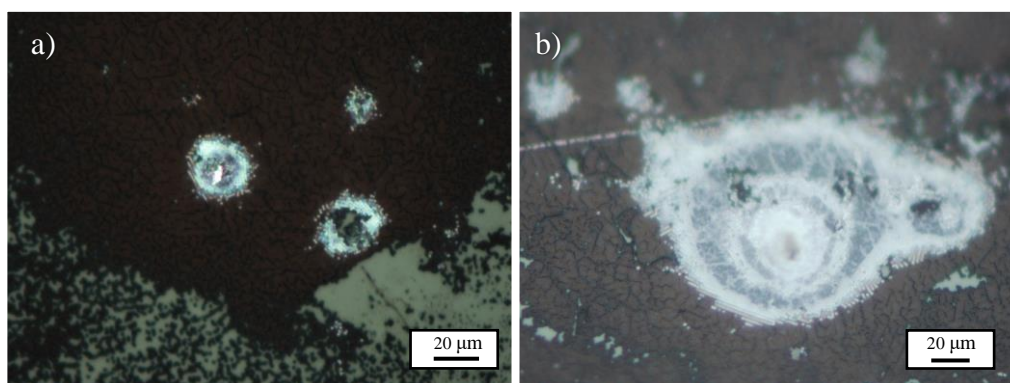


Figure 6.4 Visible-light microscopy images of sample P1-SED
(Images acquired using Nikon Reflected Light Microscope Mag=500x)

Sample P1-CENT, obtained by centrifugation of the nanobead suspension produced a densely packed material with low mechanical stability, which was broken off with the spatula before being sprinkled over a microscope slide. The image in Figure 6.5 shows a discontinuous material forming the thickest agglomerates across the seven samples, characterised by their reflective brightness.

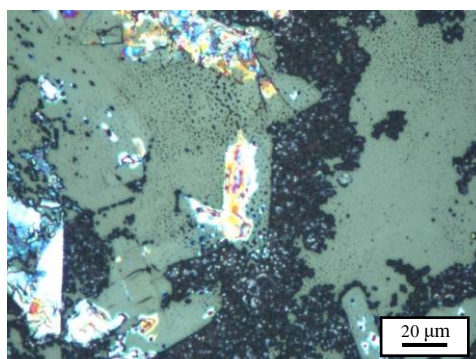


Figure 6.5 Visible-light microscopy image of sample P1-CENT.
(Image acquired using Nikon Reflected Light Microscope Mag=500x)

Thin regions of material are also present across the sample, but these do not appear to form an ordered structure. The arrangement of the beads at the nanoscale cannot be discerned from the VLM image. At this stage, however, the centrifugation method appeared to have formed the most discontinuous and heterogeneous ordering among the seven samples.

6.1.2.2 Scanning electron microscopy

The materials deposited onto glass substrates were characterised using an Inspect F50 scanning electron microscope in secondary electron detection mode. Further details of the equipment can be found in chapter 3. The images in figure 6.6 highlight the arrangement of the polystyrene beads at the nanoscale. The micrographs correspond to the sample obtained by crystallising the nanobead:ethanol suspension at room temperature. The only difference in the preparations of samples shown in 6.6(a, b) and 6.6(c, d) was the angle at which the glass substrate was placed during crystallisation. Images 6.6(a) and (b) show a large-scale ordering of the beads mostly following the behaviour of close-hexagonal packing, where each bead is surrounded by six others. Image 6.6(b) shows that the material has not formed a monolayer of spheres but has indeed crystallised in three-dimensions.

By comparing the results across figure 6.6, it is possible to estimate the effect of the position of the substrate. Mainly, images 6.6(c) and (d) show a group of homogeneous colloidal crystals with continuous structure. The arrangement of the spheres appears much more ordered than its counterpart with a vertical substrate. Furthermore, the preparation of this sample included a step of light grinding of the deposited opal. The result is a much more illustrative sample which provides information on the crystallisation of the material in three-dimensions. The higher magnification of image 6.6(d) allows distinguishing a consistent thickness of three layers across the material. The observations at the nanoscale are consistent with the results of early VLM characterisation. That is, the use of an inclined substrate significantly affects the distribution of the beads across the substrate and favours the fabrication of continuous colloidal crystals.

Further samples were prepared by accelerating the crystallisation as described in the previous sections. The increase in temperature resulted in differences visible at the macroscale, as seen in figure 6.3. Mainly, an increase in temperature produced materials, which spread over narrower areas, particularly following the patterns of evaporation lines. The images shown in Figure 6.7 correspond to the scanning electron microscopy characterisation of the same three samples prepared via colloidal vertical deposition above room temperature. Notably, all three processes produced colloidal crystals with large-scale arrangements. This is evidenced by the

images which show multi-layer depositions of nanobeads arranged periodically, with each PS sphere appearing surrounded by six others in a hexagonal close-packed arrangement.

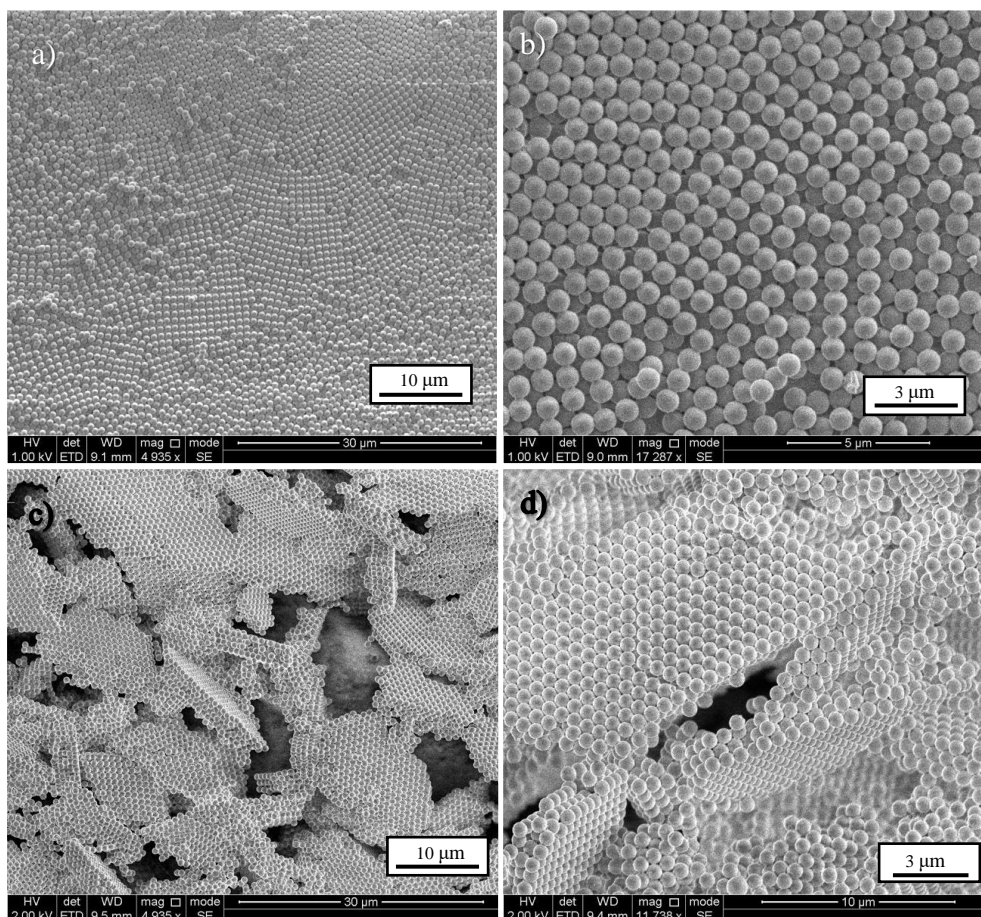


Figure 6.6 SEM images of samples (a, b) P1-CoVD-19(V) and (c, d) P1-CoVD-19(T) (Images acquired using FEI Inspect F50 at 2 kV in SE mode. Magnification values: (a) 4935x, (b) 17287x, (c) 4935x, (d) 11738x)

Comparison of images 6.6(b) and 6.6(d) provides information on the effect of temperature on the thickness of the deposited material. Namely, both products appear to have formed materials of similar thickness with most regions of each material varying between two and four layers of well-ordered spheres. There was no significant difference in the arrangement of spheres at the nanoscale between the samples prepared at 30 and 50 °C.

The third pair of images shows the results of a second sample prepared at 50 °C, but which was deposited onto a substrate inclined at 60°. The image at low magnification shows a fragment with a smaller area than 6.6(a), which was suggested by the VLM observations in figure 6.3. Regardless of the rapid crystallisation, the arrangement of spheres coincides with the requirements of opal and exhibits the same arrangement as all other products of colloidal vertical

deposition in the present study. Furthermore, image 6.7(d) at higher magnification shows a fracture across the opal structure, which allows appreciating the thickness of the crystal. The limitations of SEM imaging make it difficult to quantify exactly the number of layers composing the crystal, but it is estimated that the opal crystal has a thickness of ten to twelve layers. This is significantly higher to the number of layers in samples prepared at 30 and 19 °C which used a vertical substrate. These results indicate that the position of the substrate during colloidal vertical deposition is the main factor influencing the crystalline product, while the surface area is largely dictated by the operating temperature.

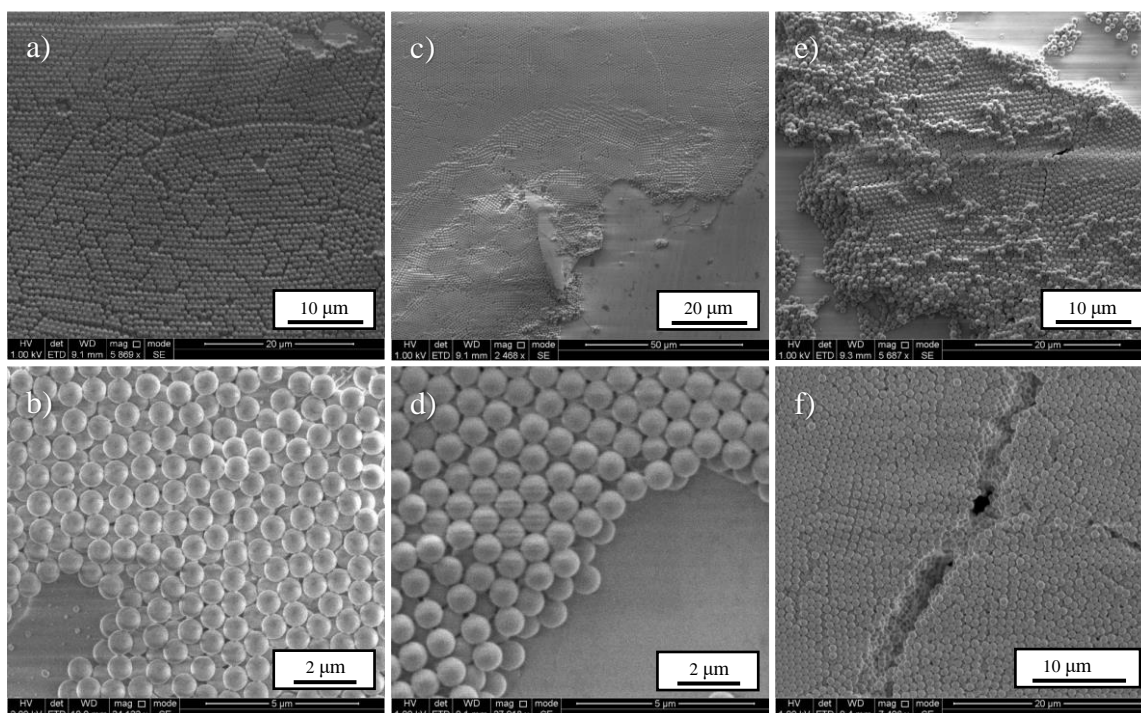


Figure 6.7 SEM images of samples (a, b) P1-CoVD-30(V),
(c, d) P1-CoVD-50(V) and (e, f) P1-CoVD-50(T)

(Images acquired using FEI Inspect F50 at 1 kV in SE mode. Magnification values:
(a) 5869x, (b) 24122x, (c) 2468x, (d) 27918x, (e) 5687x, (f)7406x)

Figure 6.8 shows the opals fabricated using gravitational sedimentation and centrifugation methods. The crystal fabricated by sedimentation exhibits a large surface area of the fragment, owing to the slow crystallisation. However, image 6.8(b) suggests that the arrangement of the spheres at the nanoscale does not show the periodical close-packed ordering exhibited by samples fabricated via CoVD. A possible mechanism for this result is that the first layer of sedimentation produced an ordered arrangement like those in previous samples, but that as the sedimentation continued, the reduced volume of liquid caused the spheres to

deposit in a disorderly manner. This effect would be excluded from vertical deposition because the reduction in the volume of suspension upon evaporation would not alter the lateral distance occupied by the liquid, which is determined by the distance between the substrate and the walls of the container. Finally, the SEM characterisation of sample P1-CENT is shown in images 6.8 (c) and (d). The resulting structure coincides with the characteristics suggested by early observations under visible-light microscopy. The material shows a large agglomerate of variable thickness with no significant ordering at the nanoscale.

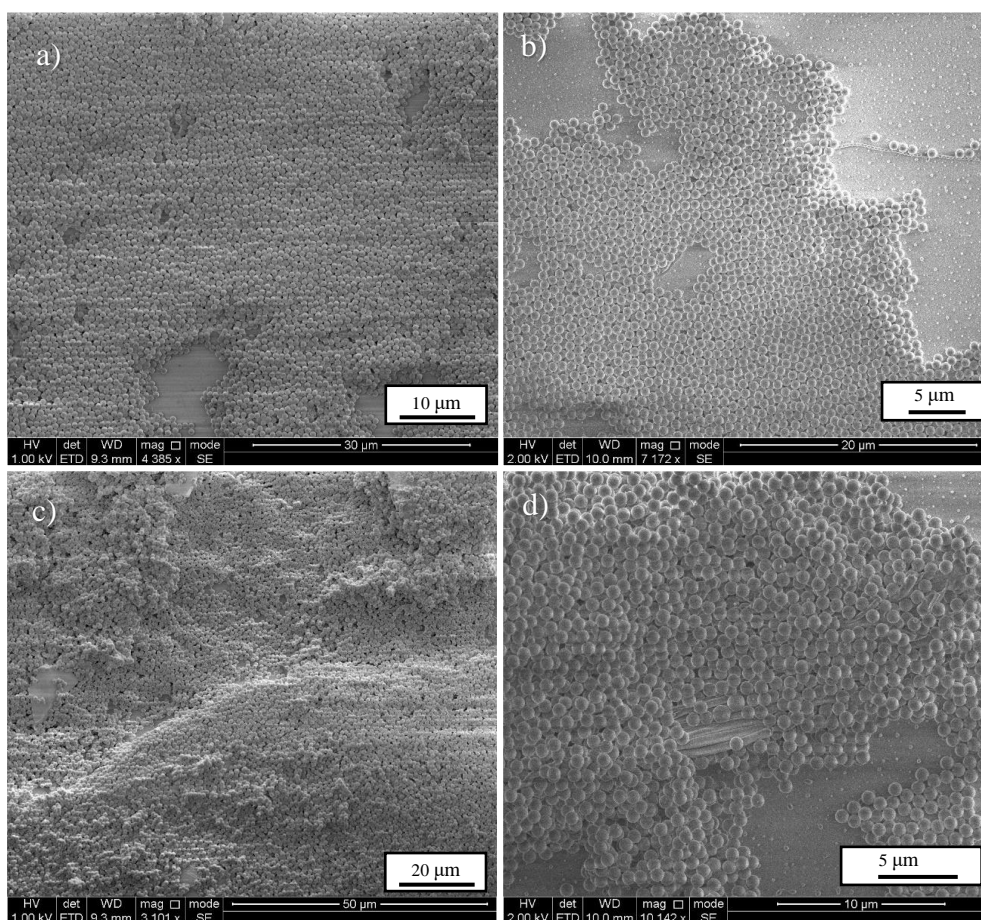


Figure 6.8 SEM images of samples (a, b) P1-SED and (c, d) P1-CENT
(Images acquired using FEI Inspect F50 at 1 kV in SE mode.
Magnification values: (a) 4385x, (b) 7172x, (c) 3101x, (d) 10142x)

6.1.2.3 Transmission electron microscopy

Following SEM characterisation of the materials obtained by several crystallisation methods, an attempt was made to deposit an opal directly onto a standard-grade carbon-coated copper grid for TEM imaging. The same 400 nm PS spheres were selected as building blocks of the

colloidal crystal. In order to achieve the desired product, the TEM grid was placed on a clean glass substrate, and the process of colloidal vertical deposition was carried out as described in section 6.1.1.1. A challenge was encountered to immobilise the TEM copper grid for the duration of the crystallisation without causing damage to the carbon film. Since most adhesive tapes would leave behind volatile residues which are not suitable considering the vacuum conditions of the TEM. A small fragment of carbon conductive tape was used, which is suitable for electron microscopy applications. However, the substrate had an uneven surface which can be a significant impediment to crystal growth.

The products were observed under the transmission electron microscope to give the images shown in Figure 6.9. The images show that the beads were deposited onto the carbon film. Image 6.9(a) shows a particularly large agglomerate extending over several micrometres. Another significant quality of the sample was the small-scale ordering that some groups of nanobeads showed, as seen in image 6.9(b). However, the product does not exhibit large-scale periodicity and is therefore not considered an opal or colloidal crystal. Possible reasons for this product were the unevenness of the substrate as well as the instability of the TEM grid under the suspension. A possible alternative would be to use a carbon film to coat a glass substrate or some other smooth surface. After the crystallisation, the carbon film can be used to coat an empty TEM-copper grid. This methodology has not been incorporated into the present body of experiments, as it escapes the objectives of the project to understand the formation and microstructure of porous nanomaterials.

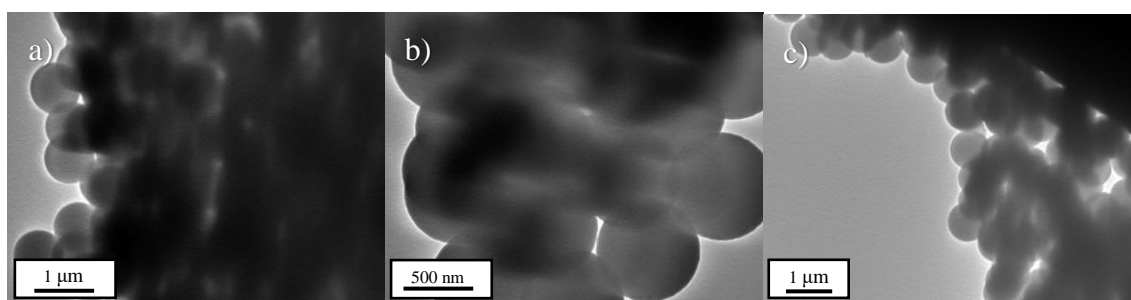


Figure 6.9 TEM images of CoVD-on-TEM-grid PS-opal (Images acquired using Philips TEM 420 at 120 kV. Magnifications: (a) 8000x, (b) 12350x, (c) 8000x)

6.1.3 Self-assembly of colloidal crystals from green-synthesised SiO₂ beads

The experiments reported here complement the work of collaborators by exploring the opal-formation capabilities of silica products of different sizes and shape factors. The products of bioinspired synthesis tend to be less spherical than the polystyrene nanobeads employed in the experiments above. Therefore, this work can provide information on the boundary conditions

of colloidal vertical deposition methods, which proved successful for the self-assembly of opals from PS spheres. This section outlines the characterisation of CoVD-self-assembled colloidal crystals made from silica materials synthesised using bioinspired methods and explores their ability to assemble into opal structures.

The suspensions of nanospheres were prepared by collaborators in the Department of Chemical and Biological Engineering at the University of Sheffield as described in their publication [383]. For the present study, the collaborators supplied two samples of interest: Sample S1, which was fabricated using a modified Stöber synthesis; and sample S2, which was prepared via modified Yokoi synthesis. The synthesis methodologies are described in the respective publications by Stöber et al. [384] and Yokoi et al. [385]. The materials studied in this work represent promising green SiO₂ synthesis approaches, as the products were obtained under ambient conditions and incorporate a bioinspired organic additive. For comparison, a third sample was prepared using a commercial polishing-grade nanosilica suspension (Mastermet® Buehler 40-6370-064), which was expected to present a wide variety of shapes and sizes.

Each of the suspensions was diluted 1:1 with ethanol and allowed to crystallise onto inclined substrates at room temperature, as described in 6.1.1.1. Once the crystallisation products were dry, the deposits from samples S1 and S2 were prepared for TEM characterisation by gently scraping them from the glass substrate and transferring to a mortar. The products were gently crushed and suspended briefly in acetone before depositing on carbon-coated copper grids. The dispersant was selected for its rapid drying time in an attempt to minimise re-dispersion of the particles and destruction of the structures formed during colloidal vertical deposition.

The TEM characterisation of the crystallisation product from sample S1 is shown in figure 6.10. Low-magnification images 6.10(a) and (b) show the products agglomerated in the long-range, forming a nearly continuous material. The product consisted of particles of two distinct sizes, which can be measured in image 6.10(c). The sample contained nanoparticles of 60 nm in diameter, which have a nearly spherical shape and low distribution of size and aspect ratio. The second product occupies the majority of the images and consists of 10 nm particles. This category presented a larger variety of shape factors and sizes. The statistical measurements are summarised below in table 6.2.

Table 6.2 particle size and aspect ratio measurements sample S1

Category	Average size	Standard deviation	Average aspect ratio	Standard deviation
60 nm	59.27	7.08 (12%)	0.87	0.07 (8%)
10 nm	11.02	2.08 (19%)	0.71	0.15 (21%)

The crystallising behaviour appears to be driven by the smaller particles, which have formed a continuous structure in three-dimensions, where the 60 nm particles appear isolated from each other. The three-dimensional quality of the agglomerate can be estimated from the transmission of several layers of small nanoparticles overlapping with larger ones, which is visibly prevalent across image 6.10 (c). The TEM characterisation suggests that the product of CoVD crystallisation of sample S1 did not form an opal structure. A proposed explanation is that the presence of particles of more than one size has impeded the long-range hcp ordering. However, hexagonal close-packing arrangement is also absent in regions of the sample where there were mostly 10 nm particles, as seen in image 6.10 (c). Therefore, the failure to crystallise into opals can also be attributed to the variations in shape across the 10 nm particles. Nevertheless, sample S1 agglomerated into a continuous material, which presents high porosity in three-dimensions. Although such a product is not expected to present the optical properties of opals, it can be eligible for a number of catalytic applications.

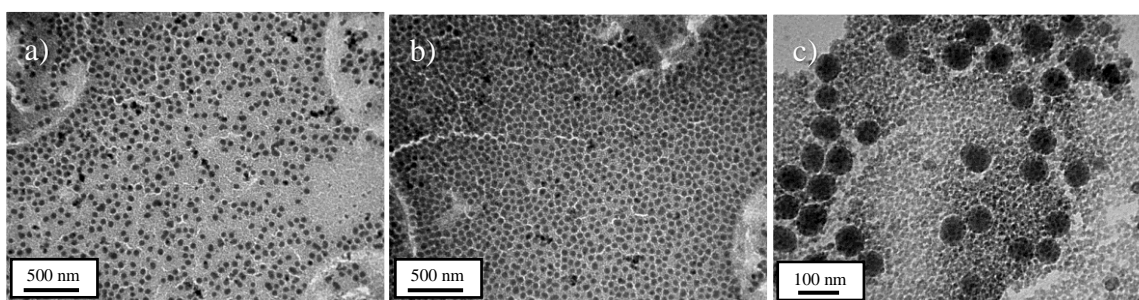


Figure 6.10 TEM images of self-assembled material from S1 silica
(Images acquired using JEOL 3010 at 200 kV. Samplings:
(a) 2.43 nm/pixel, (b) 2.43 nm/pixel, (c) 0.5 nm/pixel)

The product of colloidal crystallisation of sample S2 was also characterised using conventional TEM, and the images are shown in figure 6.11. A statistical description of the product has been obtained from the medium-magnification image 6.11(c). The sample is reported to consist of nanoparticles with a diameter of 12 nm, which appears to vary up to 2 nm (16%) throughout the sample. As for the shape of the particles, these appear to be random but mostly maintain a high aspect ratio of 0.91. Notably, the standard deviation of the aspect ratio was 0.019, which represents only 2% of the average. This value indicates that the shape of the particles varies very little throughout the sample, even though they are not spherical.

Image 6.11(a) shows a large agglomerate, which appears to extend over several micrometres in three dimensions. The image shows a crack in the agglomerate, which highlights the contrast between the material and the background. The thickness of the agglomerate can be appreciated

based on the dark contrast at the edges of the panel compared to the transparent particles appearing along the edges of the crack. Image 6.11(b) shows a much smaller agglomerate, which contains pores up to ten times the size of the building blocks of the material.

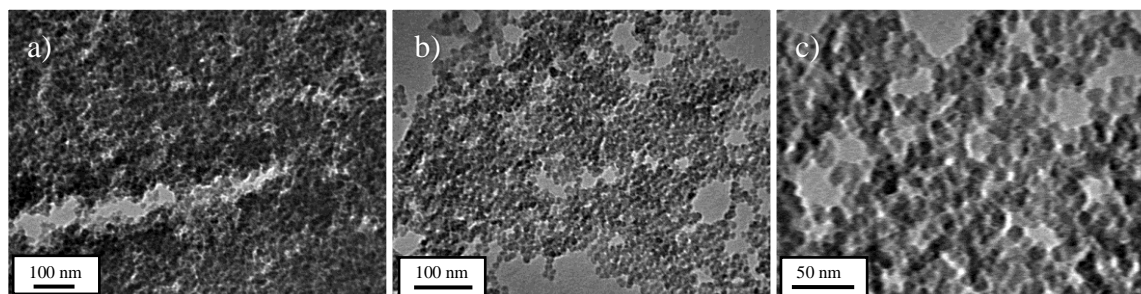


Figure 6.11 TEM images of self-assembled material from S2 silica (Images acquired using Philips TEM 420 at 120 kV. Magnifications: (a) 10000x, (b) 13500x, (c) 25000x)

The product of colloidal vertical deposition of a colloidal suspension of sample S3 was characterised using SEM, as shown in figure 6.12. The product was not deemed suitable for TEM characterisation as the crystal did not survive the attempts to resuspend in acetone, as explained above for S1 and S2. The low specifications of the product were expected to reflect in a product with wide distributions of dimensionality and morphology at the nanoscale. Accordingly, the sample consisted of nanoparticles with an average diameter of 100 nm which varies widely with a standard deviation of 51% of the mean.

The shape of the particles has a low average aspect ratio of 0.65 ± 0.14 (21%), which also varies significantly. The product agglomerated into a large material although more loosely packed than the products of samples S1 and S2, as evidenced by the vast number of small disordered pores in image 6.11(c). This type of agglomeration is expected to result in low mechanical properties, which explains the product easily reverting to a suspension upon contact with acetone.

The product shown in figure 6.12 serves to highlight the mid-range crystallising capabilities of materials S1 and S2. These samples did not exhibit the highly ordered self-assembly of commercial PS nanospheres, or that reported by others using conventional Stöber-silica nanospheres [386], [387]. Nevertheless, the materials formed by S1 and S2 are not randomly agglomerated but have crystallised to a legitimate extent. S3 serves as a contrast of a nanomaterial with no self-assembly capabilities in the colloidal vertical deposition. It is worth underlining that the product used as sample S3 is sold for polishing applications, for which it is used in suspension. Therefore, the wide distribution of shapes and sizes can be considered a positive factor for the fabrication of polishing materials, which are required to remain in suspension and not crystallise in storage.

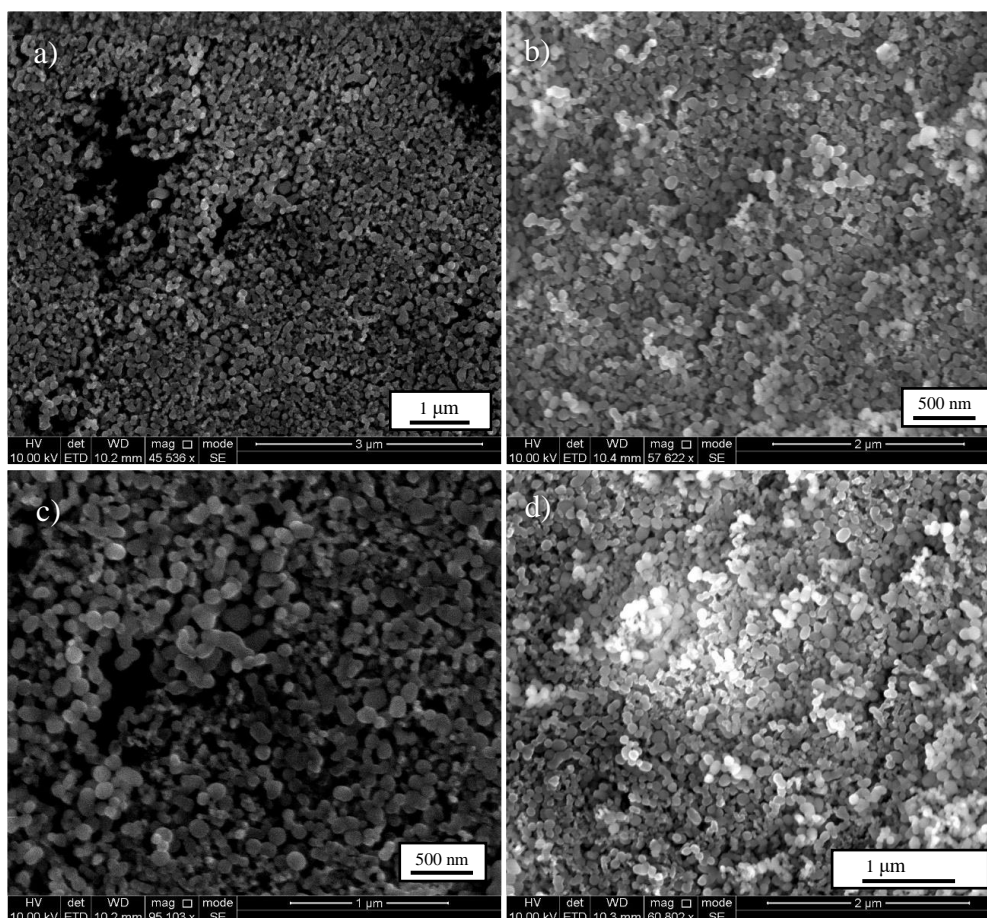


Figure 6.12 SEM images of self-assembled material from S3 silica
 (Images acquired using FEI Inspect F50 at 10 kV in SE mode.
 Magnification values: (a) 45536x, (b) 57622x, (c) 95103x, (d) 60802x)

6.1.4 Infiltration of polystyrene opals with ceria precursor

Following the successful fabrication of colloidal crystals from polystyrene nanospheres, a methodology of infiltration was implemented to achieve nanocasting of the opals. A [0.1 M] solution of cerium(III) nitrate hexahydrate was used as the infiltrating material, which forms cerium(IV) dioxide upon heating. The main objective was to achieve infiltration of the porous structure without resuspending the spheres, which would destroy the opal template. The method of infiltration was designed to prioritise these two conditions.

Firstly, the opal labelled above as P1-CoVD-19(T) was left on its original glass substrate, and the 0.1 M aqueous solution of $\text{Ce}(\text{NO}_3)_3 \cdot 6\text{H}_2\text{O}$ was added dropwise. By performing the infiltration on the original substrate, it was not necessary to scrape off the opal before infiltra-

tion. Therefore, the integrity of the opal remained the same as when it was deposited. Furthermore, the wide surface area of the glass substrate and the absence of container walls maximised the dispersion of the infiltrating solution. The dropwise addition was stopped as soon as the entire surface of the opal was visibly wet. The product was allowed to dry at room temperature overnight, followed by imaging using visible light microscopy. The results are shown in Figure 6.13, which can be compared to Figure 6.1(b) to observe the effects of the infiltration step.

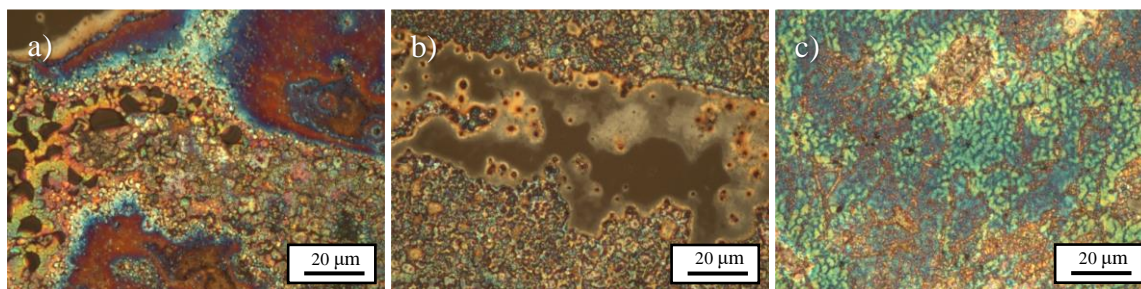


Figure 6.13 Visible-light microscopy images of sample P1-CoVD-19(T) after the addition of $\text{Ce}(\text{NO}_3)_3 \cdot 6\text{H}_2\text{O}$ [0.1 M] and drying at RT
(Images acquired using Nikon Reflected Light Microscope Mag=500x)

The images in Figure 6.13 show significant variations in colour compared to Fig. 6.1(b), which suggests variations in thickness across a thin layer of continuous material. Image 6.13(b) shows an area with no changes in colour, indicating a region of the material with continuous thickness. This region can be identified as the glass substrate coated by a thin layer of $\text{Ce}(\text{NO}_3)_3 \cdot 6\text{H}_2\text{O}$. The patterns of colouring in the images resemble the ordering of the material in the original CoVD opals characterised in section 6.1.2.1. These results are an early suggestion that the opal structure survived the infiltration.

Once the products were sufficiently dry, a section of the coated substrate was cut using a fine carbide glass cutter to be fitted onto an SEM aluminium pin stub aided by an adhesive conductive-carbon dot. SEM characterisation was mostly aimed at determining the distribution of $\text{Ce}(\text{NO}_3)_3 \cdot 6\text{H}_2\text{O}$, as well as assessing the integrity of the opal structure at the nanoscale. Figure 6.14 shows the results of SEM characterisation combining two techniques, secondary electrons and energy-dispersive X-ray mapping. The SE image shows a continuous opal distribution of spheres across the upper half of the panel. Each sphere appears surrounded by six others, indicating hcp-ordering. Additionally, the spaces between spheres appear completely filled by the amorphous infiltrating material, which is distributed evenly across the single layer of opal.

Two more features of interest can be identified in the secondary electron image. First, the empty regions of the opal do not appear filled in or blocked by the ceria precursor. Instead, the

amorphous infiltrate appears to form a defined boundary where the opal ends, and the large pore begins. Secondly, the bottom third of the panel shows a region of heavy precursor deposition, which appears to cover the opal beyond covering it. The precursor has formed into an even surface and appears to have cracked in some regions during drying. The spheres are still visible under the heavy layer of precursor, and most of them still appear ordered in hexagonal close-packing. The penetration of secondary electrons is limited, which means that the spheres that are clearly resolved occur at the same level as the precursor while the spheres appearing faint occur one or two layers underneath.

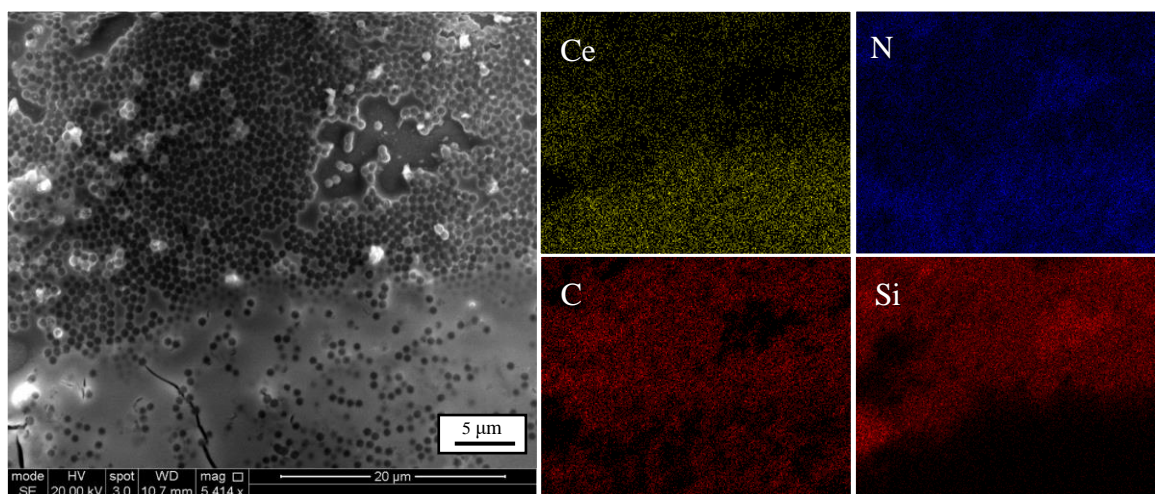


Figure 6.14 SEM study of PS/Ce(NO₃)₃·6H₂O composite showing secondary electron image and relevant EDX maps of the same panel. (SE image and EDX maps acquired using FEI Inspect F50 at 20 kV. Magnification value=5414x)

EDX mapping confirms and complements the information obtained from secondary electrons. Firstly, a carbon map is shown to indicate the distribution of the polymeric spheres. The distribution of carbon appears heavy in the top two thirds of the panel, which confirms the observations above that the top two-thirds of the SE image was showing a monolayer of opal and the bottom third a multilayer arrangement. The distribution of carbon appears continuous, especially in the multilayer region, which confirms the integrity of the opal structure. If the spheres had been suspended upon addition of the infiltrating solution, the carbon map would be expected to appear fragmented, with the carbon appearing in isolated regions separated by regions of infiltrating material. However, this result indicates that the opal and the sol precursor appear in the same regions of the sample, with the precursor depositing more heavily over multilayer regions. The second and third maps, cerium and nitrogen, appear nearly identical in

distribution, which is expected as they are both signals from $\text{Ce}(\text{NO}_3)_3 \cdot 6\text{H}_2\text{O}$. The heavier cerium appears to give an adequate signal owing to its higher Z. The distribution matches the results from the carbon map and confirms the observations above that the precursor has successfully infiltrated the opal structure in its entirety. Notably, the pore at the top right of the panel appears to contain no cerium atoms, confirming the observations above. This is a promising result, as it suggests that the precursor is selectively deposited onto the opal region and does not form heavy deposits blocking the pores and impeding penetration of the structure.

The Ce and N maps shown indicate that the infiltrating precursor has been distributed evenly across the opal template. Finally, the silicon map is shown to illustrate the effects of thickness in the material. The brightest region is the pore mentioned above, which appears to contain only silicon atoms from the glass substrate. Then, the top region of the panel still transmits Si signals, which confirms the even thickness of a monolayer as suggested above. Finally, across the bottom third of the panel, the silicon appears completely obscured by the thickness of the composite. The results of this study indicate that the infiltration procedure was adequate and produced a composite of indeed a composite of polystyrene opal filled in with $\text{Ce}(\text{NO}_3)_3 \cdot 6\text{H}_2\text{O}$.

6.1.5 Calcination of PS-opal/ $\text{Ce}(\text{NO}_3)_3 \cdot 6\text{H}_2\text{O}$ composite

Following the successful incorporation of a material of interest into the porous opal structure, as described in the previous section, the composite sample was heated to convert the $\text{Ce}(\text{NO}_3)_3 \cdot 6\text{H}_2\text{O}$ into ceria and to sublime the polystyrene spheres. This procedure aimed to obtain an inverse opal structure consisting of cerium(IV) oxide forming a continuous structure with periodic porosity. The calcination steps were defined by the two reactions of interest. I. e., the conversion of cerium(III) nitrate hexahydrate to cerium(IV) oxide and the conversion of polystyrene to carbon dioxide and water.

Figure 6.15 shows the relevant weight-temperature diagrams found in the cited literature [388], [389]. The steep changes in weight are associated with the transition of one product to the next, while a constant weight is associated with a stable phase such as ceria. The diagram presented as Figure 6.15 (a) shows more than one transition temperature. First, a steep decrease in weight is initiated at 55 °C and shows a constant slope until the end of that transformation at 240 °C. This first step of thermally-induced transformation is generally associated with the loss of water in the product, with superficial dehydration being followed by the loss of crystallising water found in the molecules of hexahydrate. The second step of transformation is observed between 240 °C and 550 °C, which presents a shallower slope associated with the loss of NO_x products and the subsequent production of ceria.

The curve in Figure 6.15(b) represents the loss of weight associated with the decomposition of polystyrene. The temperatures of interest identified in this diagram are the initiation of the

sublimation at around 350 °C and the complete evaporation of the product at 450 °C. An important difference between the two diagrams is that only the decomposition of ceria in diagram 6.15(a) renders a solid product, marked by a final weight different from zero. The temperatures of experimental calcination were chosen based on the transition points seen in these references. A first step was performed at 350 °C aiming to start the conversion of ceria, as well as the sublimation of polystyrene. The product was expected to show incomplete transformations, which could provide information on the interactions between the compounds forming the composite during the transformation. A second calcination step was defined as 550 °C. This temperature was expected to produce an inverse opal structure containing only ceria.

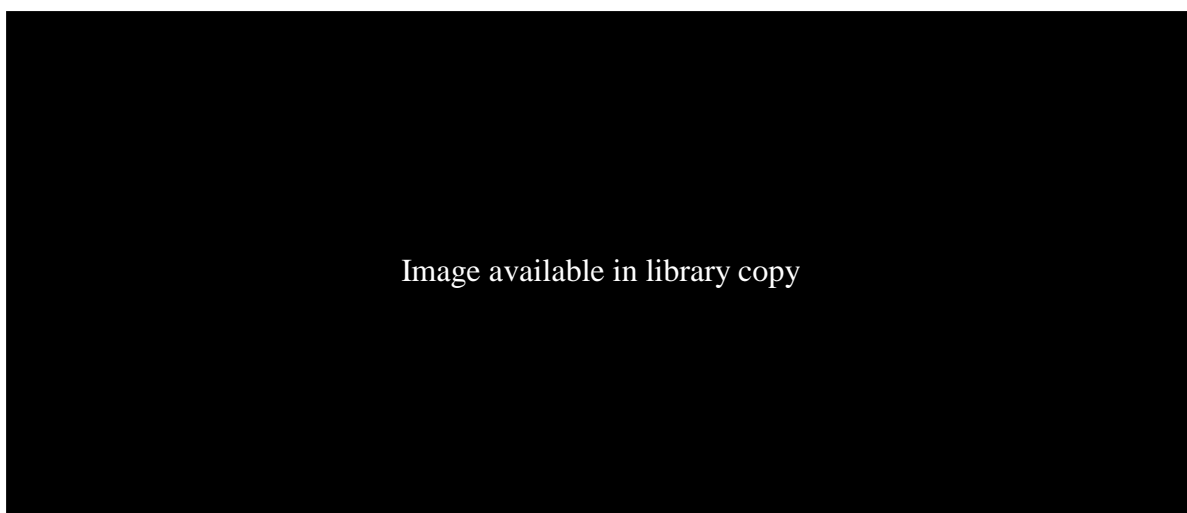


Figure 6.15 Thermal decomposition diagrams of (a) $\text{Ce}(\text{NO}_3)_3 \cdot 6\text{H}_2\text{O}$ [389] and (b) polystyrene [388]

The product of the first step of calcination was characterised using SEM secondary electron imaging, as shown in Figure 6.16. The images acquired at lower magnifications, labelled 6.16(a) and (b) show a porous product with a periodic structure in the long-range. Another interesting feature present in the images is the presence of large flakes of material resembling the dry $\text{Ce}(\text{NO}_3)_3 \cdot 6\text{H}_2\text{O}$ in Figure 6.14. This feature is associated with the incomplete transformation of ceria precursor, which is unsurprising as the heating temperature of the specimen was intentionally chosen to show the state of the materials mid-transformation.

Images 6.16(c) and (d) present higher magnification acquisitions revealing distinct aspects of the structure. Image 6.16(c) shows an area mostly occupied by smooth solid material with empty spherical pores with sizes matching the polystyrene nanospheres. This image suggests that the spheres have been completely removed from the composite without destroying the periodic structure. This statement is confirmed by image 6.16(d), which shows periodical pores

forming a negative structure of the original opal. The long-range arrangement of the material is promising, considering that the spheres have already been removed. Especially, the loss of material in $\text{Ce}(\text{NO}_3)_3 \cdot 6\text{H}_2\text{O}$ between 55 and 350 °C does not appear to have destroyed the continuous structure of the colloidal crystal. This was considered a successful removal of the polystyrene phase from the composite resulting in an inverse opal structure consisting only of a cerium salt.

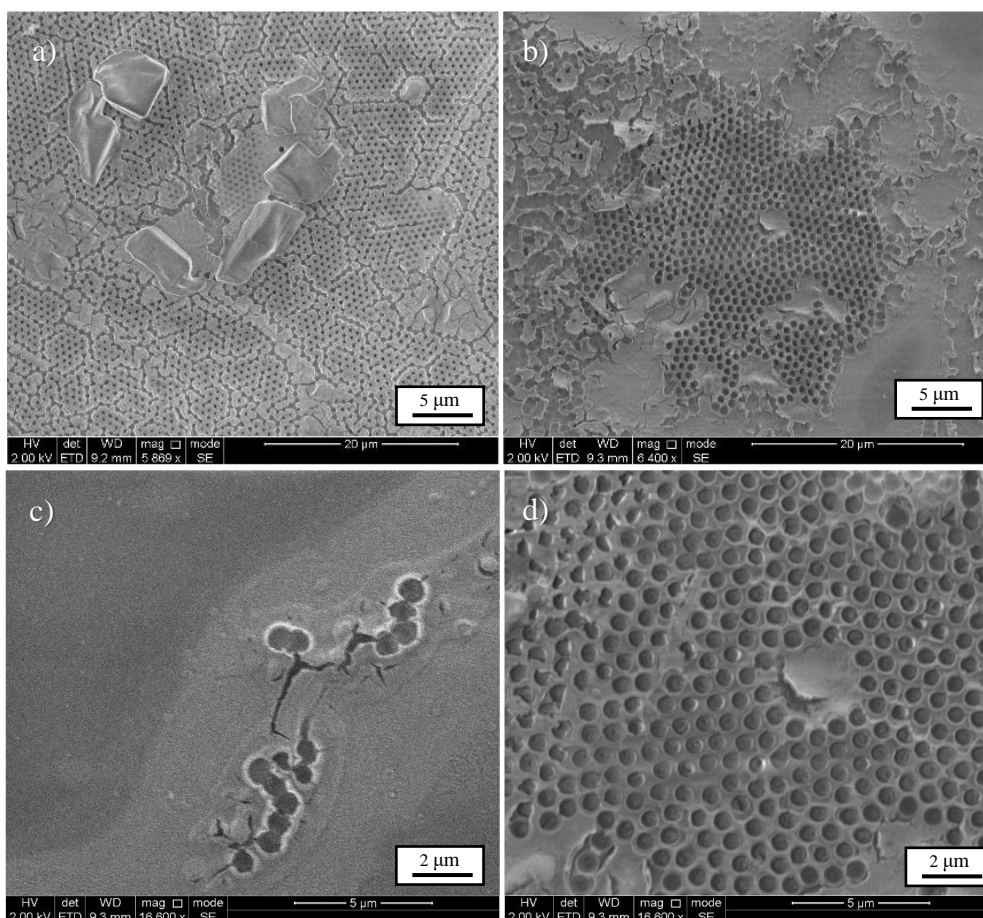


Figure 6.16 SEM images of the composite system after heating at 350 °C
 (Images acquired using FEI Inspect F50 at 2 kV in SE mode.
 Magnification values: (a) 5869x, (b) 6400x, (c) 16600x, (d) 16600x)

Following the successful removal of the polystyrene template from the composite, the second step of heating was performed on the sample. This step was performed at 550 °C, which would transform all the cerium salts into cerium(IV) oxide. The product of the second calcination step was characterised using a combination of methods within SEM, and the results are

shown in Figure 6.17. Image 6.17(a) was acquired using a secondary electron detector to emphasise the surface properties of the material. Notably, the material continues to exhibit a periodic structure after the second step of calcination.

Moreover, the sample presents a homogeneous thickness with no deposits of oxide covering the structure. The flake-like features observed in Figure 6.15 (a) appear to have disappeared upon heating at 550 °C. Image 6.17(b) has been captured with particularly high contrast, which emphasises the surface texture throughout the sample. The low magnification of the image allows to appreciate the periodicity of pores and the continuity of the sample, with fragments extending over several tens of micrometres.

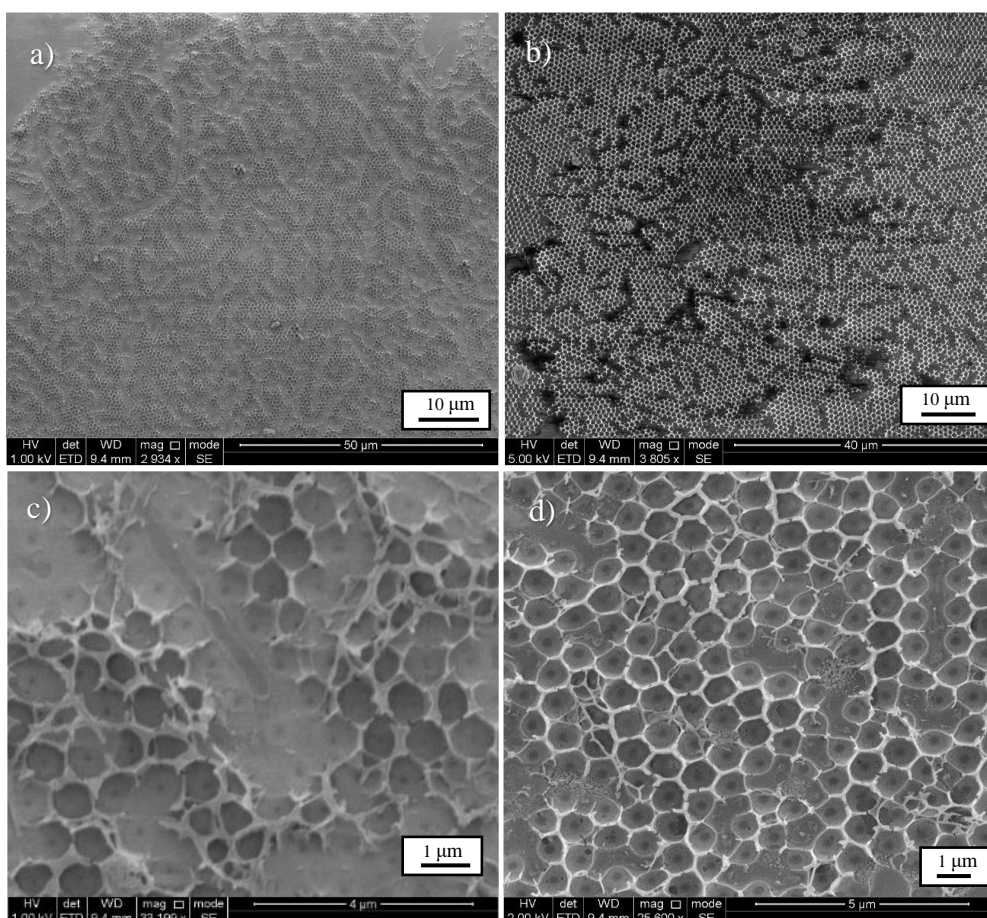


Figure 6.17 SEM images of the composite system after heating at 550 °C
 (Images acquired using FEI Inspect F50 at 1 kV in SE mode.
 Magnification values: (a) 2934x, (b) 3805x, (c) 33199x, (d) 25600x)

Image 6.17(c) shows a secondary electron image at high magnification showing the walls surrounding the pores to be connected and forming a network of several pores. The region selected for the image also illustrates the mechanical behaviour by showing a region where the

inverse opal appears to have torn causing the film of porous ceria to roll onto itself and the adjacent pores to distort.

Finally, image 6.17(d) shows a typical region of inverse opal with continuous walls extending over several micrometres. The contrast between the walls and the background allows identifying a significant loss of thickness during the second step of conversion, as seen by comparing to image 6.16(d). Also, the pores exhibit a significant change in shape, with pores after one step of calcination showing distinct sphericity, which is significantly lost after the second step of calcination. This loss of material is associated with the successful conversion of $\text{Ce}(\text{NO}_3)_3 \cdot 6\text{H}_2\text{O}$ to CeO_2 . Overall, the results in this section indicate that the proposed process of two-step calcination produced a continuous inverse opal with periodical porosity in the long-range. Image 6.17(d) shows a significant change in the morphology of pores, which have developed facets and lost their spherical morphology. This is likely associated with the early removal of the opal template before the complete conversion of the ceria precursor.

6.2 Study of mesoporous silica and MPS-based catalytic composites

Mesoporous silicates (MPS) are a large family of materials that consist mostly of ordered arrays of pores separated by thin walls of silica. It may contain small amounts of aluminium, magnesium and other elements. For this work, we have selected two types of MPS known as MSU-F and SBA-15. MSU-F is exceptional in that its pores are random in distribution and the range of their sizes is wide relative to their diameter (10-25 nm). The relevance of these materials has been outlined in section 2.1.2 of the literature review. Each of these materials poses a different challenge for their characterisation. The random distribution of pores in MSU-F, as well as their size distribution, makes a thorough TEM study of the material particularly relevant since porosimetry techniques would not be able to resolve the structure of non-periodic pores.

On the other hand, SBA-15 has proved useful in a number of applications as described in section 2.1.2. The periodicity of the pores and the narrow distribution of pore sizes of SBA-15 makes it an interesting material for comparison of the infiltration behaviour in nanocasting procedures. Analogous to the fabrication of inverse opals, the MSU-F sample was infiltrated with a ceria precursor, generating a composite material that lends itself for a variety of interesting studies. A large proportion of this section is devoted to the study of an MSU-F/ CeO_2 composite combining a variety of techniques in electron microscopy, as well as the effect of repeated cycles of impregnation/calcination. Finally, a novel approach is proposed for the production of a negative-silica structure, which seeks to minimise the hazards associated with the usual template removal by HF-etching.

6.2.1 TEM study of MSU-F mesoporous silica and MSU-F/CeO₂ composite

The TEM study of MSU-F poses a significant challenge of electron-beam sensitivity. The thin walls of silica tend to sinter when heated by a strong electron beam, which causes the structure to collapse. In addition, the three-dimensional nature of MPS at the nanoscale, makes the preparation of TEM samples more challenging than that of nanoparticles, like the ones seen in chapters 4 and 5. An initial exploration of the material using high-resolution TEM is shown in Figure 6.18. Image 6.18(a) shows a fragment of MSU-F extending over a surface of several hundred nanometres. The random distribution of the pores can be appreciated, as well as the open structure of the material. Notably, the three-dimensional qualities of MPS suggest that the fragment being imaged is as thick as it is wide, suggesting that the electron beam is travelling across several hundred nanometres to generate the transmission image 6.18(a).

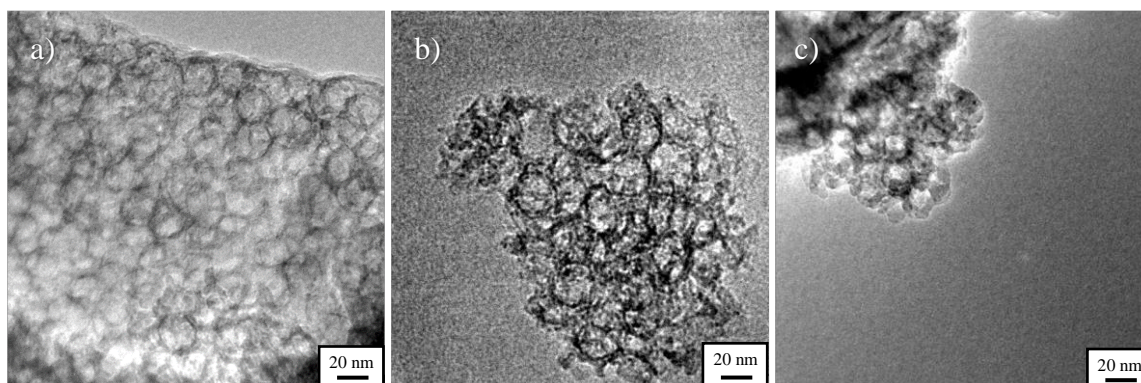


Figure 6.18 TEM images of MSU-F mesoporous silica
(Images acquired using JEOL 3010 at 200 kV. Samplings=0.23 nm/pixel)

Considering the dimensions of the fragment, it is remarkable that it is possible to resolve the porous structure and the distribution of the silica network even at the centre of the panel. This result can be attributed to the openness of the material as well as the transparency of amorphous silica. Image 6.18(b) shows an example of a small fragment with a diameter of 160 nm occupied by 15 pores. Image 6.18(c) shows a third different case, where a small array of porous material protrudes from a large agglomerate. These three types of samples proved possible to image over several minutes as long as the intensity of the electron beam was not intensified. That is, the material regardless of its thickness, proved suitable for TEM study by maintaining a low electron count, even over an extended period of time.

6.2.1.1 *Three-dimensional TEM of MSU-F*

Following the evaluation of the resistance of MSU-F to electron-beam irradiation, the material was deemed suitable for the long periods of exposure involved in electron tomography. A tomography sample of MSU-F was prepared by grinding the powder with a pestle and mortar. This step sought to produce smaller fragments that would not obscure themselves upon rotation. Then, the solid was suspended in 1 ml of isopropanol and ultrasonicated for 15 minutes. A drop of the suspension was added to a standard-grade carbon-coated copper grid, and allowed to dry at room temperature. Once the sample was inserted in the microscope, precautions were taken not to focus the beam too much on the silica material, in order to avoid deterioration of the structure caused by the high intensities used during beam alignment.

In contrast to the tomography presented in Chapter 5, the specimen selection in this study was based mostly on electron transparency, i.e. thickness. As mentioned above, most powder fragments or three-dimensional arrays of this type can be roughly described as being as thick as they are wide. This is because it would be improbable for a material to randomly arrange into plates lying flat on the plane of the sample holder. It is important to note this because fragments of MSU-F, due to their low long-range density, as well as its low atomic number, tend to appear thinner in transmission images than they really are, as shown in Figure 6.17 (a). This can cause major problems at high tilt angles, such as low to no electron counts in the thicker regions of the material, as well as finding that at certain tilt angles the specimen no longer fits inside the field of view at the selected magnification.

Two tilt series were acquired and are shown in Figure 6.19. For the sake of conciseness, only five representative images across each of the tilt series are shown. Each acquisition was intended to be performed over an interval of 120° and images acquired between every 5° rotation. However, the geometrical constraints of the sample impeded the successful acquisition of a complete tilt series that could be used for reconstruction of the porous structure in three-dimensions. Series 6.19(a) shows the rotation of a large fragment of porous material was the material rolls over itself at around 30° making it impossible to resolve the individual pores. Also, the fragment was considered too large for the purposes of this study. Series 6.19(b) shows a smaller fragment which also obscured the individual pores upon rotation. Furthermore, the specimen was located too close to the copper grid, which came into view at -15° and obscured the fragment from view for subsequent tilt angles.

b)

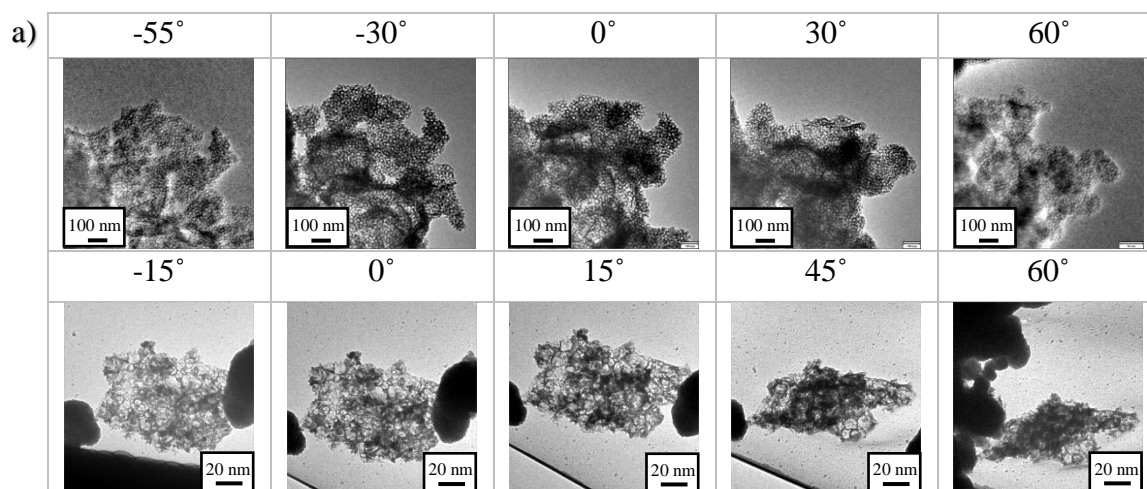


Figure 6.19 Electron tomography tilt-series of MSU-F mesoporous silica.
Instrumental tilt-axis orientation calculated to 35.75°
(Images acquired using JEOL 3010 at 200 kV. Samplings=0.23 nm/pixel)

Although the tilt series acquisitions were unsuccessful, they provide information about the distribution of pores in three-dimensions. For example, the individual structure of pores appears unrelated to their location within a grain of MSU-F. This means that the pores in the terminal structure of a fragment could be studied with electron tomography and be considered representative of the porous structure as a whole. Furthermore, the tilt series corroborates earlier observations that MPS tend to form into three-dimensional fragments even after the mechanical grinding step involved in the preparation of this sample. Finally, the material did not distort visibly during the several hours of irradiation involved in tilt-series acquisition. This is evidenced by the fact that the size of the pores at 60° are consistent with those at 0°. The pores would be expected to change drastically in size upon electron beam damage. Furthermore, although the material appears electron transparent throughout most of the analysis, the pores cannot be resolved as soon as more than a couple of them overlap. This means that to obtain a successful tomography series, it would be advised to study a very small system containing no more than four or five pores across.

6.2.1.2 Preparation and characterisation of MSU-F/CeO₂ composite

A composite material consisting of cerium dioxide filling a network of porous silica was prepared using two different methods. For the so-called Dry Method, pre-fabricated mesoporous silica of the type MSU-F (Agar Scientific) was pre-treated at 100 °C for 8 hours. This was to promote evaporation of water, volatiles or any substance that could be occupying the pores in

the material, which could affect the efficiency of the infiltration. Then, the powder was placed on a watch glass and spread to generate a thin layer of MSU-F. 5 ml of high concentration [5 M] aqueous solution of cerium nitrate hexahydrate was prepared using an ultrasonic bath to ensure that the $\text{Ce}(\text{NO}_3)_3 \cdot 6\text{H}_2\text{O}$ was fully dissolved. Then, the 500 μl of the solution was added to the watch glass. The resulting gel was dried at 100 °C for 1 hour. This resulted in a yellow vitreous solid, which was then calcined at 400 °C for 4 hours to convert the $\text{Ce}(\text{NO}_3)_3 \cdot 6\text{H}_2\text{O}$ into ceria. The resulting product was a highly packed white powder. After cooling, the product was broken into a fine powder using a pestle and mortar and formed into a thin layer, which was impregnated again with 500 μl of a second solution of [3.75 M] $\text{Ce}(\text{NO}_3)_3 \cdot 6\text{H}_2\text{O}_{(\text{aq})}$. The gel was subjected to the same heating cycle as above. The cycle was repeated a third time with a solution of [2.5 M] $\text{Ce}(\text{NO}_3)_3 \cdot 6\text{H}_2\text{O}_{(\text{aq})}$. This method is often referred to in the literature as incipient wetness impregnation.

For the so-called Wet Method, the porous silica was pre-treated at 100 °C for 8 hours. 100 mg of silica was added to 3 ml of [1.5 M] aqueous solution of $\text{Ce}(\text{NO}_3)_3 \cdot 6\text{H}_2\text{O}$. The suspension was treated in an ultrasonication bath for 1 hour to promote infiltration of the pores. The resulting suspension was allowed to dry at room temperature, then resuspended again in 3 ml of [0.75 M] aqueous solution of $\text{Ce}(\text{NO}_3)_3 \cdot 6\text{H}_2\text{O}$. The suspension was ultrasonicated again and allowed to dry at room temperature. The resulting product was calcined at 400 °C for 4 hours to convert the $\text{Ce}(\text{NO}_3)_3 \cdot 6\text{H}_2\text{O}$ to CeO_2 . Both wet and dry methods produced white to yellow powders. A small sample of each was ground using a pestle and mortar. This was meant to reduce the size of the fragments to dimensions that were suitable for TEM. The powders were suspended in isopropanol and pipetted onto carbon-coated copper grids.

An initial exploration of the samples is shown in Figure 6.20. Images 6.20(a) and (b) show the product of ultrasound-assisted infiltration. The product appears much darker than the empty MSU-F specimens shown in previous figures, suggesting that the infiltration was effective. However, comparison between the product of wet impregnation in images 6.20(a) and (b) with the product of dry impregnation in images 6.20(c) and (d) suggest that most efficient methods were incipient wetness impregnation (IWI) with three cycles of infiltration/calcination, which produced a heavy continuous product and was selected for further study. Although this initial exploration cannot be used as a conclusive indicator of the effectiveness of the different infiltration methods, the difference in contrast between particles of similar thickness suggests a difference in the distribution of the infiltrating phase.

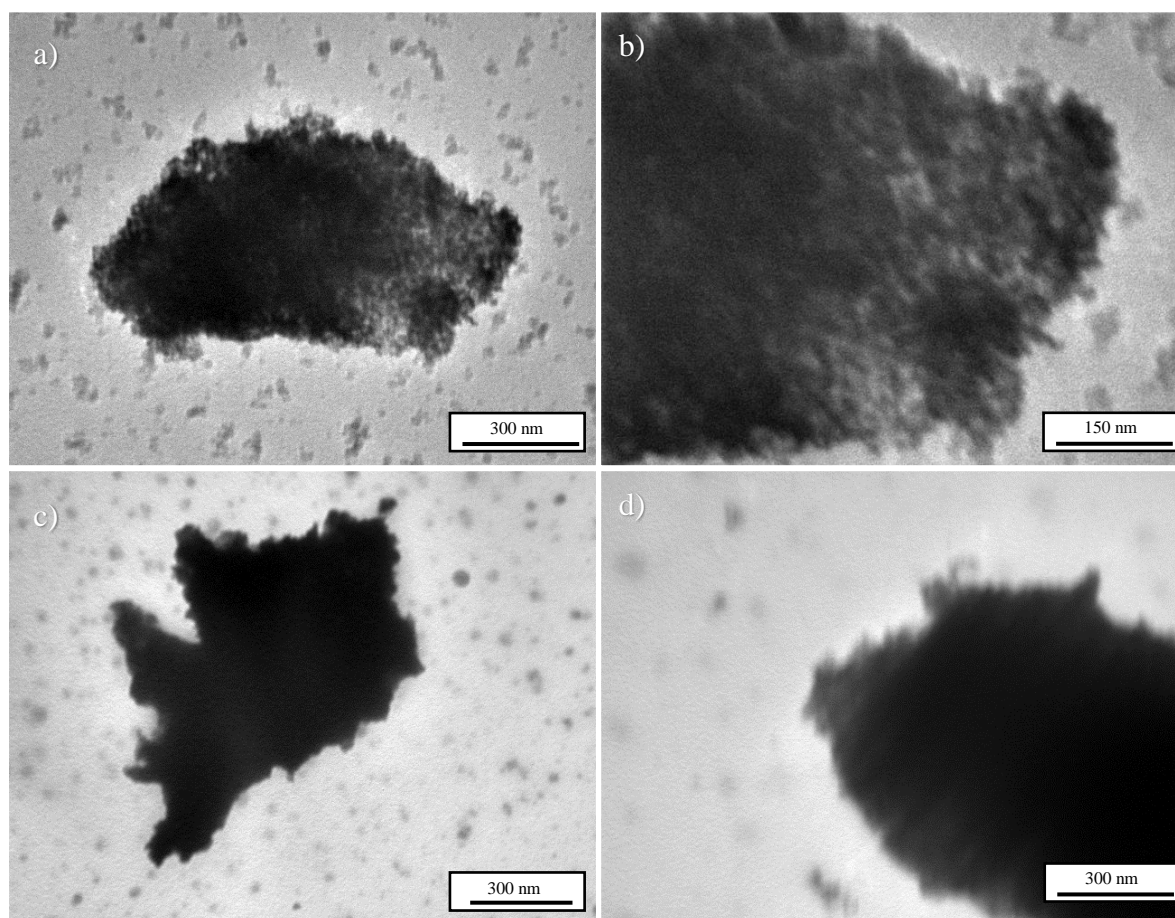


Figure 6.20 Initial TEM explorations of MSU-F/CeO₂ composites obtained via (a, b) ultrasound-assisted infiltration and (c, d) incipient wetness impregnation (Images acquired using Philips TEM 420 at 120 kV. Magnifications: (a) 10000x, (b) 20000x, (c) 10000x, (d) 10000x)

The IWI-prepared composite was characterised by employing a diversity of imaging, and analytical methods were combined to provide further information on the material. The characterisations were performed using the High-Resolution TEM JEOL 2010F, which is described in detail in Chapter 3. The samples were mounted onto a beryllium double tilt holder for analyses to avoid signals from the holder during the Energy-dispersive X-ray Spectroscopy (EDX). The results of a TEM study of the composite are shown in Figure 6.21. This study combined the high-resolution capabilities of the microscope with the incorporation of the objective aperture to generate dark-field images, which highlight the crystalline ceria in the sample. Image 6.21(a) shows an array of nanoparticles with sizes ranging between 3 and 20 nm. The dark-field counterpart shown in image 6.21(d) highlights the crystallinity of the nanoparticles. The cluster of nanoparticles in these images does not appear to be contained within the structure of an MSU-F fragment, although the size and shape of the larger nanoparticles appear to match

those of the pores in the MSU-F networks elsewhere in the sample. The hierarchy of sizes of the nanoparticles could be explained by an infiltration mechanism where the particles are formed inside a fragment of mesoporous silica but do not occupy the entire structure. This mechanism of nanocasting does not produce a continuous material like the inverse opals in previous sections, but form clusters of nanoparticles inside the template material. The size of the pores, in this case, would limit the growth of nanoparticles producing a result consistent with the observations in image 6.21(a).

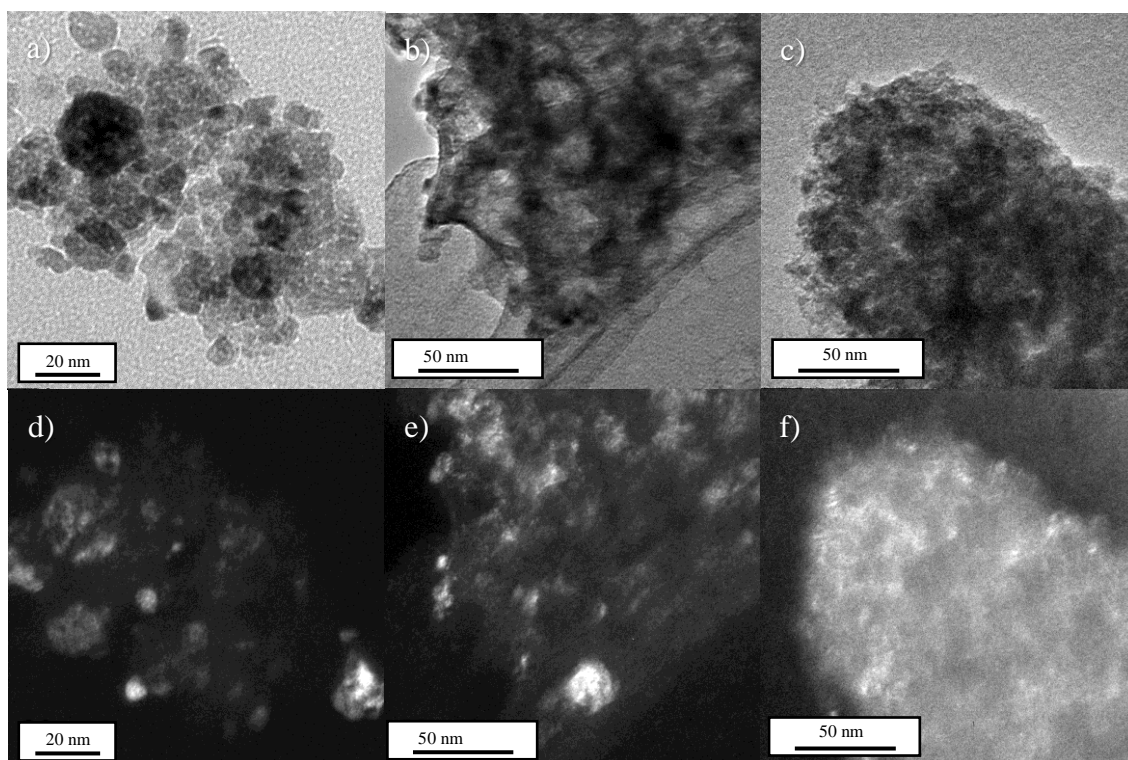


Figure 6.21 Bright-field (a-c) and dark-field (d-f) TEM of MSU-F/CeO₂ composite
 (Images acquired using JEOL 2010F at 200 kV. Samplings:
 (a,d)=0.07 nm/pixel (b,e)=0.15 nm/pixel, (c,f)=0.17 nm/pixel)

Image 6.21(b) shows a fragment of mesoporous silica material with most of its pores still resolved and showing similar transparency to the empty material. However, when compared to image 6.21(e), the presence of bright areas of high crystallinity indicates that the structure has been successfully infiltrated by CeO₂. Consistently with the statements above, the shapes and sizes of the nanoparticles appear to be equal or smaller than the size of the pores in the MSU-F structure. Image 6.21(c) shows the most typical occurrence across the sample, where a fragment consistent in size and appearance to the MSU-F appears completely occupied by ceria. This type of composite suggests a successful infiltration. However, the amorphous nature of

silica and its electron transparency make it almost invisible when combined with ceria. Image 6.21(f) reiterates the high density of the infiltrating ceria while showing faint rounded features about 20 nm in diameter consistent with the pores in MSU-F.

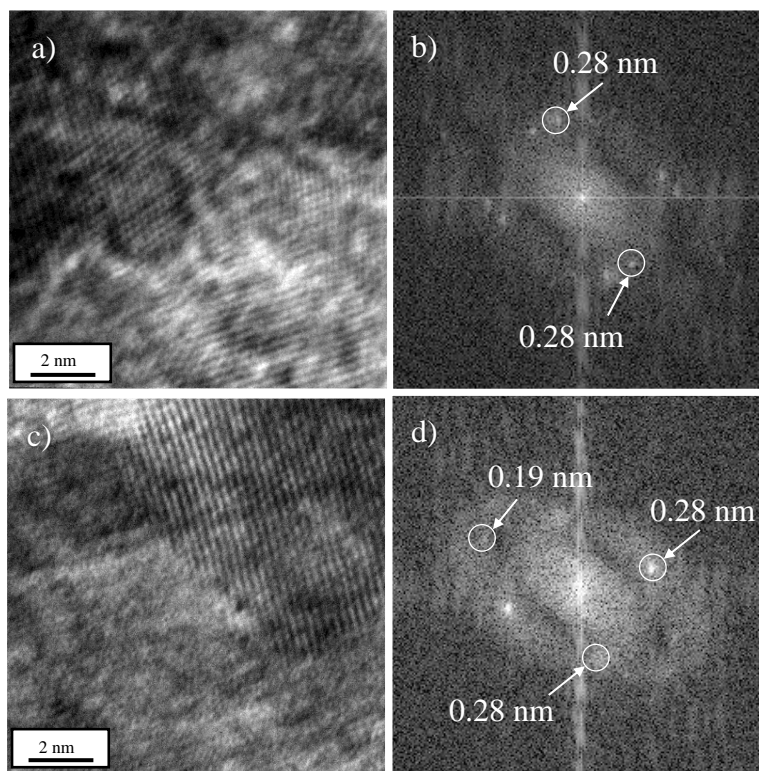


Figure 6.22 HRTEM images of MSU-F/CeO₂ composite with calculated FFTs (Images acquired using JEOL 2010F at 200 kV. Samplings=0.007 nm/pixel)

Further high-resolution imaging of the composite allowed to identify the crystallography of the composite. The images in Figure 6.22 show acquisitions with resolution of atomic lattice fringes and their respective FFT-space peaks. Image 6.22(a) shows a region mostly occupied by fringes. The FFT calculated for the whole panel is shown in image 6.22(b) and provides significant information on the general sample. Firstly, peaks are associated with the [200] plane family, which confirms that the deposited product is in fact CeO₂. Then, the peaks appear scattered with each pair of peaks presenting an identical pair at equal distances. This is indicative of the polycrystalline nature of the infiltrating material, as suggested above. Image 6.22(c) shows a well-defined ceria nanoparticle which has crystallised into a faceted shape with sharp edges parallel to the [200] and [110] planes.

Since the silica walls of the MSU-F structure are composed of amorphous material, they cannot be identified using the FFT peaks in Figure 6.22. Further investigation was performed by acquiring the EDX spectrum of a representative region of material, as shown in Figure 6.23.

The copper peaks can be attributed to the copper grid holding the sample. Quantification of selected elements in this analysis showed approximate atomic percentages of 70% Oxygen, 12% Silicon and 18% Cerium. As both oxides contain two atoms of oxygen per molecule, the proportions can be held true for silica and ceria respectively. A higher percentage of ceria is consistent with the open structure of the porous template. The presence of both species within the same space is indicative of successful infiltration.

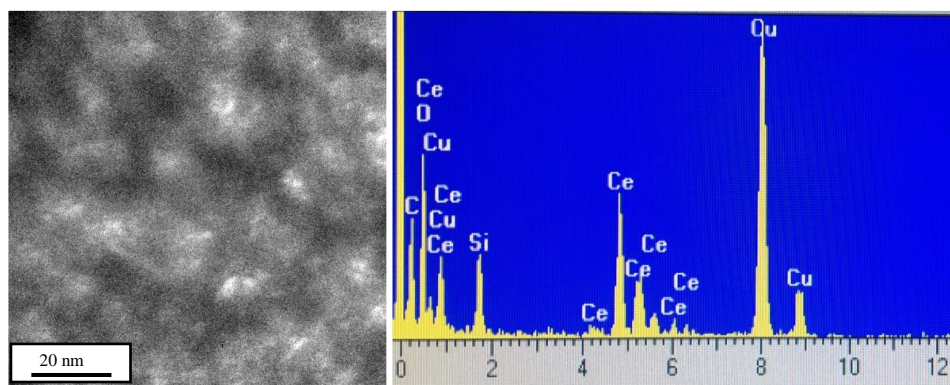


Figure 6.23 EDX spectrum of MSU-F/CeO₂ composite (x-axis indicates keV)
(Image and spectrum acquired using JEOL 2010F at 200 kV. Sampling=0.08 nm/pixel)

EDX analysis was able to successfully confirm the presence of silica and ceria, forming a composite system in the material. However, the nature of the sample made it impossible to produce a conclusive EDX mapping result, as was used for the composite in Figure 6.14. Mainly, the intricate network of pores meant that ceria and silica appeared to be occupying the entire material simultaneously. To obtain the spatial distribution of silica and ceria at the nanoscale, further imaging was performed using BF-STEM and HAADF-STEM, which produced the results shown in figure 6.24.

The bright-field images acquired using STEM show higher contrast than those from TEM mode seen in Figure 6.21. This improvement allowed to resolve that the regions where the fragments appeared lighter did not have the same intensity as the background, suggesting that they are not pores, but rather silica-rich areas. The images also allow resolving the structure of the infiltrating material, which consist of nanoparticles with a distribution of sizes ranging from 5 to 20 nm. The HAADF images allow discarding those features whose contrast stems from thickness rather than their mass. Significantly, the region imaged in 6.24(c) shows three dark circles with diameters of 10, 25 and 30 nm. These features could suggest heavy depositions of ceria on the silica-rich region. However, the absence of these features from the dark field image in 6.24(d) indicates that these are features associated with thickness and not an atomic number.

Therefore, it can be stated that the fragment is entirely filled with ceria and that the lighter contrast regions are changes of thickness, which are directed during the growth of the material by the network of silica walls and the shape of the fragment of MSU-F.

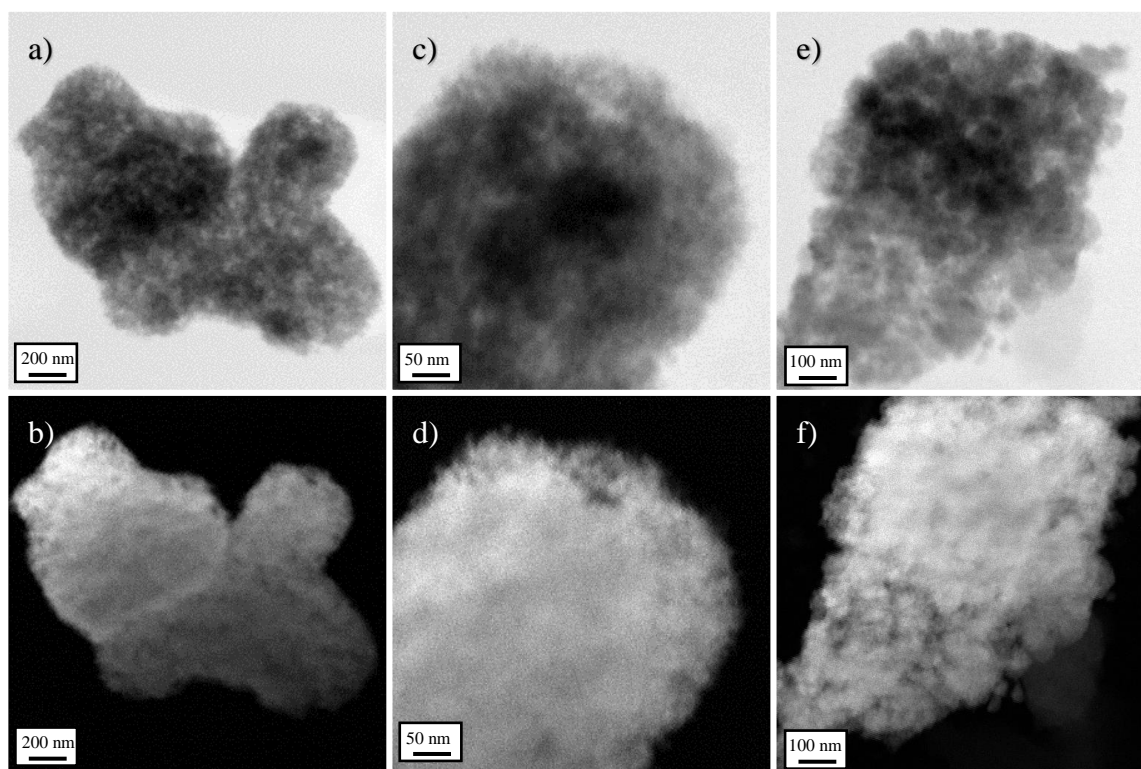


Figure 6.24 STEM of MSU-F/CeO₂ composite. Bright-field images (top) and respective HAADF images (bottom) (Images acquired using JEOL 2010F at 200 kV Samplings: (a,b)=0.2 nm/pixel, (c,d)=0.05 nm/pixel, (e,f)=0.1 nm/pixel)

The studies above successfully identified the presence of silica and the infiltrating product, as well as their distribution at the nanoscale. However, further analysis was performed to ensure that the infiltrating product was indeed CeO₂. An incomplete transformation of Ce(NO₃)₃·6H₂O could lead to unwanted by-products occupying the structure. The amorphous nature of cerium nitrate would make it invisible in the FFT patterns, and the identical masses of Ce⁴⁺ and Ce³⁺ would make them indiscernible in HAADF-STEM images. The chemical identification performed using EDX and shown in Figure 6.23 would not be suitable to differentiate Ce(NO₃)₃·6H₂O from CeO₂, since the cerium peaks would appear the same and nitrogen is not suitable for identification in most EDX instrumentations. Figure 6.25 shows the results of an EELS analytical study identifying the peaks most relevant to this work. Initial exploration is shown in 6.25(a), which also contains a transmission image of the area selected for this analysis.

Spectrum 6.25(a) shows four significant peaks CK at 284 eV, which is associated with the carbon film substrate used to suspend the sample; OK at 532 eV, which corresponds to the silica and ceria and two peaks of cerium, CeM₅ at 883 eV and CeM₄ at 901 eV. The areas containing these peaks have been magnified in spectra 6.25(b) and (c) for illustration. Spectrum 6.25(d) also provides significant information. The spectrum shows a strong edge at 110 eV associated with CeN_{4,5}. Notably, the spectrum shows no edge at 401 eV, which would correspond to the presence of nitrogen associated with Ce(NO₃)₃·6H₂O.

The absence of a nitrogen edge at 401 eV, as well as the CeM₄ peak having a notably larger area than the CeM₅, indicate that the product filling the structure of the MSU-F is entirely cerium(IV) oxide with no unconverted precursor. The absence of a signal at 99 eV, which would be expected from SiL_{2,3} from the silica in the composite could suggest that the particular area used for this study was particularly rich in ceria. However, a more likely interpretation is that the region being analysed was too thick.

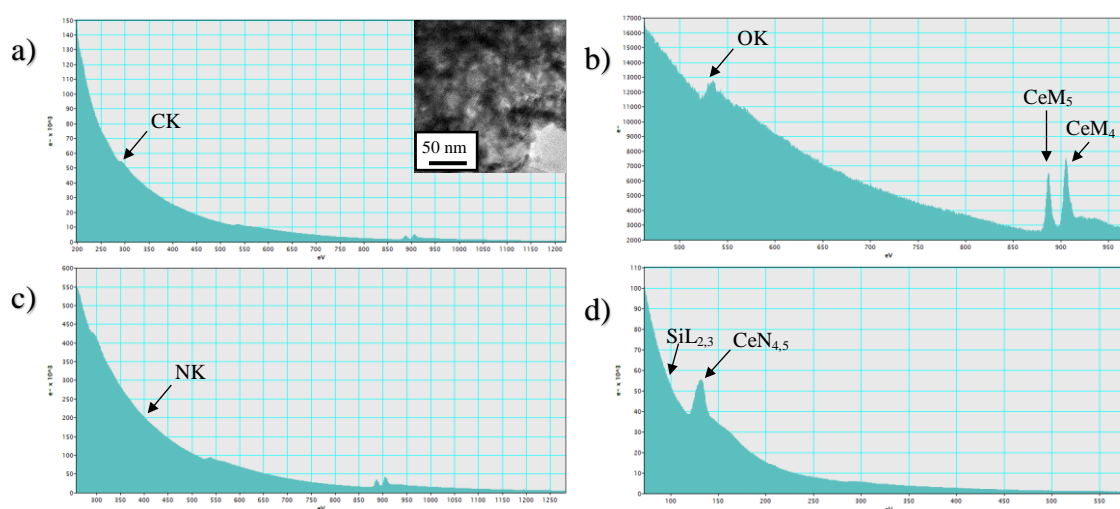


Figure 6.25 EELS spectra of MSU-F/CeO₂ composite (Image and spectra acquired using JEOL 2010F at 200 kV. Sampling=0.05 nm/pixel)

6.2.1.3 Chemical etching of MSU-F/CeO₂ composite

Template removal is a process usually associated with nanocasting. In section 6.1.5, a process was implemented for the removal of the polystyrene template using calcination. Given the high evaporation point of silica, it is not possible to remove an MPS template with the same method. Therefore, the removal of silica templates has to be performed via chemical etching. A large majority of publications use solutions of hydrofluoric acid to dissolve the silica template leav-

ing behind a negative silica structure of the infiltrating material. The use of HF carries significant health and environmental hazards and requires elaborate considerations for its operation and disposal. Furthermore, HF also reacts strongly with CeO_2 . Thus it would dissolve both phases in the composite. In this work, it is proposed that the products can instead be etched in alkaline high-concentration solutions of sodium hydroxide at 80 °C. This method can be found in the literature as an effective alternative to HF for the dissolution of silica [390]. It has also been used for the treatment of MCM-41, as reported by Shao et al. [391]. However, it has not been implemented in the fabrication of negative MSU-F ceria nanomaterials.

The remaining powder of MSU-F/ CeO_2 composite studied above was treated in [2 M] aqueous solution of sodium hydroxide at 80 °C. The solution was stirred continuously throughout to promote temperature distribution as well as aiding the alkaline solution to penetrate the structure of the composite. Samples were collected after two, four and six hours stopping the reaction in each tube by adding deionised water, which diluted the alkali and lowered the temperature. The products were washed by rinsing with deionised water, ultrasonicing for 15 minutes, centrifuging and decanting. This process was repeated five times until the wastewater had a neutral pH value. The 6-hour sample was mounted on carbon-coated copper grids for TEM imaging and analysis. The chemical analysis of the etched sample collected after six hours of reaction is shown in Figure 6.26.

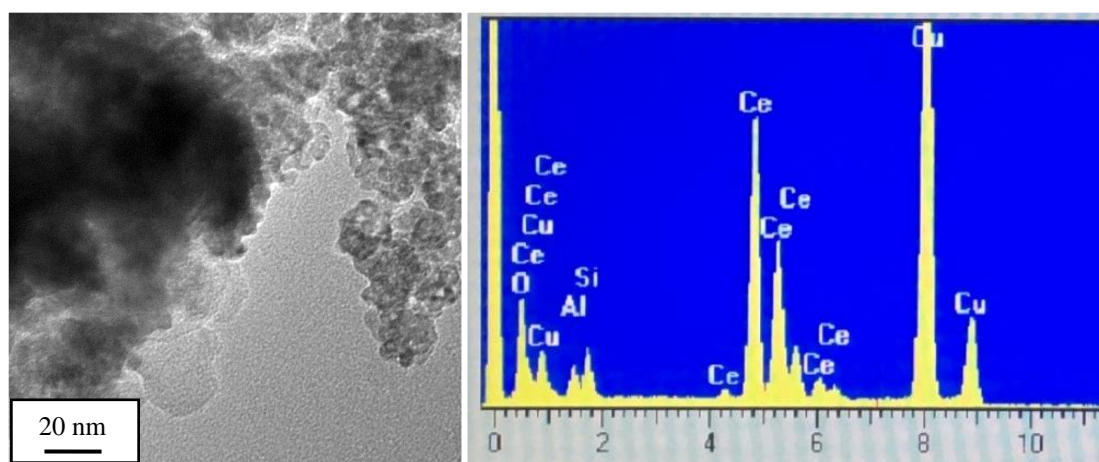


Figure 6.26 EDX spectrum of NaOH-etched MSU-F/ CeO_2 composite (x-axis indicates keV) (Image and spectrum acquired using JEOL 2010F at 200 kV. Sampling=0.014 nm/pixel)

The region selected for analysis was considered representative of the sample and contained a thick region of material, which could provide elemental information of the material to a significant extent. The spectrum in the figure shows strong signals from copper. These are associated with the sample holder and are not quantified as part of the product of interest. That

aside, the sample shows strong signals of cerium and weak peaks associated with silicon and aluminium. The presence of aluminium is not unexpected and is likely associated to the carbon film used as support for the TEM specimen, as discussed in section 6.1.1 of the Experimental Methods. Aluminium also appears as a common by-product in MSU-F, as reported by the manufacturer.

Quantification of the spectrum selecting the three elements associated with the composite rendered approximate atomic percentages of 62 at% O, 6 at% Si and 32 at% Ce. This constitutes a reduction of around 50% in the content of silica when compared to the results of EDX analysis of the composite before etching, shown in Figure 6.22. Although the removal of the template was incomplete, the results are promising. The dissolution of silica template could continue with longer etching times.

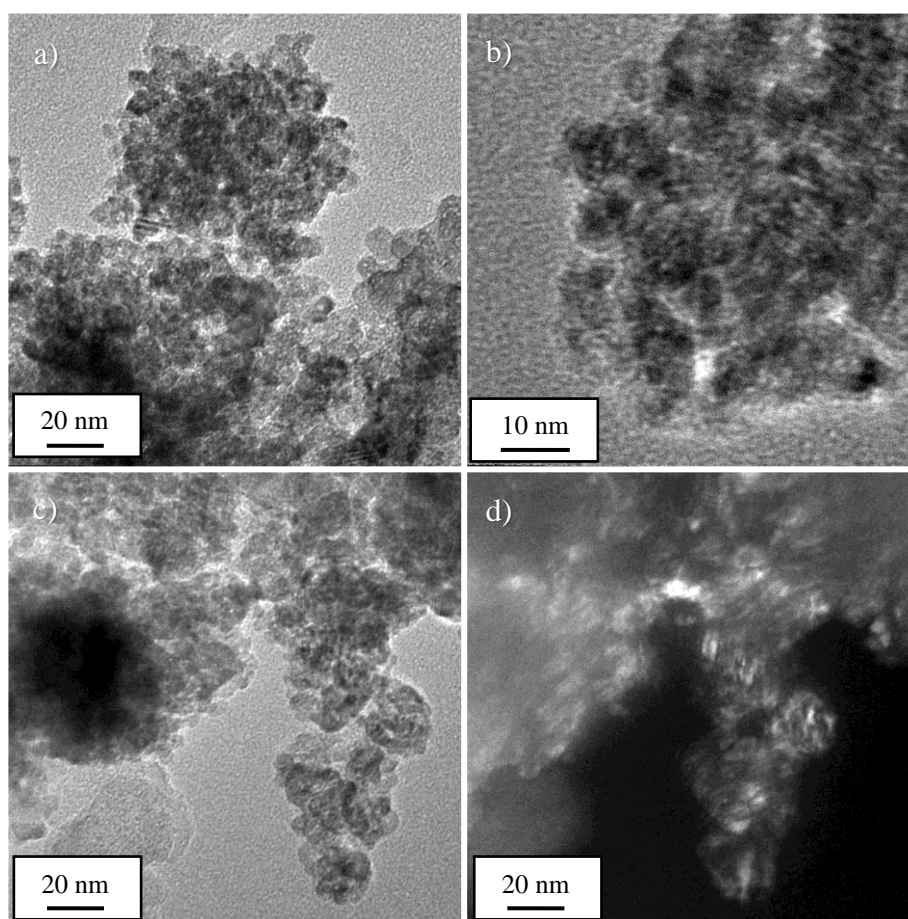


Figure 6.27 TEM images of etched MSU-F/CeO₂ composite (Images acquired using JEOL 2010F at 200 kV Samplings: (a)=0.02 nm/pixel, (b)=0.01 nm/pixel, (c,d)= 0.022 nm/pixel)

The prevalence of aluminium signals could be associated with an impaired ability of NaOH to dissolve aluminium oxide compared to its capacity to attack and dissolve silica. However, the content of aluminium in most mesoporous-silica materials is marginal or non-existent. Therefore, it is more likely a stray-signal generated by the sample holder.

TEM images of the etched composite are shown in Figure 6.27. The material continues to form long-range agglomerates in spite of the partial removal of the silica template. The ceria nanoparticles forming the agglomerate are closely packed, and they maintain sizes and shapes consistent with the porous structure of MSU-F. The dark-field image 6.27(d) shows the same area as 6.27(c) and emphasises the polycrystalline nature of the material, which can also be appreciated in the high-magnification image 6.27(b). The prevalence of a system of nanoparticles with sizes ranging between 5-20 nm is illustrative of the nanocasting mechanism of ceria in MSU-F, which does not create a continuous solid of ceria like the inverse opals in section 6.1.5. Instead, the product of nanocasting in MSU-F produces a close-packed array of nanoparticles with sizes limited by the pores in the starting silica material.

6.2.2 Study of SBA-15 and SBA-15-based composites

SBA-15 is one of the most common mesoporous-silica materials for a diversity of applications, as described in section 2.1.2 of the literature review. The determining characteristics of SBA-15 are the high periodicity of its pores and the pore-diameter uniformity. For the present study, this material provides an appropriate comparison to the MSU-F structure studied in the previous section. Mainly, this work seeks to elucidate the mechanisms of infiltration involved in the fabrication of SBA-15/metal oxide composites via nanocasting. For comparison, two different infiltrating materials have been selected, a ceria precursor and a copper(II) oxide precursor.

Initial characterisation of the SBA-15 material as-received was performed by lightly crushing the powder in a mortar and suspending it in isopropanol. A drop of the suspension was added to a standard-grade carbon-coated copper grid for TEM imaging. The results are shown in Figure 6.27. The images show a highly porous material, which is periodical in a hexagonal arrangement. All pores show a symmetrical shape with square walls suggesting a tetrahedral geometry in three-dimensions. The pores have a projected diameter of 7.5 nm with narrow size distribution. Both images show large fragments of material extending over several hundred nanometers.

Both sets of images in Figures 6.28 and 6.18 were acquired using a high-tension beam of 200 kV. However, the fragments in Fig. 6.28 show a much darker contrast with the background C-film than a fragment of similar dimensions in Figure 6.17(a). Given that both materials have similar chemical compositions, the contrast can be attributed to the difference in periodicity. MSU-F has a random arrangement of pores, which causes the electrons to travel through fewer

layers of solid material at most orientations of the MPS object. In opposition, the highly-ordered arrangement of SBA-15 causes the walls between pores to align across the direction of the electron beam interrupting the transmission at shorter intervals than MSU-F.

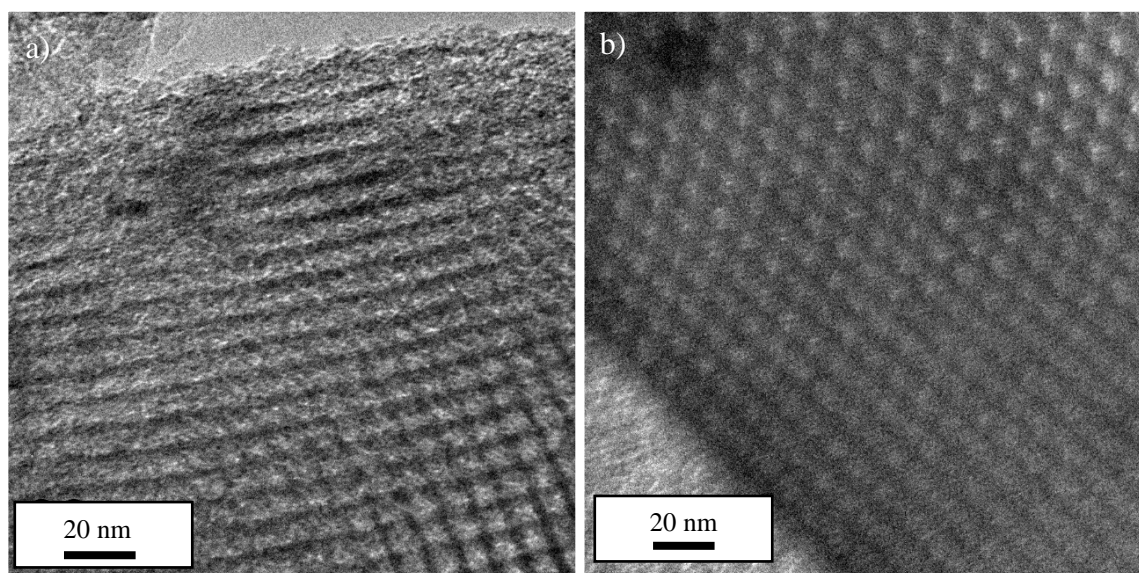


Figure 6.28 TEM images of MSU-F mesoporous silica
 (Images acquired using JEOL 2010F at 200 kV Samplings:
 (a)=0.02 nm/pixel, (b)=0.018 nm/pixel)

This effect serves to illustrate the complications encountered during the acquisition of tilt series of MSU-F intended for tomography, described in section 6.2.1.1. At certain angles of rotation, the walls in the MSU-F structure will align across the direction of the electron beam causing the apparent thickness to increase suddenly and obscure regions, which appeared transparent at other angles of projection. Consistently, at viewing directions where the walls align more narrowly across the path of the electrons, so do the pores. This produces a high-contrast view like the one in image 6.28 (b), where the walls appear dark even at the thinner terminal region of the fragment, and the pores appear bright.

6.2.2.1 Preparation and characterisation of SBA-15/CeO₂ composite

A composite of SBA-15 and cerium(IV) oxide was prepared following the experimental procedures outlined in section 6.2.3. As the procedure of incipient wetness impregnation proved more effective in the fabrication of MSU-F/CeO₂ composite, this method was chosen for the infiltration of SBA-15 silica template. First, the template was heat-treated at 100 °C for four hours to eliminate water and volatile products. The SBA-15 powder was spread on a watch

glass to form a thin layer. 500 μl of [5 M] $\text{Ce}(\text{NO}_3)_3 \cdot 6\text{H}_2\text{O}_{(\text{aq})}$ were added to the powder and allowed to dry at room temperature before heating at 400 $^\circ\text{C}$ for 4 hours. The steps were repeated twice more lowering the concentration of ceria precursor to [3.75 M] and then to [2.5 M]. The product was a light-yellow powder consistent with ceria products. The solid was ground and suspended in isopropanol for mounting onto a carbon-coated copper grid for TEM imaging and analysis. The TEM images of the SBA-15/ CeO_2 products are shown in Figure 6.29.

The products characterised in Figure 6.29 appear to be heavier than the empty SBA-15 in Figure 6.28, yet still, show periodical pores. The periodicity of the SBA-15 template can be appreciated in image 6.29(a), which shows a product oriented in such a way that the electrons can travel between thick layers of material. Another way to highlight the structure of the silica phase in the composite is to acquire images deliberately out of focus, as seen in image 6.29(c). This results in the walls of silica appearing bright in the transmission image before the dark fill-in material.

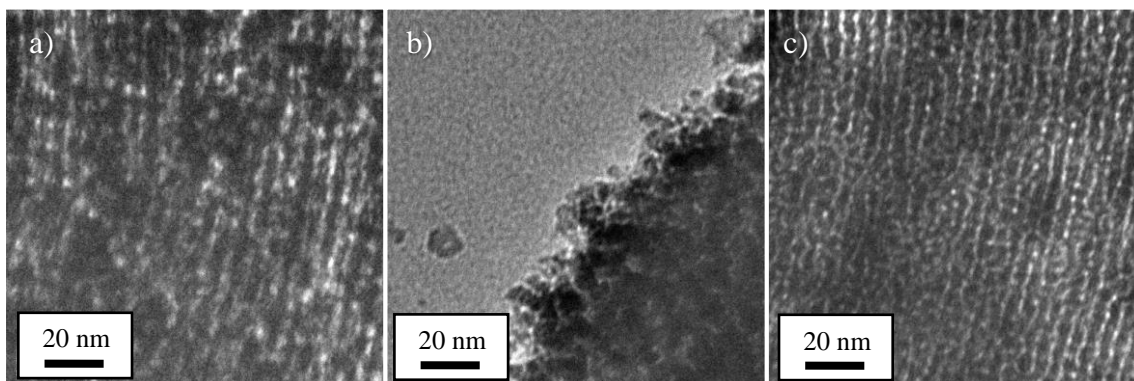


Figure 6.29 TEM images of SBA-15/ CeO_2 composite
(Images acquired using JEOL 2010F at 200 kV Samplings=0.011 nm/pixel)

Image 6.29(b) shows a view of the terminal structure of the composite, which provides information on the nanocasting mechanism at the nanoscale. Namely, the infiltrating agent has solidified into closely-packed nanoparticles occupying the structure of the SBA-15 template. The diameter of the nanoparticles seems to be 8 nm or smaller, suggesting that the growth of nanoparticles has occurred entirely inside the structure of SBA-15 and the size of the pores has determined the maximum size of the nanoparticles. Image 6.29(b) shows a group of nanoparticles sitting outside of the porous structure, which individually is below the range of pore diameter.

Further characterisation involved the acquisition of energy-dispersive X-ray spectra, such as the one shown in Figure 6.30. The results of EDX elemental analysis were consistent

throughout the sample. The spectrum shows strong signals of copper which can be attributed to the standard-grade copper grid used to mount the nanomaterials. Therefore, the copper signals, in this case, do not relate to the composition of the material. The remaining signals are consistent with a composite system of SiO_2 and CeO_2 . This data is supported by the quantification of the spectrum which showed atomic percentages of 33.12%_a O, 44.55%_a Si and 21.24%_a Ce. The oxygen signal is weaker than would be expected for the multi-oxide composite. However, EDX is not a reliable tool for oxygen quantification and is more appropriate for the identification of heavier elements.

Nevertheless, the 1:2 atomic ratio of both CeO_2 and SiO_2 means that the proportions of silica and ceria in the composite are directly correlated to the difference in area under the Si and Ce peaks in EDX spectrum. Silica appears to be predominant in the composition, in contrast with the composite of MSU-F and CeO_2 characterised by EDX in Figure 6.22. This is attributed to the larger pores in MSU-F which are on average 12 nm wider than those in SBA-15 structure. Furthermore, the random pore distribution of MSU-F can increase the connectivity throughout the network of pores, making it easier for the infiltrating material to penetrate the structure.

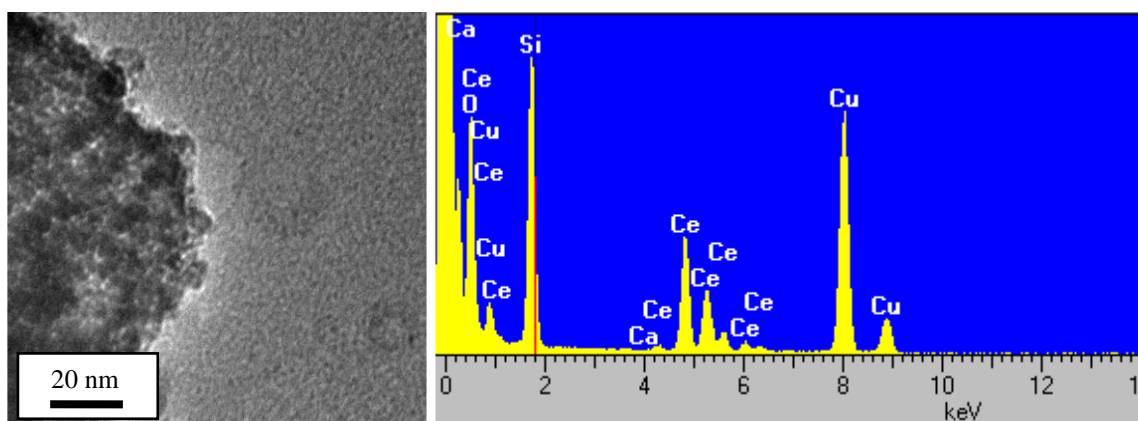


Figure 6.30 EDX spectrum and corresponding panel of SBA-15/ CeO_2 composite (Image and spectrum acquired using JEOL 2010F at 200 kV Sampling=0.011 nm/pixel)

6.2.2.2 Preparation and characterisation of SBA-15/ CuO composite

In order to study the influence of the infiltrating compound on the formation of MPS-based composites, a second composite was fabricated using a copper(II) oxide precursor. The preparation of the composite followed the procedures outlined previously of incipient wetness impregnation. First, the SBA-15 powder was heated for four hours at 100 °C. The powder was allowed to cool inside the furnace before spreading it into a thin layer to maximise the contact with the infiltrating solution, as well as facilitating more rapid evaporation of its water content.

A volume of 500 μl of [5 M] $\text{Cu}(\text{NO}_3)_2 \cdot 6\text{H}_2\text{O}_{(\text{aq})}$ was added to the solid and dried at room temperature to allow for the copper hydroxynitrate solution to penetrate the porous structure of SBA-15. The dry product was heat-treated for four hours at 300 $^\circ\text{C}$ based on the thermal decomposition curves of $\text{Cu}(\text{NO}_3)_2 \cdot x\text{H}_2\text{O}$ from the literature [392], shown in Figure 6.31.

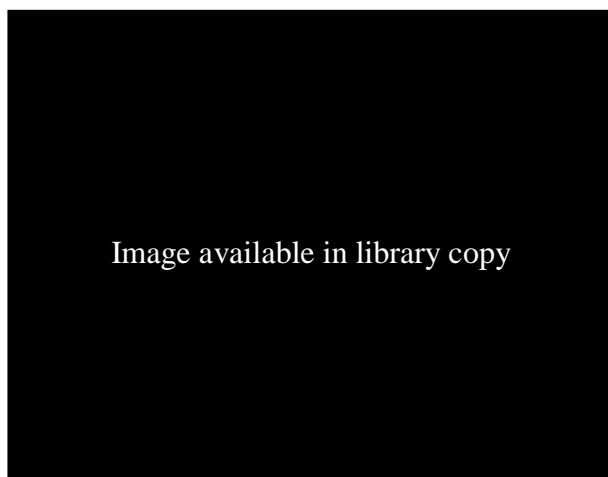


Figure 6.31 Thermogravimetric analysis curves, published by [392],
(a) DTG and (b) TGA of $\text{Cu}(\text{NO}_3)_2 \cdot x\text{H}_2\text{O}$

The steps of infiltration and heating were repeated twice more with [3.75 M] and [2.5 M] solutions of copper(II) oxide precursor. The final product was a black matte powder, which provided a strong indication that the oxidation state of the cation was +2. Copper(II) oxide can be easily differentiated from the also common copper(I) oxide, which consists of distinctly red powder. The solid was ground into smaller fragments using a pestle and mortar and briefly suspended in isopropanol before being added to the standard-grade carbon-coated gold grid for TEM imaging and analysis. The choice of a gold TEM grid was motivated by the potentially indiscernible elemental spectroscopy signals from the copper oxide in the and the metal conforming a standard-grade TEM copper grid. The first stage of TEM characterisation of SBA-15/CuO composite is shown in Figure 6.32, which shows high-resolution images of representative regions of the sample. Image 6.32(a) highlights the periodical porous structure of SBA-15 and displays several nanoparticles at the edge of the structure. The symmetrical shapes and 8-nm diameter of these nanoparticles are consistent with the pore structure of SBA-15. Image 6.32(b) shows a region where the SBA-15 structure is oriented against the electron beam creating high-contrast in the structure.

The constant image contrast across the structure suggests the absence of CuO nanoparticles in the region. Images 6.32(c) and (d) show the bright-field and dark-field acquisitions of a region showing a typical SBA-15 and a fragment with no periodical features. The dark-field image allows identifying the distribution of crystalline regions of CuO in the silica structure.

Mainly, the region presenting periodicity in 6.32(c) is virtually absent from view in 6.32(d), which suggests that the region is rich in silica and contains small amounts or no copper(II) oxide. However, in the region conformed by the second fragment in the panel, there are several bright features consistent with CuO nanoparticles. These particles show diameters equal to the pore diameter or smaller, with the smallest being 2 nm. These results support the mechanism put forward in previous sections that nanocasting of mesoporous silicas with sol-gel oxide precursors results in arrays of nanoparticles filling up the porous structure.

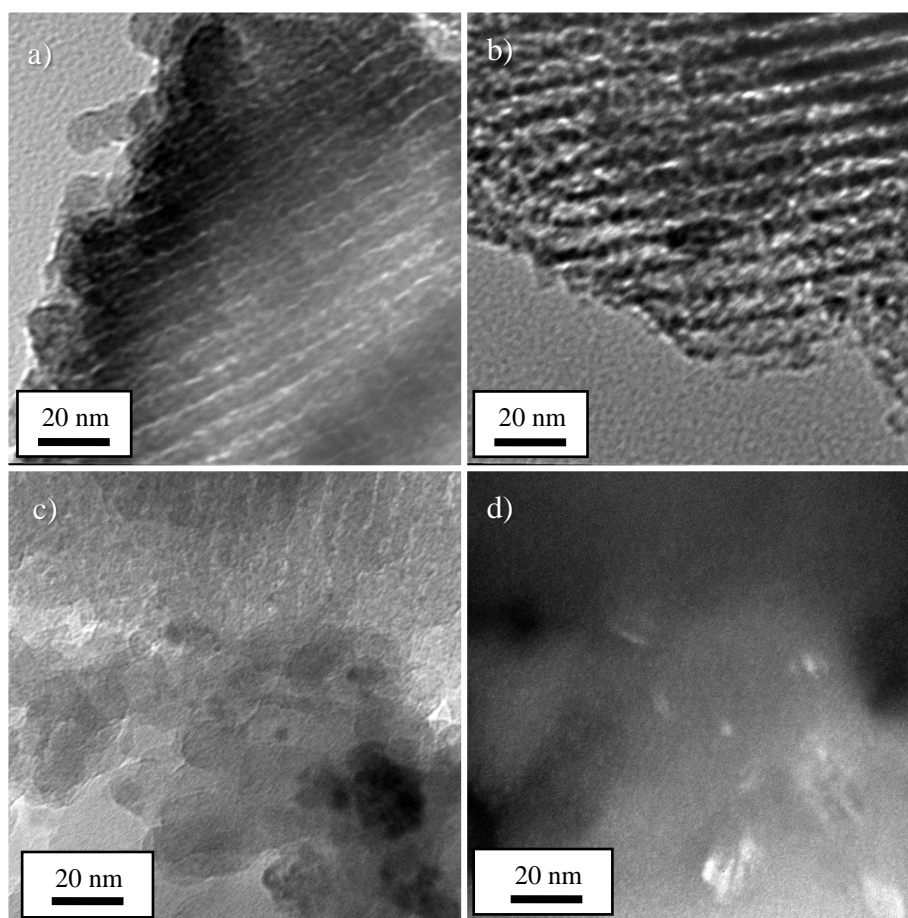


Figure 6.32 TEM images of SBA-15/CuO composite acquired in conventional (a-c) bright-field and (d) dark-field modes (Images acquired using JEOL 2010F at 200 kV Samplings=0.011 nm/pixel)

The composition of the material was analysed, acquiring an EDX spectrum of a representative region, as shown in Figure 6.33. The spectrum shows peaks representative of gold, which are associated with the metal in the TEM grid containing the nanomaterial. The remaining peaks are associated with the elemental composition of a silica/copper oxide composite.

The analytical results show strong peaks for both Cu and Si, which suggest a prevalence of both CuO and SiO₂. These signals are consistent with the structures observed in the images in Figure 6.32. Namely, if the nanocasting mechanism resulted in a continuous solid occupying the mesoporous structure of SBA-15, the content of copper would be several times higher than the content of silica. This has not been observed in any of the samples, except for the etched MSU-F/CeO₂ composite. This estimation can be based on the structural properties of SBA-15, which has walls with smaller lateral dimensions than the diameters of the pores they contain. This correlation results in the SBA-15 bulk material having a characteristically low density compared to non-porous silica. Therefore, the similar intensities of the Cu and Si peaks indicate that the volume of the material is still mostly occupied by empty space contained by the network of thin walls of silica, which also hosts copper(II) oxide nanoparticles with dimensions smaller or equal to the mesopores.

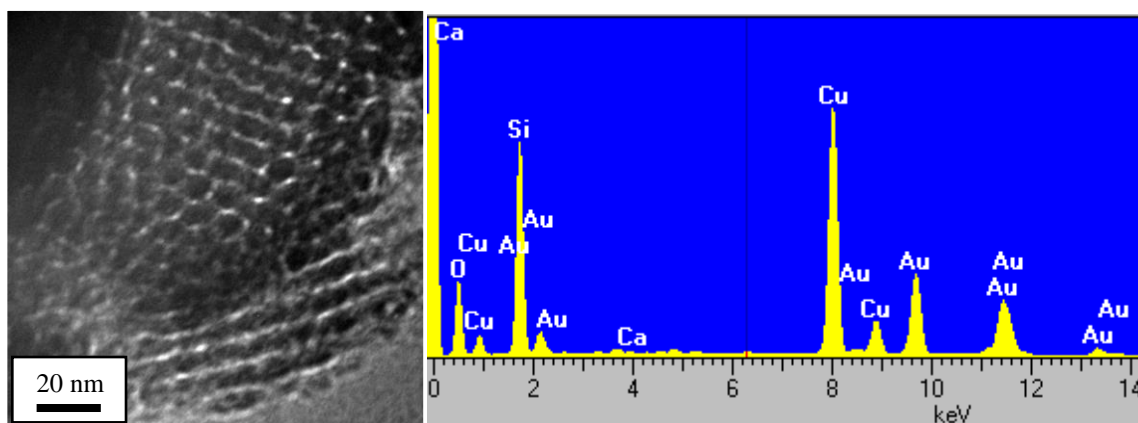


Figure 6.33 EDX spectrum and corresponding panel of SBA-15/CuO composite
(Image acquired using JEOL 2010F at 200 kV Sampling=0.012 nm/pixel)

Further characterisations of SBA-15/CuO composite utilised the lower magnification capabilities of SEM imaging and elemental analysis. These methods sought to identify the behaviours of species during nanocasting at the micrometre-scale. An SEM specimen was prepared by placing small amounts of powder directly onto an adhesive conductive-carbon dot. The area of the carbon dot was used to contain three powders representative of the different stages of fabrication of the SBA-15/CuO composite: Empty SBA-15; SBA-15/Cu(NO₃)₂·6H₂O, collected during the first cycle of infiltration; and SBA-15/CuO after three cycles of infiltration/calcination. The results of this characterisation can also be used to assess the efficacy of the incipient-wetness impregnation method described in previous sections for the fabrication of composite products. Mainly, these results serve to complement the SEM characterisations

published by Gaudin et al. [393], who evaluated the efficacy of several methods to fabricate SBA-15/CuO.

Figure 6.34 shows the SEM characterisation of as-received SBA-15 in secondary electron imaging mode. The images highlight the preferential formation of rough spindles of MPS material, which extend beyond 100 μm . The material also appears as fragments with a higher image ratio and smaller size than the spindles. Image 6.34(c) shows a close-up of one of these small fragments, which appears to be an agglomerate of needle-shaped fragments.

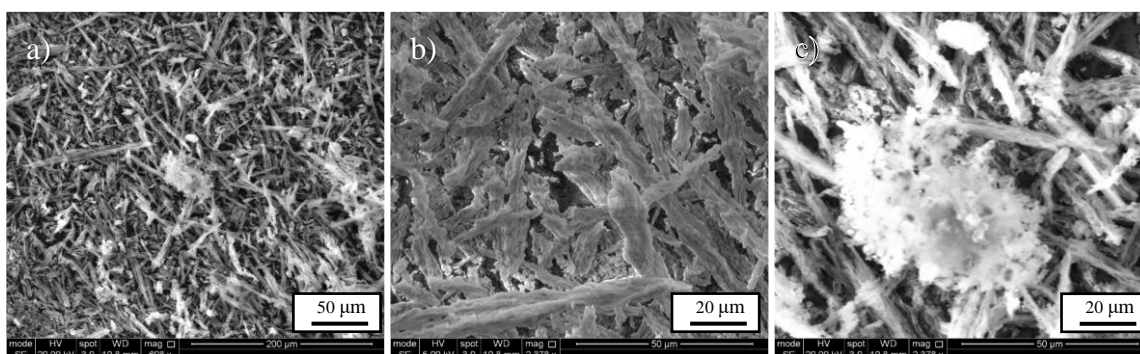


Figure 6.34 SEM images of as-received SBA-15 (Images acquired using FEI Inspect F50 at 20 kV in SE mode. Magnification values: (a) 608x, (b) 2378x, (c) 2378x)

The medium magnification images 6.34(b) and (c) also reveal the structure of each fragment to be porous at the μm -scale. The results of this characterisation suggest that SBA-15 has a hierarchy of porosity in at least three levels; the macroscale porosity formed by the arrangement of spindle-shaped fragments larger than 100 μm , the microscale porosity contained in each spindle-shaped fragment, and the nanoscale highly-ordered porosity characterised in Figure 6.28.

In order to understand the mechanism of infiltration driving the processes of nanocasting, it was useful to study the intermediate products that occur during the infiltration/calcination cycles. Here is reported an SEM characterisation of the dried product of the infiltration of SBA-15 with an aqueous solution of $\text{Cu}(\text{NO}_3)_2 \cdot 6\text{H}_2\text{O}$ [5 M], before heat-treatment steps. Figure 6.35 shows a set of SEM images at medium magnification. The images show secondary-electron and back-scattered-electron acquisitions of the same area at the same magnification.

The comparison of these two images has been used to discern the regions of variable thickness as well as the regions of variable composition. Image 6.35(a) shows a product with smaller fragments on average than the one characterised in Figure 6.34. This is easily explained by the necessary grinding step which reverts the dried SBA-15/ $\text{Cu}(\text{NO}_3)_2 \cdot 6\text{H}_2\text{O}$ product to a powder

form. This observation is consistent with the fact MPS products seemed unaffected at the nanoscale by the grinding step used to create suspensions for TEM. This statement is based on the SBA-15 fragments maintaining their average dimensions throughout the nanocasting process, in spite of the multiple steps of grinding necessary for each cycle of infiltration/calcination. These results indicate that manual grinding of the products affects the size of fragments at the microscale more significantly than at the nanoscale.

The product in image 6.35(a) is formed by continuous spindles unlike the porous ones seen in Figure 6.34 (c) this is a significant difference since it implies that these pores have been filled by the copper salt. Image 6.35(b) shows the BSE image of the same area, which shows no major changes in contrast. Considering the Z values of Si (14) and Cu (29), the results in image 6.35(b) suggest further that the infiltrating copper salt has occupied the SBA-15 structure homogeneously and penetrated at least the microscale pores which can be resolved by the imaging methods shown here.

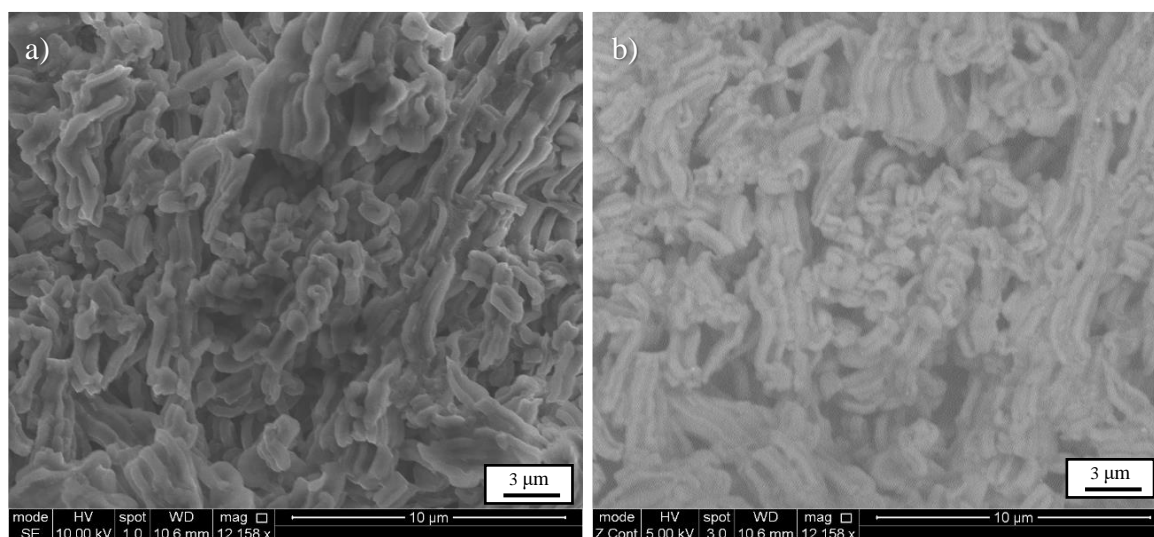


Figure 6.35 SEM images of SBA-15/ $\text{Cu}(\text{NO}_3)_2 \cdot 6\text{H}_2\text{O}$ composite acquired using (a) SE and (b) BSE modes (Images acquired using FEI Inspect F50 at 5 kV. Magnification values=12158x)

Following the steps of the fabrication method, the next phase of advanced SEM characterisation studied the distribution of silica and copper(II) oxide in the final composite product. That is a product which has been treated with $\text{Cu}(\text{NO}_3)_2 \cdot 6\text{H}_2\text{O}$ three times at decreasing concentrations and calcinated according to the transformation temperatures seen in Figure 6.31. Initial characterisation of the multi-oxide composite is presented in Figure 6.36, which shows two pairs of images, each pair consisting of a secondary-electron and back-scattered-electron acquisitions of the same area. Image 6.36(a) shows the material agglomerating into shapes with

high image ratio maximising their area of contact, which diverts significantly from the behaviour observed during the previous stages, as seen in Figures 6.33 and 6.34.

The change in the shape of the fragments from spindle-like geometries to the nearly spherical morphologies seen in Figure 6.36 is explained by the multiple steps of heat treatment. Meanwhile, the reduction of particle size is counterintuitive after heat treatment but can be explained by the multiple stages of grinding involved in the preparation. There are major changes in contrast across SE images 6.36(a) and (c), which indicate that the material continues to exhibit porosity at the macroscale and has not agglomerated into a continuous solid.

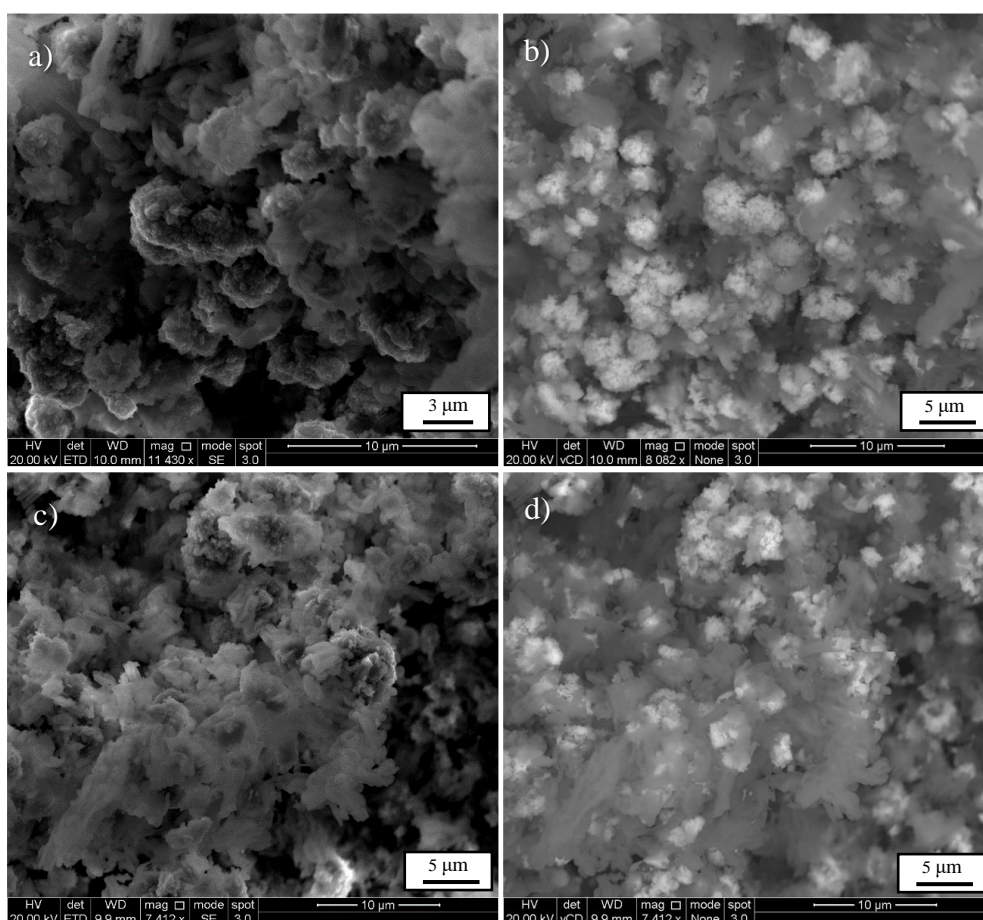


Figure 6.36 SEM images of SBA-15/CuO composite in (a,c) SE and (b,d) BSE modes (Images acquired using FEI Inspect F50 at 20 kV. Magnification values: (a)11430x, (b)8082x, (c)7412x, (d)7412x)

On the other hand, the presence of contrasting features in the BSE images 6.36(b) and (d) indicates a clear separation of phases with regions of the sample being much higher in Z than others. I. e., the composite consists of silica-rich regions and cupric-oxide-rich regions, the latter appearing much brighter in BSE imaging mode. This result is surprising considering the

lack of contrast in the BSE image in Figure 6.34, which showed the copper salt evenly distributed across the silica material. The characterisations in this study at multiple stages of the nanocasting process show that the segregation occurs during the calcination stage and is not a product of an incomplete infiltration.

Given the findings above, which could suggest the occurrence of segregation in the production of the silica/cupric oxide composite, a comprehensive EDX study was performed to identify the extent of the segregation. That is, whether there is a significant presence of CuO in the silica-rich phases and vice versa. Figure 6.37 shows a BSE image of the area selected for the EDX study. There are visible differences in composition across the panel, as identified by the differences in brightness of each feature. The regions of interest for subsequent studies have been annotated on the BSE image.

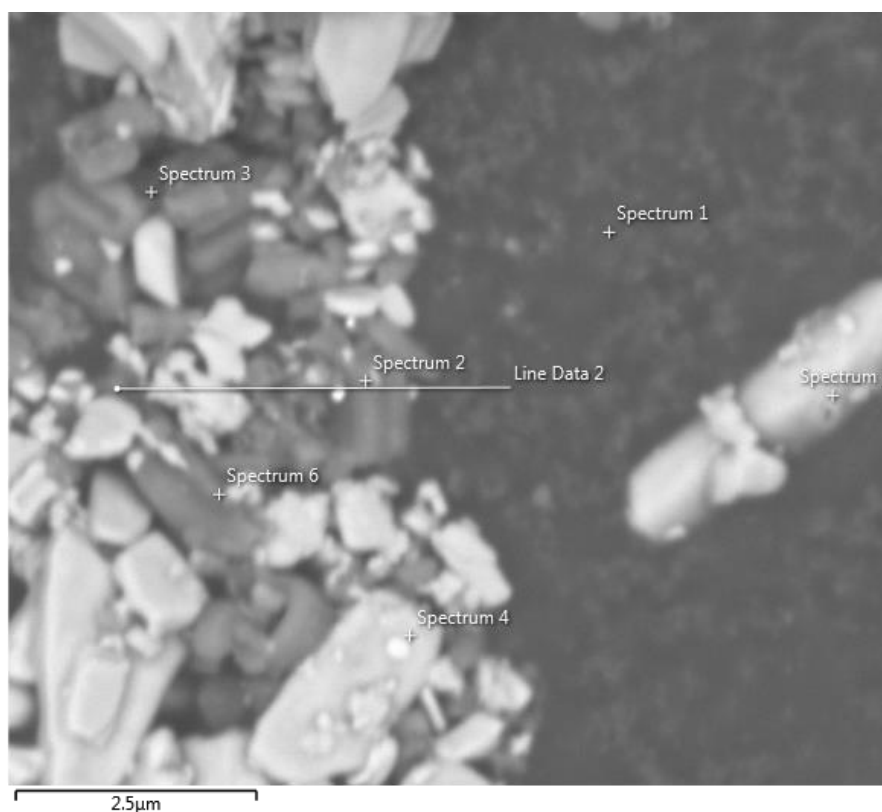


Figure 6.37 SEM/BSE image of SBA-15/CuO composite (Image acquired using FEI Inspect F50 at 20 kV in BSE mode. Magnification value=7412x)

The initial step of EDX characterisation showed the composition at specific points of interest identified in the image above. The spectra are shown in Figure 6.38 and summarised in table 6.3 where each individual spectrum corresponds to a point annotated in Fig. 6.37, as indicated at the top right corner of each frame. The first spectrum corresponds to the darkest

region in the BSE image and, accordingly, contains the elemental composition with the lowest atomic number.

The spectrum showed a strong signal of carbon, which produced the most counts per second per eV across all the spectra in the figure. Therefore, the dark region containing the point selected for Spectrum 1 can be associated with the conductive carbon tape used to suspend the sample. Significantly, the signal associated with oxygen content was weak. This result is indicative of the appropriateness of carbon-based films and supports used throughout this experimental work. The traces of copper oxide found on the carbon support are an expected product of the nanocasting process, which relies on heavily saturated infiltration solutions. The high concentrations of these solutions can produce significant amounts of oxide by-product, which does not occupy the silica structure.

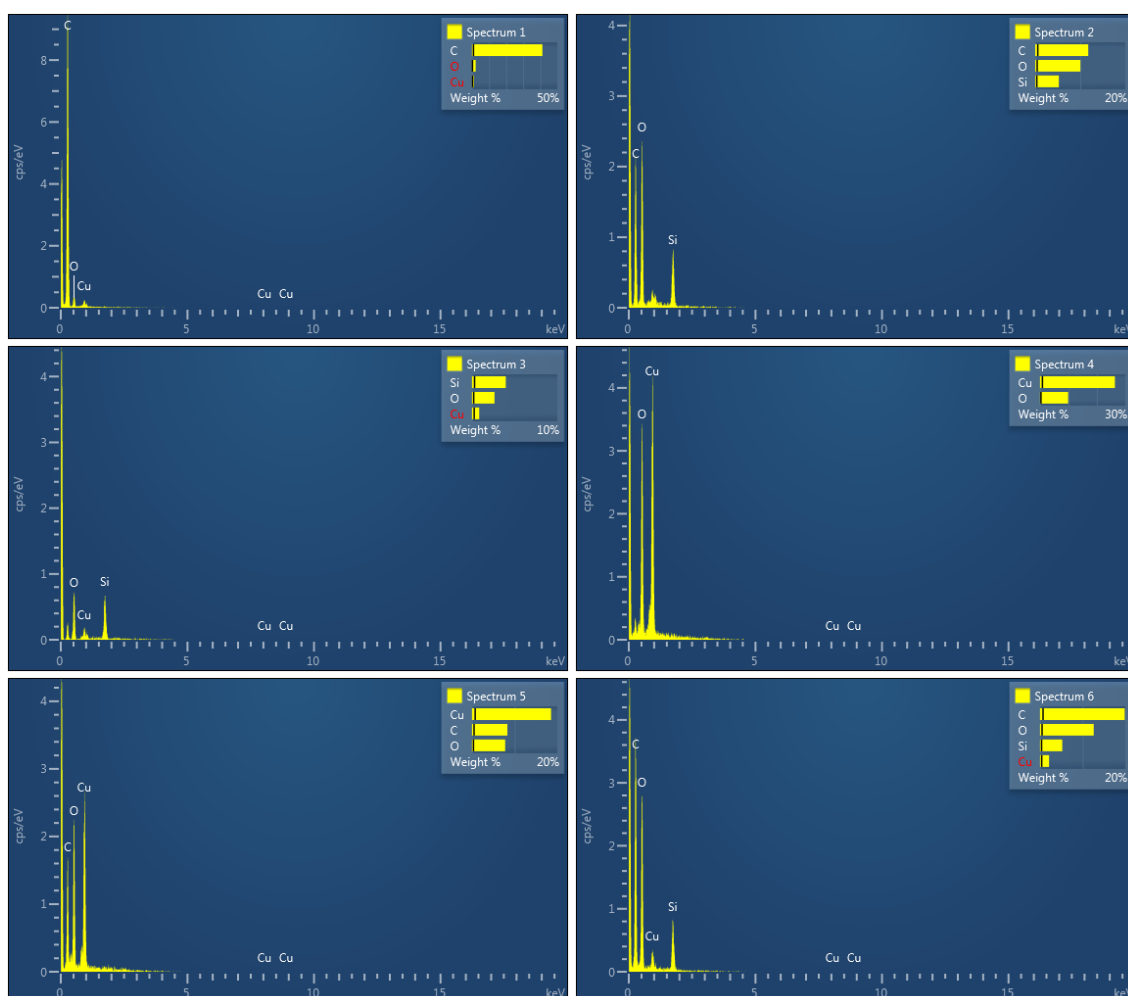


Figure 6.38 EDX point spectra of selected regions in SBA-15/CuO composite on carbon tape.

The correlation to Fig. 6.37 is indicated at the top-right corner of each frame (Spectra acquired using FEI Inspect F50 at 20 kV. Corresponding panel shown in Fig. 6.37)

Table 6.3 Outputs of EDX point spectra shown in Fig. 6.38

Spectrum	Relative wt%			
	C	O	Cu	Si
1	95.6%	4.4%	-	-
2	44.6%	37.2%	-	18.2%
3	-	37.2%	8.9%	53.9%
4	-	25.2%	74.8%	-
5	24.3%	21.6%	54.1%	-
6	48.8%	3.4%	6.1%	41.7%

The second spectrum corresponds to a dark grey portion of the material identified in Fig. 6.37, which was expected to be rich in silica owing to the lower Z of Si than Cu. Consistently, the spectrum shows clear signals of silicon and oxygen accompanied by a weak signal at around 1 keV, which can be attributed to a low concentration of copper. This result suggests a minimal infiltration of the region with copper oxide. The considerable intensity of the C peak also indicates a porous light material allowing the electrons to penetrate to the background carbon tape and X-rays to produce a strong signal, which are indications of empty SBA-15 silica. Spectrum 3 was acquired in a region of dark grey appearance similar to spectrum 2. However, the results show concentrations of silicon and copper that are consistent with a SiO₂/CuO composite. More specifically, the area under the Si peak is 3 times larger than the Cu one, suggesting an incomplete infiltration.

Spectrum 4 corresponds to a bright region of material in figure 6.37, which rendered strong Cu and O signals consistent with deposition of copper oxide material outside the porous silica network. Spectrum 5 was acquired near the edge of an isolated heavy fragment of bright appearance in BSE imaging, which rendered strong copper oxide signals, as well as a marked carbon peak corresponding to the conductive tape in the background. Spectrum 6 was acquired in an area of dark-grey appearance in BSE imaging consistent with the silica-rich areas in spectra 2 and 3. The corresponding spectrum shows concentrations of silicon, copper and oxygen consistent with a composite of CuO nanoparticles partially occupying the pores of SBA-15 network. Overall, the EDX point analyses shown in Figure 6.38 suggested a range of significantly diverse compositions across the sample. Specifically, the CuO-rich regions showed no detectable content of silica, while the SiO₂-rich regions showed varying concentrations of CuO.

In order to expand on the results of the EDX point analysis, a comprehensive EDX-mapping study was conducted, as shown in Figure 6.39. First, a C map is presented which shows the

background consisting almost entirely of carbon, consistently with point-spectrum 1. Nevertheless, the presence of weak carbon signals elsewhere in the map can provide useful information on the porosity of the composite. Namely, the CuO-rich areas appear particularly dark whilst the regions rich in SiO₂ show varying intensities of carbon signal.

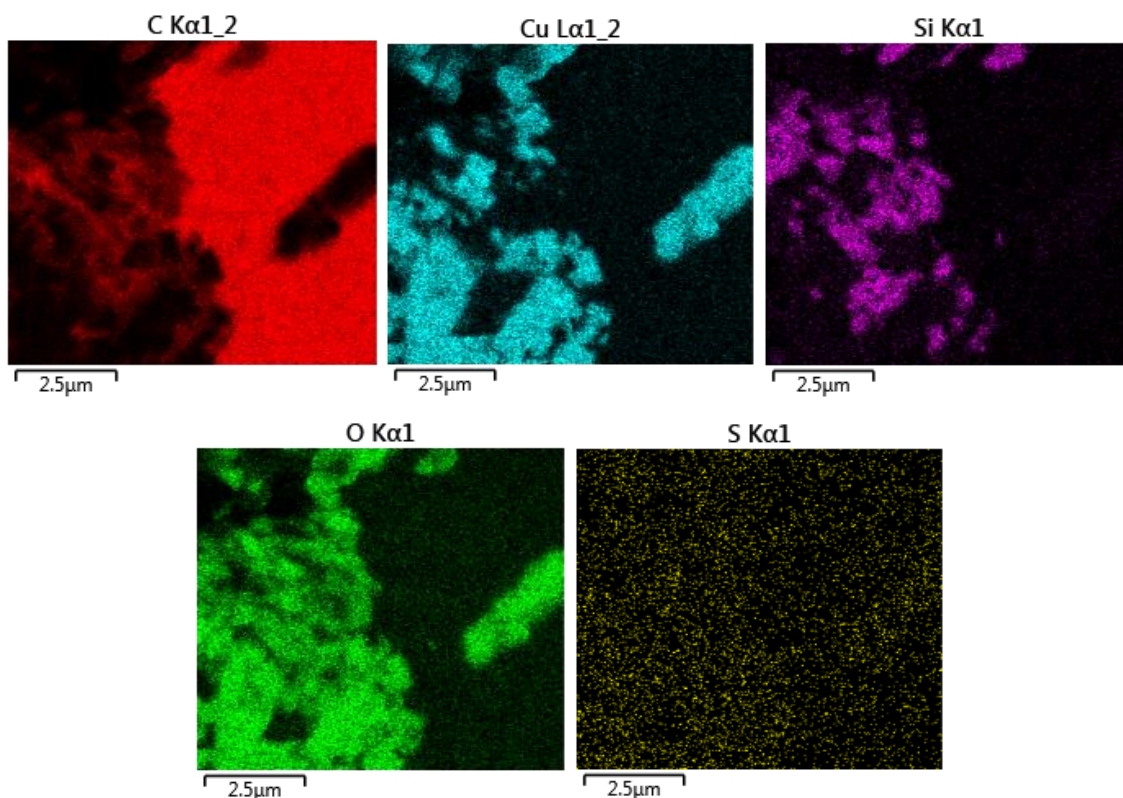


Figure 6.39 SEM/EDX mapping of SBA-15/CuO sample (Maps acquired using FEI Inspect F50 at 20 kV. Corresponding panel shown in Fig. 6.37)

These results confirm the hypothesis above that the CuO-rich areas contain only copper(II) oxide, while the SiO₂-rich areas can contain varying concentrations of CuO. The copper map presented next in the figure shows clearly defined fragments of oxide occupying the entire surface of the CuO-rich areas. However, smaller bright areas can be seen in the SiO₂-rich regions, which have a significantly different shape and dimension than the fragments in CuO-rich areas. This result suggests that the growth of copper(II) oxide material is dictated by the porous structure of SBA-15 and that the CuO signals observed in Si-rich areas are not associated with a powder by-product, but belong indeed to a composite material. The Si map confirms these statements as the concentration of silica does not appear to form well-defined fragments like the ones in the Cu map. A significant feature in this map is the continuity of Si signal across the silica-rich regions of the sample, which further suggests that the CuO nanoparticles generating the scattered signals in the Cu map occur inside of the mesoporous silica network.

The oxygen map shown in the figure illuminates both regions observed in copper and silicon maps. Most significantly, the map shows no intensity on the carbon background either near or away from the regions of catalytic CuO. This result confirms the observations above that conductive carbon is adequate to support and coating for the study of the catalytic oxide nanomaterials used in this study. The fragmented intensities of carbon signals across the C map are explained by the limited capacity of EDX to detect oxygen, especially below the immediate surface of the material. Finally, a background map of sulphur was acquired to show the systematic error present across the maps. The map is similar to the scattered oxygen signals seen in the carbon tape region of the O map. On the other hand, the S map signals are significantly different from the signals in the Cu map identified above as CuO nanoparticles, which have a higher intensity and are markedly localised.

A final step of EDX characterisation sought to examine the distribution of copper(II) oxide inside the SBA-15 networks across the silica-rich areas of the sample. To this end, a long-acquisition line-scan analysis is presented in Figure 6.40. The elements selected for this analysis are consistent with the signals identified in the point spectra, as well as the EDX maps above. The use of line-scan mode allowed to acquire EDX signals over a longer period to obtain accurate distributions of elements across the region of interest. The one-dimensional segment selected for this analysis is shown at the top of the figure and annotated as “line scan 2” in Figure 6.37.

The section of the material selected for analysis was considered to contain fragments that were representative of all the features of interest in the sample. Namely, the line section crosses through silica-rich areas, CuO-rich areas, as well as carbon tape areas. A sulphur line scan was recorded for the elimination of error-related signals. The signals of atomic percentage in the sulphur profile remain consistently below 1.5%_a and form sharp peaks associated with isolated signals. This result suggests that changes in concentration above 1.5%_a can be associated with the composition of the sample and are not the product of systematic error.

The carbon profile shows high continuous concentrations at both ends of the scanned section, which are consistent with the dark areas in the sample identified as the carbon tape supporting the powder. Nevertheless, the detected concentration of carbon reaches zero only at one individual point, which is located in a Cu-rich region. The continuous presence of carbon signals across the sample suggests that the material is porous throughout with the porosity decreasing significantly as the concentration of CuO increases, as seen by comparing the C and Cu profiles. The intensity of C-signals remains nearly constant across the Si-rich region visible in the Si profile.

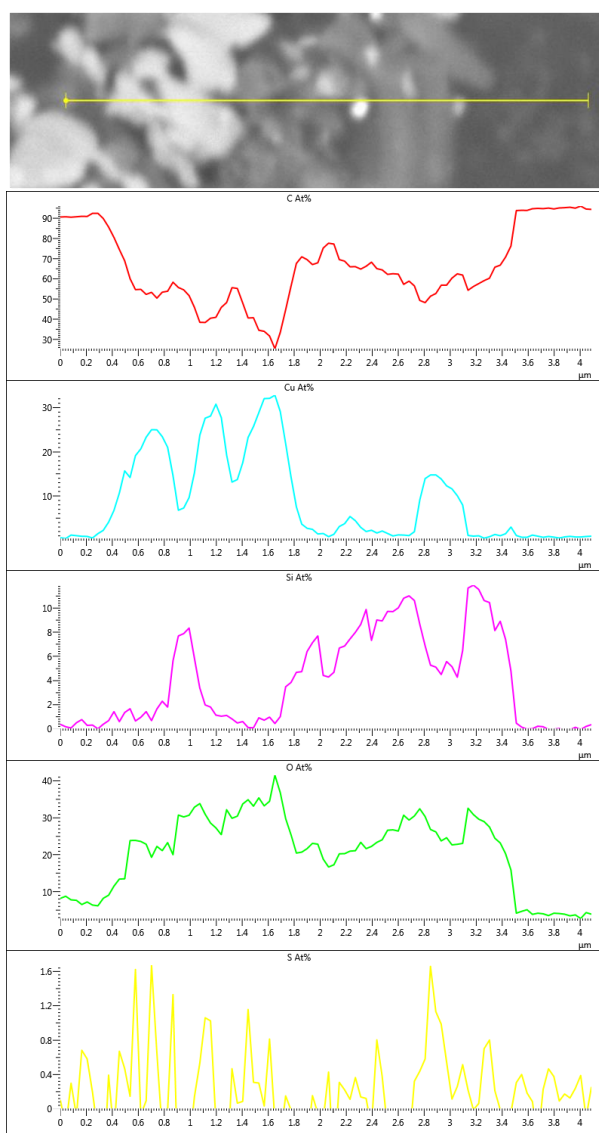


Figure 6.40 SEM/EDX line-scan of SBA-15/CuO sample (Maps acquired using FEI Inspect F50 at 20 kV. Corresponding panel shown in Fig. 6.37)

The Cu profile shows strong variations throughout the sample with its concentration dropping below detection in C-rich areas and remaining below 4% in Si-rich areas. Although these signals are weak, they are not negligible, as they have higher intensities than the S profile. The silicon profile shows strong signals predominantly in Si-rich areas, while the signals in Cu-rich areas stay below detectable limits. However, there are important exceptions at the locations of 1 μm, 1.8 μm and most notably 3 μm. These points in the profile show significant intensities of both copper and silicon signals. All of which have significantly higher atomic percentages of Cu than Si. This result suggests that the Cu-rich regions are not entirely lacking in silica, but the difference in atomic numbers makes the silicon atoms more difficult to detect. The results

of these study, therefore suggest that both CuO-rich and SiO₂-rich phases contain significant concentrations of both oxides. Nonetheless, these results could also be generated by some cases of overlapping particles, which would continue to discard the successful fabrication of an infiltrated product.

Chapter Seven

Discussion

Here is presented a critical interpretation of the major findings detailed across chapters 4-6. This section explores the extent to which the findings have addressed the research questions presented in the introduction of this report. Furthermore, this discussion highlights the links correlating the diversity of experimental investigations.

7.1 Main findings

Here are explored the different ways in which the experimental work has met the research objectives set out for this project. The relevance of these objectives has been validated in chapters 1 and 2. Moreover, here are discussed the several fortuitous findings, which were not outlined at the outset of the project but constituted significant additions nonetheless to this work and its contribution to the field of nanomaterials.

7.1.1 The effect of heat treatment on ceria nanomaterials

As detailed at the beginning of Chapter 4, intentional heat treatment of nanomaterials is limited as an experimental approach. However, heating procedures are found as a necessary step in the fabrication and application of a wide range of nanomaterials. As described in section 2.2.3.1, researchers have sought to optimise the shape-selectivity of hydrothermal preparation methods by generating empirical morphological phase diagrams, which normally feature reaction temperature as a significant variable [214].

On the other hand, studies concerning the deactivation or deterioration of catalytic nanomaterials often subject materials of interest to high temperatures in order to evaluate their catalytic performance under operation conditions [394]. This experimental approach provides a valuable point of comparison for the present work. Namely, the general belief throughout the research community is that heating is always detrimental to the performance of catalytic nanomaterials, albeit unavoidable in most applications. In contrast, the present work has shown that annealing at 800 °C consolidates the disturbed single-crystalline structure of ceria nanorods without altering their morphology. Furthermore, the annealed nanorods showed faceted mesopore defects

that have been credited for an improvement in the catalytic activity of nanorods [2]. The present work has shown that the size and shape of these pores are not dependent on the dimensions of the particle. Furthermore, the work in chapter 4 shows the unprecedented occurrence of porous defects in annealed nanocubes, which coincide in appearance to the pores inside nanorods, suggesting that the growth of porous defects is not dictated by the morphology of the containing particle.

The experiments reported in Chapter 5 showed the effects of subjecting ceria nanomaterials to previously unreported high temperatures. Near-sintering heat treatment at 950 °C produced the expected transformations to the morphology of nanorods. Namely, a reduction in surface area and rounding the sharp corners and edges. However, mesopores were also prevalent, which did not lose their faceted nanostructure, nor did they seem to travel to the surfaces of the rods, but remained as internal cavities with cuboctahedral geometry. Surprising, the concentration of pores decreased at a higher temperature without increasing the size of the remaining pores. This is a significant finding, which indicates that the growth of porous defects can be enhanced by longer holding times instead of higher temperatures.

7.1.2 Formation mechanism of heat-induced defects in CeO₂ nanomaterials

The growth history of nanorods is often explained as being directed by a mechanism of oriented attachment, as first defined by Penn and Banfield [379]. This mechanism explains the characteristic formation of ceria nanorods as a product of the attachment of solid Ce(OH)₃ [215] nanocubes. Upon attachment, the sides of these cubes form distortions in the crystalline structure of the nanorod. Accordingly, authors have sought to explain the occurrence of heat-induced pores as a secondary effect of the oriented attachment mechanism [271]. Specifically, the porous defects have been suggested as an effect of the imperfect attachment of the Ce(OH)₃ cubes, which form defects owing to slight misalignments. However, the present work has shown for the first time that heat-induced mesopore defects can also appear in ceria nanocubes, whose symmetrical crystal growth is not associated with the oriented attachment mechanism. Therefore, the appearance of pores in nanocubes suggests that the defects are formed by an alternative mechanism, such as the consolidation of vacancies or the diffusion of oxygen through a semipermeable surface.

Previously, other authors have proposed various contradicting structures for the heat-induced pores [2], [3], [13], as summarised in Figure 2.16. The experimental work reported in Chapter 5 has shown, for the first time, a reliable electron tomography reconstruction of the porous rods in three dimensions. This study established that the pores are located exclusively

inside the structure of the rod and that they have a faceted geometry, which coincides with cuboctahedra or negative nanoparticles.

The heating schedule used to anneal rods at 800 °C entailed a holding time of two hours, as opposed to the holding time of one hour used for the treatment at 950 °C. This longer holding time produced a higher concentration of pores, as well as a previously unreported type of defect described here as negative nanorods, as reported in section 4.2.2.2. This defect consisted of elongated pores, which extend exclusively in a direction parallel to the axis of the nanorod. These defects appear to be formed by the agglomeration of several pores along the body of the rod. The tomography studies reported in Chapter 5 showed that the growth of the pores is dictated by the crystallography of the rod. Consequently, it is proposed that longer holding times at 800 °C could promote the attachment of pores along the growth-direction of the rod, leading to a novel fabrication method of ceria nanotubes.

7.1.3 Microstructure of casted porous nanomaterials and composites

The results reported in Chapter 6 provide valuable insight into the fabrication of materials via nanocasting. As reported in section 2.1.4.1, nanocasting is one of the most common techniques for the production of three-dimensional porous materials. By its own nature, nanocasting always produces composite materials, which can be a final product, such as supported nanoparticles, or an intermediate product before template removal, which produces a negative porous structure.

The present work has shown the different products obtained by casting an active oxide precursor into a porous template. The characteristics of the porous template significantly influenced the ability of the infiltrating phase to form a continuous material. Namely, the use of an opal template, which contained a periodic network of 200 nm-wide pores formed by the aggregation of 400 nm spheres, produced a continuous inverse material after one cycle of infiltration/calcination. The use of mesoporous silica template, MSU-F, which has an irregular structure of pores with an average diameter of 20 nm, produced a network of closely aggregated nanoparticles of variable size.

The contrast between these results does not discard the lack of periodicity or the smaller pore diameter as the limiting factor for the fabrication of a continuous oxide structure. However, the infiltration of SBA-15, which has a periodic structure of 8-nm pores, produced an array of nanoparticles of smaller or equal diameter to the size of the pores. Furthermore, the concentration of the infiltrating phase was significantly lower than in the composites resulting from infiltration of opal and MSU-F structures.

Therefore, the present work contributes to the understanding that the fabrication of a composite via nanocasting is limited by the pore size of the template more significantly than by its

periodicity. On the contrary, the use of a non-periodic template appeared to benefit the infiltration of the template by providing a more open structure with better connectivity between the pores and wider pore windows for accessibility.

As discussed above, the findings reported in Chapter 4 showed, for the first time, the consolidation of a distorted single-crystalline nanostructure into a cleaner continuous monocrySTALLINE nanorod via controlled annealing. These results suggest that heat treatment could also consolidate such a polycrystalline structure as the one conforming the ceria-phase in the MSU-F/CeO₂ composites shown in section 6.2.1.2. The strong attraction forces between the ceria nanoparticles are particularly evident after the silica-etching step. The resulting structure was still continuous and preserved the microstructure dictated by the silica template, as observed in Figure 6.27. Thus, the material can be said to be structurally similar to the non-heat-treated nanorods characterised in section 4.1.2, regardless of their significant difference in morphology. Furthermore, the random agglomeration of nanorods naturally forms a porous network during sample drying, which is unaffected by the heat-treatment procedure, as seen by comparing Figures 4.4 and 4.12. Therefore, it is reasonable to suggest that an annealing procedure at 800 °C could consolidate the polycrystalline structure of ceria without collapsing the porous network or affecting the morphology of the material.

7.1.4 Formation mechanisms of nanocasting products

The experimental work presented in Chapter 6 entails unprecedented studies of the intermediate phases during the formation of nanocasting products. Namely, the present report contains the first published account of the changes in distribution between the unconverted and calcined phases. For the present study, these phases consisted of a metal hydroxynitrate and its derived oxide, respectively. This approach coincides with the sol-gel method in its use of a colloidal solution of oxide precursor. However, the fabrication method reported here used calcination steps for the rapid conversion into oxide. Thus, nanocasting diverts from sol-gel methods in that it does not involve the characteristic gradual formation of a polymeric network from the colloidal solution. The review in section 2.1.4 showed that most template-replication procedures rely on this or a similar method for the fabrication of porous materials.

The most significant finding of the studies concerning the intermediate hydroxynitrate phase was the continuity of the infiltrate phase, as evidenced by EDX studies in section 6.2.2.2. The analyses show that the copper hydroxynitrate infiltrated the porous network of mesoporous silica completely. Remarkably, the precursor phase of the intermediate composite was homogeneously distributed throughout the SBA-15 structure, which coincided with the most limited production of oxide phase. This disparity indicates that the limited concentration of copper(II)

oxide in SBA-15/CuO composite does not arise from an incomplete infiltration, but is a product of the transformations occurring during the conversion of $\text{Cu}(\text{NO}_3)_2 \cdot 6\text{H}_2\text{O}$ to CuO.

Morphological transformations were also visible after calcination steps during the fabrication of inverse opals, as reported in section 6.1.5. Nonetheless, the final product obtained by this method consisted of a continuous network of pores separated by walls of ceria. By incorporating a two-step calcination method, the present work provides unprecedented insight into the stages involved in the transformation of a continuous hydroxynitrate-infiltrate phase into a porous ceria network. Namely, after the first step of calcination at 350 °C, the material maintained the architecture dictated by the opal template, while showing indications of an incomplete transformation, such as large crystalline deposits outside of the porous structure. Further heating at 550 °C produced a much cleaner structure with no residues on the surface of the pores. However, there was a significant evolution in the shape of the pores, which did not appear spherical anymore but became distorted. There was also a clear shrinkage of the walls containing the pores, with a change of thickness from 200 to 70 nm on average. These studies have thus revealed that the morphological evolution of the inverse opals is analogous to the growth history of the infiltrate phase in MPS/metal oxide composites. The implementation of a two-step calcination process showed that the polystyrene template was eliminated before the full calcination of the ceria precursor, nonetheless producing a stable solid. This is a potentially influential finding, as cerium(III) hydroxynitrate is not generally understood as having enough mechanical integrity for the construction of structures such as the inverse opals reported here.

When combined with the reasoning discussed in 7.1.3, this study has revealed at least five stages in the heat-evolution of porous nanomaterials. First, drying of the colloidal solution of oxide precursor results in the deposition of a continuous solid, which easily occupies the entirety of the porous template, as well as forming solid layers on the surface of the template. Then, heating at calcination-onset temperature, 350 °C for cerium(III) hydroxynitrate, creates a continuous porous network. Although the infiltrating phase exhibits the dimensions dictated by the porous template, the prevailing deposits on the surface of the composite block the porous/composite structure. The third stage of transformation was found after heating at the final calcination temperature, 550 °C for ceria and 300 °C for CuO. The product at this stage exhibits significant shrinkage and lacks the undesired surface deposits. Significantly, the structure at this stage depends highly on the pore size of the infiltrating material, with smaller pore sizes considerably limiting the concentration of the infiltrating phase. The material at this stage is not continuous but is composed of closely aggregated nanoparticles smaller or equal in diameter to the pores in the template. Then, heating at 800 °C consolidates the distorted crystalline structure without causing changes in the morphology of the nanomaterial or collapsing the porous structure. Finally, the heating at 950 °C, or sintering-onset temperature, produces ther-

momechanical transformations to the morphology of the material. At this stage, the concentration of crystalline defects reduces significantly, and individual particles start to flow and aggregate into larger solids, potentially collapsing the porous structure.

7.1.5 The capabilities of electron microscopy in the study of porous nanomaterials

The work accounted in this report has presented a diversity of applications of electron microscopy across a diversity of studies of porous nanomaterials. The results of this project evidence the significant advantages of electron microscopy over other methodological approaches that are common in the research of porous materials. As reported in section 2.1.3, the growing relevance of porous materials has brought about a significant production of innovative porous structures at the nanoscale. Consistently with other applications, the ever-decreasing dimensions of functional porous materials have brought about significant challenges for their characterisation and general understanding. Specifically, conventional porosimetry techniques are significantly limited in their capabilities to resolve the structure and distribution of novel porous materials at the nanoscale. These limitations have been surveyed across the literature and summarised in section 2.1.4.2. The present work forms part of a growing body of research that establishes the central role of electron microscopy in overcoming the research challenges present in the development of porous nanomaterials. Specifically, here are reported the characterisation of novel porous nanomaterials that remained largely unexplored in that respect in the available literature. This is especially true for mesoporous CeO₂ nanorods and MSU-F silica.

The ability of electron microscopy to combine imaging and analysis at the nanoscale has revealed the distribution and structure of porous nanomaterials at multiple stages of the nanocasting process. Furthermore, the combined results of SEM and TEM studies have shown the multiple hierarchies of porosity and phase distribution in the composites formed by incipient wetness impregnation. These in-depth characterisations provided an unprecedented understanding of the formation mechanisms of these highly relevant products. Notably, the HRTEM studies of atomic lattices in ceria nanorods before and after annealing procedures revealed the structural changes beyond the formation of internal pores, as it evidenced the consolidation of the chaotic nanostructures of as-synthesised nanorods into monocrystalline structures.

7.1.6 The adoption of geometric tomography to the study of porous nanomaterials

The present work has reported significant achievements in implementing the first characterisation of a porous material by geometric tomography. The benefits and limitations of geometric tomography have been reported in detail in section 2.3.3 of the literature review. The tilt series used for the reconstruction of a porous ceria nanorod in section 5.1 presented several artefacts,

which made it unsuitable for conventional reconstruction algorithms. Namely, the images in the series presented significant regions of Bragg-enhanced contrast, especially in the high-magnification series.

An alternative workaround could have been to use only the low-magnification series for the reconstruction, which presented significantly fewer artefacts. However, these images (Fig. 5.3) did not resolve the crystallography of the rods and the important alignment of the faceted defects with the atomic planes. A second alternative could have been to acquire the high-magnification series using HAADF-STEM, which would have been able to resolve the facets while suppressing the effects of Bragg-enhanced contrast. However, no instruments with those imaging capabilities were available at that stage of experimental work, as mentioned in Chapter 3. Nevertheless, these instrumental limitations motivated a significant achievement beyond the 3D-characterisation of the object of interest. Specifically, the lack of advanced TEM techniques was overcome by developments in image processing techniques. Therefore, the findings of this work can be a valuable resource for reconstructing porous materials in three dimensions without the need for highly specialised instrumentation.

Mainly, the new modified method of geometric tomography presented in Chapter 5 has been proven to successfully reconstruct porous materials by working around the principle of non-convexity. This was achieved by separating each projection into its components, therefore avoiding overlaps and non-convex rotational objects. After reconstructing each feature individually, the separate 3D-objects were integrated into a single model which corresponded to a reliable reconstruction of the porous ceria nanorod. The re-incorporation step was made possible by systematically maintaining the relative position of each object during their individual reconstructions. It can be deduced from this summary that this new methodology can be applied to a variety of multiphase systems, not only porous. By separating each feature of interest and suppressing artefacts in the background and the material, this new technique could be used to reconstruct highly complex systems.

Section 6.2.1.1 reported an attempt to apply the new method of geometric tomography to MSU-F. This material has never been characterised by electron tomography in the literature and could potentially benefit from the developments in the present work. Namely, by isolating a limited number of pores and features of interest, it would be possible to reconstruct the complex structure of MSU-F. The main limitation of this study in the present work was the absence of a high throughput HRTEM, which could have allowed systematic sample preparation. Specifically, the times of grinding of the powder, as well as the amount and selection of the dispersant during sample preparation need to be controlled in order to obtain a suitable object for tilt series acquisition. This significant challenge is not prevalent in systems such as the ceria nanorods, since almost any isolated nanorod is a suitable object for tomography, as long as its orientation does not cause self-shadowing. In contrast, fragments of MSU-F can extend several

micrometres in three dimensions, and their terminal structure is not always visible. Furthermore, as seen in Figure 6.19b, the irregular shape of fragments can cause them to be electron-transparent at certain tilt angles and not others. As mentioned above, these limitations could be potentially overcome by carefully controlling the variables during sample preparation and using a high-throughput HRTEM, such as the F200, which was unavailable at the time of MSU-F characterisations. Nevertheless, the experiments in section 6.2.1.1 did manage to prove for the first time that the porous structure of MSU-F could survive the long exposure to electron beam necessary for tilt-series acquisition. This study showed that the material was sensitive to a threshold of intensity but could withstand long exposures to the electron beam below the brightness threshold.

Section 5.2.3 of this report showed the capabilities of the new modified GT algorithm to reconstruct selected cross-sectional slices from reduced linear information. This methodology constitutes a pragmatic approach to the characterisation of 3D objects. Expressly, a large number of applications do not require the reconstruction of an entire system but call only for the shape and distribution of cross-sectional features. In these cases, simplified tomography algorithms can be an adequate alternative. The techniques shown in this work adapt the reduced-information GT algorithms proposed by Saghi et al. [9], so they can also be applied to cross-sections containing pores. The GT-from-1D-information techniques shown here can benefit a multitude of applications by not only eliminating the need for advanced TEM methods but also by minimising processing memory requirements and maximising speed.

7.1.7 The impacts of findings in catalysis applications and the science of porous materials

As described throughout the literature review, the catalytic potential of the materials studied in the present work has been explored in plenty by other groups. Specifically, section 2.2.1 details the advantages and limitations of ceria and its related materials, as reported by numerous authors for over three decades. On the other hand, mesoporous silica materials such as MSU-F and SBA-15 have been tested under a multitude of reaction conditions, making them a popular choice as a support material, as well as templates for nanocasting, as detailed in section 2.1.4.1.

However, a significant disparity has been found between the catalytic and structural explorations of these materials throughout the literature. The lack of comprehensive imaging studies of porous ceria-related nanomaterials is shown in section 2.3.4. In-depth structural studies, such as the present work, provide important contributions by elucidating the underlying nanoscale-phenomena, which drive the catalytic performance of the porous nanomaterials at the macroscale.

The experimental work presented across chapters 4-6 has produced significant results, which can benefit a multitude of applications by providing a better understanding of relevant

porous materials. As an example, Chapter 4 reported the study of transformations of ceria nanomaterials under different heat-treatment conditions. By incorporating comprehensive TEM characterisations, this work provides valuable insight into the effect of longer holding times at constant temperature, as opposed to heating at higher temperatures. Furthermore, this work provided the first implementation of a heat-resistant TEM sample for in-air heating experiments. In other words, by revealing the formation mechanisms of a diversity of porous nanomaterials, this work contributes to the improvement of their preparation methodologies.

The present work has used advanced electron microscopy techniques to explore the products of nanocasting methods at the nanoscale. The findings reported throughout Chapter 6 have considerable significance for catalytic applications. For instance, the experiments in section 6.2 have shown that the use of porous templates of low dimensionality renders products composed of agglomerated nanoparticles. Therefore, here has been shown that this popular methodology produces a hierarchy of several dimensionalities of pores, as detailed in sections 6.2.1.2 and 6.2.2. Such a structure can be expected to have a higher catalytic activity owing to an increase in surface area. However, the multiple pore diameters can also reduce the selectivity of the material when used for synthetic applications. Hence, the present work has provided valuable information on the nanostructure of casted nanomaterials, which can be used to explain different aspects of their catalytic behaviour beyond their activity or performance.

Similarly, the work reported in Chapter 5 has shown, for the first time, that the heat-induced defects in ceria nanomaterials consist of internal cuboctahedral pores. This finding is of great significance to the catalytic applications of these materials. Specifically, by showing that the porosity is internal and does not reach the walls, it has been shown that the exposed surface area of the material remains the same after annealing of the nanorods. Therefore, a different reason has to be credited for the enhanced catalytic activity reported by others [2]. Here it has been suggested that gases can reach the pores inside the rods through a mechanism of permeability of the walls.

7.2 Consensus of findings across experimental areas

The diversity of experiments detailed throughout this report have complemented each other to form the contributions listed above. Figure 7.1 shows a Venn diagram summarising the main areas of consensus between the three major experimental areas in this work. Certain commonalities across these experiments are evident from the standpoint of the proposed methodologies, such as the use of electron microscopy or the study of porous materials. Consistently, the use of similar methodologies for all the experimental areas in this work has provided strong confirmatory results. For instance, the ceria nanorods heat-treated during this project, studied in

section 4.2.2, showed the same nanostructure as the sample prepared by collaborators as reported in [3], which was characterised in Chapter 5.

More significantly, the results of each experimental area have influenced the interpretation of the other experiments in this work. For instance, the findings reported in Chapter 5, that the growth of porosity in ceria nanorods is dictated by the crystal structure, is a valuable insight into the discovery in section 4.2.2.2 of negative-rod defects. As for Chapter 6, the characterisation of a polycrystalline nano-casted product is reminiscent of the chaotic structures observed in metastable nanorods in Chapter 4. Therefore, the findings in Chapter 4 that the chaotic nanostructure of rods is consolidated during heat treatment provides a viable way to transform the polycrystalline structures produced by the calcination of ceria precursors in Chapter 6 into continuous materials.

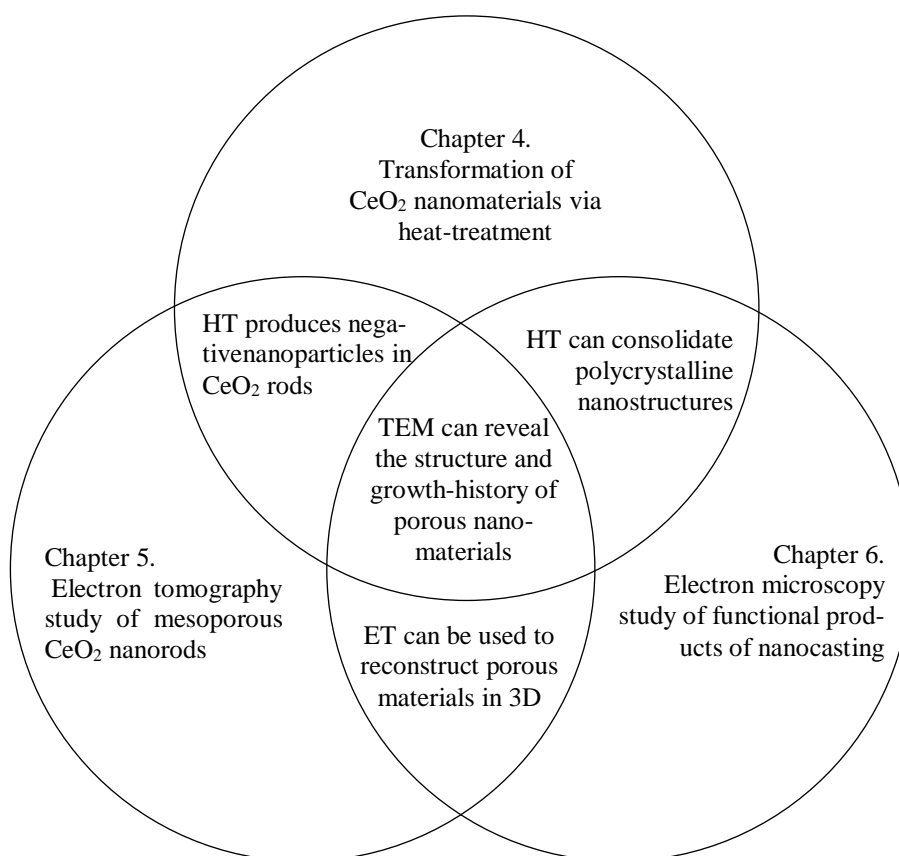


Figure 7.1 Venn diagram of major experimental areas

The novel methodologies proposed in Chapter 5 for the adaptation of geometric tomography to the reconstruction of porous materials influenced the methods applied in Chapter 6. Namely, the acquisition of a tilt series in section 6.2.1.1 has shown for the first time that MSU-F silica can potentially be characterised using electron tomography, as the sensitivity of the material to

electron beam damage is not dictated by the length of the exposure, but by the intensity of the beam. Furthermore, all nanomaterials are best described as three-dimensional objects, which means they cannot be fully described by two-dimensional techniques.

As seen in Figure 7.1, the findings in the present work coincide in the contribution to a wider scientific conversation regarding the role of transmission electron microscopy in the study of porous materials. As discussed several times throughout this report, the applications of TEM and electron tomography in this area have been limited by numerous experimental challenges. However, the present work has shown that the challenges can be overcome with new methodological approaches, such as the use of a heat-resistant TEM sample in section 4.2.4, or the implementation of reduced-information tomography algorithms in section 5.2.3. As a result, the studies in this work have provided valuable insights into the formation mechanisms of relevant porous materials, thus suggesting that the benefits of electron-microscopy studies make those experimental efforts worthwhile.

Another significant overlap between the findings of chapters 4 and 6 concerns further experimentation, which could incorporate the formation of ceria nanomaterials inside mesoporous silica by introducing the metastable composite, MPS/Ce(NO₃)₃·6H₂O, to a hydrothermal synthesis process. Such a combined synthesis is predicted to produce continuous networks of nanorods, which can be heat treated to develop a second hierarchy of pores inside the walls.

Conclusions

The surveyed literature has established that porous ceria nanorods exhibit increased catalytic performance. The present work provides a significant contribution to this discovery by exploring the nanoscale transformations that give rise to this enhanced activity. The comprehensive study presented here of the effects of high-temperature heat treatment of ceria nanomaterials has shown that 800 °C heat treatment can improve the quality of the crystalline structure of ceria nanorods without altering their morphology. The materials prepared in this work showed heat-induced defects, consistent with the results found in the literature. The present work has expanded this knowledge by showing that the size and shape of these pores are not dependent on the dimensions of the particle. Furthermore, here is reported the first occurrence of pores in cube-shaped particles annealed at 950 °C. Significantly, the present study has shown the unprecedented growth of negative-rod defects, which can lead to a novel fabrication strategy of ceria nanotubes.

The tomography studies reported here provide an unprecedented understanding of the morphology and distribution of the aforementioned heat-induced defects in porous ceria nanomaterials. The reliable 3D-reconstructions have shown that annealing at high temperatures produced cuboctahedral cavities in ceria nanorods, which appear exclusively inside the body of the particles and whose growth is directed by the crystallography of the rods. By incorporating a novel algorithm of segmentation, it has been possible to reconstruct porous nanomaterials using geometric tomography back-projection operation. This contribution has not only improved the understanding of the porous structure of heat-treated CeO₂ nanorods but provided, as well, a pathway to simplify the 3D-reconstruction of complex multi-phase materials without the use of advanced TEM techniques.

The literature review has identified the importance of nanocasting processes for the fabrication of catalytic materials, which are central to current and future environmental and energy applications. The experiments in this work provided valuable explorations into the nanostructure of materials fabricated via nanocasting. A notable influence of the pore window dimensions has been identified, with narrower pores leading to nanoparticulate aggregations. Such materials could be improved by the incorporation of controlled heating steps such as the ones shown throughout this work. Here is reported the first infiltration of MSU-F to fabricate a silica/ceria composite. The advanced characterisations of this material have shown that the random distribution of pores in MSU-F is beneficial for the infiltration process. Significantly, the present work shows the first studies of the intermediate phases formed during nanocasting, which provide valuable insight into the mechanical transformations produced by the conversion of hydroxinitrates into catalytic oxides.

Future work

The work reported here can serve as motivation for a number of future research objectives. Primo, the acumen explored here and previously proposed by others [2], [12], [13], that heat treatment can have a positive effect on catalytic activity by consolidation of porous defects, still needs to be explored in the context of its catalytic performance under different reactions, such as noxious gas oxidations and conversion of hydrocarbons. The latter is of particular relevance, since the porous structure revealed by the tomographic studies in the present work showed that the enhanced oxidation behaviour of heat-treated ceria nanorods must rely on a diffusion mechanism. Therefore, larger molecules and higher density media such as those involved in hydrocarbon conversion and waste-water treatment may pose significant limitations to the catalytic activity of these novel materials.

Furthermore, the formation of negative shaped nanopores has only been evidenced here, but not fully explained. Particularly, future research work could explore the nanoscale phenomena taking place at low temperatures (<350 °C). The present work has reported the behaviour of defects at high temperatures of 800 °C and 950 °C. The behaviour at lower temperatures was first explored by Sakthivel et al. [3], who showed the onset of pore formation at around 350 °C and the consolidation of those pores into negative nanoparticle morphology at around 650 °C. Therefore, there remains a gap in the knowledge of the formation mechanisms at low temperature, which must take place at atomic and near-atomic scale, requiring a combination of theoretical studies, as well as experimental. Furthermore, heat-treatment procedures herein and those published by Sakthivel et al. were performed on nanorods exhibiting the characteristic chaotic crystalline structure first addressed by Florea et al. [4]. Given such starting materials, the results in the present work have confirmed previous assertions that porous defects grow by oriented attachment of atomic vacancies trapped in the initial disordered structure. The coincidence in starting materials leaves a clearly open question, as there is no available account of the effects of heat treatment on nanorods such as synthesised by Du et al. [271], which do not present a disordered crystal structure. Therefore, such a study could provide confirmation that these vacancies are the ‘seeds’ for the cuboctahedral pores, or otherwise show that a different formation mechanism is at play.

As mentioned in section 4.2.2.2, the present work shows the first evidence of elongation of pores and aggregation thereof into ‘negative rod’ morphology. Such results are a small indication that a novel fabrication technique for metal oxide nanotubes could be possible. A future study should explore the interactions between adjacent pores and the crystal-structure-directed growth of such unprecedented defects. Particularly, the heating conditions driving these phenomena should be explored to establish a reproducible method for the template-free conversion of cerium(IV) oxide nanorods into nanotubes. Such conditions could include the holding time,

the use of reducing atmospheres and the heating rate and heating steps coinciding with the temperatures so far identified as key in the pore formation mechanisms (350 °C, 650 °C and 800 °C). Such study could be complemented by the use of a TEM heating holder, bearing in mind that thermal behaviour is often different under vacuum conditions. These studies of the oriented attachment of negative nanoparticles could be complemented by exploration into the attachment of rods such as displayed throughout section 4.2.2 of the present work. The results herein have shown evidence of nanorod morphing illustrated by the seamless lattice fringes extending across previously unconnected rods. Such a study could also benefit from the use of novel *in situ* capabilities like a heating holder or a liquid cell TEM.

Foremost, future work could incorporate capabilities of the novel segmented geometric tomography method proposed in Chapter 5 to a growing myriad of porous materials. The need for tomographic reconstructions of porous materials has been highlighted before by Ersen et al. [395]. Such explorations will not only benefit catalytic materials research, but all applications of porous materials such as adsorption and drug delivery. The tomographic reconstruction via segmented geometric tomography of new porous materials could also benefit the research of materials chemistry, as the lack of three-dimensional characterisation has been identified as a limitation in the precipitation of novel nanosilicas [396].

Furthermore, the 3D symmetry of the porous defects reported in Chapter 5 could make the cuboctahedral voids candidates for missing-wedge-suppression algorithms, such as reported by [353], [397]. Other helpful studies could incorporate the more traditional weighted-back projection tomographic algorithms with images obtained using high-resolution EFTEM or HAADF-STEM, therefore minimising the imaging artefacts associated with the Bragg-enhanced contrast in bright-field HRTEM.

As for the various forms of template-replication products reported in Chapter 6, further experimental studies could continue to develop infiltration methods to achieve complete infiltration of more complex systems like the MSU-F porous template studied in section 6.2.1. Meanwhile, theoretical studies could seek to establish the infiltration mechanisms suggested throughout Chapter 6. Section 6.1.2.3 shows an attempt to crystallise an opal directly onto a TEM-grid, which did not result in a colloidal crystal with long-range periodicity. Future work could incorporate different templates and experimental designs to successfully fabricate a TEM-ready opal sample. Such a product would simplify future investigations on the formation mechanisms of inverse opals. A natural future work stemming from the early investigations into the 3D microstructure of MSU-F silica in section 6.2.1.1 would be its successful tomographic reconstruction. As discussed in section 7.1.6, such a reconstruction could be potentially achieved by carefully controlling the variables during sample preparation.

Publications

Main publications

C. Brambila, J. Nutter, T. X. T. Sayle, D. Sayle, M. Molinari, T. Sakthivel, S. Seal, G. Möbus, “Tomographic Study of Meso-pore Formation in Ceria Nanorods” [In preparation]

D. Sayle, L. Morgan, R. L. Neale, M. C. I. Thompson, M. Molinari, J. M. Flitcroft, J. Majimel, G. Möbus, C. Brambila, J. Nutter, S. Seal, “Aging Mechanisms of Metastable Ceria Nanostructures; Transformations of Ceria Nanocubes and Nanorods into Nanopolyhedra” [In preparation]

J. R. H. Manning, C. Brambila, A. Balashanmugam, S. V. Patwardhan, “Colloidal Seeding of Mesoporous Materials Using Bioinspired Methods: A Sustainable and Scalable Approach” [In preparation]

Conference presentations

C. Brambila, G. Möbus, “Advanced TEM of Catalytic Ceria Nanostructures,” presented at the Sheffield Catalysis Forum, 2018

C. Brambila, G. Möbus, “Electron Tomography of Mesoporous Ceria Nanorods,” to be presented at the Future Materials Conference, Leeds, 2019

References

- [1] K. Zhou, X. Wang, X. Sun, Q. Peng, and Y. Li, “Enhanced catalytic activity of ceria nanorods from well-defined reactive crystal planes,” *J. Catal.*, vol. 229, no. 1, pp. 206–212, Jan. 2005.
- [2] J. Li *et al.*, “Low pressure induced porous nanorods of ceria with high reducibility and large oxygen storage capacity: Synthesis and catalytic applications,” *J. Mater. Chem. A*, vol. 2, no. 39, pp. 16459–16466, 2014.
- [3] T. S. Sakhthivel, D. L. Reid, U. M. Bhatta, G. Möbus, D. C. Sayle, and S. Seal, “Engineering of nanoscale defect patterns in CeO₂ nanorods via ex situ and in situ annealing,” *Nanoscale*, vol. 7, no. 12, pp. 5169–5177, Jan. 2015.
- [4] I. Florea, C. Feral-Martin, J. Majimel, D. Ihiwakrim, C. Hirlimann, and O. Ersen, “Three-dimensional tomographic analyses of ceo₂ nanoparticles,” *Cryst. Growth Des.*, vol. 13, no. 3, pp. 1110–1121, Mar. 2013.
- [5] I. Park and T. J. Pinnavaia, “Mesocellular Silica Foam as an Epoxy Polymer Reinforcing Agent,” *Adv. Funct. Mater.*, vol. 17, no. 15, pp. 2835–2841, Oct. 2007.
- [6] R. Brent *et al.*, “Unstitching the Nanoscopic Mystery of Zeolite Crystal Formation,” *J. Am. Chem. Soc.*, vol. 132, no. 39, pp. 13858–13868, Oct. 2010.
- [7] I. Diaz and A. Mayoral, “TEM studies of zeolites and ordered mesoporous materials,” *Micron*, vol. 42, no. 5, pp. 512–527, Jul. 2011.
- [8] Z. Liu *et al.*, “A review of fine structures of nanoporous materials as evidenced by microscopic methods,” *J. Electron Microsc. (Tokyo)*, vol. 62, no. 1, pp. 109–146, 2013.
- [9] Z. Saghi, X. Xu, Y. Peng, B. Inkson, and G. Möbus, “Three-dimensional chemical analysis of tungsten probes by energy dispersive x-ray nanotomography,” *Appl. Phys. Lett.*, vol. 91, no. 25, p. 251906, Dec. 2007.
- [10] L. Vradman, M. V. Landau, D. Kantorovich, Y. Koltypin, and A. Gedanken, “Evaluation of metal oxide phase assembling mode inside the nanotubular pores of mesostructured silica,” *Microporous Mesoporous Mater.*, vol. 79, no. 1–3, pp. 307–318, Apr. 2005.
- [11] N. M. Deraz and A. Alarifi, “Structural, Surface, and Catalytic Properties of Nano-sized Ceria Catalysts,” *Adsorpt. Sci. Technol.*, vol. 27, no. 4, pp. 413–422, Aug. 2009.
- [12] W. Gao, Z. Zhang, J. Li, Y. Ma, and Y. Qu, “Surface engineering on CeO₂ nanorods by chemical redox etching and their enhanced catalytic activity for CO oxidation,” *Nanoscale*, vol. 7, no. 27, pp. 11686–11691, May 2015.
- [13] Y. Ma *et al.*, “Regulating the surface of nanoceria and its applications in heterogeneous catalysis,” *Surf. Sci. Rep.*, vol. 73, no. 1, pp. 1–36, Mar. 2018.
- [14] A. Trovarelli and J. Llorca, “Ceria Catalysts at Nanoscale: How Do Crystal Shapes Shape Catalysis?,” *ACS Catal.*, vol. 7, no. 7, pp. 4716–4735, Jul. 2017.
- [15] P. A. Midgley and M. Weyland, “3D electron microscopy in the physical sciences: the development of Z-contrast and EFTEM tomography,” *Ultramicroscopy*, vol. 96, no. 3–4, pp. 413–431, Sep. 2003.
- [16] X. Xu, Z. Saghi, R. Gay, and G. Möbus, “Reconstruction of 3D morphology of polyhedral nanoparticles,” *Nanotechnology*, vol. 18, no. 22, p. 225501, Jun. 2007.
- [17] Z. Saghi, X. Xu, and G. Möbus, “Electron tomography of regularly shaped nanostructures under non-linear image acquisition,” *J. Microsc.*, vol. 232, no. 1, pp. 186–195, 2008.

- [18] J. C. Védrine, “Metal Oxides in Heterogeneous Oxidation Catalysis: State of the Art and Challenges for a More Sustainable World,” *ChemSusChem*, vol. 12, no. 3, pp. 577–588, Feb. 2019.
- [19] K. Lin, B. Ma, Y. Sun, and W. Liu, “Comparison between liquid and solid acids catalysts on reducing sugars conversion from furfural residues via pretreatments,” *Bioresour. Technol.*, vol. 167, pp. 133–136, Sep. 2014.
- [20] R. Schlögl, “Heterogeneous Catalysis,” *Angew. Chemie Int. Ed.*, vol. 54, no. 11, pp. 3465–3520, Mar. 2015.
- [21] E. Marceau, X. Carrier, and M. Che, “Impregnation and Drying,” in *Synthesis of Solid Catalysts.*, K. P. de Jong, Ed. Weinheim, Germany: Wiley-VCH Verlag GmbH & Co. KGaA, 2009, pp. 59–82.
- [22] J. T. Roberts, “Surface chemistry at size-selected, aerosolized nanoparticles,” in *Environmental Catalysis*, V. H. Grassian, Ed. Boca Raton, USA: CRC Press, 2005, pp. 177–194.
- [23] A. Lloyd Spetz, P. Tobias, L. Unéus, H. Svenningstorp, L.-G. Ekedahl, and I. Lundström, “High temperature catalytic metal field effect transistors for industrial applications,” *Sensors Actuators B Chem.*, vol. 70, no. 1–3, pp. 67–76, Nov. 2000.
- [24] J. Y. Park and G. A. Somorjai, “The Catalytic Nanodiode: Detecting Continuous Electron Flow at Oxide-Metal Interfaces Generated by a Gas-Phase Exothermic Reaction,” *ChemPhysChem*, vol. 7, no. 7, pp. 1409–1413, Jul. 2006.
- [25] P. Y. Yu and M. Cardona, “A Pedestrian’s Guide to Group Theory,” in *Fundamentals of semiconductors: physics and materials properties*, 4th ed., New York, USA: Springer, 2010, pp. 26–47.
- [26] F. D. Morrison, D. C. Sinclair, and A. R. West, “Doping mechanisms and electrical properties of La-doped BaTiO₃ ceramics,” *Int. J. Inorg. Mater.*, vol. 3, no. 8, pp. 1205–1210, Dec. 2001.
- [27] U. Zavyalova, M. Holena, R. Schlögl, and M. Baerns, “Statistical Analysis of Past Catalytic Data on Oxidative Methane Coupling for New Insights into the Composition of High-Performance Catalysts,” *ChemCatChem*, vol. 3, no. 12, pp. 1935–1947, Dec. 2011.
- [28] L. Liu and A. Corma, “Metal Catalysts for Heterogeneous Catalysis: From Single Atoms to Nanoclusters and Nanoparticles,” *Chem. Rev.*, vol. 118, no. 10, pp. 4981–5079, May 2018.
- [29] N. Guo, K. M. Yam, and C. Zhang, “Substrate engineering of graphene reactivity: towards high-performance graphene-based catalysts,” *npj 2D Mater. Appl.*, vol. 2, no. 1, pp. 1–6, Dec. 2018.
- [30] J. Pang, J. Sun, M. Zheng, H. Li, Y. Wang, and T. Zhang, “Transition metal carbide catalysts for biomass conversion: A review,” *Appl. Catal. B Environ.*, vol. 254, pp. 510–522, Oct. 2019.
- [31] O. Weisser and S. Landa, “The Significance, Technical Application and Specific Position of Sulphide Catalysts,” in *Sulphide Catalysts, their Properties and Applications*, Prague, Czechoslovakia: Academia, 1973, pp. 15–16.
- [32] J. S. Kim, B. Kim, H. Kim, and K. Kang, “Recent Progress on Multimetal Oxide Catalysts for the Oxygen Evolution Reaction,” *Adv. Energy Mater.*, vol. 8, no. 11, p. 1702774, Apr. 2018.
- [33] J. Védrine, “Heterogeneous Catalysis on Metal Oxides,” *Catalysts*, vol. 7, no. 11, p. 341, Nov. 2017.
- [34] J. Ross, “The Scientific Literature on Catalysis,” in *Contemporary Catalysis*,

- Amsterdam, Netherlands: Elsevier, 2019, pp. 35–36.
- [35] M. B. Gawande, R. K. Pandey, and R. V. Jayaram, “Role of mixed metal oxides in catalysis science—versatile applications in organic synthesis,” *Catal. Sci. Technol.*, vol. 2, no. 6, pp. 1113–1125, Feb. 2012.
- [36] L. Lloyd, “Petrochemical Catalysts,” in *Handbook of Industrial Catalysts*, Boston, USA: Springer, 2011, pp. 261–310.
- [37] S. Caron, R. W. Dugger, S. G. Ruggeri, J. A. Ragan, and D. H. B. Ripin, “Large-Scale Oxidations in the Pharmaceutical Industry †,” *Chem. Rev.*, vol. 106, no. 7, pp. 2943–2989, Jul. 2006.
- [38] J.-L. Dubois, “Main industrial processes using metal oxides as catalysts or support and future trends in heterogeneous catalysis,” in *Metal Oxides in Heterogeneous Catalysis*, J. C. Védrine, Ed. Amsterdam, Netherlands: Elsevier, 2018, pp. 401–450.
- [39] M. Shao, Q. Chang, J.-P. Dodelet, and R. Chenitz, “Recent Advances in Electrocatalysts for Oxygen Reduction Reaction,” *Chem. Rev.*, vol. 116, no. 6, pp. 3594–3657, Mar. 2016.
- [40] J. F. Le Page, “The Preparation of Catalysts,” in *Applied heterogeneous catalysis: design, manufacture, use of solid catalysts*, Paris, France: Institut Français du Pétrole, 1987, pp. 75–123.
- [41] F. Schmidt, “The Importance of Catalysis in the Chemical and Non-Chemical Industries,” in *Basic principles in applied catalysis*, M. Baerns, Ed. Heidelberg, Germany: Springer-Verlag, 2004, pp. 3–17.
- [42] M. S. Wong, “Nanostructured Supported Metal Oxides,” in *Metal Oxides: Chemistry and Applications*, vol. 128, no. 34, J. L. G. Fierro, Ed. Boca Raton, USA: CRC Press, 2006, pp. 31–54.
- [43] R. Sadeghbeigi, “FCC Catalysts,” in *Fluid Catalytic Cracking Handbook*, 3rd ed., Amsterdam, Netherlands: Elsevier, 2012, pp. 87–115.
- [44] W. L. Schuette and A. E. Schweizer, “Bifunctionality in Catalytic Cracking Catalysis,” in *Studies in Surface Science and Catalysis*, M. L. Ocelli and P. O’Conner, Eds. Netherlands: Elsevier B.V., 2001, pp. 263–278.
- [45] E. I. Al Naimi and A. A. Garforth, “The effect of zeolite structure and pore systems on maximizing propylene production in FCC unit,” *Chem. Eng. Trans.*, vol. 43, pp. 859–864, May 2015.
- [46] N. Hosseinpour, Y. Mortazavi, A. Bazyari, and A. A. Khodadadi, “Synergetic effects of Y-zeolite and amorphous silica-alumina as main FCC catalyst components on triisopropylbenzene cracking and coke formation,” *Fuel Process. Technol.*, vol. 90, no. 2, pp. 171–179, Feb. 2009.
- [47] S. Al-Khattaf, “The influence of alumina on the performance of FCC catalysts during hydrotreated VGO catalytic cracking,” *Energy and Fuels*, vol. 17, no. 1, pp. 62–68, Jan. 2003.
- [48] J. F. Brazdil, “A critical perspective on the design and development of metal oxide catalysts for selective propylene ammoxidation and oxidation,” *Appl. Catal. A Gen.*, vol. 543, pp. 225–233, Aug. 2017.
- [49] S. Pudar, J. Oxgaard, and W. A. Goddard, “Mechanism of Selective Ammoxidation of Propene to Acrylonitrile on Bismuth Molybdates from Quantum Mechanical Calculations,” *J. Phys. Chem. C*, vol. 114, no. 37, pp. 15678–15694, Sep. 2010.
- [50] J. C. Vedrine, “Heterogeneous catalytic partial oxidation of lower alkanes (C 1 –C 6) on mixed metal oxides,” *J. Energy Chem.*, vol. 25, no. 6, pp. 936–946, Nov. 2016.
- [51] D. Duprez and C. Descorme, “Oxygen Storage/Redox Capacity and Related Phenomena

- on Ceria-Based Catalysts,” in *Catalysis by Ceria and Related Materials*, A. Trovarelli, Ed. London, UK: Imperial College Press, 2002, pp. 243–276.
- [52] J. Seth, P. Dubey, V. R. Chaudhari, and B. L. V. Prasad, “Preparation of metal oxide supported catalysts and their utilization for understanding the effect of a support on the catalytic activity,” *New J. Chem.*, vol. 42, no. 1, pp. 402–410, Jan. 2018.
- [53] A. Galal, N. F. Atta, and S. M. Ali, “Optimization of the synthesis conditions for LaNiO₃ catalyst by microwave assisted citrate method for hydrogen production,” *Appl. Catal. A Gen.*, vol. 409–410, pp. 202–208, Dec. 2011.
- [54] C. Alvarez-Galvan *et al.*, “Microwave-assisted coprecipitation synthesis of LaCoO₃ nanoparticles and their catalytic activity for syngas production by partial oxidation of methane,” *Front. Energy Res.*, vol. 6, no. 18, pp. 1–11, Apr. 2018.
- [55] S. Esposito, “‘Traditional’ sol-gel chemistry as a powerful tool for the preparation of supported metal and metal oxide catalysts,” *Materials (Basel)*, vol. 12, no. 4, p. 668, Feb. 2019.
- [56] M. H. Tran, H. Ohkita, T. Mizushima, and N. Kakuta, “Hydrothermal synthesis of molybdenum oxide catalyst: Heteropoly acids encaged in US-Y,” *Appl. Catal. A Gen.*, vol. 287, no. 1, pp. 129–134, Jun. 2005.
- [57] S. Zhang *et al.*, “Controllable synthesis of hierarchical nanoporous ε-MnO₂ crystals for the highly effective oxidation removal of formaldehyde,” *CrystEngComm*, vol. 21, no. 25, pp. 3863–3872, Mar. 2019.
- [58] T. J. Gardner, L. I. McLaughlin, L. R. Evans, and A. K. Datye, “Preparation and evaluation of Novel Hydrous Metal Oxide (HMO)-supported noble metal catalysts,” in *Studies in Surface Science and Catalysis*, vol. 118, P. Delmon, P. A. Jacobs, R. Maggi, J. A. Martens, P. Grange, and G. Poncelet, Eds. Amsterdam, Netherlands: Elsevier Science Publishers B.V., 1998, pp. 245–254.
- [59] K. Martina, M. Manzoli, E. C. Gaudino, and G. Cravotto, “Eco-Friendly Physical Activation Methods for Suzuki–Miyaura Reactions,” *Catalysts*, vol. 7, no. 12, p. 98, Mar. 2017.
- [60] M. S.-I. Veitía and C. Ferroud, “New activation methods used in green chemistry for the synthesis of high added value molecules,” *Int. J. Energy Environ. Eng.*, vol. 6, no. 1, pp. 37–46, Mar. 2015.
- [61] Defra, “Clean Air Strategy 2019: executive summary,” 2019. [Online]. Available: www.gov.uk/government/publications. [Accessed: 03-Aug-2019].
- [62] R. Evans, “Catalysts: Key to the quest for clean air,” *Ingenia*, pp. 35–39, Aug-2001.
- [63] T. Muroi, “Role of Precious Metal Catalysts,” in *Noble Metals*, Y.-H. Su, Ed. 2012, pp. 301–334.
- [64] J. Giménez-Mañogil and A. García-García, “Opportunities for ceria-based mixed oxides versus commercial platinum-based catalysts in the soot combustion reaction. Mechanistic implications,” *Fuel Process. Technol.*, vol. 129, pp. 227–235, Jan. 2015.
- [65] J. A. Rodriguez, “Electronic and chemical properties of mixed-metal oxides: basic principles for the design of DeNO_x and DeSO_x catalysts,” *Catal. Today*, vol. 85, no. 2–4, pp. 177–192, Oct. 2003.
- [66] L. Treccani, T. Yvonne Klein, F. Meder, K. Pardun, and K. Rezwan, “Functionalized ceramics for biomedical, biotechnological and environmental applications,” *Acta Biomater.*, vol. 9, no. 7, pp. 7115–7150, Jul. 2013.
- [67] L. Zhang, W. Shi, and B. Zhang, “A review of electrocatalyst characterization by transmission electron microscopy,” *J. Energy Chem.*, vol. 26, no. 6, pp. 1117–1135, Nov. 2017.

- [68] N. Sharma, H. Ojha, A. Bharadwaj, D. P. Pathak, and R. K. Sharma, "Preparation and catalytic applications of nanomaterials: a review," *RSC Adv.*, vol. 5, no. 66, pp. 53381–53403, Jun. 2015.
- [69] R. Luque and J. Garcia Martinez, "Editorial: From Mesoporous Supports to Mesoporous Catalysts: Introducing Functionality to Mesoporous Materials," *ChemCatChem*, vol. 5, no. 4, pp. 827–829, Apr. 2013.
- [70] H. Nasrallah and J.-C. Hierso, "Porous Materials Based on 3-Dimensional Td-Directing Functionalized Adamantane Scaffolds and Applied as Recyclable Catalysts," *Chem. Mater.*, vol. 31, no. 3, pp. 619–642, Feb. 2019.
- [71] H. Bildirir, V. G. Gregoriou, A. Avgeropoulos, U. Scherf, and C. L. Chochos, "Porous organic polymers as emerging new materials for organic photovoltaic applications: current status and future challenges," *Mater. Horizons*, vol. 4, no. 4, pp. 546–556, Feb. 2017.
- [72] I. Luz, L. Toy, F. Rabie, M. Lail, and M. Soukri, "Synthesis of Soluble Metal Organic Framework Composites for Mixed Matrix Membranes," *ACS Appl. Mater. Interfaces*, vol. 11, no. 17, pp. 15638–15645, May 2019.
- [73] Y. Xue, S. Zheng, H. Xue, and H. Pang, "Metal–organic framework composites and their electrochemical applications," *J. Mater. Chem. A*, vol. 7, no. 13, pp. 7301–7327, Feb. 2019.
- [74] V. R. Remya and M. Kurian, "Synthesis and catalytic applications of metal–organic frameworks: a review on recent literature," *Int. Nano Lett.*, vol. 9, no. 1, pp. 17–29, Mar. 2019.
- [75] H. Furukawa, K. E. Cordova, M. O’Keeffe, and O. M. Yaghi, "The Chemistry and Applications of Metal-Organic Frameworks," *Science*, vol. 341, no. 6149, p. 1230444, Aug. 2013.
- [76] V. F. Cheong and P. Y. Moh, "Recent advancement in metal–organic framework: synthesis, activation, functionalisation, and bulk production," *Mater. Sci. Technol.*, vol. 34, no. 9, pp. 1025–1045, Jun. 2018.
- [77] H.-C. Zhou, J. R. Long, and O. M. Yaghi, "Introduction to Metal–Organic Frameworks," *Chem. Rev.*, vol. 112, no. 2, pp. 673–674, Feb. 2012.
- [78] M. Safaei, M. M. Foroughi, N. Ebrahimpour, S. Jahani, A. Omid, and M. Khatami, "A review on metal-organic frameworks: Synthesis and applications," *TrAC Trends Anal. Chem.*, vol. 118, pp. 401–425, Sep. 2019.
- [79] C. Perego and R. Millini, "Porous materials in catalysis: challenges for mesoporous materials," *Chem. Soc. Rev.*, vol. 42, no. 9, pp. 3956–3976, Jun. 2013.
- [80] T. Mirkovic, N. S. Zacharia, G. D. Scholes, and G. A. Ozin, "Nanolocotion-Catalytic Nanomotors and Nanorotors," *Small*, vol. 6, no. 2, pp. 159–167, Jan. 2010.
- [81] A. Yusuf *et al.*, "Advances on transition metal oxides catalysts for formaldehyde oxidation: A review," *Catal. Rev.*, vol. 59, no. 3, pp. 189–233, Jul. 2017.
- [82] A. Remiro, A. Arandia, L. Oar-Arteta, J. Bilbao, and A. G. Gayubo, "Stability of a Rh/CeO₂–ZrO₂ Catalyst in the Oxidative Steam Reforming of Raw Bio-oil," *Energy & Fuels*, vol. 32, no. 3, pp. 3588–3598, Mar. 2018.
- [83] A. Ruiz Puigdollers, P. Schlexer, S. Tosoni, and G. Pacchioni, "Increasing Oxide Reducibility: The Role of Metal/Oxide Interfaces in the Formation of Oxygen Vacancies," *ACS Catal.*, vol. 7, no. 10, pp. 6493–6513, Oct. 2017.
- [84] P. Sudarsanam, E. Peeters, E. V. Makshina, V. I. Parvulescu, and B. F. Sels, "Advances in porous and nanoscale catalysts for viable biomass conversion," *Chem. Soc. Rev.*, vol. 48, no. 8, pp. 2366–2421, May 2019.

- [85] G. Leofanti, M. Padovan, G. Tozzola, and B. Venturelli, "Surface area and pore texture of catalysts," *Catal. Today*, vol. 41, no. 1–3, pp. 207–219, May 1998.
- [86] S. Shalini, S. Nandi, A. Justin, R. Maity, and R. Vaidhyanathan, "Potential of ultramicroporous metal–organic frameworks in CO₂ clean-up," *Chem. Commun.*, vol. 54, no. 96, pp. 13472–13490, May 2018.
- [87] A. Kumar *et al.*, "Hybrid ultramicroporous materials (HUMs) with enhanced stability and trace carbon capture performance," *Chem. Commun.*, vol. 53, no. 44, pp. 5946–5949, Nov. 2017.
- [88] I. Fechete and J. C. Vedrine, "Nano-Oxide Mesoporous Catalysts in Heterogeneous Catalysis," in *Nanotechnology in Catalysis*, M. Van de Voorde and B. Sels, Eds. Weinheim, Germany: Wiley-VCH Verlag GmbH & Co. KGaA, 2017, pp. 57–90.
- [89] J. Rouquérol, "Characterization of porous solids III," in *Proceedings of the IUPAC Symposium (COPS III), Marseille, France, May 9-12, 1993*.
- [90] J. Rouquérol *et al.*, "Recommendations for the characterisation of porous solids," *Pure Appl. Chem.*, vol. 66, no. 8, pp. 1739–1758, May 1994.
- [91] J. S. Beck *et al.*, "A New Family of Mesoporous Molecular Sieves Prepared with Liquid Crystal Templates," *J. Am. Chem. Soc.*, vol. 114, no. 27, pp. 10834–10843, Dec. 1992.
- [92] C. T. Kresge, M. E. Leonowicz, W. J. Roth, J. C. Vartuli, and J. S. Beck, "Ordered mesoporous molecular sieves synthesized by a liquid-crystal template mechanism," *Nature*, vol. 359, no. 6397, pp. 710–712, Oct. 1992.
- [93] S. E. Lehman and S. C. Larsen, "Zeolite and mesoporous silica nanomaterials: greener syntheses, environmental applications and biological toxicity," *Environ. Sci. Nano*, vol. 1, no. 3, pp. 200–213, Dec. 2014.
- [94] I. Schmidt, C. Madsen, and C. J. H. Jacobsen, "Confined Space Synthesis. A Novel Route to Nanosized Zeolites," *Inorg. Chem.*, vol. 39, no. 11, pp. 2279–2283, May 2000.
- [95] A. Chica, "Zeolites: Promised Materials for the Sustainable Production of Hydrogen," *ISRN Chem. Eng.*, vol. 2013, pp. 1–19, Feb. 2013.
- [96] N. Alam and R. Mokaya, "Crystalline mesoporous silicates from layered precursors," *J. Mater. Chem.*, vol. 18, no. 12, pp. 1383–1391, Feb. 2008.
- [97] M. E. Davis, "Ordered porous materials for emerging applications," *Nature*, vol. 417, no. 6891, pp. 813–821, Jun. 2002.
- [98] C. Pantalei *et al.*, "Interaction of single water molecules with silanols in mesoporous silica," *Phys. Chem. Chem. Phys.*, vol. 13, no. 13, pp. 6022–6028, Jan. 2011.
- [99] M. Vallet-Regí, M. Colilla, I. Izquierdo-Barba, and M. Manzano, "Mesoporous Silica Nanoparticles for Drug Delivery: Current Insights," *Molecules*, vol. 23, no. 1, p. 47, Dec. 2017.
- [100] N. Shadjou and M. Hasanzadeh, "Bone tissue engineering using silica-based mesoporous nanobiomaterials: Recent progress," *Mater. Sci. Eng. C*, vol. 55, pp. 401–409, Oct. 2015.
- [101] C. Y. Lai, "Mesoporous Silica Nanomaterials Applications in Catalysis," *J. Thermodyn. Catal.*, vol. 5, no. 1, p. 124, May 2014.
- [102] Q. N. Chu, Pochen; Landis, Michael E.; Le, "Production of ethylbenzene," US Patent 5334795, Jan-1996.
- [103] H. Koch and W. Reschetilowski, "Is the catalytic activity of Al-MCM-41 sufficient for hydrocarbon cracking?," *Microporous Mesoporous Mater.*, vol. 25, no. 1–3, pp. 127–129, Dec. 1998.
- [104] A. Corma, M. S. Grande, V. Gonzalez-Alfaro, and A. V. Orchilles, "Cracking Activity and Hydrothermal Stability of MCM-41 and Its Comparison with Amorphous Silica-

- Alumina and a USY Zeolite,” *J. Catal.*, vol. 159, no. 2, pp. 375–382, Apr. 1996.
- [105] K. R. Kloetstra and H. van Bekkum, “Base and acid catalysis by the alkali-containing MCM-41 mesoporous molecular sieve,” *J. Chem. Soc. Chem. Commun.*, no. 10, pp. 1005–1006, Mar. 1995.
- [106] K. R. Kloetstra and H. van Bekkum, “Solid mesoporous base catalysts comprising of MCM-41 supported intraporous cesium oxide,” in *Progress in Zeolite and Microporous Materials*, vol. 105, H. Chon, S.-K. Ihm, and Y. S. Uh, Eds. Amsterdam, Netherlands: Elsevier, 1997, pp. 431–438.
- [107] K. R. Kloetstra, M. Van Laren, and H. Van Bekkum, “Binary caesium-lanthanum oxide supported on MCM-41: A new stable heterogeneous basic catalyst,” *J. Chem. Soc. - Faraday Trans.*, vol. 93, no. 6, pp. 1211–1220, Jan. 1997.
- [108] E. Li and V. Rudolph, “Transesterification of Vegetable Oil to Biodiesel over MgO-Functionalized Mesoporous Catalysts,” *Energy & Fuels*, vol. 22, no. 1, pp. 145–149, Jan. 2008.
- [109] T. Wang, G. Wu, N. Guan, and L. Li, “Nitridation of MgO-loaded MCM-41 and its beneficial applications in base-catalyzed reactions,” *Microporous Mesoporous Mater.*, vol. 148, no. 1, pp. 184–190, Jan. 2012.
- [110] M. C. G. Albuquerque *et al.*, “CaO supported on mesoporous silicas as basic catalysts for transesterification reactions,” *Appl. Catal. A Gen.*, vol. 334, no. 1–2, pp. 35–43, Jan. 2008.
- [111] N. Kumar *et al.*, “Synthesis and characterization of solid base mesoporous and microporous catalysts: Influence of the support, structure and type of base metal,” *Microporous Mesoporous Mater.*, vol. 152, pp. 71–77, 2012.
- [112] J. Fan *et al.*, “Facile preparation of Cu-Mn/CeO₂/SBA-15 catalysts using ceria as an auxiliary for advanced oxidation processes,” *J. Mater. Chem. A*, vol. 2, no. 27, pp. 10654–10661, Jun. 2014.
- [113] R. Chal, C. Gérardin, M. Bulut, and S. van Donk, “Overview and Industrial Assessment of Synthesis Strategies towards Zeolites with Mesopores,” *ChemCatChem*, vol. 3, no. 1, pp. 67–81, Jan. 2011.
- [114] M. Mazaj *et al.*, “Synthesis and structural investigations on aluminium-free Ti-Beta/SBA-15 composite,” *Microporous Mesoporous Mater.*, vol. 117, no. 1–2, pp. 458–465, Jan. 2009.
- [115] J. Vernimmen *et al.*, “Immersion Calorimetry as a Tool To Evaluate the Catalytic Performance of Titanosilicate Materials in the Epoxidation of Cyclohexene,” *Langmuir*, vol. 27, no. 7, pp. 3618–3625, Apr. 2011.
- [116] R. Ryoo, S. H. Joo, and S. Jun, “Synthesis of Highly Ordered Carbon Molecular Sieves via Template-Mediated Structural Transformation,” *J. Phys. Chem. B*, vol. 103, no. 37, pp. 7743–7746, Sep. 1999.
- [117] K. Na, M. Choi, W. Park, Y. Sakamoto, O. Terasaki, and R. Ryoo, “Pillared MFI Zeolite Nanosheets of a Single-Unit-Cell Thickness,” *J. Am. Chem. Soc.*, vol. 132, no. 12, pp. 4169–4177, May 2010.
- [118] J. Zhang, J. E. Kielbasa, and D. L. Carroll, “Controllable fabrication of porous alumina templates for nanostructures synthesis,” *Mater. Chem. Phys.*, vol. 122, no. 1, pp. 295–300, Jul. 2010.
- [119] F. Esch *et al.*, “Chemistry: Electron localization determines defect formation on ceria substrates,” *Science*, vol. 309, no. 5735, pp. 752–755, Jul. 2005.
- [120] M. R. Castell, “Wulff shape of microscopic voids in UO₂ crystals,” *Phys. Rev. B - Condens. Matter Mater. Phys.*, vol. 68, no. 23, p. 235411, Dec. 2003.

- [121] W. D. Dozier, J. M. Drake, and J. Klafter, "Self-diffusion of a molecule in porous Vycor glass," *Phys. Rev. Lett.*, vol. 56, no. 2, pp. 197–200, Jan. 1986.
- [122] T. Désaunay *et al.*, "Surface-dependent oxidation of H₂ on CeO₂ surfaces," *J. Catal.*, vol. 297, pp. 193–201, Jan. 2013.
- [123] E. Aneggi, D. Wiater, C. De Leitenburg, J. Llorca, and A. Trovarelli, "Shape-dependent activity of ceria in soot combustion," *ACS Catal.*, vol. 4, no. 1, pp. 172–181, Jan. 2014.
- [124] Z. Liu, X. Li, M. Mayyas, P. Koshy, J. N. Hart, and C. C. Sorrell, "Growth mechanism of ceria nanorods by precipitation at room temperature and morphology-dependent photocatalytic performance," *CrystEngComm*, vol. 19, no. 32, pp. 4766–4776, Jul. 2017.
- [125] H. Zhu, J. Tao, and X. Dong, "Preparation and Photoelectrochemical Activity of Cr-Doped TiO₂ Nanorods with Nanocavities," *J. Phys. Chem. C*, vol. 114, pp. 2873–2879, May 2010.
- [126] W. Q. Han, L. Wu, R. F. Klie, and Y. Zhu, "Enhanced optical absorption induced by dense nanocavities inside titania nanorods," *Adv. Mater.*, vol. 19, no. 18, pp. 2525–2529, Sep. 2007.
- [127] C. Weinberger, J. Roggenbuck, J. Hanss, and M. Tiemann, "Synthesis of Mesoporous Metal Oxides by Structure Replication: Thermal Analysis of Metal Nitrates in Porous Carbon Matrices," *Nanomaterials*, vol. 5, no. 3, pp. 1431–1441, Aug. 2015.
- [128] S. Jun *et al.*, "Synthesis of New, Nanoporous Carbon with Hexagonally Ordered Mesostructure," *J. Am. Chem. Soc.*, vol. 122, no. 43, pp. 10712–10713, Nov. 2000.
- [129] J. R. A. Sietsma, A. Jos van Dillen, P. E. de Jongh, and K. P. de Jong, "Application of ordered mesoporous materials as model supports to study catalyst preparation by impregnation and drying," in *Studies in Surface Science and Catalysis*, E. Gaigneaux, M. Devillers, D. E. De Vos, S. Hermans, P. A. Jacobs, J. A. Martens, and P. Ruiz, Eds. Amsterdam, Netherlands: Elsevier, 2006, pp. 95–102.
- [130] Xiaoyun He, Min Zeng, and D. Brabazon, "Recent Progress in Fabrication of Nanostructured Carbon Monolithic Materials," in *Reference Module in Materials Science and Materials Engineering*, M. S. J. Hashmi, Ed. Amsterdam, Netherlands: Elsevier, 2016, pp. 245–290.
- [131] X. Deng, K. Chen, and H. Tüysüz, "Protocol for the Nanocasting Method: Preparation of Ordered Mesoporous Metal Oxides," *Chem. Mater.*, vol. 29, no. 1, pp. 40–52, Jan. 2017.
- [132] J. Parmentier *et al.*, "New carbons with controlled nanoporosity obtained by nanocasting using a SBA-15 mesoporous silica host matrix and different preparation routes," *J. Phys. Chem. Solids*, vol. 65, no. 2–3, pp. 139–146, Mar. 2004.
- [133] T. Tsoncheva *et al.*, "Iron oxide nanoparticles supported on mesoporous MgO and CeO₂: A comparative physicochemical and catalytic study," *Microporous Mesoporous Mater.*, vol. 110, no. 2–3, pp. 339–346, Apr. 2008.
- [134] Q. Liu, A. Wang, X. Wang, and T. Zhang, "Ordered Crystalline Alumina Molecular Sieves Synthesized via a Nanocasting Route," *Chem. Mater.*, vol. 18, no. 22, pp. 5153–5155, Oct. 2006.
- [135] W. Birnbaum, C. Weinberger, V. Schill, S. Haffer, M. Tiemann, and D. Kuckling, "Synthesis of mesoporous alumina through photo cross-linked poly(dimethylacrylamide) hydrogels," *Colloid Polym. Sci.*, vol. 292, no. 11, pp. 3055–3060, Nov. 2014.
- [136] S. Haffer, C. Weinberger, and M. Tiemann, "Mesoporous Al₂O₃ by Nanocasting: Relationship between Crystallinity and Mesoscopic Order," *Eur. J. Inorg. Chem.*, vol. 2012, no. 20, pp. 3283–3288, Jul. 2012.

- [137] A. Dong *et al.*, “General synthesis of mesoporous spheres of metal oxides and phosphates,” *J. Am. Chem. Soc.*, vol. 125, no. 17, pp. 4976–4977, Apr. 2003.
- [138] X. Lai, X. Li, W. Geng, J. Tu, J. Li, and S. Qiu, “Ordered Mesoporous Copper Oxide with Crystalline Walls,” *Angew. Chemie Int. Ed.*, vol. 46, no. 5, pp. 738–741, Jan. 2007.
- [139] J. Roggenbuck and M. Tiemann, “Ordered Mesoporous Magnesium Oxide with High Thermal Stability Synthesized by Exotemplating Using CMK-3 Carbon,” *J. Am. Chem. Soc.*, vol. 127, no. 4, pp. 1096–1097, Feb. 2005.
- [140] J. Roggenbuck, G. Koch, and M. Tiemann, “Synthesis of Mesoporous Magnesium Oxide by CMK-3 Carbon Structure Replication,” *Chem. Mater.*, vol. 18, no. 17, pp. 4151–4156, Aug. 2006.
- [141] A. Chernikov, S. Horst, T. Waitz, M. Tiemann, and S. Chatterjee, “Photoluminescence properties of ordered mesoporous ZnO,” *J. Phys. Chem. C*, vol. 115, no. 5, pp. 1375–1379, Feb. 2011.
- [142] W. M. Kwok, A. B. Djurišić, Y. H. Leung, W. K. Chan, and D. L. Phillips, “Time-resolved photoluminescence study of the stimulated emission in ZnO nanoneedles,” *Appl. Phys. Lett.*, vol. 87, no. 9, p. 093108, Aug. 2005.
- [143] T. Wagner, T. Waitz, J. Roggenbuck, M. Fröba, C.-D. Kohl, and M. Tiemann, “Ordered mesoporous ZnO for gas sensing,” *Thin Solid Films*, vol. 515, no. 23, pp. 8360–8363, Sep. 2007.
- [144] T. Waitz, M. Tiemann, P. J. Klar, J. Sann, J. Stehr, and B. K. Meyer, “Crystalline ZnO with an enhanced surface area obtained by nanocasting,” *Appl. Phys. Lett.*, vol. 90, no. 12, p. 123108, Mar. 2007.
- [145] S. Polarz, A. V. Orlov, F. Schüth, and A.-H. Lu, “Preparation of High-Surface-Area Zinc Oxide with Ordered Porosity, Different Pore Sizes, and Nanocrystalline Walls,” *Chem. - A Eur. J.*, vol. 13, no. 2, pp. 592–597, Jan. 2007.
- [146] G. Zu *et al.*, “Highly thermally stable zirconia/silica composite aerogels prepared by supercritical deposition,” *Microporous Mesoporous Mater.*, vol. 238, pp. 90–96, Jan. 2017.
- [147] N. Pal, E.-B. Cho, A. K. Patra, and D. Kim, “Ceria-Containing Ordered Mesoporous Silica: Synthesis, Properties, and Applications,” *ChemCatChem*, vol. 8, no. 2, pp. 285–303, Jan. 2016.
- [148] E. B. Cho, S. Yim, D. Kim, and M. Jaroniec, “Surfactant-assisted synthesis of mesoporous silica/ceria-silica composites with high cerium content under basic conditions,” *J. Mater. Chem. A*, vol. 1, no. 40, pp. 12595–12605, Mar. 2013.
- [149] J. Roggenbuck, H. Schäfer, T. Tsoncheva, C. Minchev, J. Hanss, and M. Tiemann, “Mesoporous CeO₂: Synthesis by nanocasting, characterisation and catalytic properties,” *Microporous Mesoporous Mater.*, vol. 101, no. 3, pp. 335–341, Apr. 2007.
- [150] L. M. Anovitz and D. R. Cole, “Characterization and analysis of porosity and pore structures,” *Rev. Mineral. Geochemistry*, vol. 80, no. 1, pp. 61–164, Jan. 2015.
- [151] O. Ersen, I. Florea, C. Hirlimann, and C. Pham-Huu, “Exploring nanomaterials with 3D electron microscopy,” *Mater. Today*, vol. 18, no. 7, pp. 395–408, Sep. 2015.
- [152] N. Jiang, “Electron beam damage in oxides: a review,” *Reports Prog. Phys.*, vol. 79, no. 1, p. 016501, Jan. 2016.
- [153] A. Nafari, J. Angenete, K. Svensson, A. Sanz-Velasco, and P. Enoksson, “MEMS sensor for in situ TEMnanoindentation with simultaneous force and current measurements,” *J. Micromechanics Microengineering*, vol. 20, no. 6, Jun. 2010.
- [154] Y. Wang, T. Li, X. Zhang, H. Zeng, and Q. Jin, “In situ TEM/SEM electronic/mechanical characterization of nano material with MEMS chip,” *J.*

- Semicond.*, vol. 35, no. 8, p. 081001, Aug. 2014.
- [155] M. R. Ward, E. D. Boyes, and P. L. Gai, "In situ aberration-corrected environmental TEM: Reduction of model Co_3O_4 in H_2 at the atomic level," *ChemCatChem*, vol. 5, no. 9, pp. 2655–2661, Sep. 2013.
- [156] P. L. Gai and E. D. Boyes, "In-situ environmental (scanning) transmission electron microscopy of catalysts at the atomic level," *J. Phys. Conf. Ser.*, vol. 522, no. 1, p. 012002, Jun. 2014.
- [157] P. L. Gai and E. D. Boyes, "Angstrom analysis with dynamic in-situ aberration corrected electron microscopy," *J. Phys. Conf. Ser.*, vol. 241, p. 012055, Jul. 2010.
- [158] H. Zheng, Y. S. Meng, and Y. Zhu, "Frontiers of in situ electron microscopy," *MRS Bull.*, vol. 40, no. 1, pp. 12–18, Jan. 2015.
- [159] H. Zheng and Y. Zhu, "Perspectives on in situ electron microscopy," *Ultramicroscopy*, vol. 180, pp. 188–196, Sep. 2017.
- [160] M. L. Taheri *et al.*, "Current status and future directions for in situ transmission electron microscopy," *Ultramicroscopy*, vol. 170, pp. 86–95, Nov. 2016.
- [161] R. Sinclair, "In situ high-resolution transmission electron microscopy of material reactions," *MRS Bull.*, vol. 38, no. 12, pp. 1065–1071, Dec. 2013.
- [162] T. Montini, M. Melchionna, M. Monai, and P. Fornasiero, "Fundamentals and Catalytic Applications of CeO_2 -Based Materials," *Chem. Rev.*, vol. 116, no. 10, pp. 5987–6041, May 2016.
- [163] C. Sun, H. Li, and L. Chen, "Nanostructured ceria-based materials: synthesis, properties, and applications," *Energy Environ. Sci.*, vol. 5, no. 9, pp. 8475–8505, Jun. 2012.
- [164] T. X. T. Sayle, S. C. Parker, and C. R. A. Catlow, "The role of oxygen vacancies on ceria surfaces in the oxidation of carbon monoxide," *Surf. Sci.*, vol. 316, no. 3, pp. 329–336, Sep. 1994.
- [165] OSHA, "Factsheet 3522: Carbon Monoxide Poisoning," 2012. [Online]. Available: www.osha.gov. [Accessed: 12-Aug-2019].
- [166] D. D. Parrish *et al.*, "Relationships between ozone and carbon monoxide at surface sites in the North Atlantic region," *J. Geophys. Res. Atmos.*, vol. 103, no. D11, pp. 13357–13376, Jun. 1998.
- [167] N. Guillén-hurtado, V. Rico-pérez, D. Lozano-castelló, and A. Bueno-lópez, "Three-way catalysts: Past, Present and Future," *Dyna*, vol. 79, pp. 114–121, Oct. 2012.
- [168] Q. Wang, B. Zhao, G. Li, and R. Zhou, "Application of Rare Earth Modified Zr-based Ceria-Zirconia Solid Solution in Three-Way Catalyst for Automotive Emission Control," *Environ. Sci. Technol.*, vol. 44, no. 10, pp. 3870–3875, May 2010.
- [169] E. Ruiz-Trejo and J. Maier, "Electronic Transport in Single Crystals of Gd-Doped Ceria," *J. Electrochem. Soc.*, vol. 154, no. 6, p. B583, May 2007.
- [170] Z. Kang and Z. Kang, "Quaternary Oxide of Cerium, Terbium, Praseodymium and Zirconium for Three-Way Catalysts," *J. Rare Earths*, vol. 24, no. 3, pp. 314–319, Jun. 2006.
- [171] C. Shao *et al.*, "Oxygen Vacancies Enhanced CeO_2 :Gd Nanoparticles for Sensing a Tumor Vascular Microenvironment by Magnetic Resonance Imaging," *ACS Nano*, vol. 12, no. 12, pp. 12629–12637, Dec. 2018.
- [172] Z. Yang, J. Wei, H. Yang, L. Liu, H. Liang, and Y. Yang, "Mesoporous CeO_2 Hollow Spheres Prepared by Ostwald Ripening and Their Environmental Applications," *Eur. J. Inorg. Chem.*, vol. 2010, no. 21, pp. 3354–3359, May 2010.
- [173] C. Pan, D. Zhang, L. Shi, and J. Fang, "Template-Free Synthesis, Controlled Conversion, and CO Oxidation Properties of CeO_2 Nanorods, Nanotubes, Nanowires,

- and Nanocubes,” *Eur. J. Inorg. Chem.*, vol. 2008, no. 15, pp. 2429–2436, May 2008.
- [174] C. Ho, J. C. Yu, T. Kwong, A. C. Mak, and S. Lai, “Morphology-Controllable Synthesis of Mesoporous CeO₂ Nano- and Microstructures,” *Chem. Mater.*, vol. 17, no. 17, pp. 4514–4522, Aug. 2005.
- [175] Z. Wu, M. Li, and S. H. Overbury, “On the structure dependence of CO oxidation over CeO₂ nanocrystals with well-defined surface planes,” *J. Catal.*, vol. 285, no. 1, pp. 61–73, Jan. 2012.
- [176] K. Liu, A. Wang, and T. Zhang, “Recent Advances in Preferential Oxidation of CO Reaction over Platinum Group Metal Catalysts,” *ACS Catal.*, vol. 2, no. 6, pp. 1165–1178, Jun. 2012.
- [177] Z. Hu, X. Liu, D. Meng, Y. Guo, Y. Guo, and G. Lu, “Effect of Ceria Crystal Plane on the Physicochemical and Catalytic Properties of Pd/Ceria for CO and Propane Oxidation,” *ACS Catal.*, vol. 6, no. 4, pp. 2265–2279, Apr. 2016.
- [178] S. Chen, L. Luo, Z. Jiang, and W. Huang, “Size-dependent reaction pathways of low-temperature CO oxidation on Au/CeO₂ catalysts,” *ACS Catal.*, vol. 5, no. 3, pp. 1653–1662, Mar. 2015.
- [179] C. T. Campbell and C. H. F. Peden, “Oxygen vacancies and catalysis on ceria surfaces,” *Science*, vol. 309, no. 5735, pp. 713–714, Jul. 2005.
- [180] A. Sood and S. Vyas, “Carbon Capture and Sequestration- A Review,” *IOP Conf. Ser. Earth Environ. Sci.*, vol. 83, p. 012024, Aug. 2017.
- [181] K. Yoshikawa, M. Kaneeda, and H. Nakamura, “Development of Novel CeO₂-based CO₂ adsorbent and analysis on its CO₂ adsorption and desorption mechanism,” *Energy Procedia*, vol. 114, pp. 2481–2487, Jul. 2017.
- [182] T. Sakakura, J.-C. Choi, Y. Saito, T. Masuda, T. Sako, and T. Oriyama, “Metal-Catalyzed Dimethyl Carbonate Synthesis from Carbon Dioxide and Acetals,” *J. Org. Chem.*, vol. 64, no. 12, pp. 4506–4508, Jun. 1999.
- [183] B. A. V. Santos, C. S. M. Pereira, V. M. T. M. Silva, J. M. Loureiro, and A. E. Rodrigues, “Kinetic study for the direct synthesis of dimethyl carbonate from methanol and CO₂ over CeO₂ at high pressure conditions,” *Appl. Catal. A Gen.*, vol. 455, pp. 219–226, Mar. 2013.
- [184] M. Honda *et al.*, “Tandem Carboxylation-Hydration Reaction System from Methanol, CO₂ and Benzonitrile to Dimethyl Carbonate and Benzamide Catalyzed by CeO₂,” *ChemCatChem*, vol. 3, no. 2, pp. 365–370, Feb. 2011.
- [185] M. Honda, M. Tamura, K. Nakao, K. Suzuki, Y. Nakagawa, and K. Tomishige, “Direct Cyclic Carbonate Synthesis from CO₂ and Diol over Carboxylation/Hydration Cascade Catalyst of CeO₂ with 2-Cyanopyridine,” *ACS Catal.*, vol. 4, no. 6, pp. 1893–1896, Jun. 2014.
- [186] M. Honda *et al.*, “Ceria-Catalyzed Conversion of Carbon Dioxide into Dimethyl Carbonate with 2-Cyanopyridine,” *ChemSusChem*, vol. 6, no. 8, pp. 1341–1344, Aug. 2013.
- [187] R. K. Grasselli, “Genesis of site isolation and phase cooperation in selective oxidation catalysis,” *Top. Catal.*, vol. 15, no. 2–4, pp. 93–101, Jun. 2001.
- [188] K. Reed *et al.*, “Exploring the properties and applications of nanoceria: is there still plenty of room at the bottom?,” *Environ. Sci. Nano*, vol. 1, no. 5, pp. 390–405, Oct. 2014.
- [189] W. C. Chueh and S. M. Haile, “Ceria as a thermochemical reaction medium for selectively generating syngas or methane from H₂O and CO₂,” *ChemSusChem*, vol. 2, no. 8, pp. 735–739, Aug. 2009.

- [190] S. Sato, F. Sato, H. Gotoh, and Y. Yamada, "Selective Dehydration of Alkanediols into Unsaturated Alcohols over Rare Earth Oxide Catalysts," *ACS Catal.*, vol. 3, no. 4, pp. 721–734, Apr. 2013.
- [191] M. Tamura, K. Shimizu, and A. Satsuma, "CeO₂-catalyzed Transformations of Nitriles and Amides," *Chem. Lett.*, vol. 41, no. 11, pp. 1397–1405, Nov. 2012.
- [192] L. Vivier and D. Duprez, "Ceria-Based Solid Catalysts for Organic Chemistry," *ChemSusChem*, vol. 3, no. 6, pp. 654–678, May 2010.
- [193] S. Zhang *et al.*, "Towards highly active Pd/CeO₂ for alkene hydrogenation by tuning Pd dispersion and surface properties of the catalysts," *Nanoscale*, vol. 9, no. 9, pp. 3140–3149, Feb. 2017.
- [194] S. D. Senanayake *et al.*, "Hydrogenation of CO₂ to Methanol on CeO_x/Cu(111) and ZnO/Cu(111) Catalysts: Role of the Metal–Oxide Interface and Importance of Ce³⁺ Sites," *J. Phys. Chem. C*, vol. 120, no. 3, pp. 1778–1784, Jan. 2016.
- [195] N. Perret *et al.*, "Selective hydrogenation of benzoic acid over Au supported on CeO₂ and Ce_{0.62}Zr_{0.38}O₂: Formation of benzyl alcohol," *J. Catal.*, vol. 317, pp. 114–125, Aug. 2014.
- [196] S. Zhang *et al.*, "High Catalytic Activity and Chemoselectivity of Sub-nanometric Pd Clusters on Porous Nanorods of CeO₂ for Hydrogenation of Nitroarenes," *J. Am. Chem. Soc.*, vol. 138, no. 8, pp. 2629–2637, Mar. 2016.
- [197] C. Xu and X. Qu, "Cerium oxide nanoparticle: a remarkably versatile rare earth nanomaterial for biological applications," *NPG Asia Mater.*, vol. 6, no. 3, pp. 1–16, Mar. 2014.
- [198] K. L. Heckman *et al.*, "Custom cerium oxide nanoparticles protect against a free radical mediated autoimmune degenerative disease in the brain," *ACS Nano*, vol. 7, no. 12, pp. 10582–10596, Dec. 2013.
- [199] E. G. Heckert, A. S. Karakoti, S. Seal, and W. T. Self, "The role of cerium redox state in the SOD mimetic activity of nanoceria," *Biomaterials*, vol. 29, no. 18, pp. 2705–2709, Jun. 2008.
- [200] A. Karakoti, S. Singh, J. M. Dowding, S. Seal, and W. T. Self, "Redox-active radical scavenging nanomaterials," *Chem. Soc. Rev.*, vol. 39, no. 11, pp. 4422–4432, Aug. 2010.
- [201] Y. Huang, J. Ren, and X. Qu, "Nanozymes: Classification, Catalytic Mechanisms, Activity Regulation, and Applications," *Chem. Rev.*, vol. 119, no. 6, pp. 4357–4412, Mar. 2019.
- [202] D. Zhang, X. Du, L. Shi, and R. Gao, "Shape-controlled synthesis and catalytic application of ceria nanomaterials," *Dalt. Trans.*, vol. 41, no. 48, pp. 14455–14475, Sep. 2012.
- [203] S. Carrettin, P. Concepción, A. Corma, J. M. López Nieto, and V. F. Puntes, "Nanocrystalline CeO₂ increases the activity of Au for CO oxidation by two orders of magnitude," *Angew. Chemie - Int. Ed.*, vol. 43, no. 19, pp. 2538–2540, May 2004.
- [204] P. Sudarsanam *et al.*, "Highly efficient cerium dioxide nanocube-based catalysts for low temperature diesel soot oxidation: the cooperative effect of cerium- and cobalt-oxides," *Catal. Sci. Technol.*, vol. 5, no. 7, pp. 3496–3500, May 2015.
- [205] J. Qin, J. Lu, M. Cao, and C. Hu, "Synthesis of porous CuO–CeO₂ nanospheres with an enhanced low-temperature CO oxidation activity," *Nanoscale*, vol. 2, no. 12, pp. 2739–2743, Oct. 2010.
- [206] T. X. T. Sayle *et al.*, "Structure–Activity Map of Ceria Nanoparticles, Nanocubes, and Mesoporous Architectures," *Chem. Mater.*, vol. 28, no. 20, pp. 7287–7295, Oct. 2016.
- [207] D. Zhang, F. Niu, T. Yan, L. Shi, X. Du, and J. Fang, "Ceria nanospindles: Template-

- free solvothermal synthesis and shape-dependent catalytic activity,” *Appl. Surf. Sci.*, vol. 257, no. 23, pp. 10161–10167, Sep. 2011.
- [208] C. Pan, D. Zhang, and L. Shi, “CTAB assisted hydrothermal synthesis, controlled conversion and CO oxidation properties of CeO₂ nanoplates, nanotubes, and nanorods,” *J. Solid State Chem.*, vol. 181, no. 6, pp. 1298–1306, Jun. 2008.
- [209] Tana, M. Zhang, J. Li, H. Li, Y. Li, and W. Shen, “Morphology-dependent redox and catalytic properties of CeO₂ nanostructures: Nanowires, nanorods and nanoparticles,” *Catal. Today*, vol. 148, no. 1–2, pp. 179–183, Oct. 2009.
- [210] N. N. Bulgakov, V. A. Sadykov, V. V. Lunin, and E. Kemnitz, “Lattice defects and oxygen absorption/migration in ceria/ceria-zirconia solid solutions: Analysis by semiempirical interacting bonds method,” *React. Kinet. Catal. Lett.*, vol. 76, no. 1, pp. 103–110, Feb. 2002.
- [211] Y. Cui and W. L. Dai, “Support morphology and crystal plane effect of Cu/CeO₂ nanomaterial on the physicochemical and catalytic properties for carbonate hydrogenation,” *Catal. Sci. Technol.*, vol. 6, no. 21, pp. 7752–7762, Jun. 2016.
- [212] L. Liu, Z. Yao, Y. Deng, F. Gao, B. Liu, and L. Dong, “Morphology and Crystal-Plane Effects of Nanoscale Ceria on the Activity of CuO/CeO₂ for NO Reduction by CO,” *ChemCatChem*, vol. 3, no. 6, pp. 978–989, Apr. 2011.
- [213] M. Zabilskiy, P. Djinović, E. Tchernychova, O. P. Tkachenko, L. M. Kustov, and A. Pintar, “Nanoshaped CuO/CeO₂ Materials: Effect of the Exposed Ceria Surfaces on Catalytic Activity in N₂O Decomposition Reaction,” *ACS Catal.*, vol. 5, no. 9, pp. 5357–5365, Sep. 2015.
- [214] T. Sakthivel *et al.*, “Morphological Phase Diagram of Biocatalytically Active Ceria Nanostructures as a Function of Processing Variables and Their Properties,” *Chempluschem*, vol. 78, no. 12, pp. 1446–1455, Dec. 2013.
- [215] T. X. T. Sayle *et al.*, “Mechanical properties of ceria nanorods and nanochains; the effect of dislocations, grain-boundaries and oriented attachment,” *Nanoscale*, vol. 3, no. 4, p. 1823, Apr. 2011.
- [216] E. Armstrong and C. O’Dwyer, “Artificial opal photonic crystals and inverse opal structures-fundamentals and applications from optics to energy storage,” *J. Mater. Chem. C*, vol. 3, no. 24, pp. 6109–6143, May 2015.
- [217] J. Liu, L. Yan, X. Chen, S. Wang, M. Zhang, and C. Tian, “Direct synthesis of hollow polyhedral ceria nano powders via a template-free mixed solvothermal route,” *J. Rare Earths*, vol. 33, no. 8, pp. 892–897, Aug. 2015.
- [218] G. Chen, F. Zhu, X. Sun, S. Sun, and R. Chen, “Benign synthesis of ceria hollow nanocrystals by a template-free method,” *CrystEngComm*, vol. 13, no. 8, pp. 2904–2908, May 2011.
- [219] L. Zhou, X. Li, Y. Wang, M. Hong, Y. Liang, and J. Zhao, “Monodisperse, nanoporous ceria microspheres embedded with Pt nanoparticles: general facile synthesis and catalytic application,” *RSC Adv.*, vol. 4, no. 81, pp. 42965–42970, Aug. 2014.
- [220] T. X. T. Sayle, B. J. Inkson, G. Möbus, S. C. Parker, S. Seal, and D. C. Sayle, “Mechanical properties of mesoporous ceria nanoarchitectures,” *Phys. Chem. Chem. Phys.*, vol. 16, no. 45, pp. 24899–24912, Oct. 2014.
- [221] Y. Minamidate, S. Yin, and T. Sato, “Synthesis of Monodispersed rod-like and spherical CeO₂ particles by mild solution process,” *IOP Conf. Ser. Mater. Sci. Eng.*, vol. 1, p. 012003, Feb. 2009.
- [222] Q. Yuan, H.-H. Duan, L.-L. Li, L.-D. Sun, Y.-W. Zhang, and C.-H. Yan, “Controlled synthesis and assembly of ceria-based nanomaterials,” *J. Colloid Interface Sci.*, vol. 335,

- no. 2, pp. 151–167, Jul. 2009.
- [223] H. I. Chen and H. Y. Chang, “Synthesis of nanocrystalline cerium oxide particles by the precipitation method,” *Ceram. Int.*, vol. 31, no. 6, pp. 795–802, Jan. 2005.
- [224] S. H. Feng and G. H. Li, “Hydrothermal and Solvothermal Syntheses,” in *Modern Inorganic Synthetic Chemistry: Second Edition*, 2nd ed., R. Xu and Y. Xu, Eds. Amsterdam, Netherlands: Elsevier, 2017, pp. 73–104.
- [225] Z. Wu, M. Li, J. Howe, H. M. Meyer, and S. H. Overbury, “Probing Defect Sites on CeO₂ Nanocrystals with Well-Defined Surface Planes by Raman Spectroscopy and O₂ Adsorption,” *Langmuir*, vol. 26, no. 21, pp. 16595–16606, Nov. 2010.
- [226] G. Li, K. Chao, H. Peng, K. Chen, and Z. Zhang, “Facile Synthesis of CePO₄ Nanowires Attached to CeO₂ Octahedral Micrometer Crystals and Their Enhanced Photoluminescence Properties,” *J. Phys. Chem. C*, vol. 112, no. 42, pp. 16452–16456, Oct. 2008.
- [227] W. Wang *et al.*, “A surfactant and template-free route for synthesizing ceria nanocrystals with tunable morphologies,” *J. Mater. Chem.*, vol. 20, no. 36, pp. 7776–7781, Jul. 2010.
- [228] W. Q. Han, L. Wu, and Y. Zhu, “Formation and oxidation state of CeO₂-X nanotubes,” *J. Am. Chem. Soc.*, vol. 127, no. 37, pp. 12814–12815, Sep. 2005.
- [229] B. Tang, L. Zhuo, J. Ge, G. Wang, Z. Shi, and J. Niu, “A surfactant-free route to single-crystalline CeO₂ nanowires,” *Chem. Commun.*, no. 28, pp. 3565–3567, May 2005.
- [230] Y. Zhang, T. Cheng, Q. Hu, Z. Fang, and K. Han, “Study of the preparation and properties of CeO₂ single/multiwall hollow microspheres,” *J. Mater. Res.*, vol. 22, no. 6, pp. 1472–1478, Jun. 2007.
- [231] N. Ta, M. Zhang, J. Li, H. Li, Y. Li, and W. Shen, “Facile synthesis of CeO₂ nanospheres,” *Chinese J. Catal.*, vol. 29, no. 11, pp. 1070–1072, Nov. 2008.
- [232] Z.-R. Tang, Y. Zhang, and Y.-J. Xu, “A facile and high-yield approach to synthesize one-dimensional CeO₂ nanotubes with well-shaped hollow interior as a photocatalyst for degradation of toxic pollutants,” *RSC Adv.*, vol. 1, no. 9, pp. 1772–1777, Sep. 2011.
- [233] C. C. Tang, Y. Bando, B. D. Liu, and D. Golberg, “Cerium Oxide Nanotubes Prepared from Cerium Hydroxide Nanotubes,” *Adv. Mater.*, vol. 17, no. 24, pp. 3005–3009, Dec. 2005.
- [234] W. T. Chen, K. B. Chen, M. F. Wang, S. F. Weng, C. S. Lee, and M. C. Lin, “Enhanced catalytic activity of Ce_{1-x}M_xO₂ (M = Ti, Zr, and Hf) solid solution with controlled morphologies,” *Chem. Commun.*, vol. 46, no. 19, pp. 3286–3288, Mar. 2010.
- [235] Q. Wu *et al.*, “Great Influence of Anions for Controllable Synthesis of CeO₂ Nanostructures: From Nanorods to Nanocubes,” *J. Phys. Chem. C*, vol. 112, no. 44, pp. 17076–17080, Nov. 2008.
- [236] H. X. Mai *et al.*, “Shape-Selective Synthesis and Oxygen Storage Behavior of Ceria Nanopolyhedra, Nanorods, and Nanocubes,” *J. Phys. Chem. B*, vol. 109, no. 51, pp. 24380–24385, Dec. 2005.
- [237] L. Yan, R. Yu, J. Chen, and X. Xing, “Template-Free Hydrothermal Synthesis of CeO₂ Nano-octahedrons and Nanorods: Investigation of the Morphology Evolution,” *Cryst. Growth Des.*, vol. 8, no. 5, pp. 1474–1477, May 2008.
- [238] A. Vantomme, Z.-Y. Yuan, G. Du, and B.-L. Su, “Surfactant-Assisted Large-Scale Preparation of Crystalline CeO₂ Nanorods,” *Langmuir*, vol. 21, no. 3, pp. 1132–1135, Feb. 2005.
- [239] R. Yang and L. Guo, “Synthesis of cubic fluorite CeO₂ nanowires,” *J. Mater. Sci.*, vol. 40, no. 5, pp. 1305–1307, Mar. 2005.
- [240] L. Liao *et al.*, “Single CeO₂ Nanowire Gas Sensor Supported with Pt Nanocrystals: Gas

- Sensitivity, Surface Bond States, and Chemical Mechanism,” *J. Phys. Chem. C*, vol. 112, no. 24, pp. 9061–9065, Jun. 2008.
- [241] Y. Zhang, F. Hou, and Y. Tan, “CeO₂ nanoplates with a hexagonal structure and their catalytic applications in highly selective hydrogenation of substituted nitroaromatics,” *Chem. Commun.*, vol. 48, no. 18, pp. 2391–2393, Nov. 2012.
- [242] D. Zhang, L. Huang, J. Zhang, and L. Shi, “Facile synthesis of ceria rhombic microplates,” *J. Mater. Sci.*, vol. 43, no. 16, pp. 5647–5650, Aug. 2008.
- [243] T. Chen, Z. Xie, W. Jiang, W. Jiang, X. Zhang, and J. Liu, “Synthesis of CeO₂ nanosheets with a room temperature ionic liquid assisted method,” *J. Adv. Ceram.*, vol. 5, no. 2, pp. 111–116, Jun. 2016.
- [244] C. M. Phan and H. M. Nguyen, “Role of Capping Agent in Wet Synthesis of Nanoparticles,” *J. Phys. Chem. A*, vol. 121, no. 17, pp. 3213–3219, May 2017.
- [245] K. Zhou, Z. Yang, and S. Yang, “Highly Reducible CeO₂ Nanotubes,” *Chem. Mater.*, vol. 19, no. 6, pp. 1215–1217, Mar. 2007.
- [246] X. Wu and S. Kawi, “Synthesis, Growth Mechanism, and Properties of Open-Hexagonal and Nanoporous-Wall Ceria Nanotubes Fabricated via Alkaline Hydrothermal Route,” *Cryst. Growth Des.*, vol. 10, no. 4, pp. 1833–1841, Apr. 2010.
- [247] M. Melchionna and P. Fornasiero, “The role of ceria-based nanostructured materials in energy applications,” *Mater. Today*, vol. 17, no. 7, pp. 349–357, Sep. 2014.
- [248] Y. J. Feng, L. L. Liu, and X. D. Wang, “Hydrothermal synthesis and automotive exhaust catalytic performance of CeO₂ nanotube arrays,” *J. Mater. Chem.*, vol. 21, no. 39, pp. 15442–15448, Jun. 2011.
- [249] G. Hua, L. Zhang, G. Fei, and M. Fang, “Enhanced catalytic activity induced by defects in mesoporous ceria nanotubes,” *J. Mater. Chem.*, vol. 22, no. 14, pp. 6851–6855, Feb. 2012.
- [250] D. Zhang, H. Fu, L. Shi, J. Fang, and Q. Li, “Carbon nanotube assisted synthesis of CeO₂ nanotubes,” *J. Solid State Chem.*, vol. 180, no. 2, pp. 654–660, Feb. 2007.
- [251] A. Douy, “Polyacrylamide gel: An efficient tool for easy synthesis of multicomponent oxide precursors of ceramics and glasses,” *Int. J. Inorg. Mater.*, vol. 3, no. 7, pp. 699–707, Nov. 2001.
- [252] B. T. Holland, C. F. Blanford, and A. Stein, “Synthesis of Macroporous Minerals with Highly Ordered Three-Dimensional Arrays of Spheroidal Voids,” *Science*, vol. 281, no. 5376, pp. 538–540, Jul. 1998.
- [253] G. A. Umeda, W. C. Chueh, L. Noailles, S. M. Haile, and B. S. Dunn, “Inverse opal ceria–zirconia: architectural engineering for heterogeneous catalysis,” *Energy Environ. Sci.*, vol. 1, no. 4, p. 484, Jul. 2008.
- [254] D. Zhang, C. Pan, L. Shi, L. Huang, J. Fang, and H. Fu, “A highly reactive catalyst for CO oxidation: CeO₂ nanotubes synthesized using carbon nanotubes as removable templates,” *Microporous Mesoporous Mater.*, vol. 117, no. 1–2, pp. 193–200, Jan. 2009.
- [255] L. Čerović, V. Lair, O. Lupan, M. Cassir, and A. Ringuedé, “Electrochemical synthesis and characterization of nanorods, nanocolumnar ceria - Based thin films on different glass substrates,” *Chem. Phys. Lett.*, vol. 494, no. 4–6, pp. 237–242, Jul. 2010.
- [256] X. H. Lu *et al.*, “Facile electrochemical synthesis of single crystalline CeO₂ octahedrons and their optical properties,” *Langmuir*, vol. 26, no. 10, pp. 7569–7573, May 2010.
- [257] X. Lu *et al.*, “Redox cycles promoting photocatalytic hydrogen evolution of CeO₂ nanorods,” *J. Mater. Chem.*, vol. 21, no. 15, pp. 5569–5572, Apr. 2011.
- [258] C. S. Riccardi, R. C. Lima, M. L. dos Santos, P. R. Bueno, J. A. Varela, and E. Longo, “Preparation of CeO₂ by a simple microwave-hydrothermal method,” *Solid State Ionics*,

- vol. 180, no. 2–3, pp. 288–291, Mar. 2009.
- [259] C. Y. Cao, Z. M. Cui, C. Q. Chen, W. G. Song, and W. Cai, “Ceria hollow nanospheres produced by a template-free microwave-assisted hydrothermal method for heavy metal ion removal and catalysis,” *J. Phys. Chem. C*, vol. 114, no. 21, pp. 9865–9870, Jun. 2010.
- [260] Y. Li *et al.*, “Coupling oxygen ion conduction to photocatalysis in mesoporous nanorod-like ceria significantly improves photocatalytic efficiency,” *J. Phys. Chem. C*, vol. 115, no. 29, pp. 14050–14057, Jul. 2011.
- [261] X. H. Liao, J. M. Zhu, J. J. Zhu, J. Z. Xu, and H. Y. Chen, “Preparation of monodispersed nanocrystalline CeO₂ powders by microwave irradiation,” *Chem. Commun.*, no. 10, pp. 937–938, May 2001.
- [262] B. Xia, I. W. Lenggoro, and K. Okuyama, “Synthesis of CeO₂ nanoparticles by salt-assisted ultrasonic aerosol decomposition,” *J. Mater. Chem.*, vol. 11, no. 12, pp. 2925–2927, Oct. 2001.
- [263] D. Zhang *et al.*, “Synthesis of CeO₂ Nanorods via Ultrasonication Assisted by Polyethylene Glycol,” *Inorg. Chem.*, vol. 46, no. 7, pp. 2446–2451, Apr. 2007.
- [264] J. J. Miao, H. Wang, Y. R. Li, J. M. Zhu, and J. J. Zhu, “Ultrasonic-induced synthesis of CeO₂ nanotubes,” *J. Cryst. Growth*, vol. 281, no. 2–4, pp. 525–529, Aug. 2005.
- [265] J. M. Christensen, D. Deiana, J. D. Grunwaldt, and A. D. Jensen, “Ceria prepared by flame spray pyrolysis as an efficient catalyst for oxidation of diesel soot,” *Catal. Letters*, vol. 144, no. 10, pp. 1661–1666, Oct. 2014.
- [266] M. K. Devaraju, X. Liu, K. Yusuke, S. Yin, and T. Sato, “Solvothermal synthesis and characterization of ceria–zirconia mixed oxides for catalytic applications,” *Nanotechnology*, vol. 20, no. 40, p. 405606, Oct. 2009.
- [267] J. Conesa, “Computer modeling of surfaces and defects on cerium dioxide,” *Surf. Sci.*, vol. 339, no. 3, pp. 337–352, Oct. 1995.
- [268] M. M. Branda, R. M. Ferullo, M. Causá, and F. Illas, “Relative stabilities of low index and stepped CeO₂ surfaces from hybrid and GGA + U implementations of density functional theory,” *J. Phys. Chem. C*, vol. 115, no. 9, pp. 3716–3721, Mar. 2011.
- [269] M. Nolan, S. Grigoleit, D. C. Sayle, S. C. Parker, and G. W. Watson, “Density functional theory studies of the structure and electronic structure of pure and defective low index surfaces of ceria,” *Surf. Sci.*, vol. 576, no. 1–3, pp. 217–229, Feb. 2005.
- [270] M. Nolan, S. C. Parker, and G. W. Watson, “The electronic structure of oxygen vacancy defects at the low index surfaces of ceria,” *Surf. Sci.*, vol. 595, no. 1–3, pp. 223–232, Dec. 2005.
- [271] N. Du, H. Zhang, B. Chen, X. Ma, and D. Yang, “Ligand-free self-assembly of ceria nanocrystals into nanorods by oriented attachment at low temperature,” *J. Phys. Chem. C*, vol. 111, no. 34, pp. 12677–12680, Aug. 2007.
- [272] G. Möbus, Z. Saghi, D. C. Sayle, U. M. Bhatta, A. Stringfellow, and T. X. T. Sayle, “Dynamics of polar surfaces on ceria nanoparticles observed in situ with single-atom resolution,” *Adv. Funct. Mater.*, vol. 21, no. 11, pp. 1971–1976, Jun. 2011.
- [273] D. R. Mullins, “The surface chemistry of cerium oxide,” *Surf. Sci. Rep.*, vol. 70, no. 1, pp. 42–85, Mar. 2015.
- [274] J. Paier, C. Penschke, and J. Sauer, “Oxygen Defects and Surface Chemistry of Ceria: Quantum Chemical Studies Compared to Experiment,” *Chem. Rev.*, vol. 113, no. 6, pp. 3949–3985, Jun. 2013.
- [275] L. Minervini, “Defect cluster formation in M₂O₃-doped CeO₂,” *Solid State Ionics*, vol. 116, no. 3–4, pp. 339–349, Jan. 1999.

- [276] M. Nolan, J. E. Fearon, and G. W. Watson, "Oxygen vacancy formation and migration in ceria," *Solid State Ionics*, vol. 177, no. 35–36, pp. 3069–3074, Nov. 2006.
- [277] W. Xu *et al.*, "In-situ atomic-scale observation of irradiation-induced void formation," *Nat. Commun.*, vol. 4, no. 1, p. 2288, Oct. 2013.
- [278] X. Liu, K. Zhou, L. Wang, B. Wang, and Y. Li, "Oxygen Vacancy Clusters Promoting Reducibility and Activity of Ceria Nanorods," *J. Am. Chem. Soc.*, vol. 131, no. 9, pp. 3140–3141, Mar. 2009.
- [279] P. Nandi and D. Das, "Photocatalytic degradation of Rhodamine-B dye by stable ZnO nanostructures with different calcination temperature induced defects," *Appl. Surf. Sci.*, vol. 465, no. September 2018, pp. 546–556, Jan. 2019.
- [280] S. Carenco *et al.*, "The core contribution of transmission electron microscopy to functional nanomaterials engineering," *Nanoscale*, vol. 8, no. 3, pp. 1260–1279, Jan. 2016.
- [281] National Research Council, Ed., "The Importance of Nanoscale Science and Technology," in *Small Wonders, Endless Frontiers*, Washington, D.C., USA: National Academy Press, 2002, pp. 4–9.
- [282] A. Webster, J. Greenman, and S. J. Haswell, "Development of microfluidic devices for biomedical and clinical application," *J. Chem. Technol. Biotechnol.*, vol. 86, no. 1, pp. 10–17, Jan. 2011.
- [283] L. Mu and R. L. Sprando, "Application of nanotechnology in cosmetics," *Pharmaceutical Research*, vol. 27, no. 8, pp. 1746–1749, Aug-2010.
- [284] K. Sharma, "Nanomaterials for drug delivery," in *Advances in Personalized Nanotherapeutics*, A. Kaushik, R. D. Jayant, and M. Nair, Eds. Cham, Switzerland: Springer International Publishing, 2017, pp. 57–77.
- [285] J. Joy, J. Mathew, and S. C. George, "Nanomaterials for photoelectrochemical water splitting – review," *International Journal of Hydrogen Energy*, vol. 43, no. 10. Elsevier Ltd, pp. 4804–4817, 08-Mar-2018.
- [286] C. N. R. Rao and A. K. Cheetham, "Science and technology of nanomaterials: current status and future prospects," *J. Mater. Chem.*, vol. 11, no. 12, pp. 2887–2894, Nov. 2001.
- [287] S. J. Chang, T. H. Meen, S. D. Prior, L. W. Ji, and S. J. Young, "Applications of Advanced Nanomaterials to Microelectronic and Photonic Devices," *J. Nanomater.*, vol. 2015, p. 1, Aug. 2015.
- [288] F. Dong, R. T. Koodali, H. Wang, and W. K. Ho, "Nanomaterials for environmental applications," *J. Nanomater.*, vol. 2014, pp. 1–4, Jun. 2014.
- [289] K. Ojha, S. Saha, P. Dagar, and A. K. Ganguli, "Nanocatalysts for hydrogen evolution reactions," *Phys. Chem. Chem. Phys.*, vol. 20, no. 10, pp. 6777–6799, 2018.
- [290] G. Aragay, F. Pino, and A. Merkoçi, "Nanomaterials for sensing and destroying pesticides," *Chem. Rev.*, vol. 112, no. 10, pp. 5317–5338, Oct. 2012.
- [291] S. Carenco, D. Portehault, C. Boissière, N. Mézailles, and C. Sanchez, "25th anniversary article: Exploring nanoscaled matter from speciation to phase diagrams: Metal phosphide nanoparticles as a case of study," *Adv. Mater.*, vol. 26, no. 3, pp. 371–389, Jan. 2014.
- [292] D. C. Sayle *et al.*, "Mapping Nanostructure: A Systematic Enumeration of Nanomaterials by Assembling Nanobuilding Blocks at Crystallographic Positions," *ACS Nano*, vol. 2, no. 6, pp. 1237–1251, Jun. 2008.
- [293] S. Yoon, B. Lee, J. Yun, J. G. Han, J. S. Lee, and J. H. Lee, "Systematic study of interdependent relationship on gold nanorod synthesis assisted by electron microscopy

- image analysis,” *Nanoscale*, vol. 9, no. 21, pp. 7114–7123, Jun. 2017.
- [294] B. D. Yao, Y. F. Chan, X. Y. Zhang, W. F. Zhang, Z. Y. Yang, and N. Wang, “Formation mechanism of TiO₂ nanotubes,” *Appl. Phys. Lett.*, vol. 82, no. 2, pp. 281–283, Jan. 2003.
- [295] A. E. Garcia-Bennett, O. Terasaki, S. Che, and T. Tatsumi, “Structural Investigations of AMS-n Mesoporous Materials by Transmission Electron Microscopy,” *Chem. Mater.*, vol. 16, no. 5, pp. 813–821, Mar. 2004.
- [296] M. Almgren, K. Edwards, and G. Karlsson, “Cryo transmission electron microscopy of liposomes and related structures,” *Colloids Surfaces A Physicochem. Eng. Asp.*, vol. 174, no. 1–2, pp. 3–21, Nov. 2000.
- [297] Y. Talmon, “Transmission Electron Microscopy of Complex Fluids: The State of the Art,” *Berichte der Bunsengesellschaft für Phys. Chemie*, vol. 100, no. 3, pp. 364–372, Mar. 1996.
- [298] F. Gramm *et al.*, “Complex zeolite structure solved by combining powder diffraction and electron microscopy,” *Nature*, vol. 444, no. 7115, pp. 79–81, Nov. 2006.
- [299] C. B. Murray, C. R. Kagan, and M. G. Bawendi, “Synthesis and characterization of monodisperse nanocrystals and close-packed nanocrystal assemblies,” *Annu. Rev. Mater. Sci.*, vol. 30, pp. 545–610, 2000.
- [300] G. Möbus and B. J. Inkson, “Nanoscale tomography in materials science,” *Materials Today*, vol. 10, no. 12, pp. 18–25, Dec-2007.
- [301] E. J. Miller, W. Trewby, A. F. Payam, L. Piantanida, C. Cafolla, and K. Voitchovsky, “Sub-nanometer resolution imaging with amplitude-modulation atomic force microscopy in liquid,” *J. Vis. Exp.*, vol. 2016, no. 118, Dec. 2016.
- [302] A. E. Vladár, M. T. Postek, and B. Ming, “On the Sub-Nanometer Resolution of Scanning Electron and Helium Ion Microscopes,” *Microsc. Today*, vol. 17, no. 2, pp. 6–13, Mar. 2009.
- [303] A. A. Gewirth and B. K. Niece, “Electrochemical applications of in situ scanning probe microscopy,” *Chem. Rev.*, vol. 97, no. 4, pp. 1129–1162, Jun. 1997.
- [304] P. Somani and M. Umeno, “Importance of Transmission Electron Microscopy for Carbon Nanomaterials Research,” in *Modern Research and Educational Topics in Microscopy*, A. Méndez-Vilas and J. Díaz, Eds. Badajoz, Spain: Formatex, 2007, pp. 634–642.
- [305] M. A. O’Keefe *et al.*, “Sub-Angstrom high-resolution transmission electron microscopy at 300 keV,” *Ultramicroscopy*, vol. 89, no. 4, pp. 215–41, Nov. 2001.
- [306] Y. Jiang *et al.*, “Electron ptychography of 2D materials to deep sub-ångström resolution,” *Nature*, vol. 559, no. 7714, pp. 343–349, Jul. 2018.
- [307] R. F. Egerton, “Mechanisms of radiation damage in beam-sensitive specimens, for TEM accelerating voltages between 10 and 300 kV,” *Microsc. Res. Tech.*, vol. 75, no. 11, pp. 1550–1556, Nov. 2012.
- [308] J. Kotakoski, D. Santos-Cottin, and A. V. Krasheninnikov, “Stability of graphene edges under electron beam: Equilibrium energetics versus dynamic effects,” *ACS Nano*, vol. 6, no. 1, pp. 671–676, Jan. 2012.
- [309] O. Ugurlu *et al.*, “Radiolysis to knock-on damage transition in zeolites under electron beam irradiation,” *Phys. Rev. B*, vol. 83, no. 11, p. 113408, Mar. 2011.
- [310] D. Zhang *et al.*, “Atomic-resolution transmission electron microscopy of electron beam-sensitive crystalline materials,” *Science*, vol. 359, no. 6376, pp. 675–679, Feb. 2018.
- [311] B. Ye *et al.*, “TEM investigation of irradiation damage in single crystal CeO₂,” *J. Nucl. Mater.*, vol. 414, no. 2, pp. 251–256, Jul. 2011.
- [312] L. F. He *et al.*, “In situ TEM observation of dislocation evolution in Kr-irradiated UO₂

- single crystal,” *J. Nucl. Mater.*, vol. 443, no. 1–3, pp. 71–77, Nov. 2013.
- [313] B. Ye *et al.*, “Irradiation effects in UO₂ and CeO₂,” *J. Nucl. Mater.*, vol. 441, no. 1–3, pp. 525–529, Oct. 2013.
- [314] R. F. Egerton, “Control of radiation damage in the TEM,” *Ultramicroscopy*, vol. 127, pp. 100–108, Apr. 2013.
- [315] V. E. Cosslett, “Radiation damage in the high resolution electron microscopy of biological materials: A review*,” *J. Microsc.*, vol. 113, no. 2, pp. 113–129, Jul. 1978.
- [316] E. Knapek and J. Dubochet, “Beam damage to organic material is considerably reduced in cryo-electron microscopy,” *J. Mol. Biol.*, vol. 141, no. 2, pp. 147–161, 1980.
- [317] R. N. Clough, G. Moldovan, and A. I. Kirkland, “Direct detectors for electron microscopy,” *J. Phys. Conf. Ser.*, vol. 522, no. 1, p. 012046, Jun. 2014.
- [318] D. B. Williams and C. B. Carter, *Transmission Electron Microscopy*, 2nd ed. New York, USA: Springer, 2009.
- [319] T.-Y. Yung *et al.*, “Synthesis of PtNi Alloy Nanoparticles on Graphene-Based Polymer Nanohybrids for Electrocatalytic Oxidation of Methanol,” *Catalysts*, vol. 6, no. 12, p. 201, Dec. 2016.
- [320] Z. Cao *et al.*, “Platinum-nickel alloy excavated nano-multipods with hexagonal close-packed structure and superior activity towards hydrogen evolution reaction,” *Nat. Commun.*, vol. 8, no. 1, p. 15131, Apr. 2017.
- [321] H. Erikson, A. Sarapuu, J. Solla-Gullón, and K. Tammeveski, “Recent progress in oxygen reduction electrocatalysis on Pd-based catalysts,” *J. Electroanal. Chem.*, vol. 780, pp. 327–336, Nov. 2016.
- [322] J. Sen Li *et al.*, “Coupled molybdenum carbide and reduced graphene oxide electrocatalysts for efficient hydrogen evolution,” *Nat. Commun.*, vol. 7, Apr. 2016.
- [323] Y.-T. Xu *et al.*, “Cage-Confinement Pyrolysis Route to Ultrasmall Tungsten Carbide Nanoparticles for Efficient Electrocatalytic Hydrogen Evolution,” *J. Am. Chem. Soc.*, vol. 139, no. 15, pp. 5285–5288, Apr. 2017.
- [324] N.-T. Suen, S.-F. Hung, Q. Quan, N. Zhang, Y.-J. Xu, and H. M. Chen, “Electrocatalysis for the oxygen evolution reaction: recent development and future perspectives,” *Chem. Soc. Rev.*, vol. 46, no. 2, pp. 337–365, Jan. 2017.
- [325] B. Han *et al.*, “Role of LiCoO₂ surface terminations in oxygen reduction and evolution kinetics,” *J. Phys. Chem. Lett.*, vol. 6, no. 8, pp. 1357–1362, Apr. 2015.
- [326] B. Zhang *et al.*, “Tuning the surface structure of supported PtNi x bimetallic electrocatalysts for the methanol electro-oxidation reaction,” *Chem. Commun.*, vol. 52, no. 20, pp. 3927–3930, Feb. 2016.
- [327] A. Epshteyn *et al.*, “Effective strategy for improving electrocatalyst durability by adhesive immobilization of catalyst nanoparticles on graphitic carbon supports,” *ACS Catal.*, vol. 5, no. 6, pp. 3662–3674, Jun. 2015.
- [328] S. Yang, J. Kim, Y. J. Tak, A. Soon, and H. Lee, “Single-Atom Catalyst of Platinum Supported on Titanium Nitride for Selective Electrochemical Reactions,” *Angew. Chemie Int. Ed.*, vol. 55, no. 6, pp. 2058–2062, Feb. 2016.
- [329] P. Yin *et al.*, “Single Cobalt Atoms with Precise N-Coordination as Superior Oxygen Reduction Reaction Catalysts,” *Angew. Chemie Int. Ed.*, vol. 55, no. 36, pp. 10800–10805, Aug. 2016.
- [330] C. Zhu *et al.*, “Self-Assembled Fe-N-Doped Carbon Nanotube Aerogels with Single-Atom Catalyst Feature as High-Efficiency Oxygen Reduction Electrocatalysts,” *Small*, vol. 13, no. 15, p. 1603407, Apr. 2017.
- [331] D. Wang *et al.*, “Spontaneous incorporation of gold in palladium-based ternary

- nanoparticles makes durable electrocatalysts for oxygen reduction reaction,” *Nat. Commun.*, vol. 7, no. 1, p. 11941, Sep. 2016.
- [332] A. Bin Yousaf *et al.*, “Single Phase PtAg Bimetallic Alloy Nanoparticles Highly Dispersed on Reduced Graphene Oxide for Electrocatalytic Application of Methanol Oxidation Reaction,” *Electrochim. Acta*, vol. 197, pp. 117–125, Apr. 2016.
- [333] C. Hu, D. Hou, and Z. Li, “Micro-mechanical properties of calcium sulfoaluminate cement and the correlation with microstructures,” *Cem. Concr. Compos.*, vol. 80, pp. 10–16, Jul. 2017.
- [334] Y. Pi *et al.*, “Trimetallic Oxyhydroxide Coralloids for Efficient Oxygen Evolution Electrocatalysis,” *Angew. Chemie*, vol. 129, no. 16, pp. 4573–4577, Apr. 2017.
- [335] P. Song, Y. Wang, J. Pan, W. Xu, and L. Zhuang, “Structure-activity relationship in high-performance iron-based electrocatalysts for oxygen reduction reaction,” *J. Power Sources*, vol. 300, pp. 279–284, Dec. 2015.
- [336] J. Deng *et al.*, “Triggering the electrocatalytic hydrogen evolution activity of the inert two-dimensional MoS₂ surface via single-atom metal doping,” *Energy Environ. Sci.*, vol. 8, no. 5, pp. 1594–1601, May 2015.
- [337] M. Li *et al.*, “Ultrafine jagged platinum nanowires enable ultrahigh mass activity for the oxygen reduction reaction,” *Science*, vol. 354, no. 6318, pp. 1414–1419, Dec. 2016.
- [338] S. Chauhan *et al.*, “Design of Low Pt Concentration Electrocatalyst Surfaces with High Oxygen Reduction Reaction Activity Promoted by Formation of a Heterogeneous Interface between Pt and CeOx Nanowire,” *ACS Appl. Mater. Interfaces*, vol. 8, no. 14, pp. 9059–9070, Apr. 2016.
- [339] M. E. Scofield *et al.*, “Correlating the chemical composition and size of various metal oxide substrates with the catalytic activity and stability of as-deposited Pt nanoparticles for the methanol oxidation reaction,” *Catal. Sci. Technol.*, vol. 6, no. 7, pp. 2435–2450, Apr. 2016.
- [340] Q. Shi *et al.*, “Sulfur and nitrogen co-doped carbon nanotubes for enhancing electrochemical oxygen reduction activity in acidic and alkaline media,” *J. Mater. Chem. A*, vol. 1, no. 47, pp. 14853–14857, Dec. 2013.
- [341] C. Tang *et al.*, “Topological Defects in Metal-Free Nanocarbon for Oxygen Electrocatalysis,” *Adv. Mater.*, vol. 28, no. 32, pp. 6845–6851, Aug. 2016.
- [342] G.-L. Tian *et al.*, “Toward Full Exposure of ‘Active Sites’: Nanocarbon Electrocatalyst with Surface Enriched Nitrogen for Superior Oxygen Reduction and Evolution Reactivity,” *Adv. Funct. Mater.*, vol. 24, no. 38, pp. 5956–5961, Oct. 2014.
- [343] Y. Zhu, Y. Lin, B. Zhang, J. Rong, B. Zong, and D. S. Su, “Nitrogen-Doped Annealed Nanodiamonds with Varied sp²/sp³ Ratio as Metal-Free Electrocatalyst for the Oxygen Reduction Reaction,” *ChemCatChem*, vol. 7, no. 18, pp. 2840–2845, Sep. 2015.
- [344] Y. Lin, Y. Zhu, B. Zhang, Y. A. Kim, M. Endo, and D. S. Su, “Boron-doped onion-like carbon with enriched substitutional boron: The relationship between electronic properties and catalytic performance,” *J. Mater. Chem. A*, vol. 3, no. 43, pp. 21805–21814, 2015.
- [345] G. Möbus and B. J. Inkson, “Three-dimensional reconstruction of buried nanoparticles by element-sensitive tomography based on inelastically scattered electrons,” *Appl. Phys. Lett.*, vol. 79, no. 9, pp. 1369–1371, Aug. 2001.
- [346] G. Möbus, R. C. Doole, and B. J. Inkson, “Spectroscopic electron tomography,” *Ultramicroscopy*, vol. 96, no. 3–4, pp. 433–451, Sep. 2003.
- [347] R. J. Spontak, M. C. Williams, and D. A. Agard, “Three-dimensional study of cylindrical morphology in a styrene-butadiene-styrene block copolymer,” *Polymer (Guildf.)*, vol.

- 29, no. 3, pp. 387–395, Mar. 1988.
- [348] A. Klug, “From Macromolecules to Biological Assemblies (Nobel Lecture),” 1983.
- [349] D. J. De Rosier and A. Klug, “Reconstruction of three dimensional structures from electron micrographs,” *Nature*, vol. 217, no. 5124, pp. 130–134, Jan. 1968.
- [350] W. Hoppe, R. Langer, G. Knesch, and C. Poppe, “Protein-Kristallstrukturanalyse mit Elektronenstrahlen,” *Naturwissenschaften*, vol. 55, no. 7, pp. 333–336, 1968.
- [351] S. Kohjiya, A. Kato, and Y. Ikeda, “Visualization of nanostructure of soft matter by 3D-TEM: Nanoparticles in a natural rubber matrix,” *Progress in Polymer Science (Oxford)*, vol. 33, no. 10, pp. 979–997, Oct-2008.
- [352] L. F. Kourkoutis, J. M. Pitzko, and W. Baumeister, “Electron Microscopy of Biological Materials at the Nanometer Scale,” *Annu. Rev. Mater. Res.*, vol. 42, no. 1, pp. 33–58, Aug. 2012.
- [353] N. Kawase, M. Kato, H. Nishioka, and H. Jinnai, “Transmission electron microtomography without the ‘missing wedge’ for quantitative structural analysis,” *Ultramicroscopy*, vol. 107, no. 1, pp. 8–15, Jan. 2007.
- [354] A. Qin *et al.*, “Hyperbranched polytriazoles: Click polymerization, regioisomeric structure, light emission, and fluorescent patterning,” *Macromolecules*, vol. 41, no. 11, pp. 3808–3822, Jun. 2008.
- [355] H. Sugimori, T. Nishi, and H. Jinnai, “Dual-Axis Electron Tomography for Three-Dimensional Observations of Polymeric Nanostructures,” *Macromolecules*, vol. 38, no. 24, pp. 10226–10233, Nov. 2005.
- [356] J. H. Laurer *et al.*, “Microstructural analysis of a cubic bicontinuous morphology in a neat SIS triblock copolymer,” *Macromolecules*, vol. 30, no. 13, pp. 3938–3941, Jun. 1997.
- [357] A. J. Koster, U. Ziese, A. J. Verkleij, A. H. Janssen, and K. P. De Jong, “Three-dimensional transmission electron microscopy: a novel imaging and characterization technique with nanometer scale resolution for materials science,” *J. Phys. Chem. B*, vol. 104, no. 40, pp. 9368–9370, Oct. 2000.
- [358] G. Haberfehlner, A. Orthacker, M. Albu, J. Li, and G. Kothleitner, “Nanoscale voxel spectroscopy by simultaneous EELS and EDS tomography,” *Nanoscale*, vol. 6, no. 23, pp. 14563–14569, Dec. 2014.
- [359] Z. Saggi, X. Xu, and G. Möbus, “EELS fine structure tomography using spectrum imaging,” in *EMC 2008 14th European Microscopy Congress 1–5 September 2008, Aachen, Germany*, 2009, pp. 427–428.
- [360] M. Weyland and P. Midgley, “Electron Tomography,” in *Nanocharacterisation*, vol. 211–299, 2015, pp. 22–31.
- [361] T. J. A. Slater, A. Janssen, P. H. C. Camargo, M. G. Burke, N. J. Zaluzec, and S. J. Haigh, “STEM-EDX tomography of bimetallic nanoparticles: A methodological investigation,” *Ultramicroscopy*, vol. 162, pp. 61–73, Mar. 2016.
- [362] D. Wolf, A. Lubk, F. Röder, and H. Lichte, “Electron holographic tomography,” *Curr. Opin. Solid State Mater. Sci.*, vol. 17, no. 3, pp. 126–134, Jun. 2013.
- [363] N. Winckelmans, T. Altantzis, M. Grzelczak, A. Sánchez-Iglesias, L. M. Liz-Marzán, and S. Bals, “Multimode Electron Tomography as a Tool to Characterize the Internal Structure and Morphology of Gold Nanoparticles,” *J. Phys. Chem. C*, vol. 122, no. 25, pp. 13522–13528, Jun. 2018.
- [364] C. Kübel *et al.*, “Recent advances in electron tomography: TEM and HAADF-STEM tomography for materials science and semiconductor applications,” *Microsc. Microanal.*, vol. 11, no. 5, pp. 378–400, Oct. 2005.

- [365] Z. Saghi, X. Xu, and G. Mobus, "Transition from quantitative to geometric tomography," *J. Phys. Conf. Ser.*, vol. 126, p. 012063, Aug. 2008.
- [366] T. N. Kukhta, N. R. Prokopchuk, and B. A. Howell, "A research note on environmental durability of powder polyester paint coatings," in *Physical Chemistry Research for Engineering and Applied Sciences, Volume 1: Principles and Technological Implications*, E. M. Pearce, B. A. Howell, R. A. Pethrick, and G. E. Zaikov, Eds. New York, USA: Apple Academic Press, 2015, pp. 233–246.
- [367] K. Heo, J. Yoon, K. S. Jin, S. Jin, and M. Ree, "Characterisation of pore structures in nanoporous materials for advanced bionanotechnology," *IEE Proc. Nanobiotechnology*, vol. 153, no. 4, pp. 121–128, 2006.
- [368] M. J. Díaz-Cabañas, M. A. Cambor, Z. Liu, T. Ohsuna, and O. Terasaki, "Zeolite syntheses using linear diquats of varying length in fluoride media. The synthesis of ITQ-8, ITQ-10, ITQ-14 and high silica Nu-87," *J. Mater. Chem.*, vol. 12, no. 2, pp. 249–257, Jan. 2002.
- [369] G. S. Larsen, P. Lin, K. E. Hart, and C. M. Colina, "Molecular simulations of pim-1-like polymers of intrinsic microporosity," *Macromolecules*, vol. 44, no. 17, pp. 6944–6951, Sep. 2011.
- [370] L. J. Abbott and C. M. Colina, "Atomistic structure generation and gas adsorption simulations of microporous polymer networks," *Macromolecules*, vol. 44, no. 11, pp. 4511–4519, Jun. 2011.
- [371] T. X. T. Sayle, S. C. Parker, and D. C. Sayle, "Shape of CeO₂ nanoparticles using simulated amorphisation and recrystallisation," *Chem. Commun.*, vol. 10, no. 21, p. 2438, Nov. 2004.
- [372] T. X. T. Sayle *et al.*, "Strain and architecture-tuned reactivity in ceria nanostructures; Enhanced catalytic oxidation of CO to CO₂," *Chem. Mater.*, vol. 24, no. 10, pp. 1811–1821, May 2012.
- [373] C. A. Schneider, W. S. Rasband, and K. W. Eliceiri, "NIH Image to ImageJ: 25 years of image analysis," *Nat. Methods*, vol. 9, no. 7, pp. 671–675, Jul. 2012.
- [374] C. Messaoudi, T. Boudier, C. Sorzano, and S. Marco, "TomoJ: tomography software for three-dimensional reconstruction in transmission electron microscopy," *BMC Bioinformatics*, vol. 8, no. 1, p. 288, Aug. 2007.
- [375] E. F. Pettersen *et al.*, "UCSF Chimera?A visualization system for exploratory research and analysis," *J. Comput. Chem.*, vol. 25, no. 13, pp. 1605–1612, Oct. 2004.
- [376] A. M. Pourrahimi, D. Liu, V. Ström, M. S. Hedenqvist, R. T. Olsson, and U. W. Gedde, "Heat treatment of ZnO nanoparticles: new methods to achieve high-purity nanoparticles for high-voltage applications," *J. Mater. Chem. A*, vol. 3, no. 33, pp. 17190–17200, Jul. 2015.
- [377] K. A. Eswar, J. Rouhi, H. F. Husairi, M. Rusop, and S. Abdullah, "Annealing Heat Treatment of ZnO Nanoparticles Grown on Porous Si Substrate Using Spin-Coating Method," *Adv. Mater. Sci. Eng.*, vol. 2014, pp. 1–6, Feb. 2014.
- [378] F. A. Akopov and D. N. Poluboyarinov, "Some properties of sintered ceria ceramics," *Refractories*, vol. 6, no. 3–4, pp. 196–201, Mar. 1965.
- [379] R. L. Penn and J. Banfield, "Imperfect Oriented Attachment: Dislocation Generation in Defect-Free Nanocrystals," *Science*, vol. 281, no. 5379, pp. 969–971, Aug. 1998.
- [380] X. Feng *et al.*, "Converting ceria polyhedral nanoparticles into single-crystal nanospheres," *Science*, vol. 312, no. 5779, pp. 1504–1508, Jun. 2006.
- [381] A. J. V Griffiths and T. Walther, "Quantification of carbon contamination under electron beam irradiation in a scanning transmission electron microscope and its suppression by

- plasma cleaning,” *J. Phys. Conf. Ser.*, vol. 241, no. Emag 2009, p. 012017, Jul. 2010.
- [382] L. H. Radzilowski, B. O. Carragher, and S. I. Stupp, “Three-dimensional self-assembly of rodcoil copolymer nanostructures,” *Macromolecules*, vol. 30, no. 7, pp. 2110–2119, Apr. 1997.
- [383] J. R. H. Manning, E. Routoula, and S. V. Patwardhan, “Preparation of Functional Silica Using a Bioinspired Method,” *J. Vis. Exp.*, vol. 2018, no. 138, pp. 1–9, Aug. 2018.
- [384] W. Stöber, A. Fink, and E. Bohn, “Controlled growth of monodisperse silica spheres in the micron size range,” *J. Colloid Interface Sci.*, vol. 26, no. 1, pp. 62–69, Jan. 1968.
- [385] T. Yokoi, T. Karouji, S. Ohta, J. N. Kondo, and T. Tatsumi, “Synthesis of mesoporous silica nanospheres promoted by basic amino acids and their catalytic application,” *Chem. Mater.*, vol. 22, no. 13, pp. 3900–3908, 2010.
- [386] Z. Cai, J. Teng, D. Xia, and X. S. Zhao, “Self-Assembly of Crack-Free Silica Colloidal Crystals on Patterned Silicon Substrates,” *J. Phys. Chem. C*, vol. 115, no. 20, pp. 9970–9976, May 2011.
- [387] A. Galukhin, D. Bolmatenkov, A. Emelianova, I. Zharov, and G. Y. Gor, “Porous Structure of Silica Colloidal Crystals,” *Langmuir*, vol. 35, no. 6, pp. 2230–2235, Feb. 2019.
- [388] S. Malhotra, J. Hesse, and L.-P. Blanchard, “Thermal decomposition of polystyrene,” *Polymer (Guildf.)*, vol. 16, no. 2, pp. 81–93, Feb. 1975.
- [389] C. A. Strydom and C. P. J. Van Vuuren, “The thermal decomposition of cerium(III) nitrate,” *J. Therm. Anal.*, vol. 32, pp. 157–160, May 1987.
- [390] J. Park, Y. Han, and H. Kim, “Formation of Mesoporous Materials from Silica Dissolved in Various NaOH Concentrations: Effect of pH and Ionic Strength,” *J. Nanomater.*, vol. 2012, pp. 1–10, May 2012.
- [391] Y. Shao, L. Wang, J. Zhang, and M. Anpo, “Synthesis of hydrothermally stable and long-range ordered Ce-MCM-48 and Fe-MCM-48 materials,” *J. Phys. Chem. B*, vol. 109, no. 44, pp. 20835–20841, 2005.
- [392] J. M. Aguirre, A. Gutiérrez, and O. Giraldo, “Simple route for the synthesis of copper hydroxy salts,” *J. Braz. Chem. Soc.*, vol. 22, no. 3, pp. 546–551, 2011.
- [393] P. Gaudin *et al.*, “CuO/SBA-15 materials synthesized by solid state grinding: Influence of CuO dispersion and multicycle operation on DeSOX performances,” *Appl. Catal. B Environ.*, vol. 181, pp. 379–388, Feb. 2016.
- [394] M. Zhu and I. E. Wachs, “Iron-Based Catalysts for the High-Temperature Water–Gas Shift (HT-WGS) Reaction: A Review,” *ACS Catal.*, vol. 6, no. 2, pp. 722–732, Feb. 2016.
- [395] O. Ersen *et al.*, “3D-TEM characterization of nanometric objects,” *Solid State Sci.*, vol. 9, no. 12, pp. 1088–1098, 2007.
- [396] A. H. Janssen, P. Van der Voort, A. J. Koster, and K. P. De Jong, “A 3D-TEM study of the shape of mesopores in SBA-15 and modified SBA-15 materials,” *Chem. Commun.*, vol. 1, no. 15, pp. 1632–1633, Jun. 2002.
- [397] A. Bartesaghi, P. Sprechmann, J. Liu, G. Randall, G. Sapiro, and S. Subramaniam, “Classification and 3D averaging with missing wedge correction in biological electron tomography,” *J. Struct. Biol.*, vol. 162, no. 3, pp. 436–450, Jun. 2008.